

Magneto-Optical Spectroscopic Studies of Multi-Heme Enzymes

Kate Haynes, PhD Thesis

University of East Anglia, School of Chemical Sciences

June 2013

© Kate Haynes, June 2013

This copy of the thesis has been supplied on the condition that anyone who consults it is understood to recognise that its copyright rests with the author and that the use of any information derived there from must be in accordance with current UK Copyright Law. In addition, any quotation or extract must include full attribution.

Kate Haynes, 2013

Magneto-Optical Spectroscopic Studies of Multi-Heme Enzymes

Abstract

Cytochrome cd_1 (cd_1) is a soluble, diheme enzyme located in the periplasm of denitrifying bacteria that catalyses the one-electron reduction of nitrite ion to nitric oxide. *Paracoccus pantotrophus* cd_1 undergoes an unusual coordinated ligand switch upon reduction to the diferrous state, whereby a distal tyrosine ligand dissociates from the active site d_1 -heme, while the ligands at the c -heme switch from *bis*-histidinyll to histidine/methionine. The processes that take place following re-oxidation of this enzyme have been studied using a combination of electronic absorption, electron paramagnetic resonance (EPR) and magnetic circular dichroism (MCD) spectroscopies. Rebinding of tyrosine to the d_1 -heme, and loss of the bound product occurs concomitantly with a switch back to *bis*-histidinyll ligation at the c -heme at a rate of $\sim 0.24 \text{ min}^{-1}$ at pH 6.50. However, this does not represent a return to the “as-prepared” conformation: the two c -heme histidine ligands are in a novel ‘parallel’ conformation.

MCD spectroscopy has been used to characterise the state formed when reduced cd_1 reacts with stoichiometric nitrite ion, a one-electron oxidant. A pH-dependent equilibrium between two forms of the semi-reduced product-bound enzyme is observed, $[d_1^{2+}\text{-NO } c^{3+}] \rightleftharpoons [d_1^{2+}\text{-NO}^+ c^{2+}]$. A pK_a of 7.10 is assigned to protonation of a distal histidine residue. It is proposed that in the protonated form His-H^+ , this residue stabilises the $d_1^{2+}\text{-NO}$ form of the active site.

Ligand binding to the enzyme SoxAX, a tri-heme thiosulfate oxidase from *Rhodovulum sulfidophilum* has been studied using a combination of electronic absorbance and EPR

spectroscopies. The enzyme proved to be resistant to ligand binding in the 'as prepared' state. Only by redox cycling in presence of excess concentrations of potassium cyanide (KCN) has it been possible to achieve ligand binding to at least one of the three *c*-type hemes.

Contents

| | | |
|-----------|---|-----------|
| 1. | Introduction | 1 |
| 1.1 | Aim of this thesis | 1 |
| 1.2 | Introduction to hemes and hemoproteins | 2 |
| | 1.2.1 The heme cofactor | 2 |
| | 1.2.2 Structural variants of protoheme | 4 |
| 1.3 | Introduction to electron paramagnetic resonance spectroscopy | 6 |
| | 1.3.1 Spectroscopy: an overview | 6 |
| | 1.3.2 The free electron g-value | 7 |
| | 1.3.3 The Zeeman effect | 8 |
| | 1.3.4 The g-value | 11 |
| | 1.3.5 Hyperfine interactions | 14 |
| | 1.3.6 Zero-field splitting | 17 |
| | 1.3.7 Spin lattice relaxation and saturation | 20 |
| | 1.3.8 The continuous wave EPR spectrometer | 22 |
| 1.4 | Introduction to magnetic circular dichroism spectroscopy | 25 |
| | 1.4.1 The theory behind the technique | 25 |
| | 1.4.2 MCD A, B and C-Terms | 27 |
| | 1.4.3 Curie Law and the effects of temperature and magnetic field on C-term intensity | 29 |
| 1.5 | UV-visible absorbance, EPR and MCD of hemoproteins | 31 |
| | 1.5.1. Introduction to hemoprotein spectroscopy | 31 |
| | 1.5.2. Absorbance spectroscopy of hemoproteins | 31 |
| | 1.5.3. EPR spectra of low-spin ferric hemoproteins | 34 |
| | 1.5.4. UV-visible and near infra-red (NIR) MCD of low-spin ferric hemoproteins | 38 |
| | 1.5.5. UV-visible and near infra-red (NIR) MCD of low-spin ferrous hemoproteins | 42 |
| 1.6 | References | 42 |
| 2. | Structure and function of cytochrome <i>cd</i>₁ nitrite reductase | 45 |
| 2.1 | The nitrogen cycle | 45 |
| 2.2 | Nitrite reduction and cytochrome <i>cd</i> ₁ | 47 |
| | 2.2.1 The purification and isolation of <i>Pseudomonas</i> cytochrome oxidase | 47 |
| | 2.2.2 The characterisation of the <i>d</i> ₁ cofactor | 48 |
| 2.3 | <i>Paraccocus pantotrophus</i> cytochrome <i>cd</i> ₁ | 49 |
| 2.4 | The <i>P. pantotrophus</i> cytochrome <i>cd</i> ₁ electronic absorption spectrum | 51 |
| 2.5 | The X-band EPR spectrum of 'as prepared' <i>P. pantotrophus cd</i> ₁ | 52 |
| 2.6 | Crystallographic studies of <i>P. pantotrophus</i> cytochrome <i>cd</i> ₁ | 53 |
| | 2.6.1 The monoclinic crystal structure of <i>P. pantotrophus cd</i> ₁ | 53 |
| | 2.6.2 The unique ligand switch of <i>P. pantotrophus cd</i> ₁ | 57 |
| | 2.6.3 The alternative, tetragonal crystal structure of <i>P. pantotrophus cd</i> ₁ | 61 |
| 2.7 | Further crystallographic studies on <i>P. pantotrophus</i> cytochrome <i>cd</i> ₁ | 64 |
| | 2.7.1 The nitrite and nitric oxide-bound crystal structures | 64 |
| | 2.7.2 The cyanide-bound crystal structure | 66 |
| 2.8 | A pulse radiolysis study of <i>P. pantotrophus cd</i> ₁ | 68 |
| 2.9 | The Y25S mutant | 70 |

| | | |
|--------|---|----|
| 2.10 | Spectroscopic investigations of the <i>c</i> -heme ligation in semi-apo <i>P. pantotrophus cd₁</i> | 72 |
| 2.11 | An overview of the spectroscopic investigations carried out on <i>P. pantotrophus cd₁</i> as part of this thesis | 73 |
| 2.12 | Growth and purification of <i>P. pantotrophus cd₁</i> | 74 |
| 2.12.1 | Growth of <i>P. pantotrophus cd₁</i> | 74 |
| 2.12.2 | Purification of <i>P. pantotrophus cd₁</i> | 75 |
| 2.12.3 | Media details | 76 |
| 2.13 | References | 76 |

3. Spectroscopic investigations into the unique ligand switch of *P. pantotrophus cytochrome cd₁* nitrite reductase

79

| | | |
|-------|--|-----|
| 3.1 | The unique ligand switch of <i>P. pantotrophus cd₁</i> | 79 |
| 3.1.1 | The role of the Tyr ²⁵ ligand | 79 |
| 3.1.2 | Re-oxidation of ‘activated’ <i>P. pantotrophus cd₁</i> by hydroxylamine hydrochloride | 80 |
| 3.1.3 | Spectroscopic investigations by Allen <i>et al</i> | 81 |
| 3.1.4 | The rationale for a time-resolved NIR-MCD experiment to probe the <i>c</i> -heme ligand switch | 84 |
| 3.1.5 | The aims of this section of work | 86 |
| 3.2 | Experimental | 86 |
| 3.2.1 | Monitoring the hydroxylamine re-oxidation of <i>P. pantotrophus cd₁</i> by UV-visible absorbance spectroscopy | 86 |
| 3.2.2 | Monitoring hydroxylamine re-oxidation using X-band EPR spectroscopy | 88 |
| 3.2.3 | Monitoring hydroxylamine re-oxidation using NIR-MCD Spectroscopy | 89 |
| 3.2.4 | Instrument and buffer details | 93 |
| 3.3 | Results | 94 |
| 3.3.1 | Monitoring the hydroxylamine re-oxidation reaction by UV-visible absorbance spectroscopy | 94 |
| 3.3.2 | Investigating the effect of H ⁺ concentration on the ligand reversion at both hemes | 98 |
| 3.3.3 | Monitoring the hydroxylamine re-oxidation of <i>P. Pantotrophus cd₁</i> by X-band EPR spectroscopy | 108 |
| 3.3.4 | Monitoring the <i>c</i> -heme ligand reversion of <i>P. Pantotrophus cd₁</i> using a novel time-resolved NIR-MCD method | 115 |
| 3.4 | Discussion and conclusions | 125 |
| 3.5 | References | 135 |

4. Spectroscopic investigations of the *P. pantotrophus cd₁* NO-bound ferrous *d₁* intermediates

137

| | | |
|--------|--|-----|
| 4.1 | The formation of NO-bound <i>d₁²⁺</i> intermediates | 137 |
| 4.1.1. | The <i>P. pantotrophus cd₁</i> reaction mechanism | 137 |
| 4.1.2. | Spectroscopic characterisation of the reaction intermediates | 139 |
| 4.2 | Binding nitrite to ferric <i>d₁</i> -heme | 143 |
| 4.2.1. | Binding of nitrite to ferric, hydroxylamine re-oxidised <i>d₁</i> -heme | 143 |
| 4.2.2. | Reaction of nitrite with ferric <i>d₁</i> -heme in the ‘as prepared’ enzyme | 145 |
| 4.3 | The aims of this section of work | 150 |
| 4.4 | Experimental | 152 |
| 4.4.1 | Investigating the proportions of the NO-bound ferrous | |

| | | |
|--------|---|-----|
| | d_1 intermediates by absorbance spectroscopy | 152 |
| 4.4.2. | An overview of UV-visible MCD experiment | 153 |
| 4.4.3 | Experimental details of UV-visible MCD measurements | 153 |
| 4.4.4. | Instrument details | 155 |
| 4.5 | Results | 155 |
| 4.5.1 | Nitrite addition monitored by absorbance spectroscopy | 155 |
| 4.5.2. | Nitrite addition monitored by room temperature | |
| | UV-visible MCD spectroscopy | 159 |
| 4.5.3. | Calculation of the pKa for the NO-bound equilibrium | 173 |
| 4.5.4. | Observations relating to the d_1 -heme features | 176 |
| 4.6 | Discussion and conclusions | 178 |
| 4.7 | References | 184 |

5. **Ligand-binding trials on recombinant *R. sulfidophilum* SoxAX** 186

| | | |
|--------|---|-----|
| 5.1 | The TOMES mechanism | 186 |
| 5.2 | The SoxAX protein | 188 |
| 5.3 | Other cysteinyl-bound hemes: the cytochromes P450 | 194 |
| 5.4 | Experimental | 197 |
| 5.4.1 | SoxAX preparation and purification | 197 |
| 5.4.2 | Cloning of SoxAX for recombinant expression | 198 |
| 5.4.3 | Growth and purification of the SoxAX protein | 198 |
| 5.4.4 | Purification of SoxAX | 199 |
| 5.4.5 | Ligand additions to <i>R. sulfidophilum</i> SoxAX | 200 |
| 5.5 | Results | 201 |
| 5.5.1 | Spectroscopic characterisation of recombinant <i>R. sulfidophilum</i> SoxAX | 201 |
| 5.5.2. | Ligand-binding trials on <i>R. sulfidophilum</i> SoxAX | 205 |
| 5.6 | Discussion and conclusions | 213 |
| 5.7 | References | 216 |

Acknowledgements

I would like to begin by thanking my primary supervisor, Dr Myles Cheesman for his enthusiasm, support and advice over the past few years and in particular for introducing me to the wonderful world of cytochrome *cd*₁ (without which, this thesis would not have been possible!). I am also very grateful to my secondary supervisor, Professor Julea Butt, for her valuable contribution to the work on SoxAX, which I am delighted to say, resulted in a publication this year.

No words can express my gratitude to Dr Justin Bradley, who has been a wonderful mentor and friend and who has frequently gone above and beyond the call of duty to help me produce results worthy of being included in a thesis. I would also like to thank Dr John Holmes, for being a brilliant source of wisdom on all things involving the growth and purification of cytochrome *cd*₁. I am also grateful to Dr Ben Berks at Oxford University for providing the SoxAX protein used in this work. Additionally, I would like to thank Dr Rose-Marie Doyle, Dr Jason Crack, Dr Andrew Gates, Dr Gaye White and all the other past and present members of the Centre for Metalloprotein Spectroscopy and Biology (CMSB) who have provided assistance, advice and friendship.

On a personal level, I would like to thank Amber, Dave, Jonathan, Elle, Vicky M and Vicky H for providing me with an escape when needed it. Lastly, (but by no means least) I would like to thank my parents for their (seemingly) limitless support with what has undoubtedly been the biggest challenge of my life to date.

Dedication

This thesis is dedicated to my wonderful uncle, Anthony Hugh Powell (1948–2012), a man with a love of science and a never-ending thirst for knowledge.

1. Introduction

1.1 Aim of this thesis

The overall aim of this thesis is to describe two parallel spectroscopic studies on two contrasting multi-heme enzymes. The first of these, cytochrome *cd*₁ is a periplasmic, nitrite reductase protein that catalyses the one electron reduction of nitrite ion to nitric oxide. This process is carried out by denitrifying bacteria as part of the stepwise reduction of nitrate to gaseous dinitrogen. The second enzyme, SoxAX, forms part of the bacterial thiosulphate oxidising multi-enzyme system (TOMES), a pathway that is integral to the oxidative half of the global sulphur cycle.

Although these enzymes are very different in function and structural detail, their cofactors make them especially amenable to study using the specialist magneto-optical spectroscopic methods available at UEA. The techniques exploited in this work, UV-visible electronic absorption, electron paramagnetic resonance (EPR) and magnetic circular dichroism (MCD) spectroscopies offer a wealth of information about chemical species and are particularly useful for the structural characterisation of heme-containing enzymes.

This first chapter begins with an overview of hemoproteins in general and how the spectroscopic techniques named above can be used for their structural and mechanistic elucidation. Chapter 2 introduces cytochrome *cd*₁ and discusses its unique structural characteristics. A comprehensive overview of the relevant literature to date is provided, along with details of the growth and purification of the *Paracoccus pantotrophus* enzyme used in this work. Chapter 3 focusses on a novel, near-infrared MCD method that was specially adapted to probe the unique *c*-heme ligand switch that takes place following re-oxidation of the enzyme by hydroxylamine hydrochloride. In conjunction with UV-visible and EPR studies, this has led to a description of the correlation of the substantial structural

changes at the heme site that occur in each of the two domains as the enzyme is redox-cycled. Chapter 4 describes investigations using the same combination of spectroscopic techniques into the nature of d_1 -NO intermediates formed following re-oxidation of the enzyme by its substrate, nitrite.

Studies on the protein, SoxAX are described in Chapter 5. In contrast to *cytochrome cd₁*, SoxAX proved especially resistant to attempts to probe the heme sites, although some useful results were obtained towards the end of the study.

1.2 Introduction to hemes and hemoproteins

1.2.1 *The heme cofactor*

The term ‘hemoprotein’ refers to a protein containing a heme prosthetic group that may be covalently or non-covalently bound to the protein framework. The heme prosthetic group consists of an iron atom surrounded by a heterocyclic tetrapyrrole ring known as a porphyrin. The heme cofactor is arguably the most versatile and widely studied metal-factor in biochemistry, displaying a wide variety of functions, from electron transport to chemical catalysis. Over a series of enzyme-catalysed steps, a di-anionic tetrapyrrole is formed. This chelates to Fe^{2+} and undergoes further modification to form protoheme (illustrated in *Figure 1.2.1*). Also known as heme *b* (or ferriprotoporphyrin IX), protoheme is the cofactor present in a variety naturally-occurring proteins such as myoglobin, and the cytochromes P450. The latter refers to a superfamily of enzymes present throughout nature that are able to catalyse an extensive array of different processes ranging from drug and hormone metabolism in humans to fatty acid conjugation in plants (1,2).

Once formed, protoheme adopts a number of different physical and chemical properties (compared to Fe^{2+}) that can be beneficial to biological function. The ring

substituents are able to undergo further reactions to form other types of heme macrocycle (discussed in Section 1.2.2), such as heme *c*, in which the cofactor is covalently bound to the protein backbone through thioether linkages (3). The coordination of axial ligands to the iron porphyrin may also cause substantial changes in the properties of the complex, often altering the solubility, redox potential and metal spin state (1). During protein function, ligands are frequently removed or replaced in order to facilitate activity (4). Common heme axial ligands include side chains from amino acids such as histidine, methionine or cysteine, but may also be small solvent molecules such as hydroxide or water.

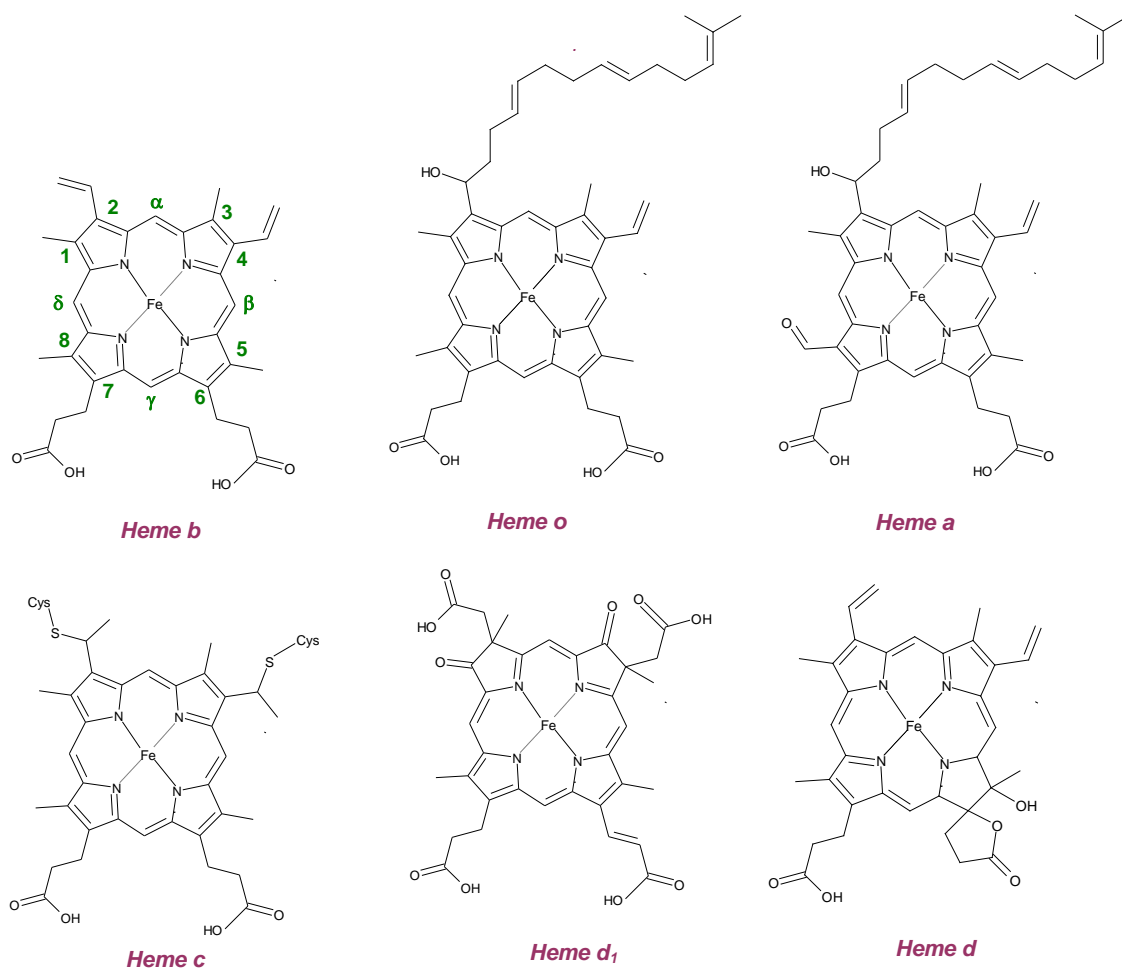


Figure 1.2.1: Some different naturally occurring structural variants of the heme cofactor. The principle carbon atoms of the *b*-heme (protoheme) pyrrole ring have also been labelled in the conventional manner.

1.2.2 *Structural variants of protoheme*

Protoheme is the starting point for the synthesis of all known naturally occurring types of heme (5). The structures of some of the most common hemes are shown in *Figure 1.2.1*. The biosynthesis of heme *o* from heme *b* is a one-step process that involves the replacement of the vinyl group at the 2-position with a 17-hydroxyethyl farnesyl residue (6).

Heme *a* possesses a closely related structure that is obtained with a further synthetic step; the hydroxylation of the methyl group at the 8-position to yield a formyl group. This particular cofactor is associated with oxidase enzymes, in particular cytochrome *c* oxidase, which is involved in the respiratory electron transport chains of mitochondria and a number of species of bacteria (7). Attachment of the heme *a* moiety to the apoprotein frequently occurs through a dative covalent bond between the iron and a conserved residue. Likewise, in heme *b*-containing proteins, the cofactor is held in this manner; in the case of myoglobin via a conserved histidine residue (8,9).

Other structural variations of heme *b* include heme *s* (located in the hemoglobin of marine worms), which is identical in structure to protoheme, apart from the replacement of the vinyl group at C-2 with a formyl group (1). Heme *m* is a form of protoheme that is covalently linked to aspartate and glutamate residues on the protein backbone through ether linkages to C-1 and C-5. Additionally, a sulphonium ion provides a covalent link between the vinyl group at C-2 and a methionine residue, a structural variation that causes the heme *m* to appear green in colour (1). This particular cofactor is found within myeloperoxidase, an enzyme expressed by neutrophil granulocytes as an integral part of the mammalian innate immune system (10).

Heme *l* is structurally equivalent to heme *b*, with the exception that it is covalently attached to glutamate and aspartate residues on the protein backbone of lactoperoxidase through

esterification of the C-1 and C-5 methyl groups. Secreted by the mucosal glands, lactoperoxidase is an oxidoreductase enzyme with antibacterial properties, and like myeloperoxidase plays an important role in the mammalian immune system (11).

Alternatively, in *c*-type hemoproteins, the heme is covalently bound to the protein backbone through thioether linkages (usually at C-2 and C-4, although a few *c*-type hemoproteins possess only one thioether linkage (12)) with the sulphydryl groups of conserved cysteine residues. This makes dissociation from the holoprotein more difficult (3). The small electron transport protein, mitochondrial cytochrome *c* is the best-known and most extensively studied example of a protein containing *c*-type heme.

In *c*-type cytochromes, the heme-binding motif CXXCH is commonly conserved. This indicates that the *c*-heme is covalently bonded to the holoprotein through linkages to two cysteine residues, while X may be any amino acid. The final amino acid in the sequence is histidine, which is axially coordinated to the metal (7). The remaining axial ligand coordinated to the heme iron (not included in the binding motif) in mitochondrial cytochrome *c* and all prokaryotic equivalent cytochromes is methionine.

The primary role of mitochondrial cytochrome *c* is respiratory electron transport, although there is some evidence to suggest that there is involvement in the process of apoptosis (cell death) (13), and in hydrogen peroxide scavenging (14). The latter function is also exhibited in the *c*-type hemoproteins of some bacterial species, along with involvement in a number of important respiratory processes.

The structure of heme *d* differs from that of protoheme in that the propionic side chain at C-6 is converted to a lactone, and that hydroxylation at the C-5 position has also occurred. This particular cofactor is largely associated with enzymes involved in the decomposition of hydrogen peroxide to oxygen and water (known as catalases), and with the reduction of oxygen in a number of bacterial species (15).

An interesting heme structural variant known as d_1 , also shown in *Figure 1.2.1*, is an iron dioxoisobacteriochlorin that is found exclusively in the homodimeric bacterial nitrite reductase protein cytochrome cd_1 (16,17). The structure of this particular cofactor exhibits oxo-groups at positions C-1 and C-3, an acrylic acid group at C-6, and acetic acid groups at C-2 and C-4. Each monomer contains both c and d_1 -type hemes (with the latter being the site of substrate binding), although the axial ligation to each of the metal centres varies with bacterial species. This particular cofactor is particularly interesting from a spectroscopy point of view as the four-fold symmetry of the porphyrin is no longer maintained. Another type of Fe-isobacteriochlorin is siroheme. In the sulphite reductase (SiR) enzyme of *Escherichia coli*, this cofactor is bridged to a cubane $[\text{Fe}_4\text{S}_4]$ cluster (18)

Hemoproteins are particularly amenable to study by absorbance spectroscopy as the spectra are diagnostic of the heme type, spin and oxidation state, as outlined in the following sections of this chapter.

1.3 Introduction to electron paramagnetic resonance spectroscopy

1.3.1 *Spectroscopy: An overview*

Spectroscopy is a valuable technique that involves the measurement and evaluation of the energy differences between atomic and molecular states by observing their interaction with electromagnetic radiation. Employed throughout the natural sciences, it allows insight into the structure, identity and behaviour of chemical and biochemical species. Planck's law states that the energy of a photon is equal to $h\nu$, where ν is the frequency of radiation, and h is Planck's constant: $6.626068 \times 10^{-34} \text{ m}^2 \text{ kg s}^{-1}$. A photon will be emitted or absorbed, causing a transition between atomic or molecular states when the difference in energy (ΔE) is equal to $h\nu$ (Equation 1).

$$\Delta E = h\nu \quad (1)$$

In techniques such as nuclear magnetic resonance (NMR) and absorbance spectroscopy, varying the frequency of radiation initiates such energy transitions. A particular transition will be strongest at the resonant frequency, when the energy of the radiation source matches the energy difference between the two states. Coupling between the two states is strongest at the resonant frequency, and the subsequent transition results in a spectral line. The radiation frequencies used in spectroscopic experiments vary, from the megahertz (1×10^6 Hz) range used for NMR experiments to those used in X-ray spectroscopy, which lie within the petahertz and exahertz (3×10^{15} and 3×10^{19} Hz respectively) regions.

1.3.2 *The free electron g-value*

Electron paramagnetic resonance (EPR) is a spectroscopic technique involving the resonant absorption of microwave radiation (within the gigahertz [10^9 Hz] region) by paramagnetic species (species containing at least one unpaired electron) in the presence of a static magnetic field. The technique can be applied to a variety of different paramagnetic species, including transition metal ions and free radicals, and has applications in a variety of scientific disciplines, including chemistry, materials science and medicine.

When an electron (or any charged species) possesses angular momentum, a magnetic dipole moment (μ) is generated. The magnitude of μ (for an electron) is given by the following equation:

$$\mu = g_e \cdot \gamma_e \cdot S \quad (2)$$

Where \mathbf{s} (the spin of the electron) and $\boldsymbol{\mu}$ itself are both vector quantities, and are hence shown in bold type. The magnitude of \mathbf{s} is calculated by Equation 3:

$$|\mathbf{s}| = \sqrt{s(s+1)} \cdot \hbar \quad (3)$$

Where \hbar is $h/2\pi$. The spin quantum number, s , is defined as $s = n/2$, where n is any non-negative integer. The proportionality coefficient, γ_e (known as the gyromagnetic ratio), represents the ratio between the z-component of the electron's magnetic dipole moment and the z-component of its spin angular momentum. This is an experimentally determined quantity, defined by Equation 4:

$$\gamma_e = -e / 2m_e \quad (4)$$

For an isolated electron, this value is $1.760859708 \times 10^{11} \text{ s}^{-1}\text{T}^{-1}$ (19), where m_e is the mass of the electron, taken to be $9.11 \times 10^{-31} \text{ kg}$ and e refers to its charge ($1.602 \times 10^{-19} \text{ C}$). The constant g_e is known as the 'free electron g-value' (20). The calculated value (2.0023193043617) has the best agreement with the experimentally-measured value of any physical constant.

1.3.3 The Zeeman effect

A free electron may align itself in either the parallel ($m_s = -1/2$) or anti-parallel ($m_s = +1/2$) direction relative to an applied magnetic field, B (*Figure 1.3.1*). In the absence of an applied magnetic field, the two spin states are of equal energy, but as the strength of B is gradually increased, they diverge linearly. This phenomenon is known as the Zeeman effect and the energy difference, ΔE , is given by $\Delta E = g_e \beta B$, as shown diagrammatically in

Figure 1.3.2 (21). The Bohr magneton (β) is the natural unit for the expression of an electron magnetic dipole moment.

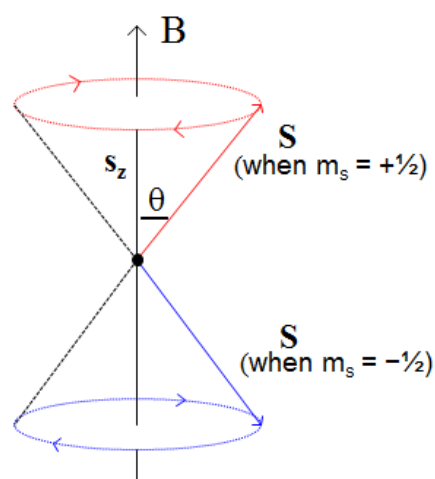


Figure 1.3.1: The unpaired electron may align itself either parallel or antiparallel to the direction of the applied magnetic field, with the former state being the lowest in energy. As the magnitude is given by $|\mathbf{S}| = \sqrt{s(s+1)}\hbar$, and the magnitude of the z-component of \mathbf{s} is $\frac{1}{2}$, the angle θ can be given by $\cos^{-1}(0.5 \times \sqrt{0.5(0.5+1)}) = 54.7^\circ$. Note that \hbar is dropped, and the value of \mathbf{s} is in atomic units.

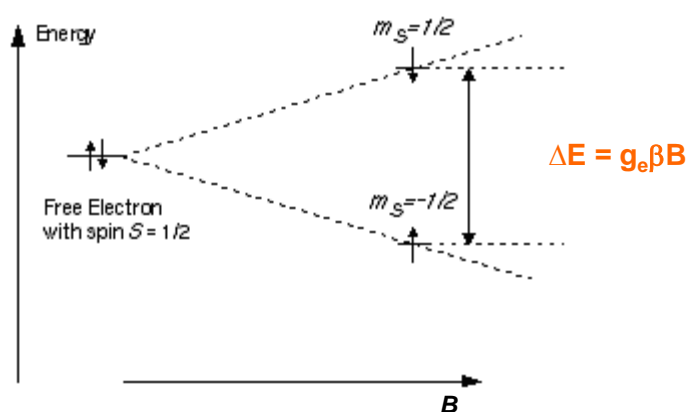


Figure 1.3.2: The Zeeman effect. The electron may align itself either parallel or antiparallel to the applied magnetic field. As the field strength (B) is gradually increased, the two energy levels diverge, leading to an energy separation defined by $\Delta E = g_e \beta B$, where β refers to the Bohr magneton, the unit of electronic magnetic moment.

The Maxwell-Boltzmann equation (Equation 5) describes the statistical distribution of a population in thermodynamic equilibrium:

$$\eta_{\text{upper}}/\eta_{\text{lower}} = \exp(-h\nu/kT) \quad (5)$$

At 298 K and a frequency of 3000 Gauss, the value of $\eta_{\text{upper}}/\eta_{\text{lower}}$ is approximately 0.998, resulting in transitions from the $m_s -1/2$ state to the $m_s +1/2$ state being more probable. This leads to a net absorption of energy and hence an EPR signal. The resonance condition is fulfilled when the energy level separation, ΔE , is equal to the photon energy. Magnetic dipole transitions are orders of magnitude less likely than electric dipole transitions as they involve the coupling of states with equal parity. According to the Laporte selection rule, this means they are ‘forbidden’ and as a result, the intensities observed in UV-visible absorbance spectroscopy are around 10^4 times stronger than those observed in EPR.

At the magnetic fields typically employed in EPR spectroscopy, the resonance condition is fulfilled for photon frequencies in the microwave region between 1 and 300 GHz. The conventional spectroscopic approach would be to fix the magnetic field strength, B_0 , and scan a range of frequencies until resonance (absorption) occurs. Owing to the fact that suitably stable, tunable microwave frequencies are not readily available, the technique adopted by basic EPR spectrometers is to hold the frequency fixed, and gradually increase the strength of the external magnetic field. Absorption occurs when the resonance condition is satisfied, resulting in an EPR spectrum, as illustrated in *Figure 1.3.3*. Due to the employment of a magnetic field modulation scheme incorporating phase sensitive detection (leading to an overall noise reduction) the first derivative (dA/dB) of the absorption curve is actually recorded.

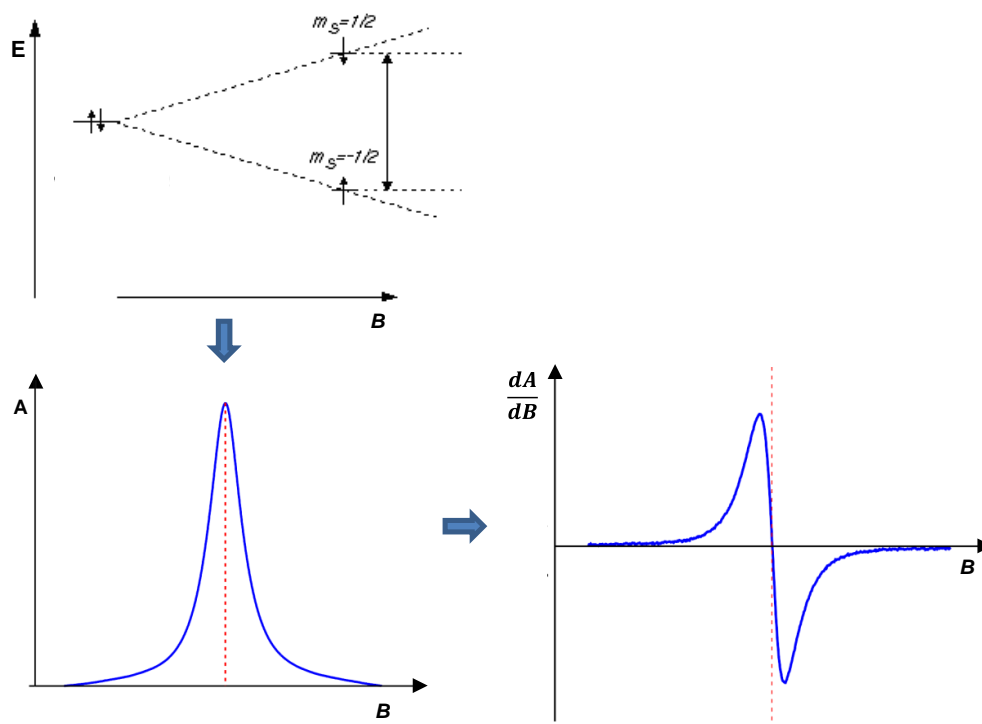


Figure 1.3.3: Absorption occurs when the resonance condition is satisfied, resulting in an EPR spectrum. Owing to the use of phase-sensitive detection, the signal displayed is the first derivative of the absorption intensity.

1.3.4 The *g*-value

EPR spectra obtained for a paramagnetic species may be acquired at several different frequencies, and hence the need arises for a parameter that is an intrinsic property of the unpaired electron itself. This parameter is the effective *g*-value, defined as $g_{\text{eff}} = \Delta E / \beta B$. For a simple spin $\frac{1}{2}$ species this is independent of microwave frequency and is essentially a measurement of how quickly the energy levels diverge with increasing magnetic field strength.

The need for an effective *g*-value arises since unpaired electrons confined in atoms and molecules may have an orbital contribution to their angular momentum. This is accounted for in the description of the EPR spectrum by assuming the angular momentum to be due only to electronic spin and by allowing the *g*-value to be a value other than the free electron value. In a low-symmetry environment, the angular momentum contribution

is directionally dependent and therefore the g -value becomes an anisotropic quantity – i.e. is not equal in all directions. This means that the g -value of a particular molecule will be dependent on the orientation of the external magnetic field to the molecular axes (21).

For a rapidly rotating molecule, this anisotropy is averaged and therefore not observed. However, EPR signals for most transition metal ions can only be obtained at low temperatures, typically at around 4–100 K. This necessitates working in frozen solution, trapping the molecules in fixed orientations relative to the magnetic field and thus making the anisotropy of the g -values visible in the EPR spectrum. For example, for a crystalline sample orientated so that B is aligned along the z -axis, resonance occurs with a particular value, g_z . If the crystal is then turned so that B is aligned along the xy plane, resonance occurs at a different field, with a different g -value, g_{xy} . If $g_x = g_y \neq g_z$, then the system is known as ‘axial’ and if $g_x \neq g_y \neq g_z$, a ‘rhombic’ spectrum is obtained. *Figure 1.3.4* demonstrates how the absorption envelopes of these two types of spectra appear.

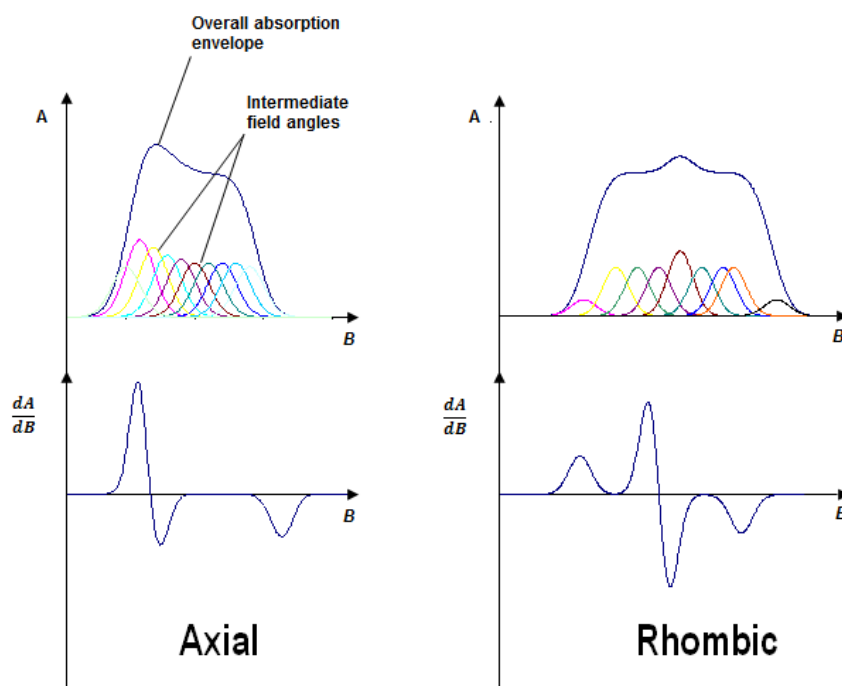


Figure 1.3.4: If $g_x = g_y \neq g_z$, the system is known as ‘axial’ (left), and if $g_x \neq g_y \neq g_z$, a ‘rhombic’ spectrum is obtained (right).

In the case of transition metal ions, shifts from the free electron g -value occur when the unpaired electron retains some orbital angular momentum but is not distributed equally among the d orbitals. The presence of a crystal field lifts this degeneracy, and rotation about one or more of the X, Y or Z-axes is impaired. For example, if the unpaired electron is spread over degenerate d_{yz} and d_{xz} orbitals in a tetragonal crystal field, it is in effect rotating about the Z-axis. Rotation about the X- or Y-axes cannot occur as there is no degenerate orbital onto which the orbital containing the electron can map (Figure 1.3.5). When the magnetic field is orientated parallel to this axis, the g_z -value is shifted from the free electron value. Conversely, as there is no angular momentum about the X or Y axes, the g_x and g_y values will be close to 2.0023.

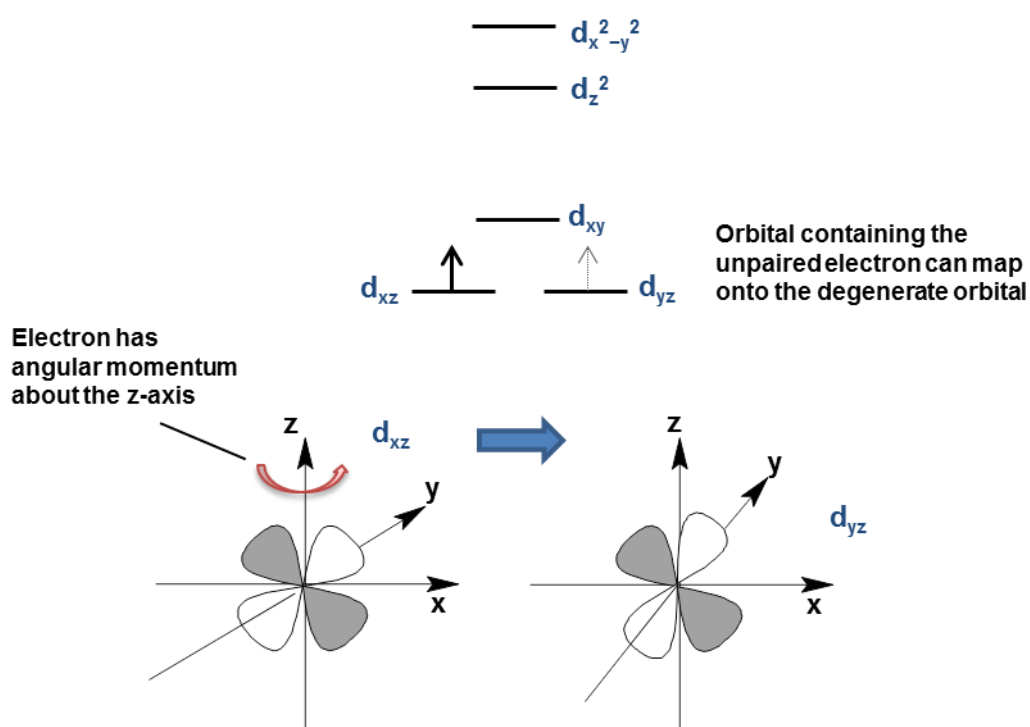


Figure 1.3.5: The unpaired electron is spread over degenerate d_{xz} and d_{yz} orbitals and is in effect rotating about the Z-axis. When the magnetic field is orientated parallel to this axis, the g_z -value is shifted from the free electron value.

Formally non-degenerate energy levels can also be 'mixed in' with each other by way of spin-orbit coupling. This is a symmetry-dependant process in which the orbital

containing the unpaired electron can interact with others and cause deviations from the free electron g - value. The magnitude of this effect is given by Equation 6:

$$g = g_e \pm n\lambda/\Delta \quad (6)$$

Where λ is the spin-orbit coupling constant, Δ is an effective energy separation to the mixing orbital and n is an integer value. This leads to typical values in the region of $g = 4.0$ – 1.0 and $g_x \sim g_y = 6.0$, $g_z = 2.0$ for low-spin and high-spin ferric hemes respectively (22,23).

1.3.5 *Hyperfine interactions*

The properties of the unpaired electron are very sensitive to the local surroundings and this makes EPR an extremely effective tool in deducing structural information, as the form and shape of the spectrum reflects the symmetry of the ligand field around the metal. For example, in a transition metal complex containing low-spin Fe^{3+} (d^5 , $S = 1/2$), the electronic moment can interact with nuclear moments of nearby ligands. The simplest case is to consider the hydrogen atom, ^1H , which contains a single unpaired electron and a single proton, each with a spin of $1/2$. Both of these possess a magnetic moment that can interact with the applied field and hence contribute to the Zeeman energy of the atom. If the electronic and nuclear spins were unaffected by each other, there would be two possible transitions, one corresponding to radio frequencies (NMR) and the other corresponding to microwave frequencies (EPR). However, interactions between the electronic and nuclear magnetic moments results in hyperfine splitting, as defined in Equation 7.

$$E_{\text{hyperfine}} = a.\mathbf{I.S} \quad (7)$$

Where 'a' is the hyperfine coupling constant. Like the unpaired electron, the magnetic moment of the nucleus behaves like a bar magnet (although considerably weaker in comparison), and produces a local magnetic field. Depending on its alignment, it may either add to, or oppose B , and thus the field for resonance is either raised or lowered accordingly (24).

In the case of the ^1H atom, if the proton's spin is orientated parallel to the applied field, its magnetic moment will add to B causing the local field experienced by the electron to increase in magnitude. The result is a greater splitting in the Zeeman energy levels. An anti-parallel alignment of the proton's spin relative to B causes the opposite effect to occur, and hence reducing the splitting of the Zeeman energy levels. As there are now two different transitions occurring at different energies (*Figure 1.3.6*), the resulting spectrum consists of two lines.

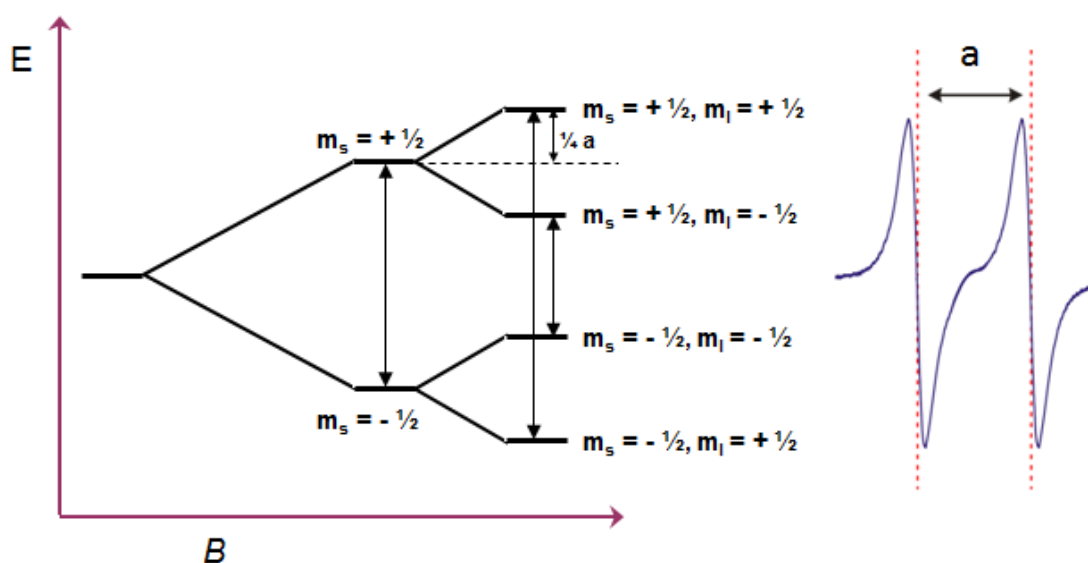


Figure 1.3.6: How the possible orientations of the electron and proton in a ^1H atom gives rise to two transitions upon the application of B_0 if they acted independently. The selection rules for an allowed transition are $\Delta m_s = \pm 1$ for the electron and $\Delta m_I = 0$ for the nucleus.

The hyperfine interaction causes the original EPR signal to be split into $2I + 1$ lines, where I is the spin of the magnetic nucleus. It therefore follows that the greater the value of I , the greater the number of hyperfine lines observed in the spectrum. The general rule is

that for N nuclei with spin of $\frac{1}{2}$ (such as that on a hydrogen atom); 2^N signals will be observed on the EPR spectrum. Therefore, if there are two more hydrogen nuclei within close proximity of the unpaired electron, there will be $2^3 =$ eight observable transitions, although depending on the relative magnitudes of line width and hyperfine interaction, these may not all be resolved.

In the case of the ^1H atom, the unpaired electron is located in an s orbital, leading to a non-zero probability that there is electron density at or inside the nucleus. The interaction between the electron and nucleus occurs via the Fermi contact interaction, an isotropic effect given by Equation 8.

$$U = -\frac{8}{3} \pi (\mu_I \cdot \mu_E) \psi^2(0) \quad (8)$$

U is the energy of interaction, μ_I and μ_E are the nuclear and electron magnetic moments respectively and $\psi^2(0)$ is the probability of the electron being located at the nucleus. The distance between the spectral hyperfine lines is known as A_{iso} , and the expected value of this quantity (in Gauss) can be calculated by measuring the spectrum. However, deviations from this expected value frequently occur due to the unpaired electron possessing less than ‘pure’ s character.

If the unpaired electron is located purely in a p or d orbital, there is a node at the nucleus and hence a zero probability that electron density will be found there. Interaction between the unpaired electron and the nuclear spin occurs via dipolar coupling in this instance, an anisotropic effect. In solution, very rapid molecular motion leads to an averaging of dipole-dipole interactions and only the isotropic contribution is observed. For frozen solutions, the sum of both the anisotropic and isotropic contributions is observed for each molecular orientation relative to the external field.

1.3.6 Zero-field splitting

Zero-field splitting describes the removal of spin microstate degeneracy for paramagnetic species with S greater than $1/2$, in the absence of an applied magnetic field. For example, a high-spin ferric ion possesses five unpaired electrons making the total spin of the system $5/2$. If this ion existed in space with perfect octahedral symmetry there would be six degenerate orientations of the spin vector. The application of an external magnetic field would lead to a Zeeman splitting, lifting the degeneracy of these energy levels and producing five possible transitions. Each allowed transition between states would be of equal energy ($\Delta E = g_e \beta B_0$) and would satisfy the selection rule $\Delta m_s = \pm 1$. This scenario is illustrated in *Figure 1.3.7*.

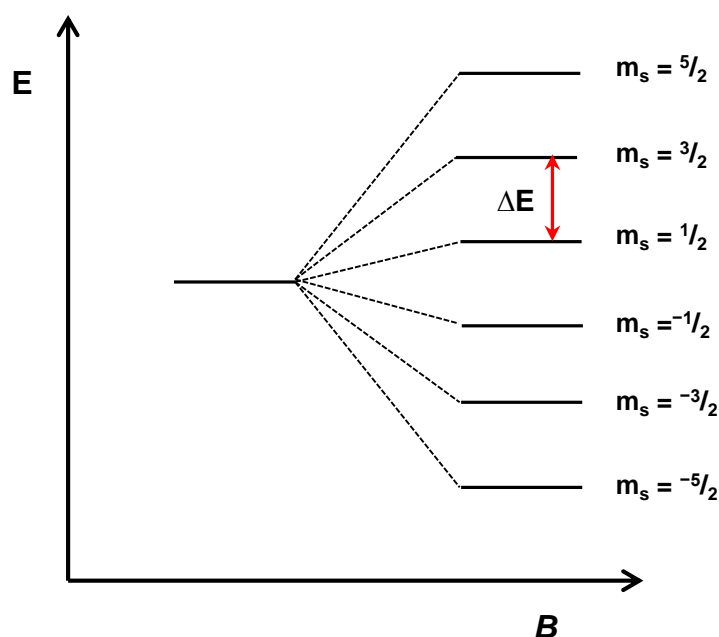


Figure 1.3.7: If a species with a total spin of $5/2$ were to exist in an environment of pure octahedral symmetry the application of an external magnetic field would lead to Zeeman splitting giving six possible m_s orientations. The allowed transitions satisfying $\Delta m_s = \pm 1$ would all be of equal energy.

However, systems with perfect octahedral symmetry are rare and certainly in the case of hemes, the plane of the porphyrin ring is not equivalent to the ‘molecular’ z-axis. This low symmetry field leads to the removal of the degeneracy between spin states in the absence of an external magnetic field, a process known as zero-field splitting. Both orbital angular momentum and spin-dipolar interactions contribute to this (25).

For systems with an odd number of unpaired electrons, the degeneracy of spin states is never totally lifted. This is known as Kramer’s theorem and species with an odd number of unpaired electrons are known as Kramer’s systems. Non-Kramer’s systems possess a total spin of integer value (but greater than zero), for example the Ni^{2+} ion, which is a d^8 system with two unpaired electrons and hence an S of 1. If the Ni^{2+} ion existed in a crystal field of perfect octahedral symmetry, the application of an external magnetic field would lead to two transitions of equal energy (left, *Figure 1.3.8*).

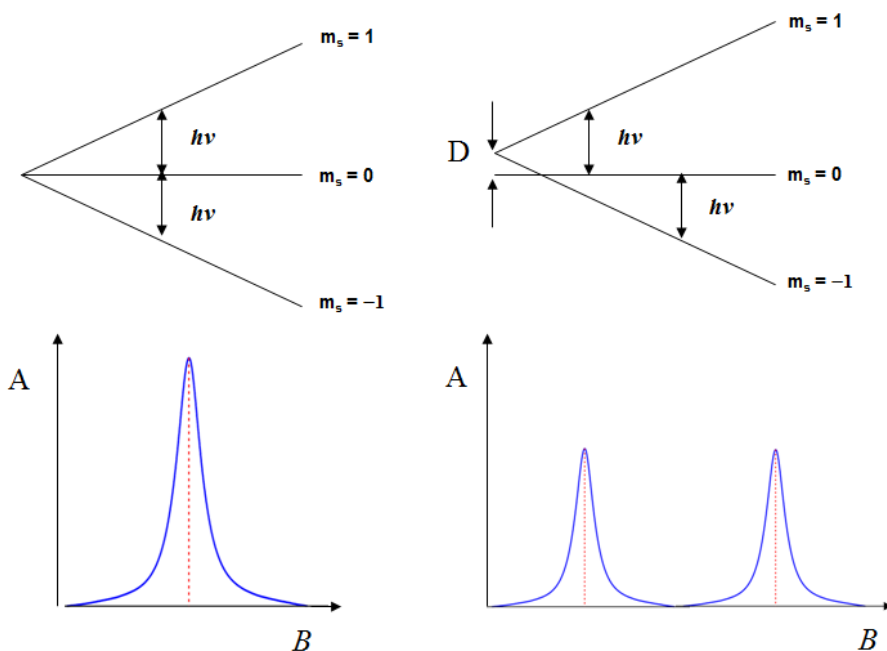


Figure 1.3.8: The Ni^{2+} ion is a d^8 species with two unpaired electrons and a total spin, S , of 1. It is therefore a non-Kramer’s system.

However, placing the Ni^{2+} ion in a low-symmetry crystal field, would lead to an offset between the $m_s \pm 1$ doublet and the $m_s = 0$ singlet, with the energies for resonance of the

two transitions subsequently occurring at a different field strengths (right, *Figure 1.3.8*). The zero-field splitting parameter, D , is the energy separation between the lowest-lying triplet and singlet states. When D is small compared to the microwave energy, this causes deviations from $g = 2$ as the energy required to produce resonance is altered for both Kramer's and non-Kramer's systems. *Figure 1.3.9* shows energy level spacings for $S = 1$ to $S = 5/2$ systems.

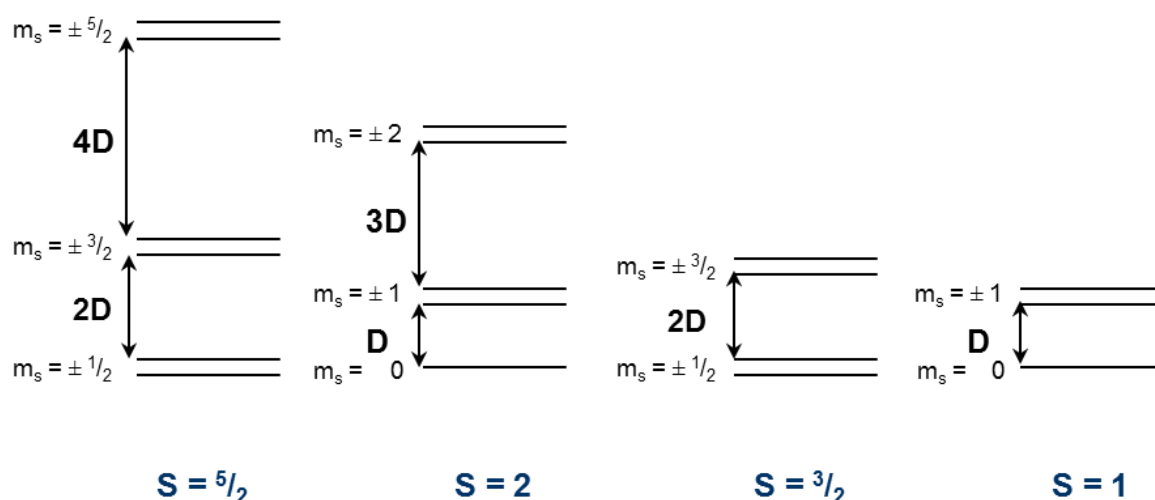


Figure 1.3.9: Zero-field splitting for (from left) $S = 5/2$, $S = 2$, $S = 3/2$, and $S = 1$ systems. The application of an external magnetic field would cause a Zeeman splitting of the doublets.

In an axial field, Kramer's systems (such as the $S = 3/2$ and $5/2$ cases shown above) with a large value of D compared to the microwave energy (left, *Figure 1.3.10*) will only have allowed transitions within the $m_s = \pm 1/2$ doublet. The spin Hamiltonian for the axial case is given by Equation 9. Further lowering of the symmetry requires the inclusion of a rhombicity term, E , as shown in Equation 10. The mixing of states then results in formally forbidden transitions within the $\pm 3/2$ and $\pm 5/2$ doublets becoming partially allowed (25,26). However, in all cases a qualitative description of the expected EPR spectrum can be obtained without recourse to simulation.

$$H_{ax} = g\beta BS + D(S_z - S^2/3) \quad (9)$$

$$H_{rhom} = g\beta BS + D(S_z^2 - S^2/3) + E(S_X^2 - S_Y^2) \quad (10)$$

Description of the EPR of systems in which D is of approximately the same magnitude as $h\nu$ (right, *Figure 1.3.10*) require simulations for spectral assignment, as the appearance of the spectrum is extremely sensitive to the ratio of D to $h\nu$. However, such systems are beyond the scope of this thesis.

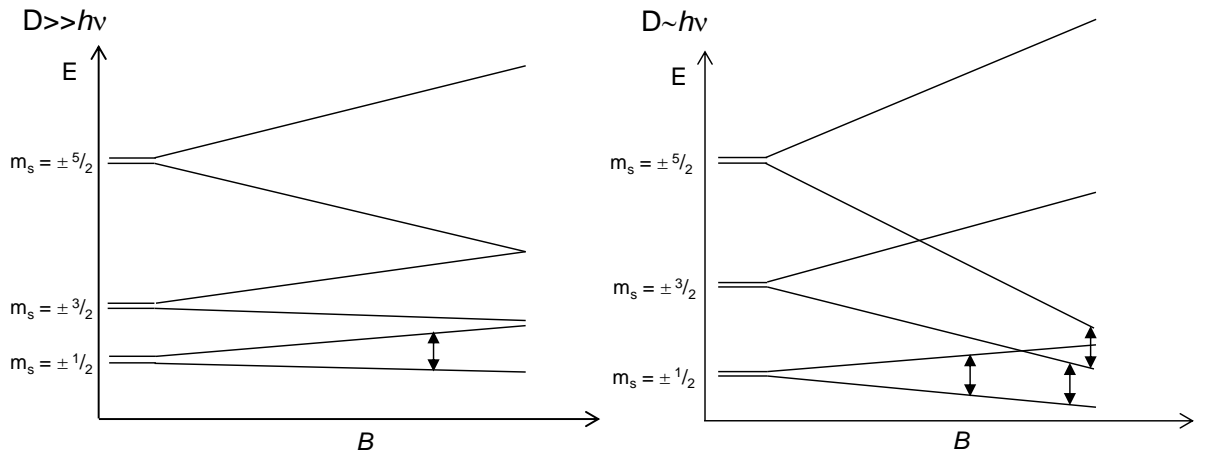


Figure 1.3.10: A Kramer's $5/2$ system with $D \gg h\nu$ (left) and with $D \sim h\nu$ (right). In the case of the former, only transitions within the $m_s = \pm 1/2$ doublet are formally allowed. When $D \sim h\nu$, $\Delta m_s = \pm 1$ transitions are allowed if the resonance conditions are fulfilled (assuming no mixing of states).

1.3.7 Spin lattice relaxation and saturation

For an EPR signal to be observed there must be a population difference between the spin states and a net absorption of microwave photon energy. The Maxwell Boltzmann equation states that at room temperature, with an applied frequency of 9.75 GHz, there is a slightly larger population in the lower energy level, $m_s = -1/2$ state. When the resonance condition is fulfilled, the transition moments for the absorption and emission of microwave energy are identical. As the probability of a transition occurring is directly proportional to the product of the population and the transition moment, a population difference is required to obtain the net absorption of microwaves. Spin lattice relaxation provides a route that acts to

restore the population difference by releasing the energy absorbed into the surrounding lattice and is the dominant mechanism of non-radiative decay for transition metal ions. The spin-lattice relaxation is very efficient for transition metal ions, resulting in a short lifetime of the excited state (25). The energy-time uncertainty principle (Equation 11) states that:

$$\Delta E \Delta t \geq \hbar/2 \quad (11)$$

Where Δt is an estimate of T_1 . This relation is evolved from the Heisenberg uncertainty principle and states that the energy of a short-lived state cannot be known to arbitrary precision. At 298 K this results in a large broadening of the EPR signals for most metalloproteins, making it necessary to perform measurements at low temperature, typically below 100 K. While making measurements at low temperatures can allow the different spectral features to be clearly observed, this is achieved by reducing the rate of relaxation. At high microwave powers and/or low temperatures, slow relaxation results in removal of the population difference and therefore loss of signal intensity. This process is known as saturation (25).

It is often the case that in metalloproteins with multiple metal centres, the relaxation rates of the individual centres will differ. In order to measure a particular centre at maximum intensity, it is often necessary to run spectra at a variety of different power levels and temperatures. This allows the non-saturating conditions to be determined and hence optimises the signals obtained. Additionally, it can be used to resolve the contributions from different centres.

1.3.8 *The continuous wave EPR spectrometer*

The first EPR signals were detected in 1944 by Yevgeny Konstantinovich Zavoisky, an Associate Professor of Physics at Kazan State University, Russia (27). It wasn't until the development of radar technology however, that scientists were able to build suitable microwave sources for use in EPR spectrometers (28). Since then, there has been much advancement in the area of EPR spectroscopy, from the application of Fourier Transform to the development of a variety of different pulsed techniques.

The basic layout of a typical continuous wave (CW) EPR spectrometer is shown in *Figure 1.3.11* (28,29). The microwave source, the attenuator, the circulator and the detector are all housed in the microwave bridge. Solid-state Gunn diodes are generally used to provide the microwave source, although older spectrometers may use Klystron vacuum tubes. The attenuator allows the power level of the microwaves to be varied. Unlike typical absorption spectrometers that measure the amount of electromagnetic radiation transmitted through (and therefore absorbed by) the sample, EPR spectrometers measure the reflected radiation. The circulator directs the incoming microwaves into the cavity and reflects them to the detector once absorption by the sample has occurred. These reflected microwaves are converted to an electrical current by a diode or silicon crystal in the detector (28).

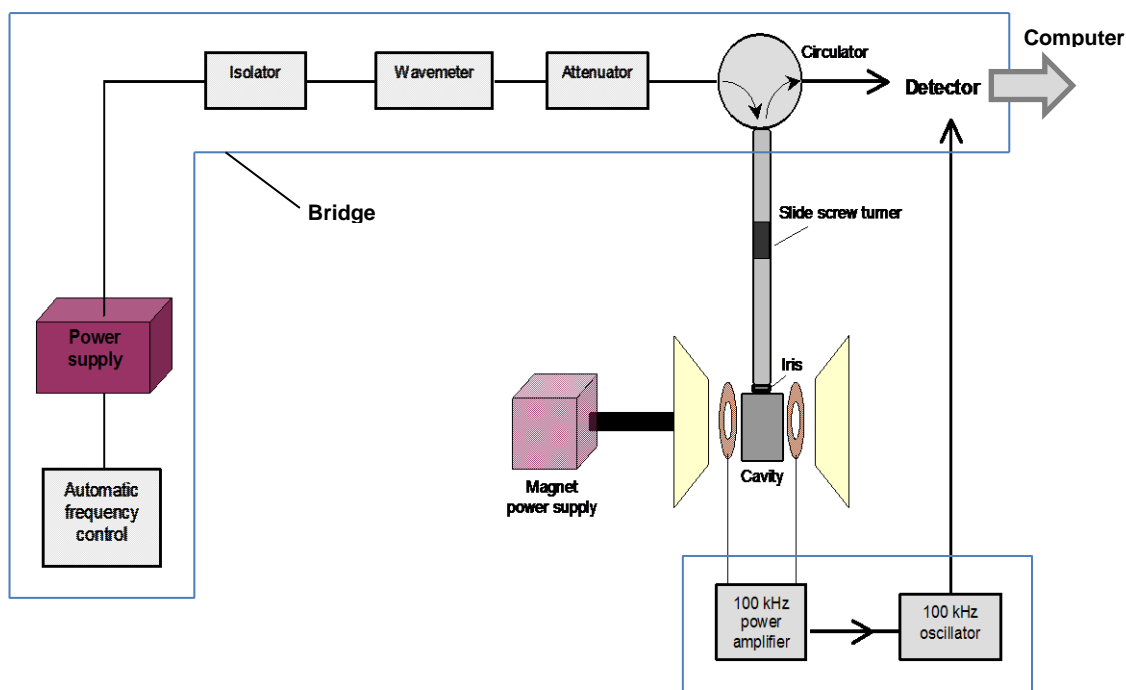


Figure 1.3.11: The basic layout of a CW EPR spectrometer. The detection system here has been generalised, but in reality would include a detector crystal or diode, a 100 kHz signal amplifier, a detector and a computer monitor with acquisition program. The 100 kHz power amplifier and oscillator comprise the modulation system (28,29).

The cavity is used to produce a standing wave of high energy density perpendicular to the applied field. The inner surface of the cavity is typically plated with a thin layer of gold over another thin layer of silver, and essentially acts as a resonator. An indication of how efficiently the cavity stores the microwave energy is given by the ‘quality’ or ‘Q’ factor, (Equation 12). This dimensionless quantity gives a ratio of the energy stored by the cavity to that lost through the walls as heat.

$$Q = 2\pi (\text{Energy stored} / \text{Energy dissipated per cycle}) \quad (12)$$

Another way of expressing Q in terms of frequency is given by Equation 13:

$$Q = \nu_{\text{res}} / \Delta\nu \quad (13)$$

Where ν_{res} is the resonant frequency of the cavity and $\Delta\nu$ is the width of half-height of the resonance (*Figure 1.3.12*).

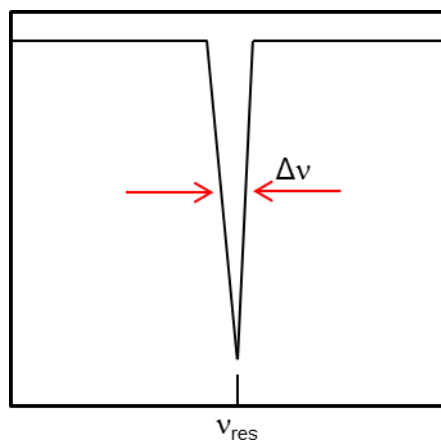


Figure 1.3.12: The 'Q' factor is a dimensionless quantity that gives a ratio of the energy stored by the cavity to that lost through the walls as heat. It can be calculated by dividing the resonant frequency (ν_{res}) by the width of half-height of the resonance ($\Delta\nu$).

As the field is swept and resonance is attained, the sample absorbs microwave energy. This leads to a reduction in the Q-factor as more energy is dissipated in the form of heat and an increase in the impedance of the cavity. The result of this increased impedance is that the critical coupling between the cavity and the microwaves is disrupted, resulting in reflection of the latter out via the circulator and into the detector. The microwaves are coupled into the cavity via the iris, which can be adjusted mechanically. The size of the iris controls the intensity of the microwaves that enter and are reflected back from the cavity by matching or transforming the impedances of the cavity and the waveguide (a pipe used to carry the microwaves).

Modulation of the magnetic field (for example at 100 kHz) is coupled with phase sensitive detection, which results in the reduction of noise. Field modulation is illustrated diagrammatically in *Figure 1.3.13*. If the modulation amplitude ($B_a - B_b$) is less than the signal linewidth, the sine wave amplitude of the detector output is equivalent to the slope of the absorption curve. The result is that the spectrum is recorded as the first derivative.

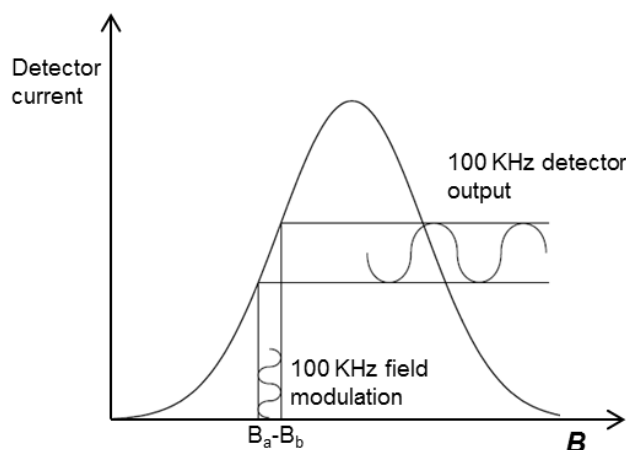


Figure 1.3.13: Effect of Modulation of the magnetic field at 100 kHz on the detector output. The detector output current is approximately equal to the slope of the absorption curve. $B_a - B_b$ is the modulation amplitude.

1.4 Introduction to magnetic circular dichroism spectroscopy

1.4.1 *The theory behind the technique*

Conventional circular dichroism (CD) spectroscopy measures the differential absorption of left-handed and right-handed circularly polarised light as a function of wavelength. Although it is a useful technique for structural characterisation, one of the main limitations is that for it to be applicable, the molecule must possess natural chirality. In magnetic circular dichroism (MCD) spectroscopy, a magnetic field is used to induce optical activity, a phenomenon known as the Faraday effect. The differential absorption of left-handed and right-handed circularly polarised light (ΔA) in the presence of the magnetic field is measured. This is the MCD signal (Equation 14) **(30)**:

$$\Delta A = A_{\text{LCP}} - A_{\text{RCP}} \quad \textbf{(14)}$$

Where LCP and RCP are left-handed and right-handed circularly polarised light respectively. The wavelength range that can be studied with MCD is 200–>2000 nm in organic solvents. The patterns of bands observed in the spectra also tend to be more detailed and can be diagnostic of a particular spin or oxidation state.

A basic schematic representation of the experimental set-up is shown in *Figure 1.4.1*. The light source produces left and right circularly polarised light alternately, which then passes through the sample located between the coils of a magnet. If the magnetic field is orientated parallel relative to the direction of light propagation, this is known as the ‘longitudinal Zeeman mode’. In a typical MCD experiment, a spectrum is taken with the field in the forward and reverse directions, and then removed completely and a final measurement made in zero-field.

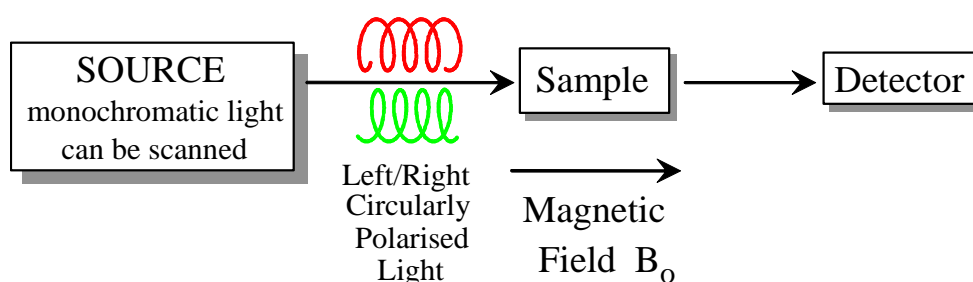


Figure 1.4.1: A basic schematic representation of the MCD experiment in longitudinal (parallel) mode. The detector measures the differential levels of left and right circularly polarised light emitted by the sample.

When the magnet is energised, with the field in either direction, small distortions within the apparatus can lead to small baseline shifts. The main purpose of making the measurement in this fashion is to ensure that the baseline remains consistent throughout the course of the experiment. The experimental MCD intensity can be given by Equation 15.

$$\Delta A(\text{MCD}) = \frac{1}{2} (\Delta A_{\text{forward field}} - \Delta A_{\text{reverse field}}) \quad (15)$$

Any natural CD of the sample is the same in all three scans and is therefore removed by this procedure. The application of a magnetic field causes a Zeeman splitting of degenerate energy levels within the molecule. The left and right hand circularly polarised (LCP and RCP respectively) photons stimulate transitions between different electronic states as illustrated in *Figure 1.4.2*. As with absorption spectroscopy, the selection rules for an allowed transition are $\Delta S = 0$, $\Delta L = 0$ or ± 1 and $\Delta m_s = 0$. In principle, all materials give rise to the Faraday effect, however, this is extremely weak in the absence of degeneracy in either the ground or excited states.

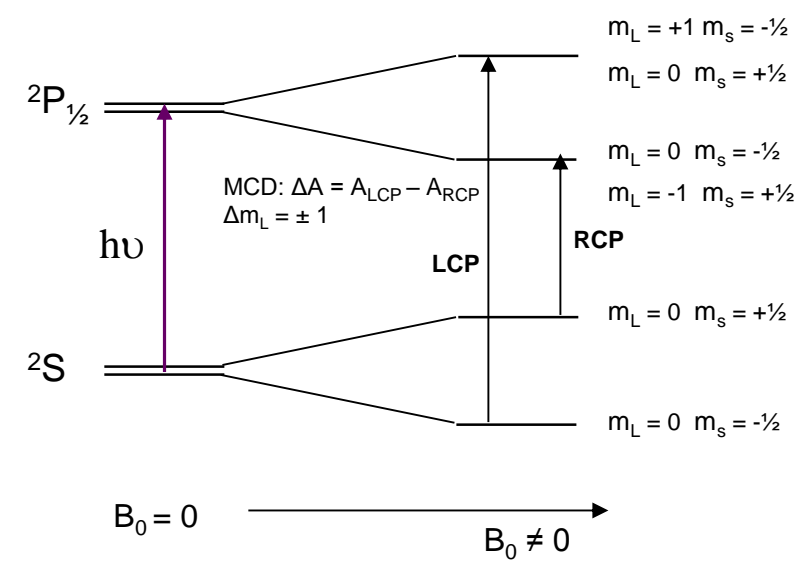


Figure 1.4.2: The application of an external magnetic field causes a Zeeman splitting in the energy levels and the left and right circularly polarised light photons are absorbed at slightly different energies.

1.4.2 MCD A, B and C-Terms

The total MCD intensity is made up of three different contributions, which are known as MCD A-, B- and C-terms. The first two contributions are temperature independent, whereas the C-term MCD intensity is inversely proportional to temperature. The total MCD intensity (I) can be written as (Equation 16):

$$I \propto \left[A_1 \left(\frac{\partial f(E)}{\partial E} \right) + \left(B_0 + \frac{C_0}{kT} \right) f(E) \right] \quad (16)$$

Where k and T are the Boltzmann constant and the temperature respectively. The function $f(E)$ represents the shape of the absorption band; hence A-term intensity shows a derivative band shape, while B and C-terms exhibit absorption band shapes. The different absorption mechanisms for MCD A-, B- and C-terms are shown in *Figure 1.4.3*. In order for A-term intensity to arise, the molecule must have degenerate excited states, which are then split upon application of the applied magnetic field. Diamagnetic species may possess degeneracy in the excited state and may therefore exhibit A-term MCD intensity. As the ground state is non-degenerate, the difference in intensity between LCP and RCP transitions is zero, leading to a derivative band shape.

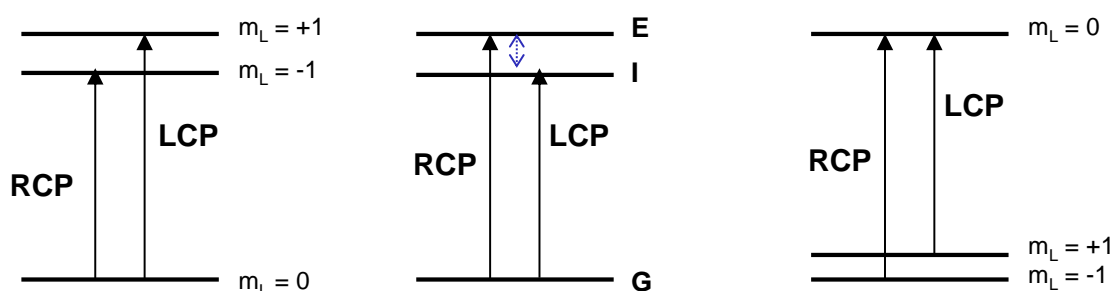


Figure 1.4.3: The absorption mechanisms of the (from left to right) A-term, B-term and C-term contributions to the MCD spectrum. The latter is only exhibited by paramagnetic species, as degenerate ground states are required.

In the case of B-term intensity, the application of the external field leads to the mixing of two energetically close states. Mixing may occur between an intermediate state (**I** in *Figure 1.4.3*) and either the ground state (**G**) or an excited state, **E**. Any signals arising in the MCD spectrum due to B-term contributions tend to be similar in shape to the absorption bands for the same transition and are temperature independent. However, if **I** is

energetically close enough to **G**, thermal population of the former may occur, leading to C-term intensity.

As with B-term MCD, signals arising due to C-term contributions tend to exhibit absorption-shaped bands in the spectrum due to the existence of degenerate ground states. The application of the external magnetic field lifts the ground state degeneracy, resulting in a Boltzmann distribution across the ground state manifold. The difference in intensity between LCP and RCP-stimulated transitions will then give rise to an overall Gaussian absorption profile. Unlike A- and B- terms, the C-term contribution is temperature dependant.

1.4.3 *Curie Law and the effects of temperature and magnetic field on C-term intensity*

Curie Law states that the magnetisation of a paramagnetic material is proportional to the strength of the applied field and inversely proportional to temperature. This relation (Equation 17) is only valid for high temperatures and low field strengths.

$$M = C.B/T \quad (17)$$

Where M is the magnetisation, C is the Curie constant, T is the absolute temperature (in K) and B is the magnetic field strength (in tesla). When the thermal quanta kT are greater than the Zeeman interaction, βB , (known as the linear limit), Curie law applies. As a result, the intensity of the MCD spectrum will vary linearly with the absolute temperature, as shown in *Figure 1.4.4*. Within the linear limit it is possible numerically to deconvolute the MCD A, B and C-term contributions to the spectrum. At very low temperatures and high magnetic field strengths, the linear relationship no longer applies. At this point the C-term contribution begins to dominate the MCD intensity as the lower-energy Zeeman sublevels become more densely populated. Lowering the temperature increases the population of the

lowest sublevel at the expense of all other ground state levels. This leads to an increased intensity of a Gaussian feature of either positive or negative sign. Once only the lowest sublevel has a significant Boltzmann population, the C-term intensity becomes independent of magnetic field intensity and temperature. When the higher energy sublevels are completely depopulated, the maximum C-term intensity is attained. Conversely, at high temperatures, all levels of the ground state spin manifold become almost equally populated and only a weak derivative band is observed due to the C-term contribution. As only the C-term intensity is temperature dependant, it can be calculated by measuring the difference in relative intensity at high and low temperatures. The dependence of this on magnetic field strength and temperature can be modelled to provide an accurate estimate of the g-values and the zero-field splitting parameter.

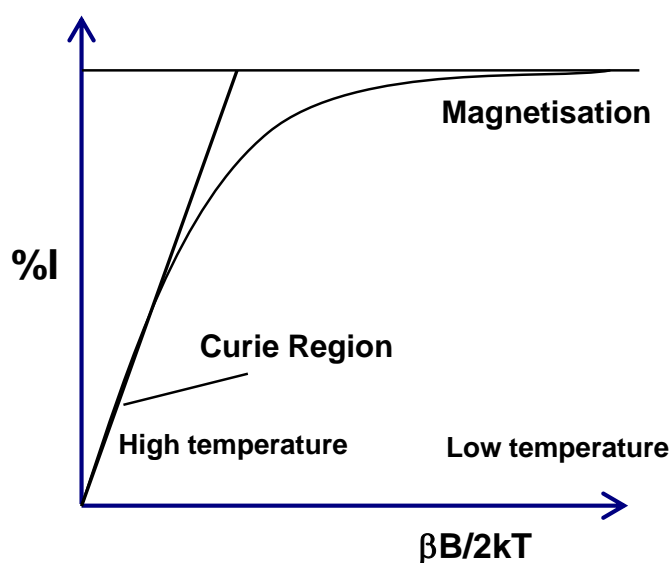


Figure 1.4.4: When Curie law applies at higher temperatures and lower magnetic field strengths ($kT > \beta B$) the intensity of the MCD spectrum will vary linearly with the absolute temperature.

1.5 UV-visible absorbance, EPR and MCD of hemoproteins

1.5.1. *Introduction to hemoprotein spectroscopy*

Proteins containing the heme cofactor are encountered throughout nature and have been the subject of intense research for many years. In order to gain a full understanding of a particular biochemical pathway, it is vital that the enzymes involved are properly characterised. The localised structure around the heme invariably has an effect on the spin and oxidation state of the metal, which in turn may influence the function of the protein as a whole, and the use of spectroscopic techniques in hemoprotein structural characterisation is well established. When used in conjunction with each other, absorbance, EPR, NMR, Mössbauer, fluorescence and MCD spectroscopies can provide a wealth of information regarding not only the spin and oxidation state of the metal but also the identities and relative orientations of the axial ligands. Through the observation of changes to the local heme environment, spectroscopic methods can be used to monitor the progress of enzymatic reactions *in vitro*. X-ray crystallography is an undeniably valuable method for hemoprotein structural characterisation, but is not always a reliable indicator of how the enzymes actually exist and behave in solution and therefore *in vivo*. The characteristic absorbance, EPR and MCD spectra of low-spin hemoproteins are outlined in the following section. Further details of high-spin species are provided in later chapters where relevant.

1.5.2. *Absorbance spectroscopy of hemoproteins*

There has been widespread investigation into the spectral properties of ferric hemoproteins and their model complexes over the past few decades (31-39). This has led to an extensive literature record of how these spectral properties relate to the electronic ground states of

the metal centres, thus assisting with the structural characterisation of newly discovered proteins. One extremely important spectroscopic technique is UV-visible spectroscopy. Strong electronic absorptions in the visible region occur due to electronic transfer from the π HOMO to the π^* LUMO orbitals within the conjugated tetrapyrrole ring. These transitions result in the strong red/brown colouration (or green in the case of *a*-type heme) observed when hemoproteins are in solution. The main diagnostic features that are observed in the UV-visible spectrum are the Soret- and α/β bands (the Q region), observed at 400–450 nm and ~ 550 nm respectively (*Figure 1.5.1*). The position and relative intensities of these bands can provide important information regarding the oxidation and spin states of the metal centre. The Soret band is the most reliable indicator of a protein-bound heme cofactor, and is typically a very intense band, with an extinction coefficient of around $100,000 \text{ M}^{-1} \text{ cm}^{-1}$ for *c*-type hemes (40).

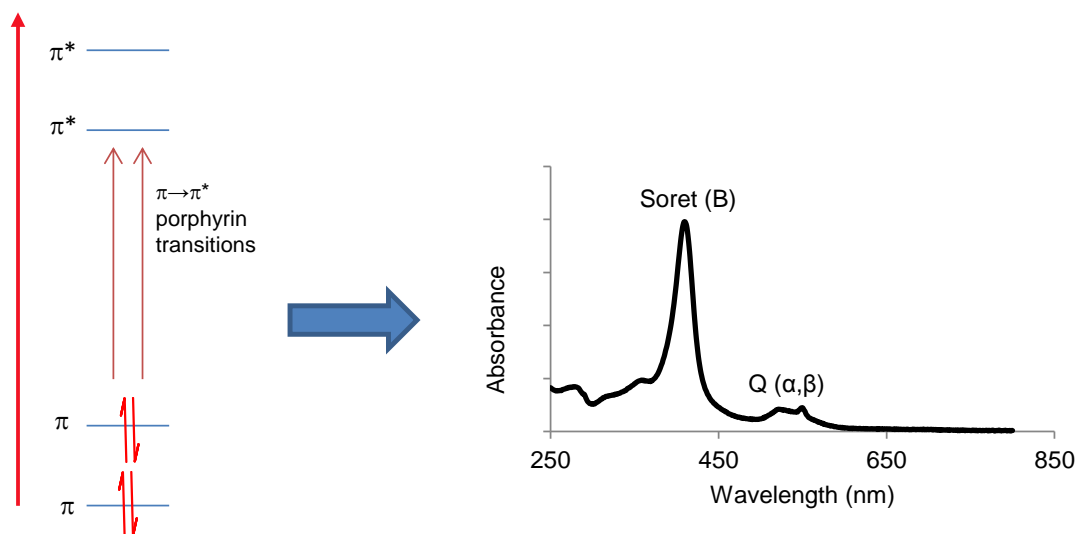


Figure 1.5.1: Electronic transfer from the π HOMO to the π^* LUMO orbitals within the conjugated tetrapyrrole ring lead to Soret and α/β bands in the visible region of the spectrum.

The Class 1 cytochromes *c* are among the most extensively spectroscopically studied family of proteins. These small, soluble proteins contained within many species of

bacteria and the mitochondria of eukaryotic cells are commonly involved in the electron transport processes that take place during respiration (41).

In the oxidised state, the *c*-type heme is low-spin ferric and is axially-coordinated by histidine and methionine residues. The absorbance spectrum of oxidised (or ‘as prepared’) horse-heart cytochrome *c* shows a Soret band at 410 nm, with a Q band at 528 nm (42) (*Figure 1.5.2*). There is also a band observed at 280 nm due to the absorbance of the aromatic ring systems of the tyrosine, tryptophan and phenylalanine residues contained within the protein structure. This is a standard feature of hemoprotein UV-visible absorbance spectra and the ratio of the absorbance of the Soret peak to the 280 nm band can be used as an approximate indicator of purity; an increased A_{Soret}/A_{280} ratio indicates a greater proportion of heme-bound protein. When the heme is reduced from low-spin ferric to the low-spin ferrous state, the Soret band increases in intensity and is red-shifted to 416 nm. The α and β bands of the Q region become sharp and well defined, with absorption maxima at 550 nm and 520 nm respectively. This red-shift of the Soret band upon reduction of the heme from low-spin d^5 to low-spin d^6 , and the sharpening of the Q region generally occur as a standard for *b* and *c*-type cytochromes, and can be used as a reliable indicator of the reduced state.

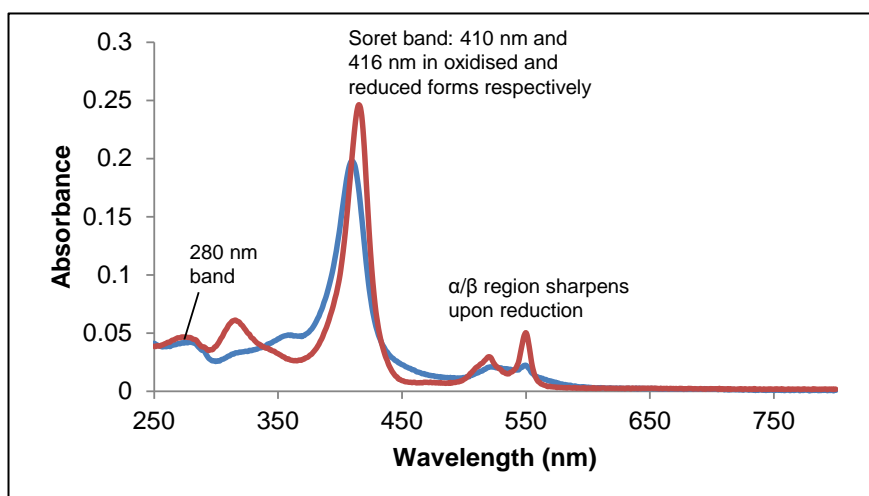


Figure 1.5.2: Absorbance spectra of oxidised (or ‘as prepared’; blue) and fully-reduced (red) horse-heart cytochrome *c*.

Myoglobin is an oxygen-binding respiratory protein contained within mammalian muscle tissue that accommodates a single *b*-type heme moiety. The prosthetic group is held in place by hydrophobic interactions as well as a covalent coordinate bond to a nitrogen atom on a nearby proximal histidine residue. The sixth coordination site is vacant, and this is where oxygen can reversibly bind. Deoxygenated myoglobin (Deoxy-Mb) contains iron in the high-spin ferrous state, although most methods of purification yield the protein entirely in the water or hydroxide-bound ferric form. Cyanide has a very high affinity for ferric Mb, and will bind to the heme at the vacant coordination site, yielding a highly stable, low-spin complex. Absorbance measurements of the ferric Mb-CN derivative show a Soret peak at approximately 420 nm, with the Q-region maximum occurring at ~ 540 nm.

The spin state of the heme in ferric Mb is also highly pH sensitive. Absorbance spectra of ferric Mb ($\text{Mb}^+ \text{OH}^-$) (horse heart and sperm whale) show the characteristics of typical low-spin Fe^{3+} at a pH of ~ 11, with a Soret peak at around 412 nm, and the sharp α , β bands at 580 and ~ 540 nm respectively. Conversely, the absorbance spectra of ferric Mb ($\text{Mb}^+ \text{H}_2\text{O}$) at a pH of less than 7 shows characteristics of high-spin ferric heme, with a Soret band blue-shifted (compared to the alkaline spectrum) to around 408–409 nm. The α and β bands appear at ~ 630 and 505 nm respectively (25,40).

1.5.3. *EPR spectra of low-spin ferric hemoproteins*

From the study of the spectroscopic data of low-spin ferric hemoproteins and their model complexes, three main types of complex have been identified. These complex types differ in terms of either the electronic ground state of the metal and/or the relative orientation of the axial ligands. The three types and the characteristic EPR spectra they give rise to are summarised in *Table 1.5.1*.

| Complex type | Axial ligand alignment | Electronic ground state | Orbital degeneracy | EPR spectral characteristics |
|--------------|------------------------|---------------------------------|--|---|
| I | Perpendicular | $(d_{xy})^2 (d_{xz}, d_{yz})^3$ | Near degeneracy of d_{xz} d_{yz} orbitals. Minimum rhombicity | Large g_{\max} $g_z > g_y > g_x$ Only g_z normally resolved |
| II | Parallel | $(d_{xy})^2 (d_{xz}, d_{yz})^3$ | There is a marked difference in energy between d_{xz} and d_{yz} . The lowest in energy is d_{xy} . Strong rhombic crystal field | Well resolved rhombic EPR with $g_z > g_y > g_x$ |
| III | | | | |
| a | Any | $(d_{xz}, d_{yz})^4 (d_{xy})^1$ | The d_{xz}, d_{yz} pair are degenerate (or nearly so) and the d_{xy} is highest in energy | Axial, with g_x ca. $g_y > g_z$ |
| b | Any | $(d_{xz}, d_{yz})^4 (d_{xy})^1$ | As with Type II, $d_{xz} \neq d_{yz} \neq d_{xy}$. The latter is highest in energy | Rhombic, with $g_x > g_y > g_z$, although the g_x and g_y are normally close together |

Table 1.5.1: Types of low-spin ferric heme complex.

Type I complexes have their axial ligands aligned in perpendicular planes and a $(d_{xy})^2 (d_{xz}, d_{yz})^3$ electronic ground state, with a near degeneracy of the latter two orbitals. This combination of axial ligand orientation and electronic ground state gives rise to ‘Large g_{\max} ’ type EPR spectra, typically with $g_z > 3.3$. The g_y and g_x values are not normally resolved, with the latter value being very small, often less than 1. Spectra of this type are also generally only observed at low temperatures; between 4 and 20 K. Type II complexes have the same electronic ground state as Type I but with the axial ligands aligned in parallel planes and give rise to well-resolved rhombic EPR spectra. These spectra can be generally observed at temperatures higher than the characteristic Type I,

often at liquid nitrogen temperatures of around 78 K. It should be noted that while Type I complexes have near degeneracy of the d_{xz} and d_{yz} orbitals, in Type II complexes they are typically markedly different in energy. Most electron transfer cytochrome proteins (*a*, *b*, *c* and *f*) are either Type I or Type II complexes and therefore possess $(d_{xy})^2 (d_{xz}, d_{yz})^3$ electronic ground states. It is accepted (43) that in both types of complex, the Z-axis is orientated normal to the plane of the heme, giving rise to g values where $g_z > g_y > g_x$. Classic examples of Type I EPR spectra are observed for Myoglobin-CN (44) and cytochrome c_{553} peroxidase (45). Mitochondrial cytochrome *c* (46) exhibits Type II EPR spectra, as does cytochrome b_5 (47).

Type III (separated into Type III_a and III_b in this work) ferric heme complexes have a $(d_{xz}, d_{yz})^4 (d_{xy})^1$ electronic ground state for the metal with axial ligands in any orientation. These can exhibit either axial or rhombic EPR spectra. *Figure 1.5.3* shows the different splitting of the 3d t_{2g} and e_g that can exist within Type I, II and III complexes. For a Type III complex to exhibit an axial spectrum (second from left in *Figure 1.5.3*) the d_{xz} and d_{yz} pair must be orbitally degenerate (or nearly so) and below the d_{xy} in energy. As with all axial-type EPR spectra, the g_x and g_y values are virtually identical and (for complexes of this type) greater than the g_z value. These complexes are known as Type III_a here. Cyanide-complexed siroheme exhibits an EPR spectrum of this type with a g_{\perp} signal at 2.38 and a g_{\parallel} of 1.76 (48). For the chlorin complexes such as *Paracoccus pantotrophus* cytochrome cd_1 (49) with axial ligands orientated in parallel planes, the EPR spectra are rhombic (Type III_b in this work) with close spacing of the two largest g values, g_x and g_y .

Theoretical calculations have shown that it is possible to use the g-values to determine the relative energies of the metal t_{2g} orbitals. These calculations make the assumption that not only are the g_x , g_y and g_z values positive, but that $g_x^2 + g_y^2 + g_z^2 = 16$, a quantity known as Σg^2 (50,51).

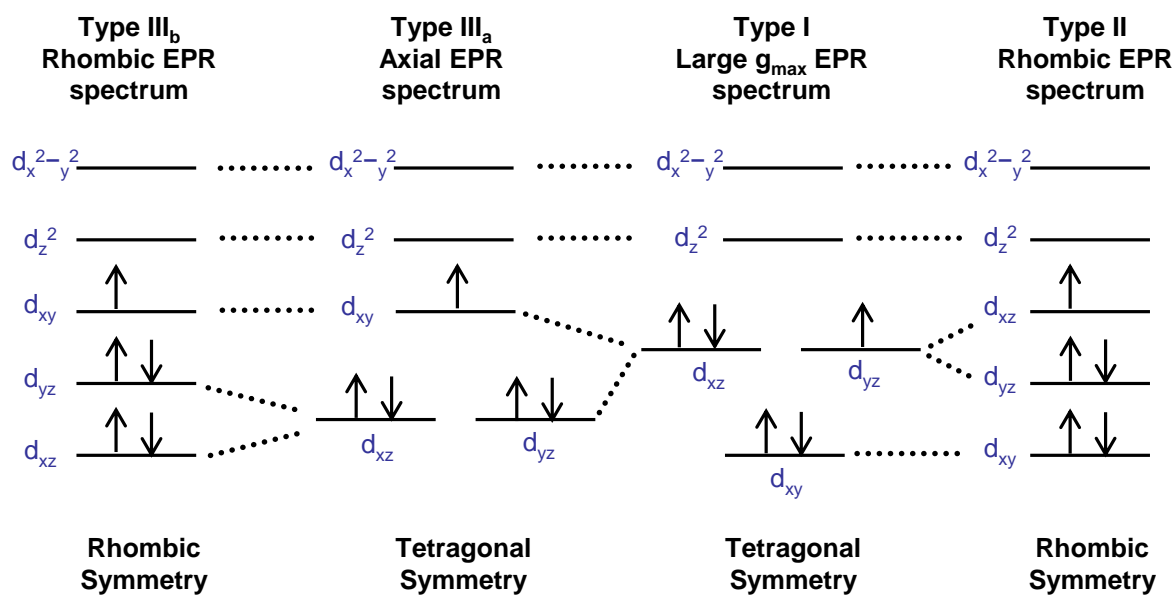


Figure 1.5.3: The various splittings of the 3d orbitals of Fe^{3+} and their respective symmetries. From left; Rhombic symmetry exhibited by a Type III_b complex with a $(d_{xz}, d_{yz})^4 (d_{xy})^1$ ground state leads to a rhombic EPR spectrum, Type III_a complex with tetragonal symmetry and also a $(d_{xz}, d_{yz})^4 (d_{xy})^1$ ground state results in an axial EPR spectrum, Type I tetragonal complexes and Type II rhombic complexes, both with a $(d_{xy})^2 (d_{xz}, d_{yz})^3$ ground state result in 'Large g_{max} ' and rhombic EPR spectra respectively.

However, these assumptions only hold for complexes with a $(d_{xy})^2 (d_{xz}, d_{yz})^3$ electronic ground state, and not for those with the $(d_{xz}, d_{yz})^4 (d_{xy})^1$ ground state. For example, the EPR spectrum of *P. pantotrophus* cd_1 gives Σg^2 value of only 14.5 (49), while the model heme complex $[(\text{TPP})\text{Fe}(t\text{-BuNC})_2]\text{ClO}_4$ has a very pure $(d_{xz}, d_{yz})^4 (d_{xy})^1$ electronic ground state (due to an almost complete quenching of the orbital angular momentum) and has a Σg^2 value of only 13.5 (52).

The relative energies of the t_{2g} and e_g orbitals of the metal are influenced by the bonding interactions with both the axial ligands and the porphyrin ring. The bonding interactions between the metal and the porphyrin ring/axial ligands are summarised in *Table 1.5.2*. Usually, both σ and π -interactions are involved, with the former occurring between filled σ -orbitals on the ligand and empty $3d_z^2/4s/4p_z$ hybrid orbitals on the metal.

The π -interactions can involve either the acceptance or donation of electron density between the iron $3d_{xz}$ and $3d_{yz}$ orbitals and p_π orbitals on the ligand.

| Ligand | σ -interaction with metal | π -interaction with metal |
|---|--|--|
| Axial | Empty $3d_z^2$, $4s$, $4p$ and hybridized metal orbitals can all receive electron density from axial ligands with σ -symmetry | Metal $3d_{xz}$, and $3d_{yz}$ can receive electron density from the axial ligand p_π orbitals. Back donation may also occur |
| Porphyrin ring (not ruffled) | | The $3e(\pi)$ and the $4e(\pi^*)$ (LUMO) orbitals on the porphyrin possess the required symmetry for interaction with the metal $3d_{xz}$ and $3d_{yz}$ orbitals. |
| Porphyrin ring (ruffled) | | Ruffling of the porphyrin ring may cause a component of the p_z ($3a_{2u}$) π orbital (may be HOMO) to be present in the xy plane. Delocalization of π electrons via the porphyrin p_z onto the metal may then occur if the d_{xy} orbital is half-filled. |

Table 1.5.2: Summary of the bonding interactions between the metal and the porphyrin ring/axial ligands (22).

1.5.4. UV-visible and near infra-red (NIR) MCD of low-spin ferric hemoproteins

The aromatic 18- π electron system of the porphyrin ring has $\pi \rightarrow \pi^*$ transitions from the A_{1g} ground state to the E_u excited states corresponding to changes in m_L of ± 1 and ± 9 (Figure 1.5.4). These transitions result in the appearance of Soret ($\Delta m_L = \pm 1$) and Q ($\Delta m_L = \pm 9$) bands in both the UV-visible and MCD spectra (53,54). In contrast to the absorbance spectrum of a diamagnetic metalloporphyrin, in which the Soret band will show a greater intensity compared to the Q band, the reverse is true in the MCD spectrum. This is because the higher orbital moment of the E_u excited state for the Q band (compared with the Soret band) results a larger A-term derivative (53). A, B and C-term MCD intensity was described in Section 1.4.2 of this chapter.

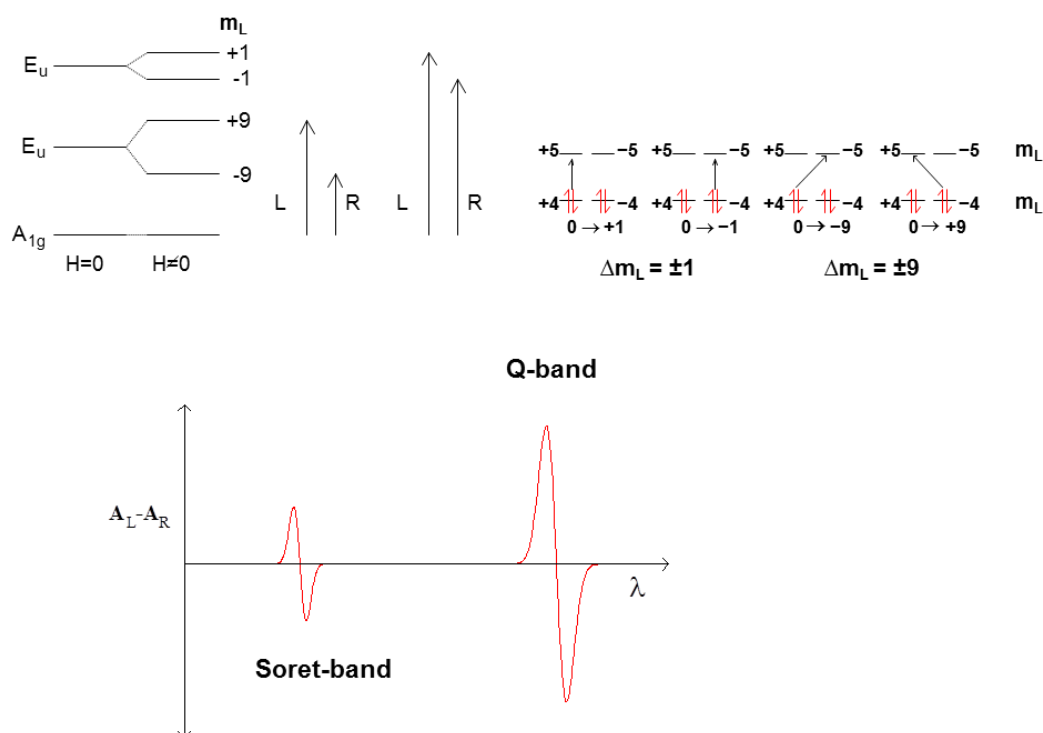


Figure 1.5.4: $\pi \rightarrow \pi^*$ transitions within the porphyrin ring give rise to characteristic Q and Soret bands.

The introduction of the iron (or any transition metal) into the centre of the porphyrin introduces d orbitals and therefore additional energy levels to the complex. This leads to a number of additional optical transitions that can, in principle, be observed in the MCD spectrum, including metal $d-d$ transitions and ligand-to-metal (or metal-to-ligand) charge transfer (CT) bands. However, these transitions are of greatly reduced intensity compared with the Soret and Q band. The optical bands of the porphyrin are very sensitive to the spin and oxidation state of the iron, giving rise to characteristic bands in the MCD spectrum. These characteristic bands in the UV-visible region can be used to diagnose the spin and oxidation state of the iron.

In the case of low-spin ferric heme, the optical transitions will possess considerable C-term intensity (compared with the high-spin case, which is orbitally non-degenerate), resulting in a temperature-dependant MCD spectrum. This C-term intensity originates from

the substantial spin-orbit coupling (SOC) that occurs within the doubly degenerate ground state 2E (*Figure 1.5.5*). This 2E ground state, arising from the configuration e^3 of D_{4h} ($d_{xz,yz}$) is split into two Kramer's doublets by the SOC and the application of a magnetic field. The configurations $a_{1u}^1 e_g^4$ and $a_{2u}^1 e_g^4$ result in $^2A_{1u}$ and $^2A_{2u}$ excited states. Transitions to these $^2A_{1u}$ and $^2A_{2u}$ excited states from the lower level of the 2E ground state are left-circularly polarised and give rise to a charge transfer band, known as CT_{ls} . This CT_{ls} transition appears as a positive band in the near infrared (NIR) MCD spectrum, and arises due to transitions from the porphyrin HOMO to the orbitals derived from the metal e_g orbitals (in the point group D_{4h}) (*Figure 1.5.5*) (53).

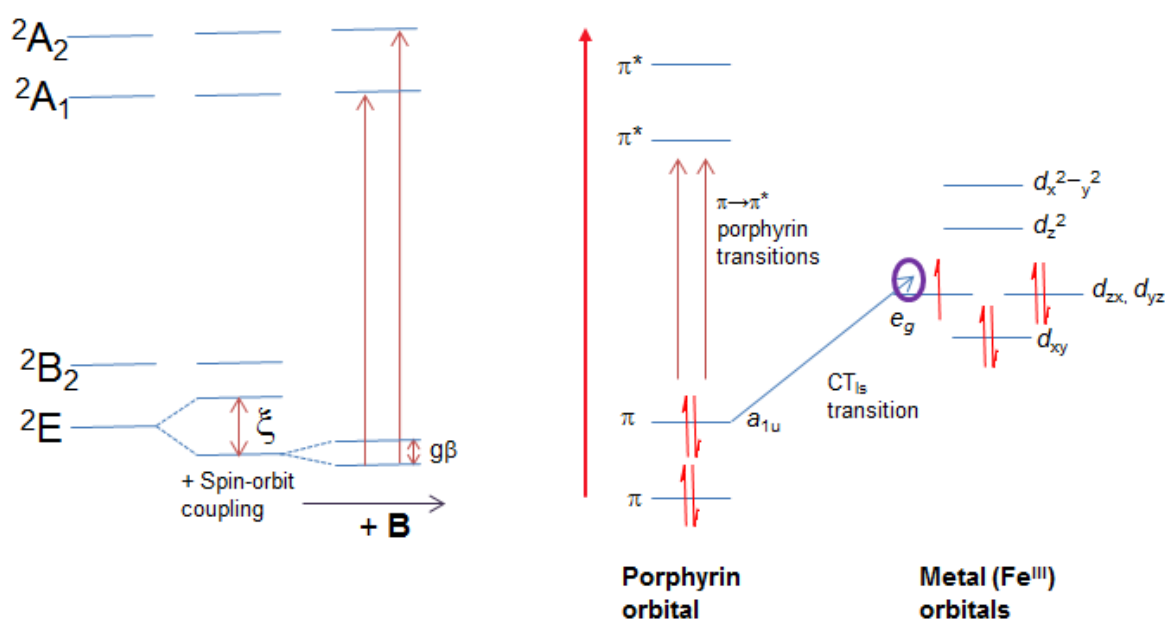


Figure 1.5.5: Ground and excited states of low spin ferric heme (left) and the CT_{ls} transition from the porphyrin HOMOs to orbitals derived from d_{zx}, d_{yz} resulting in a positive NIR MCD band (25,53).

The position of this band is sensitive to adjustments in the iron d orbital energy levels and as a consequence the identities of the heme axial ligands. This means that the position of the CT_{ls} can be used to confidently assign the heme axial ligands, as illustrated in *Figure*

1.5.6. Some of the common low-spin ferric heme axial ligand pairs and the position of their corresponding CT_{Is} bands in the NIR-MCD spectrum are shown in *Figure 1.5.7* (53).

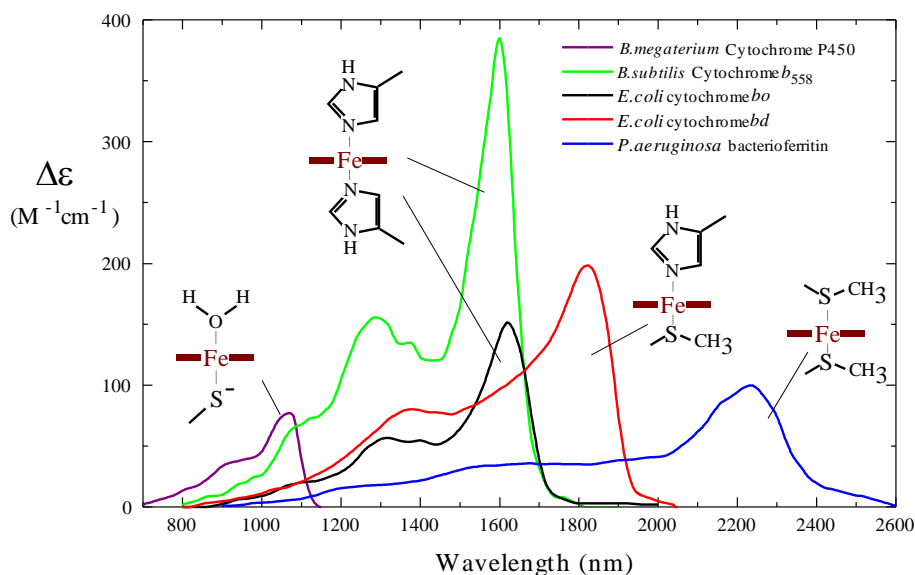


Figure 1.5.6: The position of the CT_{Is} band in the spectra of low-spin ferric hemoproteins can be used to assign the identities of the axial ligands (53).

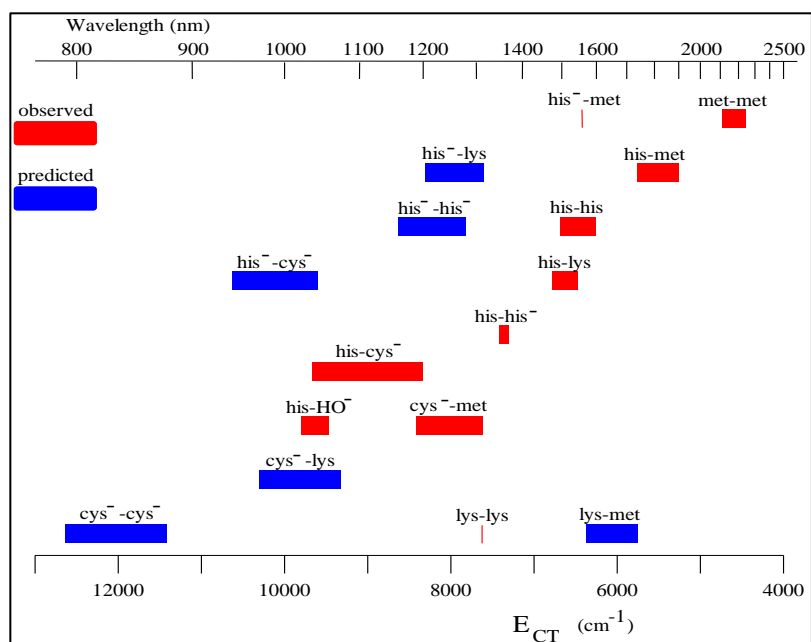


Figure 1.5.7: The energies of the CT_{Is} transition can be used to assign the axial ligands of low-spin ferric hemoproteins (53).

1.5.5 UV-visible and near infra-red (NIR) MCD of low-spin ferrous hemoproteins

As low-spin ferrous hemes are diamagnetic ($S = 0$), features in the MCD spectrum mainly arise from $\pi \rightarrow \pi^*$ transitions within the porphyrin ring. The resulting Soret and derivative Q band features contain A and B-term intensity alone, with the former dominating due to the degeneracy of the $\pi \rightarrow \pi^*$ transitions to the 1E_u excited state (53). This is strikingly similar to the general appearance of the MCD of apoporphyrin; the CT band in the NIR is not observed as the e_g orbital set of the iron is now filled and transitions to the a_{1g} and b_{1g} orbitals are symmetry forbidden (53).

1.6 References

1. Munro, A. W., Girvan, H. M., McLean, K. J., Cheesman, M. R., and Leys, D. L. (2008) *Tetrapyrroles: Their birth, life and death*, Landes Bioscience and Springer Science+Business Media
2. Denisov, I. G., Makris, T. M., Sligar, S. G., and Schlichting, I. (2005) *Chem Rev* **105**, 2253-2277.
3. Bowman, S. E., and Bren, K. L. (2008) *Nat Prod Rep* **25**, 1118-1130
4. Frausto da Silva, J. J. R., Williams, R. J. P. (1993) *The Biological Chemistry of the Elements: The Inorganic Chemistry of Life*, Clarendon Press, Oxford
5. Heinemann, I. U., Jahn, M., and Jahn, D. (2008) *Arch Biochem Biophys* **474**, 238-251
6. Mogi, T., Saiki, K., and Anraku, Y. (1994) *Mol Microbiol* **14**, 391-398
7. Michel, H., Behr, J., Harrenga, A., and Kannt, A. (1998) *Annu Rev Biophys Biomol Struct* **27**, 329-356
8. Brunori, M. (2001) *Trends Biochem Sci* **26**, 21-23
9. Garry, D. J., and Mammen, P. P. (2007) *Adv Exp Med Biol* **618**, 181-193
10. Arnhold, J. (2004) *Biochemistry (Mosc)* **69**, 4-9
11. Rae, T. D., and Goff, H. M. (1998) *J Biol Chem* **273**, 27968-27977
12. Allen, J. W. A., Barker, P. D., and Ferguson, S. J. (2003) *J Biol Chem* **278**, 52075-52083
13. Caroppi, P., Sinibaldi, F., Fiorucci, L., and Santucci, R. (2009) *Curr Med Chem* **16**, 4058-4065
14. Ow, Y. P., Green, D. R., Hao, Z., and Mak, T. W. (2008) *Nat Rev Mol Cell Biol* **9**, 532-542
15. Vos, M. H., Borisov, V. B., Liebl, V. B., Martin, J. L., and Konstantinov, A. A. (2000) *Proc Natl Acad Sci U S A* **97**, 1554-1559.
16. Chang, C. K. (1985) *J Biol Chem* **260**, 9520-9522.
17. Chang, C. K., and Wu, W. (1987) *J Am Chem Soc* **109**, 3149-3150
18. Belinsky, M. I. (1996) *Chem Phys Lett* **250**, 320-327

19. NIST. (2011) The NIST Reference on Constants, Units and Uncertainty. <http://physics.nist.gov/cgi-bin/cuu/Value?gammae>, Gaithersburg, MD
20. Odom, B., Hanneke, D., D'Urso, B., and Gabrielse, G. (2006) *Phys Rev Lett.* **97**, Epub 2006 Jul 2017
21. Wertz, J. E., and Bolton, J. R. (1986 (Reprint)) Basic Principles of Electron Spin Resonance. in *Electron Spin Resonance: Elementary Theory and Practical Applications*, Chapman and Hall, London
22. Walker, F. A. (1999) *Coord Chem Rev* **186**, 471-534
23. Wertz, J. E., and Bolton, J. R. (1986 (Reprint)) Transition Metal Ions I. in *Electron Spin Resonance: Elementary Theory and Practical Applications*, Chapman and Hall, London
24. Wertz, J. E., and Bolton, J. R. (1986 (Reprint)) Nuclear Hyperfine Interaction. in *Electron Spin Resonance: Elementary Theory and Practical Applications*, Chapman and Hall, London
25. Seward, H. E., PhD thesis (1999) Magneto-optical spectroscopy of hemoproteins., University of East Anglia, Norwich, U.K.
26. Solano-Peralta, A., Saucedo-Vazquez, J. P., Escudero, R., Hopfl, H., El-Mkami, H., Smith, G. M., and Sosa-Torres, M. E. (2009) *Dalton Trans*, 1668-1674
27. Eaton, G. R. (1998) *Foundations of modern EPR*, World Scientific
28. Bruker. (2012) CW-EPR Practice (Accessed May 2012). <http://www.bruker-biospin.com/cwpractice.html>
29. Wertz, J. E., and Bolton, J. R. (1986 (Reprint)) Basic Instrumentation of Electron Spin Resonance. in *Electron Spin Resonance: Elementary Theory and Practical Applications*, Chapman and Hall, London
30. Hales, B. J. *Methods Mol Biol* **766**, 207-219
31. Gadsby, P. M. A., and Thomson, A. J. (1990) *J Am Chem Soc* **112**, 5003-5011
32. Huynh, B. H. (1994) Mossbauer Spectroscopy in Study of Cytochrome *cd*₁ from *Thiobacillus denitrificans*, Desulfovibrin, and Iron Hydrogenase. in *Inorganic Microbial Sulfur Metabolism*, Academic Press Inc, San Diego
33. Huynh, B. H. (2011) *Methods Mol Biol* **766**, 221-235
34. Zoppellaro, G., Bren, K. L., Ensign, A. A., Harbitz, E., Kaur, R., Hersleth, H. P., Ryde, U., Hederstedt, L., and Andersson, K. K. (2009) *Biopolymers* **91**, 1064-1082
35. Zoppellaro, G., Teschner, T., Harbitz, E., Schunemann, V., Karlsen, S., Arciero, D. M., Ciurli, S., Trautwein, A. X., Hooper, A. B., and Andersson, K. K. (2006) *Chemphyschem* **7**, 1258-1267
36. Yatsunyk, L. A., Carducci, M. D., and Walker, F. A. (2003) *J Am Chem Soc* **125**, 15986-16005
37. Leone, M., Cupane, A., and Cordone, L. (1996) *Eur Biophys J* **24**, 117-124
38. Myer, Y. P. (1978) *Methods Enzymol* **54**, 249-284
39. Yonetani, T., and Leigh, J. S., Jr. (1971) *J Biol Chem* **246**, 4174-4177
40. Antonini, E., and Brunori, M. (1971) *Hemoglobin and Myoglobin in Their Reactions with Ligands*, North Holland Publishing Company, Amsterdam
41. Kassner, R. J. (1991) *Biochim Biophys Acta* **1058**, 8-12
42. Margoliash, E., and Frohwirt, N. (1959) *Biochem J* **71**, 570-572
43. Otsuka, T., Ohya, T., and Sato, M. (1987) *Inorg Chem* **26**, 2191-2192
44. Gadsby, P. M. A., and Thomson, A. J. (1990) *J Am Chem Soc* **112**, 5003-5011
45. Arciero, D. M., and Hooper, A. B. (1994) *J Biol Chem* **269**, 11878-11886
46. Morishima, I., Fujii, H., Shiro, Y., and Sano, S. I. C. (1995) *Inorg Chem* **34**, 1528-1535
47. Bois-Poltoratsky, R., and Ehrenberg, A. (1967) *Eur J Biochem* **2**, 361-365

48. Kang, L., LeGall, J., Kowal, A. T., and Johnson, M. K. (1987) *J Inorg Biochem* **30**, 273-290.
49. Cheesman, M. R., Ferguson, S. J., Moir, J. W. B., Richardson, D. J., Zumft, W. G., and Thomson, A. J. (1997) *Biochemistry* **36**, 16267-16276
50. Griffith, J. S. (1957) *Nature* **180**, 30-31
51. Taylor, C. P. (1977) *Biochim Biophys Acta* **491**, 137-148
52. Walker, F. A., Nasri H, H., Turowska-Tyrk, I., Mohanrao, K., Watson, C. T., Shokhirev, N. V., Debrunner, P. G., and Scheidt, W. R. (1996) *J Am Chem Soc* **118**, 12109-12118
53. Cheesman, M. R., Greenwood, C., and Thomson, A. J. (1991) *Adv Inorg Chem.* **36**, 201-255
54. Kobayashi, N., and Nakai, K. (2007) *Chem Commun (Camb)*, 4077-4092

2. Structure and function of cytochrome *cd*₁ nitrite reductase

2.1 The nitrogen cycle

The nitrogen cycle involves the various environmental processes that allow the different chemical forms of nitrogen to be reutilised and interchanged. It is arguably the most studied and best-known biogeochemical cycle in nature. Nitrogen is crucial for life on earth and is a major component of all amino and nucleic acids – the building blocks of proteins, DNA and RNA. The main sections of the nitrogen cycle include biological and non-biological steps, and are fixation, assimilation, ammonification, nitrification, denitrification, and anaerobic ammonium oxidation. These processes are summarised and described below. How they are interlinked is illustrated in *Figure 2.1.1*.

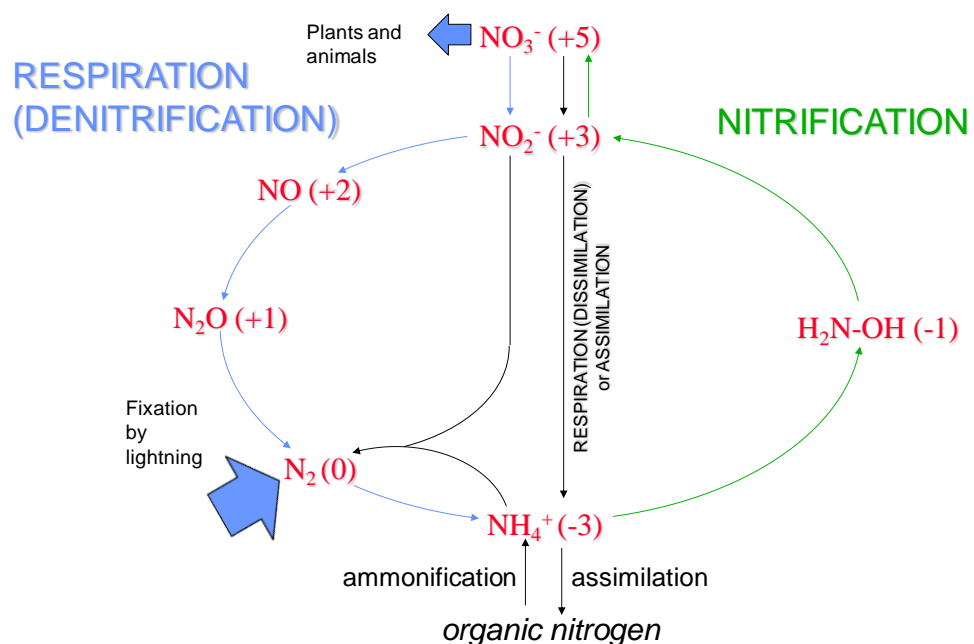


Figure 2.1.1: A schematic representation of how inorganic nitrogen is cycled through nature (Figure courtesy of Dr MR Cheesman, University of East Anglia, 2010).

The different processes involved in the nitrogen cycle are listed below (1):

Nitrogen fixation is the biological or non-biological conversion of atmospheric nitrogen to a form which is usable to plants. Bacteria such as *Rhizobium* contain nitrogenase enzymes that are able to catalyse this process. In the atmosphere, the substantial energy of lightning strikes split nitrogen molecules, allowing the individual atoms to combine with atmospheric oxygen to produce nitrogen oxides (nitric oxide [NO]; nitrogen dioxide [NO₂] and nitrous oxide [N₂O]).

Assimilation involves the absorption and utilisation of inorganic nitrogen in the form of nitrates and ammonium ions by plant tissue. The stepwise reduction of nitrate yields ammonia, which in turn is used to synthesise glutamate, the building block for all other naturally-occurring proteinogenic amino acids.

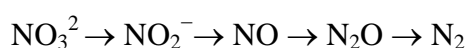
The process of **ammonification** involves the conversion of organic compounds (for example proteins, nucleic acids and urea) into inorganic nitrogen in the form of ammonium ions. Bacteria (such as *Clostridium*) and some species of fungi incorporate the use of enzymes such as glutamate dehydrogenase to carry out this process.

Nitrification encompasses the oxidative processes of the cycle that involve the conversion of ammonia to nitrate via nitrite. The latter is highly toxic to plant life and its conversion to nitrate by nitrifying bacteria such as *Nitrobacter* is essential. Electrons produced during this process are utilised by the nitrifying bacteria during respiration.

Anaerobic ammonium oxidation involves the anoxic conversion of ammonium and nitrite into nitrogen in aquatic environments by bacteria (for example the marine bacteria of the phylum *Planctomycetes*) to create 'nitrogen sinks'.

The reverse of the nitrification process is **denitrification** (shown below), which involves the stepwise reduction of nitrate back to nitrogen gas via nitrite (NO₂⁻), nitric oxide (NO) and nitrous oxide (N₂O). Denitrifying bacteria (such as *Pseudomonas denitrificans*) use the

various inorganic forms of nitrogen as electron acceptors in anaerobic respiration. At each stage, nitrogen undergoes reduction in an oxygen depleted or totally anaerobic environment. The process is catalysed by the reductase metalloenzymes of the denitrifying bacteria that use the substrate molecules as alternative electron acceptors. There has been concern in recent years that due to human effects, the balance between the nitrification and denitrification processes has altered. This has led to a build-up of nitrite and nitrate in the environment (2).



2.2 Nitrite reduction and cytochrome *cd*₁

2.2.1 *The purification and isolation of Pseudomonas cytochrome oxidase*

Nitrite, in particular is highly toxic to marine and land-based organisms and a comprehensive understanding of its dissimilation is necessary if we are to minimise environmental damage. The one electron reduction of nitrite to nitric oxide was first reported to be a part of bacterial denitrification by Wijler and Delwiche in 1954 (3). Baalsrud revealed that the product of nitrite utilisation by *Thiobacillus denitrificans* is nitric oxide (4). *Pseudomonas* cytochrome oxidase was first discovered in 1958 during the extraction and partial purification of components from the facultative anaerobe *Pseudomonas aeruginosa* (5). The enzyme was found to reduce dioxygen to water (with electrons provided by cytochrome *c*₅₅₁) and exhibited an absorption spectrum that suggested the presence of two different heme cofactors. Absorption maxima were observed at 630 nm, 535 nm and 408 nm for the oxidised enzyme and at 625 nm, 554 nm, 549 nm, 521 nm and 418 nm after dithionite reduction. When the purified enzyme was

treated with acidified acetone, only one of the two different hemes, termed ' a_2 ', was easily removed. The other cofactor, concluded to be a *c*-type heme, remained bound within the semi-apoprotein. Sedimentation analysis revealed a molecular mass of approximately 90,000 Da (5).

2.2.2 The characterisation of the d_1 cofactor

In 1969 Newton reported the isolation of an enzyme from the bacterium *Paracoccus denitrificans* (then known as *Micrococcus denitrificans*), which displayed nitrite reductase activity (6). This protein was found to possess the ability to behave as both a nitrite reductase and a cytochrome oxidase (7). It was also isolated from *Thiobacillus denitrificans* in 1979 (8) and was believed at this time to contain two different prosthetic groups, one being a standard *c*-type cofactor, and the other an iron chlorin known as a *d*-type heme. However, it was observed (9) that the latter displayed different spectral properties to those previously reported for the prototypical *d*-type heme (10). This led to the suggestion that this cofactor should be renamed d_1 , a type of heme exclusive to this class of enzyme. Previously, Yamanka *et al* (11) had explored the absorbance properties of this heme further and in 1981, Walsh *et al* (12) continued this by recording the spectra of extracted *P. aeruginosa* d_1 -heme reacted with a number of different ligands in alkaline and acidic conditions. The complexes investigated by EPR, MCD and UV-visible absorbance spectroscopies included cyanide, nitric oxide and imidazole-bound ferri and ferroheme d_1 . This work contributed to the growing library of d_1 -heme spectral properties appearing in the literature.

It was not until 1985 however, that the unusual structural nature of the cofactor was demonstrated (13). Chang noticed that there were discrepancies in the absorbance, NMR and mass spectroscopic data reported previously on the structural properties of the d_1 -

heme, which were used to form the proposal that it was a chlorin (14,15). Similarities between the absorbance spectrum of the d_1 -heme and those of sirohydrochlorin (16) and octaethylisobacteriochlorin (17) were evident and an alternative structure (Structure a, *Figure 2.2.1*) was proposed.

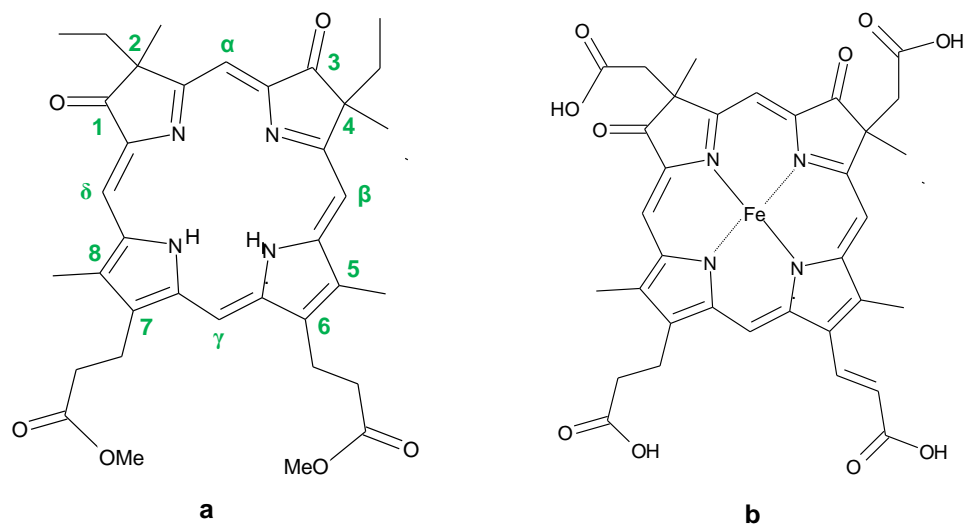


Figure 2.2.1: Left: *Structure a*, as proposed by Chang (13) and Right: *Structure b* – the accepted structure of the d_1 cofactor.

This proposed structure was supported by Chang (18) who demonstrated the importance of the acrylic group at Position 6 (marked in green, *Structure a*, *Figure 2.2.1*) on the porphyrin ring on the overall electronic structure and therefore the spectral properties of the cofactor. The accepted structure of the d_1 -heme (*Structure b*) is also shown in *Figure 2.2.1*.

2.3 *Paracoccus pantotrophus* cytochrome cd_1

Although the cytochrome cd_1 from *Paracoccus pantotrophus* is different in many ways to a number of the other known cd_1 s, it is the most extensively characterised and is also the subject of this work. It will therefore be described first and in most detail. Structural differences between cd_1 from *Paracoccus pantotrophus* (and *Paracoccus denitrificans*) and those from the *Pseudomonads* will be discussed in more detail later.

By 1993 cytochrome *cd*₁ was known to be a soluble, dimeric, periplasmic protein with nitrite reductase and oxidase activities (19). In contrast to the other known type of nitrite reductase, which is copper-containing (20), each monomer of cytochrome *cd*₁ contains two heme moieties; a *c*-type heme and the non-covalently bound *d*₁-heme that is exclusive to this type of enzyme. Heme *d*₁ was known at this time to be the active site of nitrite reduction, while it appeared that the function of the *c*-heme was to transfer electrons and facilitate reduction (21).

In 1993, Moir *et al* (22) reported the isolation and purification of cytochrome *cd*₁ nitrite reductase from the aerobic denitrifier *Paracoccus pantotrophus*, formerly known as *Thiosphera pantotropha*. This work challenged a previous publication by Robertson *et al* (23) that stated that *P. pantotrophus* utilises a copper-containing nitrite reductase.

The mass of the protein subunit was found to be approximately 60 kDa, identical to that of cytochrome *cd*₁ purified from *P. denitrificans*. Additionally, comparison of the absorbance spectrum of the ‘as prepared’ enzyme with that of *P. denitrificans* cytochrome *cd*₁ led to the conclusion that *P. pantotrophus* nitrite reductase could not be the copper-containing enzyme previously reported by Robertson *et al*. During purification, the blue, copper-containing protein pseudoazurin was isolated, and it was suggested that this enzyme acts as an electron donor to cytochrome *cd*₁. It was concluded that the only nitrite reductase present in *P. pantotrophus* was the heme-containing dimer cytochrome *cd*₁ and that this was the case whether growth was aerobic or anaerobic. Contrary to previous assumptions (11,23), the enzyme is capable of activity under both aerobic and oxygen-depleted conditions. It should be noted that the copper-type nitrite reductase (20) contained within other types of denitrifying bacteria is not capable of the four-electron reduction of oxygen to water, generating hydrogen peroxide instead (24).

2.4 The *Paraccocus pantotrophus* cytochrome *cd*₁ electronic absorption spectrum

The heme *d*₁ cofactor is a type of hydroporphyrin known as a dioxoisobacteriochlorin that is contained exclusively with the nitrite reductase enzymes cytochromes *cd*₁ (13,25). Hydroporphyrins differ in structure from the ‘normal’ hemes in that the π -electron system of the macrocycle is truncated. A typical UV-visible absorbance spectrum of the ‘as isolated’ *P. Pantotrophus* enzyme (obtained as part of this work) is shown in *Figure 2.4.1*. Features in the spectrum between 300 and 600 nm are dominated by the *c*-heme, which gives rise to a Soret band at ~ 406 nm along with α and β -bands at ~ 560 and 527 nm respectively. Although transitions within the *d*₁-heme will contribute to the overall absorbance between 300 and 600 nm, at wavelengths greater than 600 nm all spectral features can be attributed to this particular cofactor (26).

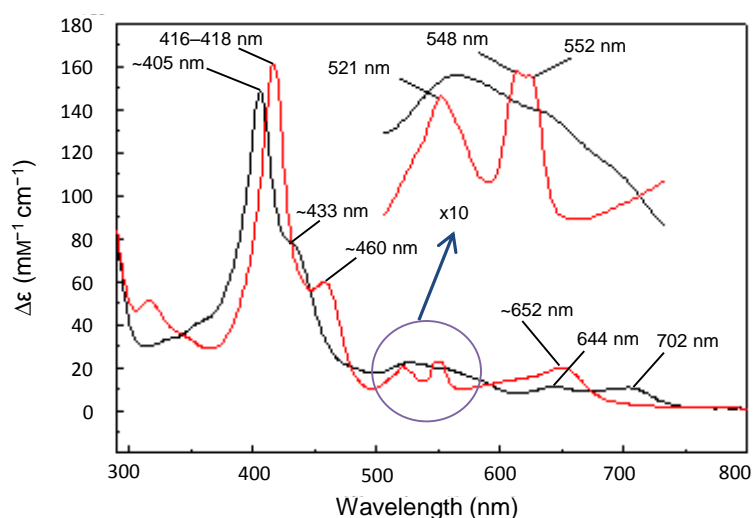


Figure 2.4.1: Electronic absorbance spectra of *P. pantotrophus cd*₁. — As prepared, — fully reduced with 0.20 mM sodium dithionite. Samples were in 48 mM mixed buffer (see Chapter 3, Section 3.2.4 for details), pH 6.5. Concentrations were calculated using the molar extinction coefficient of $148 \text{ mM}^{-1} \text{ cm}^{-1}$ for the oxidised monomer (27).

It has been suggested (28) that the ligand field generated by the axially-coordinated His²⁰⁰ and Tyr²⁵ residues causes the Fe³⁺ ion to lie close to the spin-crossover point. As a result, the spin state of the metal exists in thermal equilibrium between the low ($S = \frac{1}{2}$) and

high ($S = 5/2$) states, with the former being lowest in energy. At room temperature, the absorbance spectrum contains two visible region d_1 bands with the low- and high-spin states giving rise to maxima centred at ~644 and 702–706 nm respectively. This contrasts with the *P. aeruginosa* enzyme, in which the Tyr¹⁰ is not directly bound to the low-spin d_1 -heme, resulting in a single band in this region at around 643 nm (29). Upon full reduction of both hemes in the *P. pantotrophus* enzyme, the 702 nm and 644 nm bands (*Figure 2.4.1*) are replaced by a single more intense feature at ~ 652 nm. This amalgamation of the d_1 α/β region occurs as the iron now exists entirely in the high-spin state (30), although the band does display some asymmetry, indicating that there may be two different forms present. The d_1 -heme exhibits a small Soret band at ~433 nm in the ‘as prepared’ enzyme, which is viewed as a shoulder to the right of the *c*-heme Soret. Upon reduction of this heme to the ferrous state, this feature red shifts to ~460 nm and becomes better resolved. When the *c*-heme is reduced to ferrous, the Soret band displays behaviour typical of hemes of this type and exhibits an increase in intensity coupled with a red shift from ~405nm to 416–418 nm.

The reduction of proteins containing the ‘normal’ protoheme derivatives such as cytochrome *c* and myoglobin typically results in a sharpening of the α/β region. The appearance of this region in cytochrome cd_1 upon reduction is unusual, with the top of the α -band (centred at 551 nm) being split further into two distinct peaks.

2.5 The X-band EPR spectrum of ‘as prepared’ *P. pantotrophus* cd_1

An example of the X-band EPR spectrum of ‘as prepared’¹ *P. pantotrophus* cd_1 is shown in *Figure 2.5.1*. The spectrum is dominated by a rhombic trio, with $g_{x,y,z}$ values of ~ 2.52,

¹ Throughout this thesis, untreated ‘as purified’ enzyme is known as ‘as prepared’ rather than ‘oxidised’ where no oxidant (such as ferricyanide) was added.

2.19 and 1.84, assigned to low-spin ferric d_1 -heme. This spectrum has an unusually low $\sum g^2$ of 14.96, less than the value typically observed for low-spin ferric protohemes (31). The signal centred at $g_z \sim 3.09$, assigned to the c -heme, has been previously described as being a ‘Large g_{\max} ’ spectrum (or ‘Type I’, as described in Chapter 1 of this thesis), in which the *bis*-histidinyl ligand planes are orientated closer to perpendicular than parallel. This feature is typically heterogenous in appearance in ‘as prepared’ *P. pantotrophus* cd_1 , an observation that will be discussed in more detail in Chapter 3 of this thesis. Finally, signals at $g \sim 6.90$ and $g \sim 4.99$ can be assigned to high-spin ferric d_1 -heme and the signal at $g \sim 4.30$ to adventitious iron.

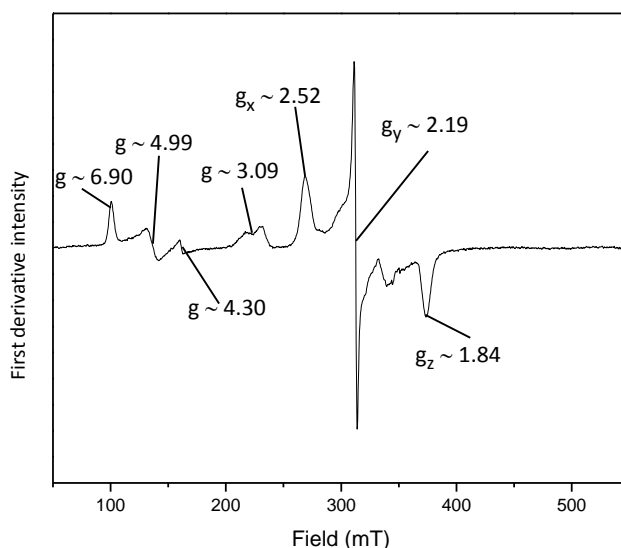


Figure 2.5.1: X-band EPR spectrum of *P. pantotrophus* cd_1 ($\sim 120 \mu\text{M}$) in 48 mM ‘mixed’ buffer. Spectrometer parameters: power, 2 mW; modulation amplitude 1 mT; temperature, 10 K. See Section 3.2.4 for buffer and spectrometer details.

2.6 Crystallographic studies of *P. pantotrophus* cytochrome cd_1

2.6.1 *The monoclinic crystal structure of *P. pantotrophus* cd_1*

In 1993, Fülöp *et al* reported the growth of crystals of cytochrome cd_1 from *P. Pantotrophus* (32) and in 1995 published the 1.55 Å resolution crystal structure of the

enzyme (24). This showed that the *c* and *d*₁-hemes are located in different domains and included a proposal for the reaction mechanism. Previous attempts to crystallise cytochrome *cd*₁ from *P. aeruginosa* to a quality suitable for structural elucidation had proved unsuccessful (11,33). Fülöp *et al* (24) provided an insight into the structural details of the enzyme that built upon the earlier spectroscopic findings. The amino acid sequence and secondary structure of *P. pantotrophus cd*₁ was deduced from the monoclinic X-ray crystal structure, and was found to share 97 % sequence identity with the *P. denitrificans* enzyme (34). The monoclinic X-ray crystal structure is shown in *Figure 2.6.1*.

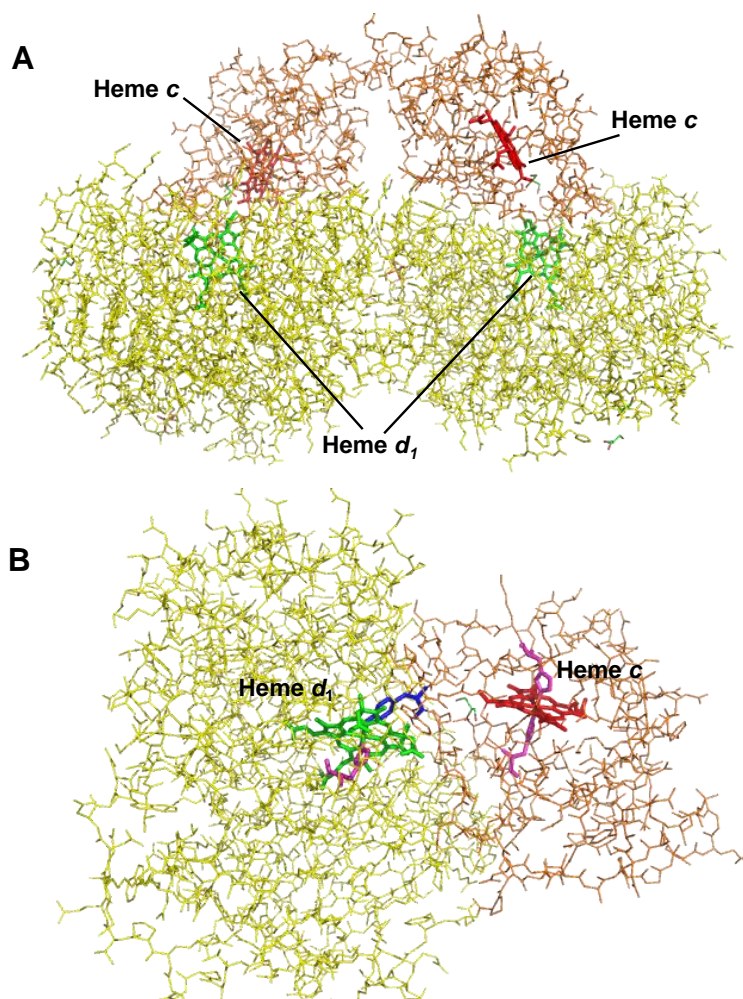


Figure 2.6.1: Monoclinic X-ray crystal structure of oxidised *P. pantotrophus* cytochrome *cd*₁. Panel A shows the homodimer; Panel B an individual monomer (PDB code 1QKS (24)).

It is now accepted that the *cd*₁ nitrite reductase present in *P. pantotrophus* is structurally identical to that from *P. denitrificans*. *P. pantotrophus cd*₁ is a homodimer and

the individual subunits are held together by hydrogen bonds joining the individual d_1 domains. The c domains of the monomers do not make direct contact in the monoclinic oxidised crystal form (Panel A, *Figure 2.6.1*) and are separated by a network of hydrogen bonds made via intervening solvent molecules (35). The domains themselves are distinctly different, with the c -heme located in a α -helical N-terminal domain comprising of residues 1-134, while the d_1 -heme is contained within a rigid C-terminal β -propeller structure. The different heme domains are shown in Panel B, *Figure 2.6.1*.

The ligation to the c -heme is *bis*-histidinyl (Panel A, *Figure 2.6.2*), with the residues His⁶⁹ and His¹⁷ axially-coordinated to the metal in a perpendicular orientation. Only the latter is a conserved residue (28) and this c -heme ligation in the resting enzyme contrasts with the His/Met coordination observed in *P. aeruginosa* (36).

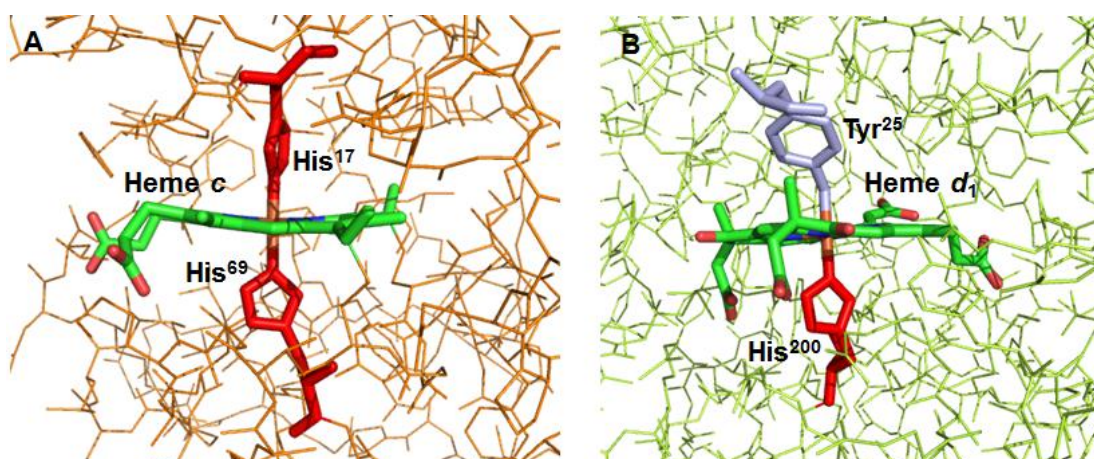


Figure 2.6.2: Monoclinic X-ray crystal structure of oxidised *P. pantotrophus* cytochrome *cd*₁. Panel A shows the His⁶⁹/His¹⁷ ligation to the c -heme; Panel B shows the His²⁰⁰/Tyr²⁵ ligation to the d_1 -heme (PDB code 1QKS (24)).

The d_1 -heme is axially coordinated to a proximal His²⁰⁰ and distal Tyr²⁵ (Panel B, *Figure 2.6.2*), with the latter being joined to the His¹⁷ of the c domain by a peptide chain seven residues long (37).

The mechanism proposed by Fülöp *et al* (*Figure 2.6.3*) involves dissociation of Tyr²⁵ (triggered by reduction of the ferric iron to ferrous) so that the substrate can bind to

the fully reduced enzyme (24). At the d_1 centre, the nitrite molecule binds to the ferrous heme with the nitrogen atom coordinated to the metal.

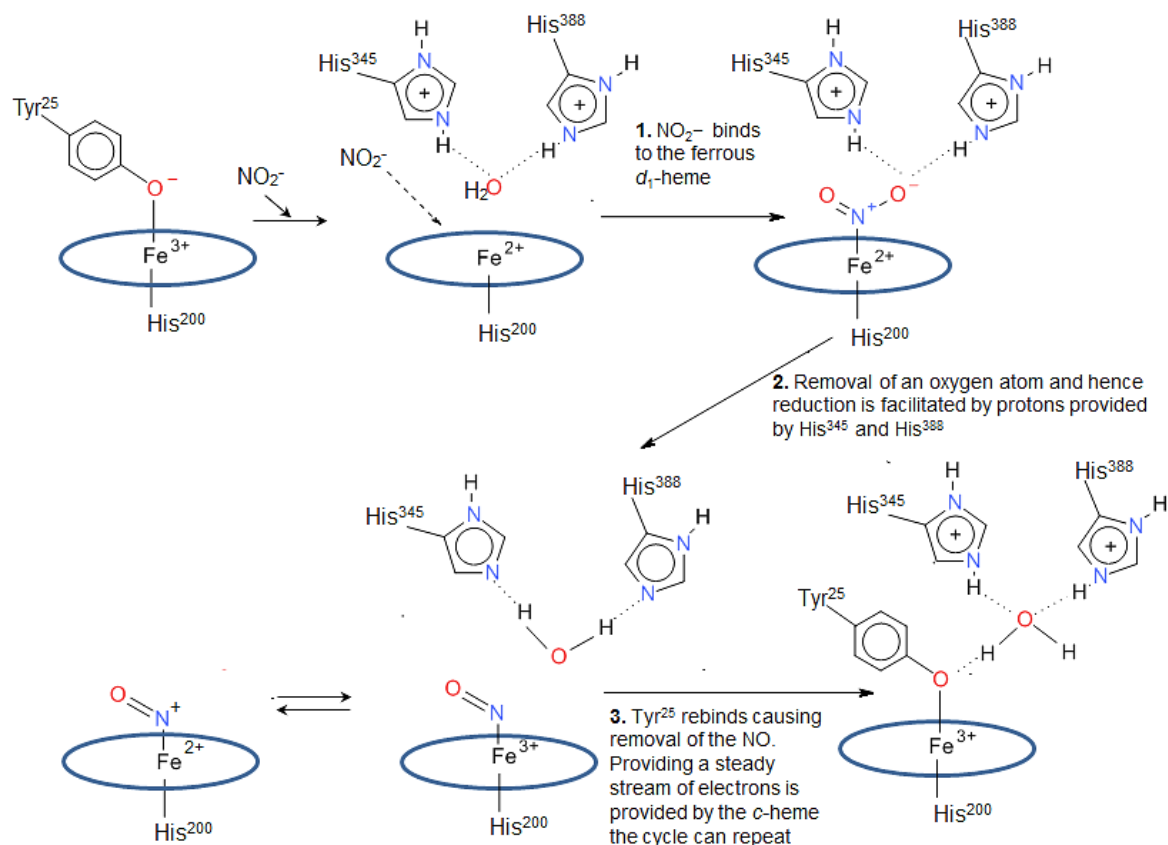


Figure 2.6.3: The reaction mechanism for the reduction of NO_2^- at the d_1 -heme for *P. pantotrophus* cytochrome cd_1 as proposed by Fülöp *et al* (24).

Reduction to nitric oxide occurs, with one of the nitrite oxygen atoms becoming coordinated to two protons from neighbouring His³⁴⁵ and His³⁸⁸ residues, and subsequently dissociating. The rebinding of the Tyr²⁵ to the ferric iron causes removal of the nitric oxide product. The sequence alignment of *P. pantotrophus* cytochrome cd_1 is shown in Figure 2.6.4. Only the His²⁰⁰ is a conserved heme axial ligand across all cytochromes cd_1 (28). In each monomer, the two hemes are arranged at a 60° angle to each other (24), with an iron-to-iron distance of 20.6 Å. However, the actual distance between the c and d_1 -heme porphyrin ring edges is only 11.0 Å. The accepted view is that for efficient electron

transfer to occur between two redox centres, without the inclusion of cofactors, these centres must be separated by 14 Å or less (38).

2.6.2 *The unique ligand switch of *P. pantotrophus* cd_1*

Previously, there had been indications from time-resolved single-crystal microspectrophotometry and X-ray crystallography (39) that cytochrome cd_1 in *P. pantotrophus* undergoes a structural rearrangement during catalysis. In 1997, it was shown in crystals of *P. pantotrophus* cd_1 that the enzyme undergoes a unique ligand switch upon reduction (40). Upon reduction of both hemes to the ferrous state, the ligation at the *c*-heme changes to Met¹⁰⁶/His⁶⁹ and the Tyr²⁵ dissociates completely from the d_1 metal centre (*Figure 2.6.5*). This is the case whether sodium dithionite or reduced methyl viologen is used, although with the former reductant, sulphur dioxide becomes bound to the d_1 centre.

| | | | | | | | | | | | |
|-------------------|------------------------------|---------------------|-----------------|---------------------|----------------|-------------|-------------|-------|---|-----|-----|
| | 1 | 11 | H17 (c) | 21 | Y25 (d) | 31 | 41 | 50 | | | |
| <i>Pa.pan.</i> | QEQVAPPKDP | AAAL <u>E</u> DHKTR | | TDNR <u>Y</u> EPSLD | | NLAQQDVAAP | GAPEGVTALS | | | | |
| <i>Ps.aer.</i> | ----AHAKDD | MKA <u>A</u> EQYQG- | | AASAVDP--- | | ----AHVVRTN | GAPD----MS | | | | |
| <i>Ps.stu. ZB</i> | ----- | ----- | | ----- | | ----LAVAQA | AAPE----MT | * | | | |
| | | | | | | | | | | | |
| | 51 | 61 | H69 (c) | 71 | | 81 | 91 | 100 | | | |
| <i>Pa.pan.</i> | DAQYNEANKI | YFERCAG <u>C</u> HG | | VLRKGATGKA | | LTPDLTRDLG | ----- | | | | |
| <i>Ps.aer.</i> | ESEFNEAKQI | YFQRCAG <u>C</u> HG | | VLRKGATGKP | | LTPDITQQRG | ----- | | | | |
| <i>Ps.stu. ZB</i> | AEEK <u>E</u> AS <u>K</u> QI | YFERCAG <u>C</u> HG | | VLRKGATGKN | | LEPHWSKTEA | DGKKTEGGTL | | | | |
| | | * ** * | | ***** | | * * | | | | | |
| | | | | | | | | | | | |
| | 101 | 111 | M106 | 121 | | 131 | M123 | 141 | ↔ | 150 | |
| <i>Pa.pan.</i> | ---FDYLSQSF | ITYASPAGMP | | NWGTSGELSA | | EQVDLMANYL | LLDPAAPPEF | | | | |
| <i>Ps.aer.</i> | ---QQYLEAL | ITYGTPLGMP | | NWGSSGELSK | | EQITLMAKYI | QHTPPQPPEW | | | | |
| <i>Ps.stu. ZB</i> | NLGT <u>K</u> RLENI | IAYGTEGGMV | | NY--DDILT <u>K</u> | | EEINMMARYI | QHTPDIPPEF | | | | |
| | | * | | * | | * | | ** * | | * | *** |
| | | | | | | | | | | | |
| | 151 | 161 | | 171 | | 181 | | 191 | | 200 | |
| <i>Pa.pan.</i> | GMKEMRESWK | VHVAPEDRPT | | QQENDWDLEN | | LFSVTLRDAG | QIALIDGTTY | | | | |
| <i>Ps.aer.</i> | GMPEMRESWK | VLVKPEDRPK | | KQLNDLDLPN | | LFSVTLRDAG | QIALVDGDSK | | | | |
| <i>Ps.stu. ZB</i> | SLQDMKDSWN | LIVPVEKRVT | | KQMNKINLQN | | VFAVTLRDAG | KLALIDGDTH | | | | |
| | | * | | * | | * | | ***** | | * | ** |
| | | | | | | | | | | | |
| | 201 | 211 | H200 (d) | 221 | | 231 | | 241 | | 250 | |
| <i>Pa.pan.</i> | EIKSVLDTGY | AV <u>H</u> ISRLSAS | | GRYLFVIGRD | | GKVN MIDLWM | KEPTTVAEIK | | | | |
| <i>Ps.aer.</i> | KIVKVIDTGY | AV <u>H</u> ISRMSAS | | GRYLLVIGRD | | ARID MIDLWA | KEPTKVAEIK | | | | |
| <i>Ps.stu. ZB</i> | KIWKVLESGY | AV <u>H</u> ISRMSAS | | GRYVYTTGRD | | GLTTIIDLWP | EEPMTVATVR | | | | |
| | * | ** * | | ***** | | ** * | | * | | ** | |

Figure 2.6.4: Sequence alignments of the N-terminal amino acid regions of cytochromes *cd*₁ from *P. pantotrophus* (*Pa. pan.*), *P. aeruginosa* (*Ps. aer.*) and *P. stutzeri* ZoBell (*Ps. Stu. ZB*). Potential metal ligands are indicated in colour. The ligands for the *c*- and *d*₁-hemes of oxidised cytochrome *cd*₁ from *P. pantotrophus* as determined from the crystal structure (24) are underlined. An asterisk * indicates a conserved residue. ↔ Indicates the beginning of the *d*₁ binding domain.

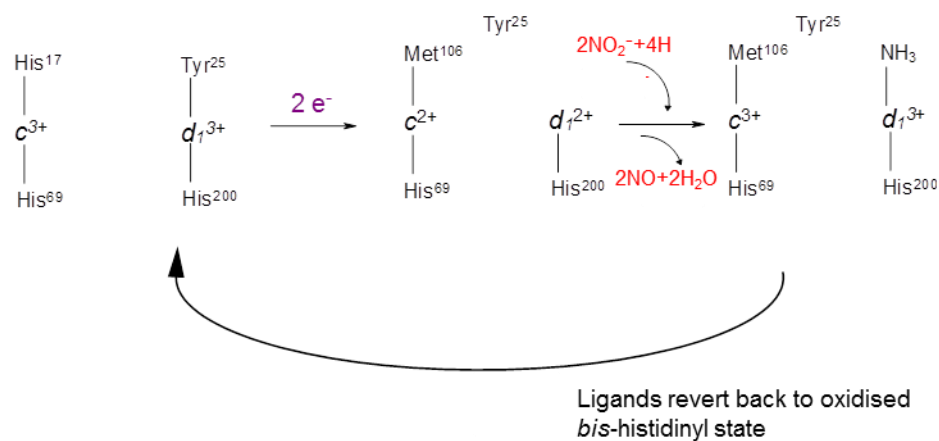


Figure 2.6.5: The unique ligand switch of *P. pantotrophus* cd_1 .

While a large part of the c domain architecture is altered upon reduction to the ferrous state, the only major change to the d_1 domain appears to be in the geometry of the heme itself. The geometry of the d_1 -heme changes from planar to a distorted ‘saddle-type shape’ causing the iron-to-iron distance between the two centres to increase from 20.0 to 21.2 Å. This change in geometry also results in the d_1 -heme becoming more solvent exposed. *Figure 2.6.6* shows the ligation to the c - and d_1 -hemes in dithionite-reduced crystals of *P. pantotrophus* cd_1 .

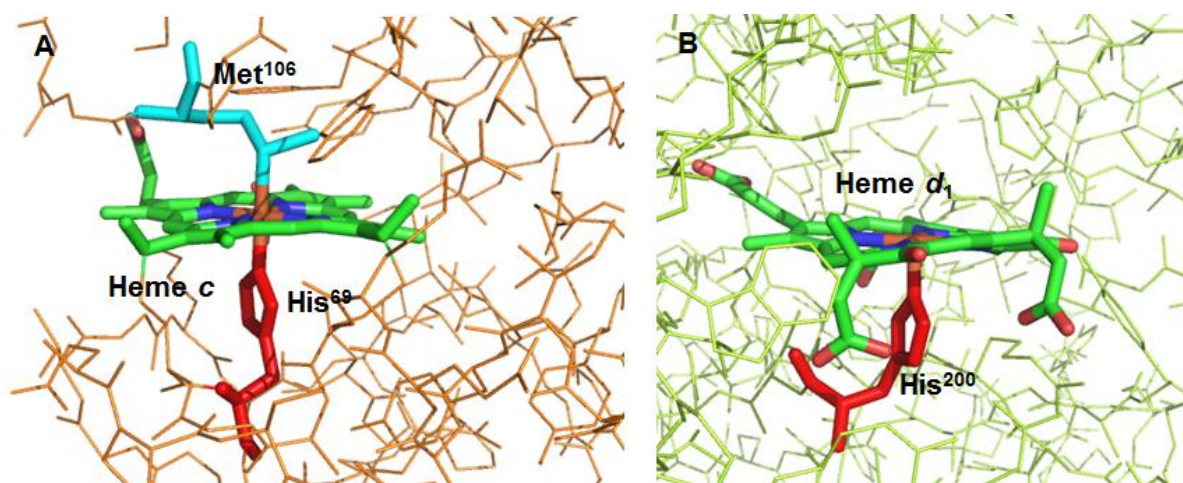


Figure 2.6.6: X-ray crystal structure of dithionite-reduced *P. pantotrophus* cytochrome cd_1 . Panel A shows the His^{69} / Met^{106} ligation to the c -heme; Panel B shows the pentacoordinate d_1 -heme (PDB code 1AOF(40)).

Interestingly, the crystal structure of oxidised *P. aeruginosa* cd_1 (also published in 1997) revealed that the ligands His⁵¹ and Met⁸⁸ coordinate the c -heme of the enzyme and His¹⁸² coordinates the d_1 centre at the proximal position (41). While the latter residue is equivalent to the His²⁰⁰ in *P. pantotrophus*, the distal ligand to the d_1 -heme is in fact a hydroxide (or water) molecule that is hydrogen-bonded to Tyr¹⁰ from the adjoining monomer. The ligation at the c -heme of the 'resting' structure of the *P. aeruginosa* enzyme is therefore identical to that of fully reduced *P. pantotrophus* cd_1 , as shown in Figure 2.6.7. Ligation to the c - and d_1 hemes is shown in Figure 2.6.8.

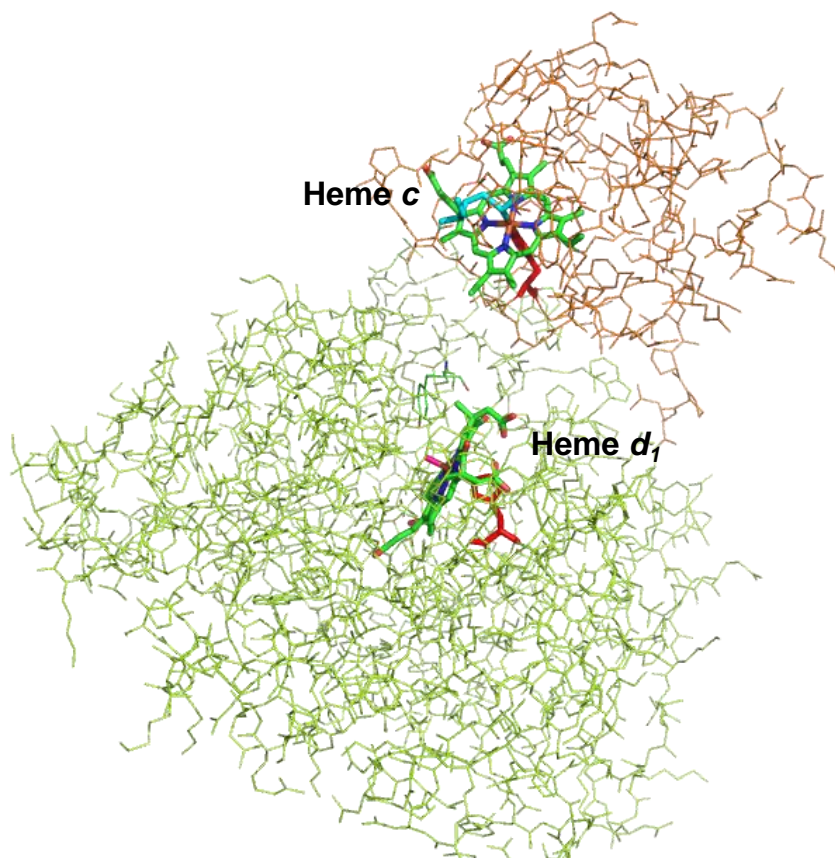


Figure 2.6.7: The X-ray crystal structure of a 'resting' (oxidised) monomer of cytochrome cd_1 from *P. aeruginosa* (PDB code 1NIR) (41).

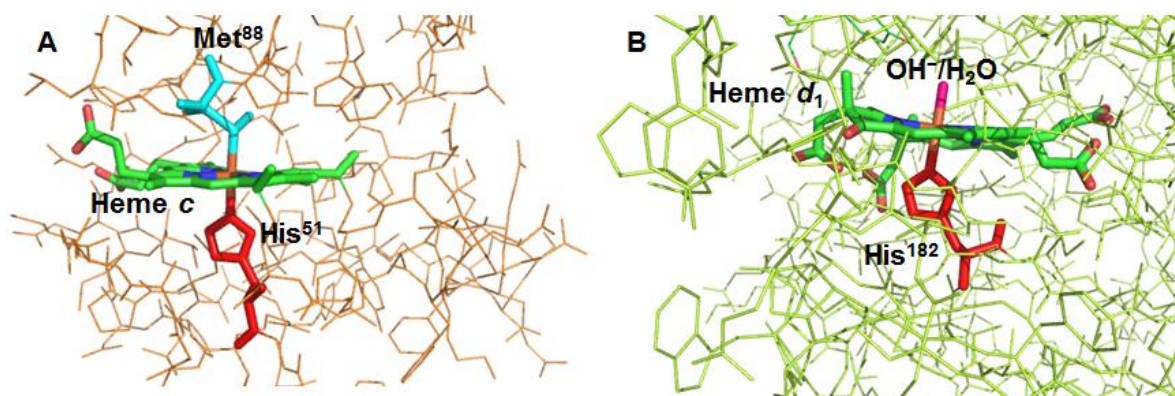


Figure 2.6.8: X-ray crystal structure of 'resting' (oxidised) cytochrome *cd*₁ from *P. aeruginosa*. Panel A shows the His⁵¹/Met⁸⁸ ligation at the *c*-heme; Panel B shows the His¹⁸²/ OH⁻ (or H₂O) ligation at the *d*₁-heme (PDB code 1NIR) (41).

2.6.3 The alternative, tetragonal crystal structure of *P. pantotrophus cd*₁

An alternative structural form of crystallised *P. pantotrophus cd*₁ was reported in 2001 by Sjögren *et al* (35). This raised a number of questions about the interaction between the individual subunits of the dimer. In contrast to previously published crystal structures of the *P. pantotrophus* enzyme that had been grown aerobically in the oxidised monoclinic form (24,32,40), tetragonal crystals of reduced protein were grown under anaerobic conditions. In the monoclinic crystal forms, a highly stable structure is adopted that is attributed to strong hydrogen bonds made between the individual *d*₁ domains. The individual *c* domains of the dimer are separated by an interface of hydrogen-bonded solvent molecules and do not make direct contact, allowing for large conformational changes within the crystal structure.

In the reduced tetragonal crystal structure, this solvent molecule interface between the *c* domains is absent, and the enzyme adopts an 'open' conformation. Overall, the *c* domain is rotated by 60° and displaced by around 20 Å compared with the monoclinic form. The overall folding of the individual *c* and *d*₁ domains in both the monoclinic and tetragonal crystal forms are similar, although in the case of the latter they are linked by a 'hinge' region comprising residues 132-136. As in the case of the reduced monoclinic

form, the reduced tetragonal crystal structure exhibits His/Met ligation at the *c*-heme, and the Tyr²⁵ ligand is displaced from the active site. Upon reoxidation in air however, the *c*-heme did not appear to revert to the ‘as isolated’ state, retaining the His/Met ligation of the reduced form. The ‘open’ and ‘closed’ forms (reduced tetragonal and oxidised monoclinic respectively) are illustrated in *Figure 2.6.9*.

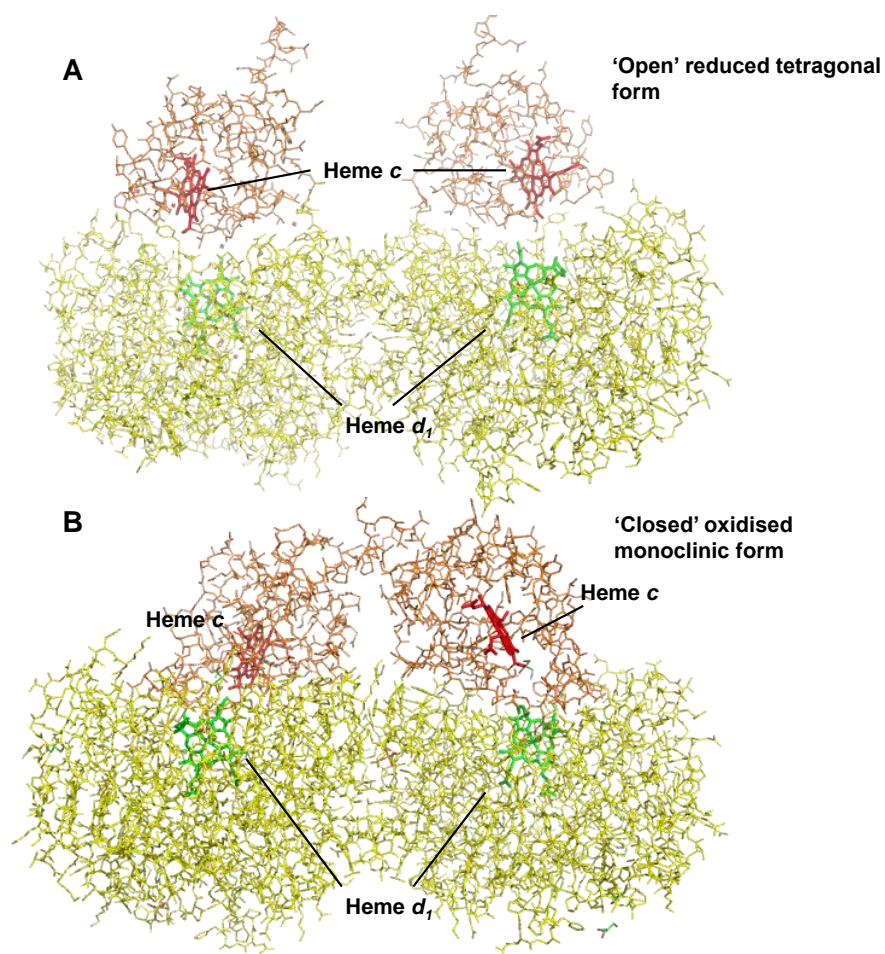


Figure 2.6.9: Panel A shows the ‘open’ reduced tetragonal crystal form of *P. pantotrophus* *cd*₁ (PDB code 1H9X (35)); Panel B shows the ‘closed’ oxidised monoclinic crystal form (PDB code 1QKS (24)).

Figure 2.6.10 shows the ligation at the *c*-heme in the reduced tetragonal form after re-oxidation in air.

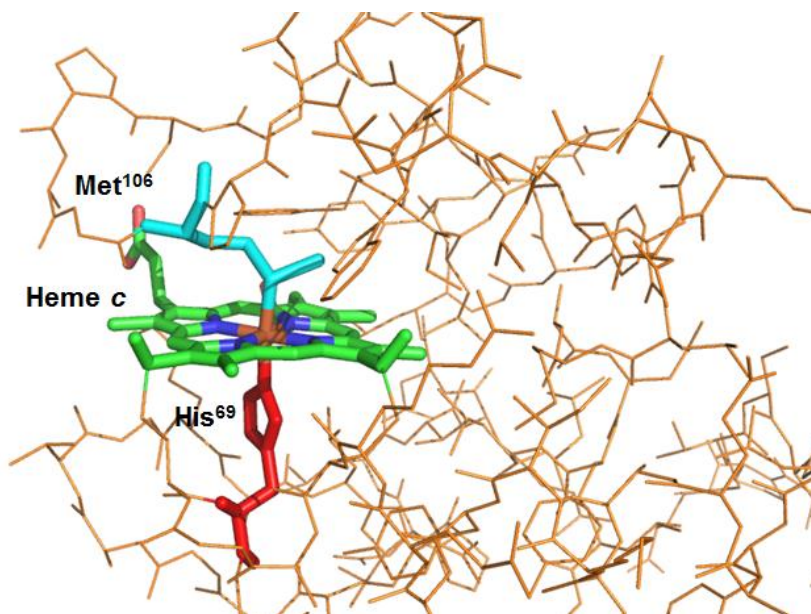


Figure 2.6.10: His⁶⁹/Met¹⁰⁶ ligation to the *c*-heme in the reduced tetragonal crystal form of *P. pantotrophus* *cd*₁ after re-oxidation in air (PDB code 1HCM (35)).

There are two histidine residues, His³⁴⁵ and His³⁸⁸ located near the entrance to the active site that were suggested by Fülöp *et al* (24) to provide the protons required during reduction of the nitrite molecule. In the reduced tetragonal form (and the oxidised monoclinic form (24)) these residues are hydrogen bonded to a solvent molecule. Separate studies on *P. aeruginosa* *cd*₁ have shown that mutation of either of these residues renders the enzyme incapable of nitrite reduction (42). The mutants were still capable of oxidase activity however, suggesting that the mechanisms for the two different reduction processes, at least in the *P. aeruginosa* enzyme, are different.

The most striking difference between the monoclinic and tetragonal crystal structures is the difference in the level of contact between the separate *c* domains in the two forms. This then leads to the question of whether crystal-packing effects influence the conformation adopted (i.e. ‘open’ or ‘closed’) and which would be the natural state for the enzyme in solution and therefore *in vivo*. As the oxidised monoclinic form adopts the

‘closed’ conformation (24), and the reduced tetragonal form the ‘open’ structure, it could be that in solution these are the forms adopted by the enzyme as part of the catalytic process. Free movement between the two states could be prevented by crystal packing effects, and hence the structural interchange could not be viewed in this, or previous crystallisation studies.

It was noted by Sjögren *et al* (35) that the alternative position of the *c* domain in the tetragonal reduced (‘open’) form leads to a change in the probable route of electron entry to the active site. In this form of the enzyme, electron entry to the active site would be likely to occur via the distal side of the *d*₁-heme. Conversely, in the monoclinic forms of the enzyme, electron transfer would most likely occur via the proximal side. There is also a proximal displacement of the *d*₁-heme by 0.5 Å in the reduced tetragonal form, which is accompanied by a notable structural alteration of the chain attached to the His²⁰⁰ ligand. While currently the mechanistic implications of these structural differences are not clear, it is likely that they are of significance to the functioning of the enzyme in the cell environment.

2.7 Further crystallographic studies on *P. pantotrophus* cytochrome *cd*₁

2.7.1 *The nitrite and nitric oxide-bound crystal structures*

Williams *et al* soaked dithionite-reduced crystals of monoclinic *P. pantotrophus cd*₁ in potassium nitrite for one minute (Crystal 1) and freeze-quenched them at 90 K (40). This was repeated with a different sample of fully-reduced enzyme; although on this occasion a reaction time of three minutes (Crystal 2) was allowed. After freeze-quenching, electron density maps from both samples were produced.

Firstly, it was observed that in Crystal 1, one of the enzyme subunits had nitrite bound to the d_1 -heme, the other nitric oxide. One of the subunits in Crystal 2 had nitrite bound to the d_1 -heme although the d_1 ligand assignment for the other subunit could not be confidently made. The bound nitric oxide was positioned at a 131° angle in a bent conformation, with a Fe-N bond length of 2.0 Å. It was noted that this angle is similar to that encountered for nitric oxide bound to iron in ferrous leghemoglobin (43). In case of Fe^{2+} -NO leghemoglobin however, the Fe-N bond length is slightly shorter at 1.7 Å.

UV-visible absorbance spectra recorded at 10 second time intervals during nitrite reduction showed several spectrally different intermediates. Crystals were able to undergo several cycles of nitrite reduction and the final spectrum showed features characteristic of oxidised *P. pantotrophus cd*₁. This led to the conclusion that the nitric oxide must be bound to the d_1 -heme in the ferric state. Assuming nitrite binds to the fully reduced enzyme, the subsequent reduction of substrate at the d_1 -heme would lead to the formation of a d_1^{3+} -NO intermediate. It was argued that the transfer of an electron from the c -heme to the d_1 centre before product removal would be catalytically disadvantageous as a putative ‘dead-end’ d_1^{2+} -NO complex would be formed. It is known that nitric oxide has a greater affinity for ferrous (compared to ferric) heme (44).

It was noted that in both nitrite-bound crystal structures, one of the nitrite oxygen atoms was positioned within hydrogen-bonding distance of the N atoms of the nearby His³⁴⁵ and His³⁸⁸ residues. The significance of these residues is a major focal point of this thesis and is explored further in Chapter 4.

The Tyr²⁵ was hydrogen bonded by the phenolate oxygen to the nearby His³⁴⁵ and His³⁸⁸ residues when the nitric oxide product was bound to the d_1 -heme. In the nitrite-bound form it appeared to be hydrogen bonded (again by the phenolate oxygen) to the Thr³⁸⁶ residue at a greater separation from the iron of the d_1 -heme, while in the

pentacoordinate (reduced) state it appeared to be in an unstructured region. This led to the conclusion that Williams *et al* had captured the return of the Tyr²⁵ residue to the d_1 centre following nitrite reduction.

In three of the intermediate structures (the c domain was difficult to see in the remaining map) the ligation at the c -heme had returned to the His/His conformation. However, it was not stated whether the relative alignment of these ligands was as viewed in the oxidised, pre-reacted enzyme. As the *bis*-histidinylligation state is characteristic of the oxidised form of the enzyme, this observation led to the conclusion that in the nitrite and nitric oxide-bound forms, the c -heme was in the ferric state. As the fully-reduced enzyme will be capable of reducing two molecules of substrate, this would imply that the second cycle of nitrite reduction had been captured in both forms of the crystal structure.

A number of important conclusions could be drawn from these observations. The first was that as both the product and substrate were bound to the d_1 -heme in all cases then this must be the catalytic centre of the enzyme. Product release is likely to be facilitated by the Tyr²⁵ owing to its positioning relative to the nitric oxide-bound d_1 -heme. From these results it is also clear that the conformational change at the c -heme is part of the catalytic cycle. As the reduction of nitrite to nitric oxide is a one electron process, in principle, a fully reduced monomer of cd_1 should be able to reduce two molecules of nitrite in one catalytic cycle. The question therefore is raised as to whether both hemes are ever simultaneously in the ferrous state during turnover *in vivo*.

2.7.2 The cyanide-bound crystal structure

Following the observation that *P. pantotrophus* cd_1 undergoes a unique ligand switch at the c -heme during catalysis, further investigation took place into the identity of the c -heme ligands in the 'activated' enzyme. In 2000 Jafferji *et al* published the 1.59 Å resolution

crystal structure of cyanide-bound *P. pantotrophus* cd_1 (37). This showed that after crystals of enzyme were dithionite-reduced and soaked in potassium cyanide, the CN^- anion became bound to the d_1 centre in the place of Tyr²⁵. Re-oxidation of this complex with ferricyanide removed the CN^- ligand and allowed the Tyr²⁵ to re-coordinate.

The X-ray diffraction data obtained for the re-oxidised complex indicated that it had returned to the ‘as isolated’ conformation. This is despite the fact that the features in the absorbance spectrum did not entirely correspond with those seen for the untreated, ‘as isolated’ complex, indicating minor structural differences between the solution and crystal forms of the re-oxidised enzyme. The Soret bands for both the c and d_1 -hemes in the re-oxidised sample were lower in intensity compared to the ‘as isolated’ and the former was slightly red shifted. It is known that at room temperature the d_1 -heme of the *P. pantotrophus* enzyme exists in a thermal spin-equilibrium mixture of high and low-spin states, giving rise to bands in the absorption spectrum at 702 and 640 nm respectively (28). The intensity of the 640 nm band compared with that at 702 nm was also larger in the re-oxidised complex, suggesting that there was less high-spin d_1 present. Possible reasons for the discrepancies between the optical spectra and the X-ray diffraction data were not discussed.

One important observation made from the results was that the c -heme in the cyanide-bound complex was coordinated by the His⁶⁹/Met¹⁰⁶, as observed in the fully-reduced enzyme (40). The suggested reason for this is that when nitrite is bound to the d_1 -heme, it is capable of being reduced, causing oxidation at that centre and subsequently that of the c -heme. Cyanide cannot be reduced and hence the c -heme remains locked in the reduced state unable to revert to the *bis*-histidinylligation. However, further studies by EPR spectroscopy (27,45,46) have indicated that the ligation of the c -heme in the nitric oxide and ‘nitrite-bound complexes’ is not as observed for the ‘as isolated’ enzyme. The

perpendicular arrangement of the *c*-heme histidine ligands in the oxidised protein gives rise to a ‘Large g_{\max} ’ type signal (31) at $g = 3.05$. In the nitric oxide and nitrite-bound complexes, this signal is replaced by a ‘rhombic trio’ with g values (for g_z , g_y and g_x respectively) of ~ 2.93 , 2.32 and 1.4 . Note, ‘rhombic trio’ is a term previously used in the literature to describe EPR signals of this type (47,48). While these values were originally assigned to His⁶⁹/Met¹⁰⁶ coordinated at the *c*-heme, EPR alone cannot be used as a reliable method of assigning ligand identity. A pair of axial histidine ligands rotated away from the perpendicular arrangement has also been suggested to account for these spectral features (27).

Additional NIR-MCD studies on nitrite-reacted and hydroxylamine-re-oxidised *P. pantotrophus cd₁* revealed that the *c*-heme does indeed adopt His/Met coordination when ‘activated’ (27,49). In the former study it was demonstrated that the enzyme can be activated by nitrite without first reducing the enzyme. This work is discussed in more detail in Chapter 4 of this thesis. The reason(s) why Williams *et al* (40) should view *bis*-histidinyl ligation at the *c*-heme in crystals of protein that still have nitrite and nitric oxide bound to the *d₁*-heme remains unclear. Clearly, crystal studies alone do not provide an adequate means of protein structure/function correlation, and should ideally be used in conjunction with spectroscopic techniques.

2.8 A pulse radiolysis study of *P.pantotrophus cd₁*

There is another case reported in the literature of *bis*-histidinyl ligation existing at the *c*-heme when the complex is reduced. A pulse radiolysis study of the enzyme designed to obtain an accurate value for the inter-heme electron transfer was carried out in 1997 (26). The technique of pulse radiolysis is intended to allow for the introduction of an electron to a specific redox centre, and hence ensure that in multi-heme enzymes such as *cd₁* only one

cofactor is selectively reduced. In this case, *P. pantotrophus* cd_1 was reacted with N-methylnicotinamide (NMA) radicals, causing reduction of the *c*-heme only. The subsequent reduction of the d_1 -heme was monitored by absorbance spectroscopy on the millisecond timescale and the experiment was also carried out in the presence of nitrite. The absorbance spectrum of the sample solution obtained immediately (the sum of the 0.1 and 2 ms kinetic difference spectra) after pulse radiolysis was different to that of the fully reduced enzyme in the *c*-heme Soret region, leading to the conclusion that the enzyme was still *bis*-histidinyll coordinated. The rationale for this was that the *c*-heme would be reduced more rapidly by the NMA radicals than when a chemical reductant such as dithionite is used. This means that the His/His \rightarrow His/Met ligand switch would not have had time to occur. Alternatively, it was suggested that either reduction of the d_1 centre (and removal of the Tyr²⁵) or the arrival of a second electron at the *c*-heme is required to initiate this process.

In the presence of nitrite, the same spectral changes were observed, again indicating the reduction of the d_1 centre via the *c*-heme. However, an increase in the intensity at 620 nm and a concomitant decrease in the absorbance at 460 nm were also observed and these changes were attributed to nitrite binding to the d_1 -heme. This species was persistent for at least 30 seconds after the introduction of the pulse. However, although it is stated that only the d_1 -heme difference spectrum was affected by the presence of nitrite, the *c*-heme Soret region was not reported in this publication. Only at wavelengths greater than 600 nm can the absorbance be confidently attributed to the d_1 -heme alone (50). This means that there could have been underlying changes in the *c*-heme present in the spectrum reported between 450 and 600 nm. It is also not possible to unambiguously assign ligation states based on absorbance spectroscopy and further work is required in order to confidently

assign the ligation at the *c*-heme in the nitrite-exposed sample and the sample obtained immediately after pulse radiolysis, as discussed above.

One important finding of this work was that the inter-heme electron transfer rate was found to be 1000 times greater than in the previous study by Silvestrini *et al* (21). Differences in technique and identity of the enzyme (*P. aeruginosa* was used by Silvestrini and co-workers) were cited as being the likely reasons for this discrepancy. If Kobayashi *et al* had indeed prepared the protein in the *bis*-histidinyll state, there is also the possibility that the lower reduction potential of the *c*-heme (compared with that of the His/Met ligated *c*-heme in the *P. aeruginosa* enzyme) facilitated electron transfer and hence increased the rate. The question would still remain, however, as to why the *P. pantotrophus* enzyme would experience a reduced electron transfer rate in the His/Met state compared to *P. aeruginosa* when the overall architecture of the two enzymes is so similar.

2.9 The Y25S mutant

In 2003 Gordon *et al* (51) investigated the function of the Tyr²⁵ ligand to ascertain whether its coordination at the *d*₁ centre is required if *bis*-histidinyll ligation is to be adopted at the *c*-heme. As *P. denitrificans* nitrite reductase is the only other form of *cd*₁ in which the Tyr²⁵ ligand is conserved, it was questioned as to whether its presence is absolutely necessary for catalytic activity. It was found that in the Y25S variant, where the Tyr²⁵ was replaced with a serine residue (Ser²⁵), the 1.4 Å resolution crystal structure showed *bis*-histidinyll coordination at the *c*-heme. When fully reduced, the Y25S variant gave an absorbance spectrum virtually identical to that of reduced wild-type enzyme, and the *k*_{cat} values for nitrite reduction were 67 s⁻¹ (Y25S mutant) and 68 s⁻¹ (wild-type) respectively. The Y25S variant was found to be able to sustain catalysis at the same rate even when the pre-reduction step was omitted, while the wild-type enzyme showed a dramatic decrease in

activity of 96 %. It was therefore concluded that the coordination of Tyr²⁵ is not necessary for catalysis to occur, as the k_{cat} values for both types of enzyme are strikingly similar. It is also suggested that this residue does not directly drive the nitric oxide product from the d_1 -heme, but may cause some disruption to the surrounding area that indirectly facilitates this process, as previously suggested by Ranghino *et al* (52).

The results also indicate that coordination of the Tyr²⁵ is not vital for *bis*-histidinyll coordination at the *c*-heme to be adopted. While this appears to be true, it is important to remember that there is no indication from this study that the *c*-heme does not adopt the His/Met form when in solution. The absorption spectra of the oxidised Y25S variant and the oxidised wild-type enzyme show dramatic differences in the d_1 region, with the former exhibiting a complete disappearance of the 702 nm band and a broadening/increase in the intensity of the 640 nm feature. The indication is, therefore, that removal of the Tyr²⁵ causes all of the d_1 -heme in the sample to adopt the low-spin state, as observed for the *P. aeruginosa* enzyme. Any differences in the *c*-heme Soret region between the oxidised wild-type and mutant forms of the enzyme were not discussed or shown, and it is not clear whether a feature at 695 nm was observed (indicating a sulphur atom coordinated to a low-spin ferric *c*-type heme (50)).

There was therefore no conclusive proof from this study that *bis*-histidinylligation was present at the *c*-heme of the mutant in both the solution and crystal forms. It was in fact proven two years later by MCD and EPR spectroscopies (53) that the *c*-heme in the Y25S variant had His/Met ligation when in solution, and would bind cyanide and nitrite when in the oxidised state. This indicated that as a result of crystal-packing effects, significant structural differences may exist between the solution (and therefore *in vivo*) and crystal forms of the enzyme.

2.10 Spectroscopic investigations of the *c*-heme ligation in semi-apo *P. pantotrophus* *cd*₁

The form of the enzyme with the *d*₁-heme group removed (the ‘semi-apo’ form) was previously thought to adopt exclusively His/Met coordination at the *c*-heme, a conclusion based on the observed ‘rhombic’ EPR spectrum (with *g*-values of 2.93 and 2.26 – the third value was not resolved) and the appearance of a small feature at 695 nm in the absorbance spectrum (50). Recent work incorporating the use of both EPR and NIR-MCD spectroscopies (Cheesman, M.R. and Kemp, G., *Unpublished*) has shown that in fact the semi-apo form contains a mixture of His/His and His/Met coordinated *c*-heme. While a rhombic EPR signal was observed for the remaining *c*-heme (with *g*-values of 2.97, 2.26 and 1.46), the NIR-MCD spectrum showed bands at 1500–1520 nm and 1760–1800 nm indicating *bis*-histidinyI and His/Met ligation respectively. Therefore, the NIR MCD results demonstrate that the EPR signatures of the His/Met coordinated *c*-heme are virtually indistinguishable from a His/His coordinated species in which the relative orientations of the planes of the histidine ligands is rotated away (i.e. in the parallel orientation) from that in the ‘as prepared’ enzyme. Therefore, using EPR spectroscopy alone as a method of assigning heme axial ligation can be misleading, as in the case of low-spin ferric hemes, it is a technique that is primarily an indicator of ligand orientation not identity. This will be discussed further in Chapter 3 of this thesis.

2.11 An overview of the spectroscopic investigations carried out on *P. pantotrophus* *cd*₁ as part of this thesis

This recent work led us to question whether re-oxidation of the ‘activated’ (fully reduced) *P. pantotrophus* enzyme by substrate does indeed cause a straight reversion to the perpendicular-orientated *bis*-histidinyl *c*-heme or whether there is an additional ‘interim’ stage where the His/His ligands adopt the parallel orientation. The rhombic EPR spectrum obtained (with *g*- values of ~2.94, 2.33, 1.40) immediately after the re-oxidation of *P. pantotrophus* *cd*₁ has previously been assigned to His/Met coordination at the *c*-heme (45,54). There has been some speculation (26,27) as to whether these features could be attributed to a pair of axial histidine residues rotated away from the perpendicular conformation observed in the ‘as prepared’ enzyme. This could produce an equivalent EPR spectrum to that observed for the proposed His/Met ligation of the ‘activated’ enzyme (31).

It has been estimated from previous NIR-MCD studies that the majority (approximately 72 %) of the *c*-heme is His/Met coordinated, approximately one minute post re-oxidation with hydroxylamine hydrochloride, but around 28 % does remain in the *bis*-histidinyl state (49). Unfortunately the ligation at the *d*₁-heme cannot be investigated using this technique as the porphyrin-to-Fe³⁺ CT_{1s} transition for the unusual (*d*_{zx}, *d*_{yz})⁴ (*d*_{xy})¹ ground state is symmetry forbidden.

Section 2.12 of this chapter describes the growth and purification of *P. pantotrophus* *cd*₁ for use in the spectroscopic studies undertaken as part of this thesis.

Chapter 3 describes an investigation into the ligation state at the *c*-heme following re-oxidation of fully reduced *P. pantotrophus* *cd*₁ using hydroxylamine hydrochloride. A number of spectroscopic techniques were used in this study, including a novel time-resolved NIR-MCD technique which allowed data collection one second post re-oxidation by hydroxylamine hydrochloride. Chapter 4 describes a UV-visible MCD investigation

into how the solution pH influences the form of d_1^{2+} -NO intermediate formed upon reaction of the fully reduced enzyme with nitrite.

2.12 Growth and purification of *P. pantotrophus* cd_1

2.12.1 *Growth of *P. pantotrophus* cd_1*

The method of Moir *et al* (22) for the growth and purification of *P. pantotrophus* cytochrome cd_1 was employed, with the inclusion of an additional, final purification step – the use of gel filtration column. Media details are provided in Section 2.12.3.

An aliquot of *P. pantotrophus* M6 glycerol stock² (50 μ L) was used to inoculate a 5 mL portion of Luria-Bertani (LB) medium containing 5 μ L, 100 mg mL⁻¹ kanamycin. The resulting LB culture was grown overnight at 37 °C with shaking at 200 rpm (in an Innova 4000 incubator shaker). Following this, a 200 μ L aliquot of the culture was added to 50 mL minimal media and supplemented with 50 μ L of 100 mg mL⁻¹ kanamycin and 100 μ L of Vishniac solution. This process was repeated three times, and the cultures grown at 30 °C with shaking at 100 rpm for ~ eight hours (incubator details as before). Each 50 mL culture was transferred into a 2 L conical flask containing 1.5 L of minimal media supplemented with 1.5 mL of 100 mg mL⁻¹ kanamycin and 3 mL Vishniac solution. After overnight growth at 30 °C (without shaking, in a Max Q 4000 shaker) the 1.5 L cultures were added to 4 L portions of minimal media supplemented with 5 mL of 100 mg mL⁻¹ kanamycin and 10 mL of Vishniac solution. The cultures were grown for 24 hours at 30 °C (without shaking, in a Excella E25 incubator) and centrifuged at 8000 rpm (in ~ 900 mL batches) for 10 minutes. Following this, the cell pellets were re-suspended in ~ 800 mL spent media.

² *P. pantotrophus* M6 was obtained from D. Andrew Gates at the University of East Anglia as a 1 mL glycerol stock.

For the next stage, the re-suspended culture was centrifuged (Beckman Avanti J-25) at 6000 rpm for 20 minutes and the pellets re-suspended in spheroplast buffer (pH 8, 100 mM TRIS, 0.5 M sucrose and 3 mM ethylenediaminetetraacetic acid [EDTA]). After re-suspension, the cells were placed in a water bath at 37 °C and 250 mg of lysozyme added with continual stirring for ~ one hour. Following centrifugation at 20,000 rpm (Allegra 64R Beckman Coulter), the resulting red/brown supernatant was purified according to the method described below.

2.12.2 Purification of *P. pantotrophus cd₁*

A DEAE-Sepharose column (500 mL column volume) was equilibrated with 1.5 column volumes of TRIS buffer (100 mM, pH 8.0). The periplasmic extract prepared according to the method described above was introduced onto the column and washed with 1.5 column volumes of the same buffer. Elution of the protein was achieved using 500 mL TRIS (100 mM, pH 8.0) with a 0-500 mM NaCl gradient at a flow rate of 4 mL min⁻¹.

The red/brown cytochrome *cd₁* fractions were collected in 5 mL portions, pooled and concentrated to ~ 3 mL in Amicon Ultra 10,000 MWCO centricons. A Phenyl-Sepharose column (15 mL column volume) was washed with a total of 10 column volumes of 100 mM TRIS buffer, pH 8.0 containing ammonium sulphate at 40 % saturation. The concentrated protein (also containing ammonium sulphate at 40 % saturation) was introduced onto the column. After washing with a further 10 column volumes of the same buffer, the protein was eluted using 200 mL TRIS buffer (100 mM, pH 8) with a salt gradient of 40–0 % at a flow rate of 1 mL min⁻¹ and the 5 mL *cd₁* fractions pooled.

The pooled fractions were concentrated (as before) to ~ 4 mL and loaded on to a S200 26/60 gel filtration column that had been pre-equilibrated with one column volume of

100 mM TRIS buffer, pH 8.0. After filtration using the same buffer, the red/brown fractions were pooled and concentrated to ~ 4 mL. Protein purity is conventionally judged by the ratio of heme to protein and can be determined from the $A_{\text{Soret}}/A_{280\text{nm}}$ value in the UV-visible absorption spectrum. Using the method detailed here, growths of ~ 20 L yielded ~ 120 mg of *P. pantotrophus cd*₁ with a purity of ~ 1.47.

2.12.3 Media details

Minimal media: sodium succinate (5.4 g L⁻¹), KNO₃ (5.05 g L⁻¹), NaCl (2.92 g L⁻¹), Na₂HPO₄ (1.7 g L⁻¹), KH₂PO₄ (1.49 g L⁻¹), NH₄Cl (0.54 g L⁻¹) and MgSO₄·7H₂O (0.1 g L⁻¹).

Vishniac solution (adjusted to pH 8): EDTA (50 g L⁻¹), ZnSO₄·7H₂O (2.2 g L⁻¹), CaCl₂ (5.54 g L⁻¹), MnCl₂·4H₂O (5.06 g L⁻¹), FeSO₄·7H₂O (4.99 g L⁻¹), CuSO₄·5H₂O (1.57 g L⁻¹), (NH₄)₆Mo₇O₂₄·4H₂O (1.10 g L⁻¹) and CoCl₂·6H₂O (1.61 g L⁻¹).

2.13 References

1. Smil, V. (2000) *Cycles of Life: Civilisation and the Biosphere* W.H. Freeman, New York
2. Zumft, W. G. (1993) *Arch Microbiol* **160**, 253-264
3. Wijler, J., and Delwiche, C. C. (1954) *Plant Soil* **5**, 155-169
4. Baalsrud, K. (1954) *Arch Microbiol* **20**, 34-62
5. Horio, T. (1958) *J Biochem* **45**, 195-205
6. Newton, N. (1969) *Biochim Biophys Acta* **185**, 316-331
7. Lam, Y., and Nicholas, D. J. D. (1969) *Biochim Biophys Acta* **180**, 459-472.
8. Sawhney, V., and Nicholas, D. J. D. (1978) *J Gen Microbiol* **106**, 119-128
9. Lemberg, R., and Barrett, J. (1973) *The Cytochromes*, Academic Press, New York
10. Barrett, J. (1956) *Biochem J* **64**, 626-639
11. Yamanaka, T., and Okunuki, K. (1963) *Biochim Biophys Acta* **67**, 407-416
12. Walsh, T. A., Johnson, M. K., Barber, D., Thomson, A. J., and Greenwood, C. (1981) *J Inorg Biochem* **14**, 15-31
13. Chang, C. K. (1985) *J Biol Chem* **260**, 9520-9522.
14. Timkovich, R., Cork, M. S., and Taylor, P. V. (1984) *J Biol Chem* **259**, 1577-1585.

15. Timkovich, R., Cork, M. S., and Taylor, P. V. (1984) *J Biol Chem* **259**, 15089-15093
16. Murphy, M. J., Siegel, L. M., Kamin., H., and Rosenthal, D. (1973) *J Biol Chem* **248**, 2801-2814.
17. Stolzenberg, A. M., Spreer, L. O., and Holm, R. H. (1980) *J Am Chem Soc* **102**, 364-370.
18. Chang, C. K., and Wu, W. (1986) *J Biol Chem* **261**, 8593-8596.
19. Alefounder, P. R., and Ferguson, S. J. (1980) *Biochem J* **192**, 231-240
20. Godden, J. W., Turley, S., Teller, D. C., Adman, E. T., Liu, M. Y., Payne, W. J., and Legall, J. (1991) *Science* **253**, 353-484
21. Silvestrini, M. C., Tordi, M. G., Musci, G., and Brunori, M. (1990) *J Biol Chem* **265**, 11783-11787
22. Moir, J. W. B., Baratta, D., Richardson, D. J., and Ferguson, S. J. (1993) *Eur J Biochem* **212**, 377-385
23. Robertson, L. A., and Kuenen, J. G. (1983) *J Gen Microbiol* **129**, 2847-2855.
24. Fulop, V., Moir, J. W. B., Ferguson, S. J., and Hajdu, J. (1995) *Cell* **81**, 369-377
25. Chang, C. K., and Wu, W. (1987) *J Am Chem Soc* **109**, 3149-3150
26. Kobayashi, K., Koppenhofer, A., Ferguson, S. J., and Tagawa, S. (1997) *Biochemistry* **36**, 13611-13616
27. Van Wonderen, J., Knight, C., Oganessian, V. S., George, S. J., Zumft, W. G., and Cheesman, M. R. (2007) *J Biol Chem* **282**, 28207-28215
28. Cheesman, M. R., Ferguson, S. J., Moir, J. W. B., Richardson, D. J., Zumft, W. G., and Thomson, A. J. (1997) *Biochemistry* **36**, 16267-16276
29. Silvestrini, M. C., Falcinelli, S., Ciabatti, I., Cutruzzola, F., and Brunori, M. (1994) *Biochimie* **76**, 641-654
30. Walsh, T. A., Johnson, M. K., Greenwood, C., Barber, D., Springall, J. P., and Thomson, A. J. (1979) *Biochem J* **177**, 29-39
31. Walker, F. A. (1999) *Coord Chem Rev* **186**, 471-534
32. Fulop, V., Moir, J. W. B., Ferguson, S. J., and Hajdu, J. (1993) *J Mol Biol* **232**, 1211-1212
33. Akey, C. W., Moffat, K., Wharton, D. C., and Edelstein, S. J. (1980) *J Mol Biol* **136**, 19-43
34. DeBoer, A. P. N., Reijnders, W. N. M., Kuenen, J. G., Stouthamer, A. H., and Van Spanning, R. J. M. (1994) *Antonie van Leeuwenhoek* **66**, 111-127
35. Sjogren, T., and Hajdu, J. (2001) *J Biol Chem* **276**, 29450-29455
36. Sutherland, J., Greenwood, C., Peterson, J., and Thomson, A. J. (1986) *Biochem J* **233**, 893-898
37. Jafferji, A., Allen, J. W. A., Ferguson, S. J., and Fulop, V. (2000) *J Biol Chem* **275**, 25089-25094
38. Page, C. C., Moser, C. C., Chen, X., and Dutton, P. L. (1999) *Nature* **402**, 47-52
39. Mozzarelli, A., and Rossi, G. L. (1996) *Annu Rev Biophys Biomol Struct* **25**, 343-365
40. Williams, P. A., Fulop, V., Garman, E. F., Saunders, N. F. W., Ferguson, S. J., and Hajdu, J. (1997) *Nature* **389**, 406-412
41. Nurizzo, D., Silvestrini, M. C., Mathieu, M., Cutruzzola, F., Bourgeois, D., Fulop, V., Hajdu, J., Brunori, M., Tegoni, M., and Cambillau, C. (1997) *Structure* **5**, 1157-1171
42. Cutruzzola, F., Brown, K., Wilson, E. K., Bellelli, A., Arese, M., Tegoni, M., Cambillau, C., and Brunori, M. (2001) *Proc Natl Acad Sci U S A* **98**, 2232-2237

43. Harutyunyan, E. H., Safonova, T., N., Kuranova, I. P., Popov, A. N., Teplyakov, A. V., Obmolova, G. V., Vainshtein, B. K., Dodson, G. G., and Wilson, J. C. (1996) *J Mol Biol* **264**, 152-161.
44. Ribeiro, J. M. C., Hazzard, J. H., Nussenzveig, R. H., Champagne, D. E., and Walker, F. A. (1993) *Science* **260**, 539-541
45. Allen, J. W. A., Higham, C. W., Zajicek, R. S., Watmough, N. J., and Ferguson, S. J. (2002) *Biochem J* **366**, 883-888
46. George, S. J., Allen, J. W. A., Ferguson, S. J., and Thorneley, R. N. F. (2000) *J Biol Chem* **275**, 33231-33237
47. Clarke, T. A., Dennison, V., Seward, H. E., Burlat, B., Cole, J. A., Hemmings, A. M., and Richardson, D. J. (2004) *J Biol Chem* **279**, 41333-41339
48. Palmer, G., Multani, J. S., Cretney, W. C., Zumft, W. G., and Mortenson, L. E. (1972) *Arch Biochem Biophys* **153**, 325-332
49. Allen, J. W. A., Cheesman, M. R., Higham, C. W., Ferguson, S. J., and Watmough, N. J. (2000) *Biochem Biophys Res Commun* **279**, 674-677
50. Koppenhofer, A., Little, R. H., Lowe, D. J., Ferguson, S. J., and Watmough, N. J. (2000) *Biochemistry* **39**, 4028-4036
51. Gordon, E. H. J., Sjogren, T., Lofqvist, M., Richter, C. D., Allen, J. W. A., Higham, C. W., Hajdu, J., Fulop, V., and Ferguson, S. J. (2003) *J Biol Chem* **278**, 11773-11781
52. Ranghino, G., Scorza, E., Sjogren, T., Williams, P. A., Ricci, M., and Hajdu, J. (2000) *Biochemistry* **39**, 10958-10966
53. Zajicek, R. S., Cheesman, M. R., Gordon, E. H. J., and Ferguson, S. J. (2005) *J Biol Chem* **280**, 26073-26079
54. Allen, J. W. A., Watmough, N. J., and Ferguson, S. J. (2000) *Nat Struct Biol* **7**, 885-888

3. Spectroscopic investigations into the unique ligand switch of *P. pantotrophus* cytochrome *cd*₁ nitrite reductase

3.1 The unique ligand switch of *P. pantotrophus* *cd*₁

3.1.1 *The role of the Tyr²⁵ ligand*

P. pantotrophus cytochrome *cd*₁ is structurally unique compared with other forms of the enzyme in that the *d*₁-heme is directly axially ligated by a distal Tyr²⁵ residue. This residue dissociates upon reduction of the metal centre to the ferrous state, allowing the nitrite substrate to bind and undergo reduction to nitric oxide. Additionally, only the *P. pantotrophus* enzyme has an associated change in ligation at the *c*-type heme that has been shown to occur in conjunction with the removal of Tyr²⁵ (1).

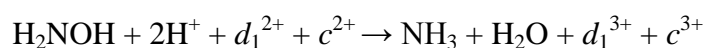
During the catalytic cycle, the reduction of nitrite at the *d*₁-heme leads to an intermediate *d*₁³⁺-NO species (2). It is currently unknown how the exact removal or displacement of the nitric oxide molecule occurs, although there have been a number of investigations into this process reported in the literature on the *P. pantotrophus* (3,4) and *P. aeruginosa* (5,6) forms of the enzyme. However, it has been suggested (2) that the re-coordination of the Tyr²⁵ ligand displaces the nitric oxide product and thus facilitates its removal from the active site. This is not a surprising suggestion as the *d*₁-heme in the 'as prepared' form of *P. pantotrophus* *cd*₁ is axially coordinated by this residue (along with His²⁰⁰), indicating that this ligation state is the 'resting' form of the enzyme.

It has also been suggested (7) that the coordination of the Tyr²⁵ ligand protects the active site and prevents the reaction of the *d*₁-heme with dioxygen and peroxide compounds. This may lead to the production of harmful side products and in the Y25S mutant form of the enzyme (which contains a serine residue in place of the Tyr²⁵), exposure of the respiring culture to an aerobic environment results in the production of

mainly semi-apo enzyme (8). As the Y25S mutant displays equal activity with respect to nitrite reduction as the wild-type enzyme, it would appear that the direct re-coordination of Tyr²⁵ to the *d*₁-heme is not the principle driving force in the dislocation of nitric oxide. It has been suggested (8) that product removal is facilitated by the approach of Tyr²⁵ (or Ser²⁵ in the Y25S mutant), which interacts with the nearby His³⁴⁵ and His³⁸⁸ residues but does not actually re-coordinate to the metal to adopt the ‘as prepared’ state. Mutation studies on the *P. aeruginosa* enzyme have shown that nitrite activity is dramatically reduced if either of the invariant His³²⁷ and His³⁶⁹ residues is substituted for alanine (9).

3.1.2 Re-oxidation of ‘activated’ *P. pantotrophus* *cd*₁ by hydroxylamine hydrochloride

In 2000, Allen *et al* used EPR spectroscopy to monitor the His/Met → His/His ligand reversion at the *c*-heme following hydroxylamine re-oxidation at pH 7 (10). Hydroxylamine hydrochloride (NH₂OH.HCl) is a convenient substitute for nitrite in experiments requiring the simultaneous re-oxidation of both *c* and *d*₁-heme centres (11). During the reaction, one molecule of hydroxylamine oxidises both heme centres to the ferric state and yields ammonia and water as by-products. It has been suggested (10) that ammonia binds transiently to the *d*₁-heme as an intermediate, *d*₁³⁺-NH₃:



Nitrite, in contrast is a one-electron oxidant that results in the semi-reduced enzyme with bound product, while the four-electron oxidation by O₂ is complicated by the formation of radicals and an oxoferryl [Fe^{IV}=O]²⁺ species.

3.1.3 Spectroscopic investigations by Allen *et al*

Allen *et al* (10) observed that soon (80 seconds) after the addition of hydroxylamine to the dithionite-reduced enzyme, a prominent positive feature was observed in the EPR spectrum at $g = 2.67$ prior to the emergence of a rhombic trio with g values of 2.53, 2.20 and 1.86. The former feature was speculatively assigned to ammonia-bound d_1 -heme, while the latter spectrum was attributed to the re-attachment of the Tyr²⁵ to this centre, resulting in the low/high-spin thermal equilibrium being re-established. The corresponding high-spin d_1 feature at $g = 6.88$ could be observed at this point, albeit with very low intensity. An additional rhombic trio with g values of $g_x = 2.94$, $g_y = 2.33$ and $g_z = 1.40$ could also be observed, which was assigned to His/Met coordinated c -heme based on earlier EPR assignments (12-14). Over the course of 60 minutes, spectra were recorded at regular intervals. The $g = 2.67$ feature was observed to collapse, while the Tyr-bound d_1 rhombic trio grew in intensity, eventually dominating the spectrum with g values (g_x , g_y and g_z respectively) of 2.51, 2.21 and 1.86.

It is not clear from the presentation of results by Allen *et al* (Figure 3.1.1) at which point over the 60 minutes this His/Met trio completely collapses, although by 60 minutes a homogeneous signal at $g = 3.03$ (attributed to the c -heme) could be seen. The authors claim that the enzyme isomerises to the ‘as isolated’ conformation in 20 minutes, although the spectrum recorded at this time point was not comparable with that obtained for oxidised *P. pantotrophus* cd_1 in the d_1 region. While the spectrum shown 60 minutes after hydroxylamine addition appeared to contain all the features expected for the ‘as isolated’ enzyme, no integration was carried out, and there was no original ‘pre-reaction’ cd_1 spectrum provided for comparison. If there was an interim period during the His/Met \rightarrow perpendicular His/His reversion where the c -heme ligands adopt a parallel His/His

conformation then this could arguably be indistinguishable from the His/Met state in the EPR spectrum (15).

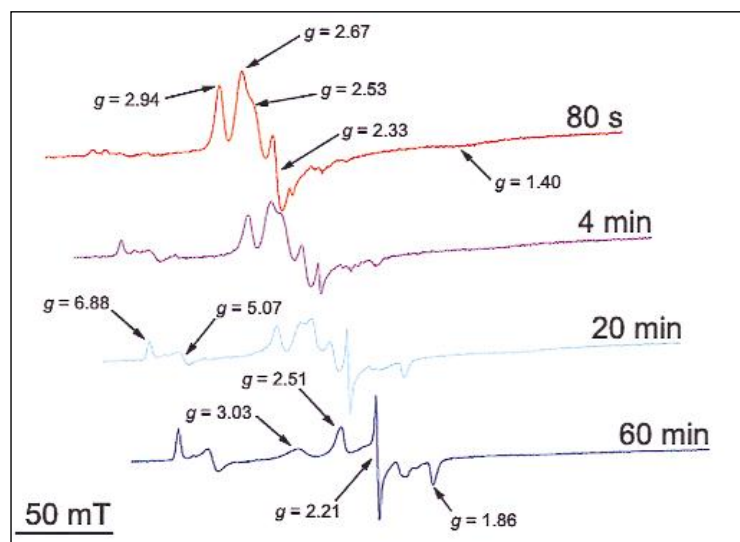


Figure 3.1.1: The progress of the hydroxylamine re-oxidation of dithionite-reduced *P. pantotrophus* cd_1 as reported by Allen *et al* (10). The spectra recorded at 80 seconds and at 4, 20 and 60 minutes post-hydroxylamine addition were reported (Reprinted by permission from MacMillan Publishers Ltd [Nature Structural Biology] Allen, J. W. A., Watmough, N. J., and Ferguson, S. J. (2000) *Nat Struct Biol* 7, 885-888. Copyright 2000).

Allen *et al* monitored the reversion at the *c*-heme by absorbance spectroscopy at 425 nm, a wavelength that has been claimed to mainly reflect the oxidation state of that particular centre (12,16), (although this is disputed, as discussed in Section 3.3 of this chapter) and calculated a first order rate constant, k_{obs} of 0.22 min^{-1} from the data. An identical value for the corresponding d_1 process (at 700 nm) was given, leading the authors to conclude that the initial reversion process at the two hemes occurs concomitantly. However, while the reversion was monitored by EPR for 60 minutes, the process appeared to be monitored by absorbance spectroscopy for only just over 20 minutes. The EPR spectra showed that there were further changes still occurring at both hemes after 20 minutes. This would appear to be reflected in the absorbance time course spectrum at 425 nm, which showed an initial rapid increase in the relative absorbance for the first ~ 10 minutes, followed by a further slower increase that continued for the remaining time the

measurement was recorded (10÷23 minutes). By ~ 17 minutes, it would appear that no further changes were taking place at 700 nm. At this wavelength only changes occurring at the d_1 -heme are expected to occur (16). Therefore, it would appear that after 17 minutes, a second slower process was occurring at the c -heme that was not associated with a corresponding change at the d_1 centre. These observations were not commented on by the authors.

In a separate experiment (17), Allen *et al* recorded the NIR-MCD spectrum of *P. pantotrophus cd₁* approximately 1 minute after the addition of hydroxylamine (at pH 7.50) and found that *ca.* 70 % of the c -type heme in the re-oxidised enzyme was in the His/Met ligation state. This means that ~ 30 % of the ferric c -heme in the sample was *bis*-histidinylligated, assuming no other ligation state (apart from His/His or His/Met) was present.

When Allen *et al* followed the ligand reversion process by EPR spectroscopy (10), the spectrum measured 1.3 minutes after hydroxylamine addition showed no sign of a feature at $g \sim 3.05$. The appearance of this feature, if it were there, would indicate that at this point in the reaction the c -heme was coordinated by two histidine ligands orientated perpendicular with respect to each other, as observed in the ‘as prepared’ enzyme. As this feature is absent, it is reasonable to assume that in the ~ 30 % of re-oxidised sample that contained *bis*-histidinylligated c -heme, these ligands were not orientated in the perpendicular conformation.

3.1.4 *The rationale for a time-resolved NIR-MCD experiment to probe the c-heme ligand switch*

Unpublished work has shown by NIR-MCD that semi-apo *P. pantotrophus cd₁* in fact contains a mixture of His/His and His/Met ligation in solution (Cheesman, M.R. and Kemp, G., *Unpublished*). This is despite the fact that the EPR spectrum shows two features

of a ‘rhombic trio’ (the third feature was unresolved) with g -values $g_z = 2.93$, $g_y = 2.26$ (12), features which have been previously assigned to His/Met ligation exclusively (10,12). It is therefore not out of the question that there is a direct link between movement of the Tyr²⁵ at the d_1 -heme and a histidine ligand rotation at the c -heme. The His/Met \rightarrow His/His reversion in which the histidine ligands are initially orientated parallel with respect to each other would still be observed as a single rhombic signal in the EPR with g -values of ~ 2.94 , 2.33 and 1.40 . Gradually, as the histidine ligands rotate back to the perpendicular conformation observed at the c -heme in the oxidised enzyme, the signal at $g \sim 3.05$ would be observed. The rotation of the *bis*-histidinyl ligands from the parallel conformation back to perpendicular could explain the second slower process viewed by Allen *et al* (10) in the absorbance time course spectra at 425 nm.

It has already been acknowledged in this thesis that EPR spectroscopy is not a reliable method of determining ligand identity unless it is employed in conjunction with NIR-MCD experiments. When the c -heme adopts the His/His coordination this will be observed in the NIR-MCD spectrum as a band at 1550 nm. Alternatively, the band seen for His/Met coordinated c -heme will be red shifted to approximately 1795 nm (17,18). A time resolved NIR-MCD study would therefore allow the reversion process to be monitored at the wavelengths that are specific to the His/Met and His/His ligand pairs. This is in contrast to the EPR measurements (10) which cannot unambiguously distinguish *bis*-histidinyl (parallel) and His/Met ligation. Observing the disappearance of the charge transfer (CT) band at 1795 nm after re-oxidation would leave no doubt that it is specifically the His/Met ligand pair that is being monitored and not a pair of histidine ligands rotated away from the perpendicular conformation. Similarly, monitoring the progress of the 1550 nm band following hydroxylamine addition would allow the re-emergence of the His/His coordination to be followed directly. As the tail of the His/Met

band (centred at 1800 nm) contributes to the spectrum at 1550 nm, this would need to be subtracted from the total intensity at 1550 nm to accurately assign the His/His ligated *c*-heme.

The charge transfer transitions which give rise to the *c*-heme MCD intensity are symmetry forbidden for *d*₁-heme (19). Such a study would therefore allow the ligation at the *c*-heme to be probed without the interference of overlapping bands from the *d*₁-heme, although the latter also undergoes changes in ligation on a similar timescale. This is in stark contrast to absorbance measurements in which the *c*-heme transitions of the oxidised state overlap with those of the *d*₁-heme for the majority of the UV-visible spectrum (16). Absorbance measurements monitor only a change in extinction coefficient, yielding no direct evidence as to the axial ligation of the hemes, whereas the energy of the NIR-MCD absorbance unambiguously defines the axial ligation of the *c*-type heme. However, comparison of rate constants obtained from the NIR-MCD time-resolved study with those obtained from an absorbance time trace at 706 nm would provide conclusive proof that a concomitant switch occurs at both hemes.

3.1.5 *The aims of this section of work*

The overall aim of this work was to investigate the nature of the structural changes that occur at the *c*- and *d*₁-hemes following the two electron re-oxidation of *P. pantotrophus* *cd*₁ by hydroxylamine hydrochloride. The methods used to monitor the rates of these processes by UV-visible absorption spectroscopy were similar to those employed by Allen *et al* (10), thus providing a link to this previously published work. Following this, the reversion was probed in greater detail by X-band EPR and NIR-MCD spectroscopies, as the use of these two methods in combination can potentially determine both the identity and orientation of the *c*-heme axial ligands. It was hoped that the combination of these spectroscopic techniques could be used to correlate the timescale of changes at the individual hemes, and link, for example, the binding of the Tyr²⁵ to a single process (either ligand switch or rotation) occurring at the *c*-heme. In doing this, the ambiguities discussed in Section 3.1.3 would also be addressed.

3.2 Experimental

3.2.1 *Monitoring the hydroxylamine re-oxidation of P. pantotrophus cd₁ by UV-visible absorbance spectroscopy*

Paracoccus pantotrophus *cd*₁ prepared and purified according to the method outlined in Chapter 2, Section 2.12 (165 µL, ~ 180 µM) was concentrated in a YM10 Microcon centrifugal filter device to give a final concentration of 424 µM (a volume of 70 µL). Following this, the sample was exchanged into 48 mM ‘mixed’ buffer at the desired pH (see Section 3.2.4 for buffer details), again using a YM10 Microcon (as above), and made up to 2 mL. This resulted in a final sample concentration of between 11 and 16 µM. Samples were prepared at solution pH values 5.50, 6.50 and 7.50. Absorbance spectra were

measured using a 1 cm pathlength quartz cuvette incorporating the use of a stirrer plate and magnetic stirrer bar. In all cases sample concentration was calculated using the Soret absorption intensity of the ‘as prepared’ enzyme and a molar extinction coefficient of $148 \text{ mM}^{-1} \text{ cm}^{-1}$ for the *P. pantotrophus* monomer (20).

A stock solution of sodium dithionite (approximately 75 mM) in argon-degassed buffer at the appropriate pH was prepared, and degassed again under argon thoroughly. The protein sample (after degassing under argon) was fully reduced in an anaerobic glove box (Belle Technology Ltd, Weymouth, UK; < 5 ppm total oxygen content) by adding a small aliquot (~ 1 μL) of stock sodium dithionite solution to give a final dithionite concentration of approximately 0.2 mM. The UV-visible absorbance spectrum of the sample was recorded following dithionite addition to ensure that the protein was fully reduced. Following this, the protein sample was passed down a PD-10 de-salting column under gravity and the UV-visible spectrum re-recorded to verify that the sample had remained fully reduced. A 1 M stock solution of hydroxylamine hydrochloride was also prepared in identical buffer. The sample cuvette was placed in the spectrometer and 8 μL of the stock hydroxylamine solution injected *in situ* through a Suba-Seal[®] using a Hamilton syringe to give a final hydroxylamine concentration of ~ 4 mM. Immediately after injection the stirrer plate was switched on for 5 seconds to ensure thorough mixing, and the measurement started simultaneously. The absorbance was recorded as a time course measurement for 60 minutes at a fixed wavelength of 706 nm.

The process was repeated on a fresh sample at the same pH, with the time course recorded for the absorption at 548 nm. Time courses were recorded at 706 and 548 nm for each of the three different solution pH values of 5.50, 6.50 and 7.50.

3.2.2 Monitoring hydroxylamine re-oxidation using X-band EPR spectroscopy

*P. pantotrophus cd*₁ (200 µL, ~ 124 µM³) was exchanged into 'mixed' buffer (see Section 3.2.4 for details) at pH 6.50. After recording the CW EPR and absorbance spectra the sample was degassed under argon, and taken into an anaerobic glove box (Belle Technology Ltd, Weymouth, UK < 5 ppm total oxygen content). Sodium dithionite (1.4 mM final concentration in sample) was titrated into the sample in small (0.5 µL) aliquots, and the progress of reduction monitored by absorbance spectroscopy. The reduced sample was transferred to an EPR tube within the anaerobic glove box, a small magnetic stirrer was added and the top of the tube sealed with a small rubber seal. After removal of the sample from the glove box, a 28 mM solution (30 µL of a 218 mM stock solution) of hydroxylamine hydrochloride was injected through the seal. Immediately after hydroxylamine addition, a large horseshoe magnet was used to agitate and remove the small magnetic stirrer within the tube, while simultaneously removing the syringe and rubber seal. The sample was immediately frozen in liquid nitrogen within one minute of hydroxylamine addition. An alternative method was employed by Allen *et al*, whereby hydroxylamine was added inside the glove box, before passing the sample out and freezing it in liquid nitrogen (10). However, this method afforded a less rapid freezing time of only 80 seconds.

. After recording the CW EPR spectrum, the sample was taken back into the glove box and allowed to thaw for approximately one minute, then frozen again and the spectrum re-recorded. This was repeated three times at various intervals in order to obtain a set of spectra representing the various stages of *cd*₁ re-oxidation.

³ For all absorbance, EPR and NIR-MCD experiments (unless otherwise stated) a molar excess of hydroxylamine was used.

3.2.3 Monitoring hydroxylamine re-oxidation using NIR-MCD spectroscopy

Using MCD to follow the reversion processes that are triggered by hydroxylamine re-oxidation of cd_1 presents practical challenges beyond those posed by the parallel EPR and absorption studies. These arise because the sample must be located in the room-temperature bore of the superconducting solenoid used in recording MCD spectra. Anaerobic samples can routinely be prepared in glove boxes and removed in sealed optical cuvettes. These are mounted on a simple cylinder-shaped holder that is then pushed into the bore of the magnet, placing the sample in the position of maximum magnetic field. While this approach works well for static samples, it is not suitable for the problem of monitoring time-dependent processes in cd_1 after re-oxidation. The procedures of sample loading, cuvette transfer and magnet energising can take many minutes and moving the sample holder in and out of the magnet bore can cause spectroscopic baseline shifts. Injecting hydroxylamine before removing the sample from the glove box in order to ensure that the sample remains anaerobic (and therefore *not* re-oxidised by traces of dioxygen) means that the MCD measurements cannot be started for many minutes. The MCD spectrum should also be recorded just prior to re-oxidation to characterise the reduced state. This would entail the additional manipulation of removing the sample from the magnet, injecting the hydroxylamine and then repositioning in the bore. Ideally the cd_1 sample would be redox cycled *within* the bore after the magnet has been energised allowing each stage to be monitored spectroscopically. At the time this work was started, such methodology to do this did not exist. However, a more versatile MCD sample holder was being designed for the purpose of incorporating electrodes in cuvettes to create small electrochemical cells for MCD-monitored redox titrations (MCD-compatible optically transparent thin layer electrochemistry or “MOTTLE”). This was made feasible by a new room temperature MCD solenoid with an increased bore size (50 mm as compared to the

previous 25 mm). With regard to the type of experiment proposed above for cd_1 , an ability to perform *in situ* chemical redox cycling was therefore incorporated into the final design of this cell holder. The cd_1 work described below therefore also served to develop and test this new apparatus. An illustration of how the cell holder would appear within the experimental set-up is shown below in *Figure 3.2.1* (21).

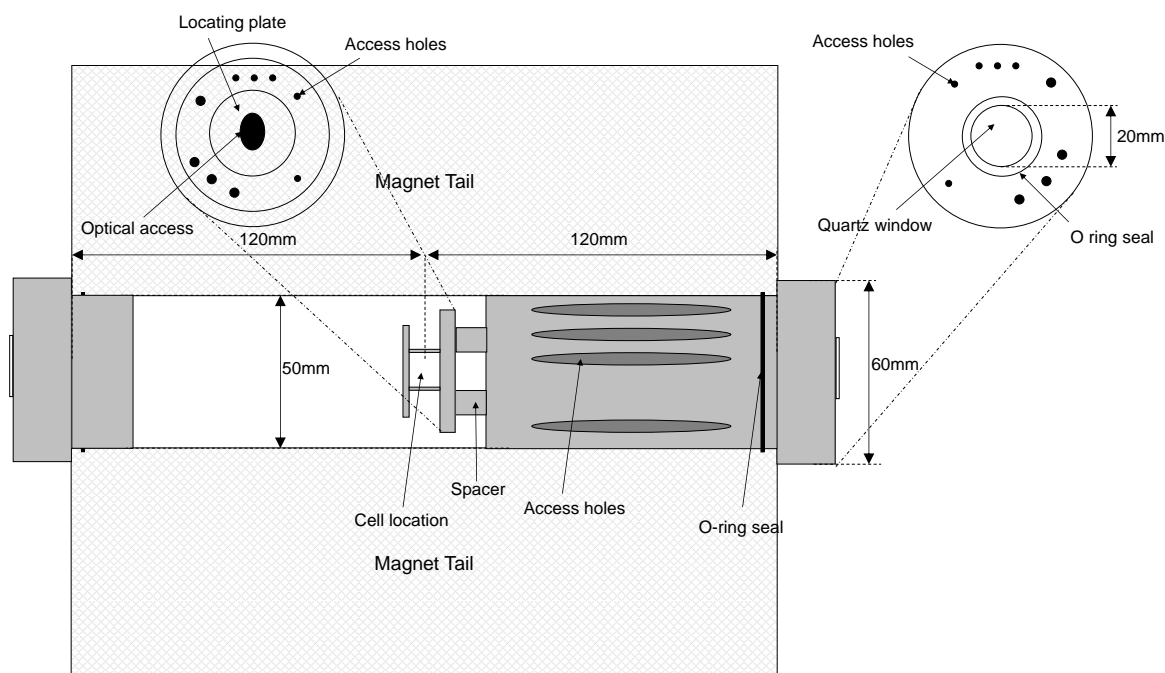


Figure 3.2.1: Diagram of the novel MCD cell holder originally designed for use in MCD-compatible optically transparent thin layer electrochemistry (MOTTLE) (21).

The cell is housed within a bespoke nylon holder (approximately 12 cm in length, constructed in the UEA Science Faculty workshop) that allows it to be placed within the bore (5 cm diameter) of the Oxford Instruments superconducting solenoid. Adjustable circular nylon plates (with cut away sections to allow optical access) are attached to the cylinder to secure the cell. The adjustable nature of these plates allows cells of varying pathlengths to be incorporated into the holder. The centre of the cylinder is bored out to provide a path to the sample for the light beam. A gas tight seal is formed between the cell holder and the magnet bore using an O-ring to ensure the maintenance of the anaerobic atmosphere. Eight holes (2–3 mm diameter) are drilled into the holder to allow access for

the injection lines, which feed into the cell and permit small, *in situ* additions of reagent. This allows any resulting reaction after the addition of reagent to be monitored immediately, without necessitating the removal of the cell from the magnet bore.

In order to ensure the rapid and even distribution of reactants a suitable stirring mechanism was required that would be safe to use in the bore of an 8 T superconducting magnet. The stirring mechanism was again designed and manufactured in-house. This is illustrated in *Figure 3.2.2*. It is driven by steady stream of nitrogen gas, that blows through a plastic cannula (threaded through a hole bored in the cell) onto the four propeller blades (~ 3 mm diameter), causing them to spin (and remain spinning) throughout the course of the experiment without disrupting the light beam. The propeller is attached to a length of polystyrene rod (15 mm in length) which passes through a hole in a Teflon lid and is held in place by two Teflon rings. The steady stream of nitrogen gas also serves to maintain the anaerobic environment inside the magnet bore.

A 250 μL aliquot of ~ 200 μM *P. pantotrophus cd*₁ in pH 6.50 buffer was transferred (inside the anaerobic glove box) to a quartz cuvette and placed into the apparatus described above. The lines 'A' and 'B' were preloaded with sodium dithionite (1 μL aliquots of a stock solution of ~ 391 mM alternated with 2 μL aliquots of identical buffer and small gaps of nitrogen) and hydroxylamine hydrochloride (19.2 μL of a 1.1 M stock solution) respectively.

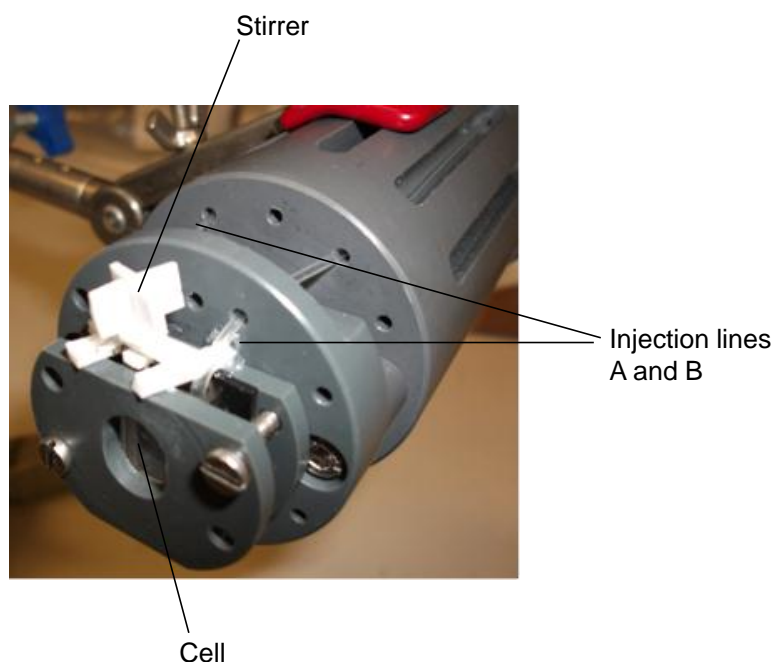


Figure 3.2.2: A photograph showing the sample cell secured in the novel MCD cell holder. The injection lines, stirrer and cell are labelled.

The apparatus containing the sample was removed from the anaerobic glove box and placed inside the bore of the MCD magnet, which was continually flushed with nitrogen gas to maintain an anaerobic environment. The sample was stirred under nitrogen within the magnet bore for ten minutes in order to remove any trace oxygen from the buffer prior to reduction. The pre-loaded aliquots of sodium dithionite were titrated into the sample and the progress of the reduction monitored by recording NIR-MCD spectra (700–2000 nm) after each addition of dithionite. The absence of characteristic ferric 1550 and 1800 nm CT bands in the spectrum indicated that full reduction of the sample had been achieved. Monitoring this gradual, *in situ* addition of reductant meant that the sample could be stoichiometrically reduced without the presence of excess dithionite. The sample was re-oxidised by the addition of the pre-loaded stock solution of hydroxylamine hydrochloride (19.2 μL of a 1.1 M stock solution so that the final concentration of substrate in the sample was approximately 43 mM) whilst monitoring the MCD response at either 1550 or 1800

nm. Comparable measurements were made on *P. pantotrophus* *cd*₁ samples in pH 7.00 buffer.

3.2.4 *Instrument and buffer details*

All absorbance spectra were recorded using a Hitachi U-4100 spectrometer.

All CW EPR spectra were recorded at a temperature of 10 K using a 2.02 mW incident microwave power and 1 mT modulation amplitude. The EPR spectrometer comprised an ER-200D electromagnet and microwave bridge interfaced to a BrukerSpectrospin EMX control system and was fitted with an ESR-9 Oxford Instruments liquid helium flow cryostat. The X-band cavity was a Bruker type ER4116DM.

The room temperature MCD apparatus comprised an Oxford Instruments Special Spectromag 1000 8 T superconducting solenoid with a 5.0 cm ambient temperature bore.

All the experiments described above were made using 48 mM ‘mixed’ buffer⁴ (12 mM sodium acetate, 12 mM MOPS, 12 mM MES, 12 mM TRIS) prepared a number of different pH values (see individual experimental sections for details).

⁴ The standard ‘mixed’ buffer solution used in this work was prepared to cover a wide pH range (3.6–9.0).

3.3 Results

3.3.1 *Monitoring the hydroxylamine re-oxidation reaction by UV-visible absorbance spectroscopy*

Allen *et al* (10) previously investigated the rate of re-oxidation of dithionite-reduced *P. pantotrophus* cd_1 by hydroxylamine hydrochloride. By monitoring the absorbance at 700 nm after the addition of hydroxylamine to fully-reduced enzyme, they were able to observe the resulting increase in absorbance at this wavelength as the Tyr²⁵ re-coordinated to the metal and the low/high spin thermal equilibrium was re-established. The features typically observed in the electronic absorption spectra of oxidised and fully-reduced *P. pantotrophus* cd_1 have already been discussed in Chapter 2, Section 2.4.

Methods were established for the hydroxylamine re-oxidation reaction as described in Section 3.2.1 and were based on those used by Allen *et al* (10). The spectra obtained during a preliminary experiment are shown in Figure 3.3.1. In this instance, hydroxylamine hydrochloride was added to the fully reduced enzyme and absorbance spectra repeatedly recorded between 650 and 750 nm until no further increase in the intensity of the d_1 high-spin band at ~ 702 nm could be observed.

At a scan rate of 600 nm min⁻¹, a single measurement took 10 seconds, with a lag time of approximately 4 seconds in between scans during which the monochromator was reset to 750 nm. The initial addition of hydroxylamine took approximately 5 seconds. At T1, (measured ~ 5–15 seconds after hydroxylamine addition), around 22 % (as judged by the intensity at 702 nm) of high-spin d_1 -heme had returned.

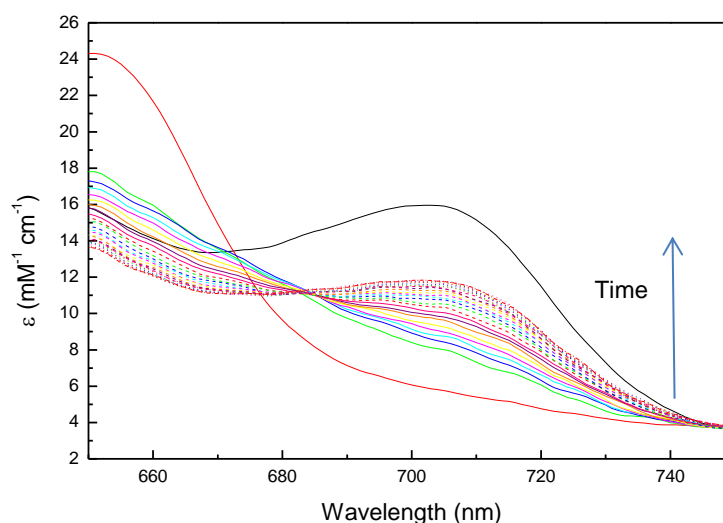


Figure 3.3.1: Electronic absorbance spectra of *P. pantotrophus* cd_1 . — As prepared, — fully reduced with 0.21 mM sodium dithionite, — T1; approximately 5–15 seconds (scan time between 750 and 650 nm was 10 seconds) after the addition of 198 mM hydroxylamine hydrochloride, — T2 to - - T27 were measurements made approximately 19–29 and 369–379 seconds after hydroxylamine addition. Samples were in 48 mM mixed buffer (see Section 3.2.4 for details), pH 6.50.

By T18 (~ 243–253 seconds after hydroxylamine addition) the rate of increase in band intensity had declined, indicating that the majority of the sample had re-oxidised. After ~ 351 seconds (T25) there was no further increase in the relative absorbance of the band, indicating that the process had reached completion. In comparison with the spectrum of the ‘as prepared’ sample, the band intensity at 702 nm of the sample upon complete re-oxidation had significantly diminished. This raised the question of whether this deficiency in the band intensity was due to loss of the d_1 -heme (leading to formation of semi-apo protein) or whether there was incomplete rebinding of the Tyr²⁵ to the metal centre.

The addition of 105 μ L of a 1 M solution of hydroxylamine to the fully-reduced *P. pantotrophus* cd_1 sample is a molar excess (hydroxylamine to protein monomer) of approximately 13,000. In their work, Allen *et al* (10) used a final hydroxylamine hydrochloride concentration of 167 μ M, which was a molar ratio (hydroxylamine:monomer) of ~ 1300:1. A ten-fold excess of hydroxylamine was initially

used in this work to investigate whether this would have an effect on the rate of reaction observed. The formation of some semi-apo protein in this case could explain why the intensity of the 702 nm d_1 high-spin band did not return to that of the as-prepared enzyme. Analysis of the full wavelength spectrum obtained at the end of the experiment revealed a corresponding deficiency in the d_1 low-spin band at 644 nm, while the Soret and α/β regions returned to the intensities observed in the ‘as prepared’ spectrum. This suggests that some of the d_1 -heme had become detached from the holoprotein after exposure to the substrate. The c -heme, being covalently bound to the protein backbone remained within the apoenzyme and hence spectral features attributing to this centre were unaltered.

A number of different amounts of molar excess were used in repeats of this experiment with the aim of ascertaining the effect on the rate observed.⁵ This was done not to obtain kinetic parameters per se but in order to fix a concentration and therefore a reaction rate convenient for the method. In light of these measurements, the amount of hydroxylamine added to the sample was reduced by approximately 50 fold so that the final concentration was approximately 4 mM, a hydroxylamine to protein monomer ratio of $\sim 260:1$. At this lower concentration of hydroxylamine, after storing the sample overnight at 4 °C and re-measuring the absorbance spectrum there were no visible changes (*Figure 3.3.2*). At this 260:1 molar excess of substrate (approximately five times less than that used by Allen *et al*), the rate of reaction was not affected and as the d_1 bands of the hydroxylamine re-oxidised spectrum were identical to those of the ‘as prepared’ enzyme it was concluded that no semi-apo protein had been formed.

⁵ These data were not included in this thesis as they were not considered relevant to the purposes of this work – i.e. to monitor the rate of ligand reversion according to pH and not to study the reaction kinetics per se. Using a 260:1 molar excess of hydroxylamine led to rates comparable with those obtained by Allen *et al*, but resulted in no precipitation of protein.

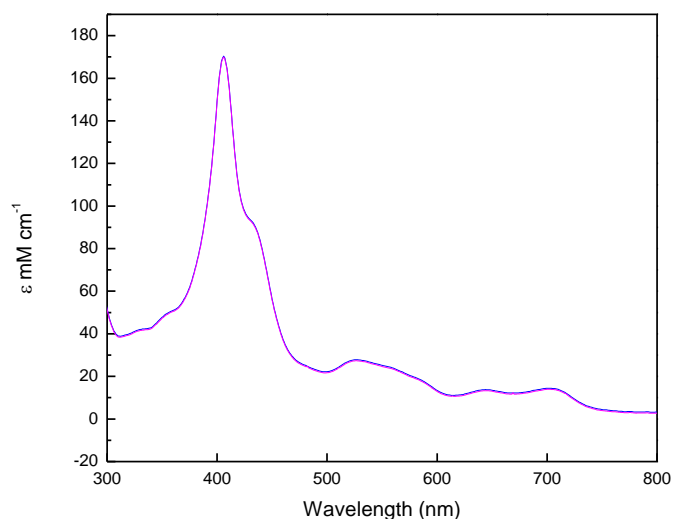


Figure 3.3.2: Electronic absorbance spectra of *P. pantotrophus* cd_1 . — 60 minutes after re-oxidation by 4 mM hydroxylamine hydrochloride. . — ~ 14 hours after re-oxidation by 4 mM hydroxylamine hydrochloride. Sample was in 48 mM ‘mixed’ buffer (see Section 3.2.4 for details), pH 7.00.

If the questions raised in Section 3.1 of this chapter were to be answered, the post-oxidation ligand reversion of the *P. pantotrophus* enzyme needed to be studied using a number of different spectroscopic techniques in parallel. Four important questions to be answered were: Are the reversion processes occurring at the *c*- and d_1 -hemes truly concomitant? Is there a separate reversion process occurring at the *c*-heme that is not observable by EPR (i.e. does the initial His/Met→His/His reversion precede a subsequent rotation of the histidine ligands from the parallel to the perpendicular orientation)? Can the rate of ligand reversion at the *c*- and d_1 -hemes following re-oxidation by hydroxylamine be affected by external factors, specifically the H^+ concentration of the solution? Finally, is the EPR spectrum recorded ~ 60 minutes after hydroxylamine addition truly identical to that of the ‘as prepared’ enzyme, as previously claimed by Allen *et al* (10)? Each of the spectroscopic techniques employed as part of this work inform on a specific physical process or change that occurs during the reaction.

3.3.2 Investigating the effect of H^+ concentration on the ligand reversion at both hemes

In order to investigate the effects of pH on the rate of ligand reversion at both hemes, UV-visible time traces were recorded at 706 nm and 548 nm at solution pH values 5.50, 6.50 and 7.50. Measurements made at 548 nm will essentially (although not entirely – to be discussed below) reflect the oxidation at the *c*-heme (12,16) while 706 nm represents the centre of the *d*₁ high-spin band (13).

It should be noted again at this point that the aim of this work was not to seek detailed quantitation of the kinetics occurring during the ligand reversion but to simply order and correlate the different processes using a number of spectroscopic techniques. All the experimental techniques used in this work are described in Section 3.2 of this chapter. A typical full wavelength room temperature UV-visible absorbance scan made between 350 and 800 nm at the different stages of the experiment is shown in *Figure 3.3.3*. It can be seen from this that the *c* and *d*₁ spectral features of the ‘as prepared’ sample compare well with those of the hydroxylamine re-oxidised protein.

This indicates that 60 minutes post addition of a 260 fold excess of hydroxylamine, the sample had returned to the ‘as prepared’ conformation in terms of heme spin and oxidation state. There is, however, a slight red shift (of 1 nm) and a slight decrease (by $\Delta\epsilon \sim 5 \text{ mM}^{-1} \text{ cm}^{-1}$) in the maximum intensity of the *c*-heme Soret band of the hydroxylamine re-oxidised sample compared with that of the ‘as prepared’ enzyme.

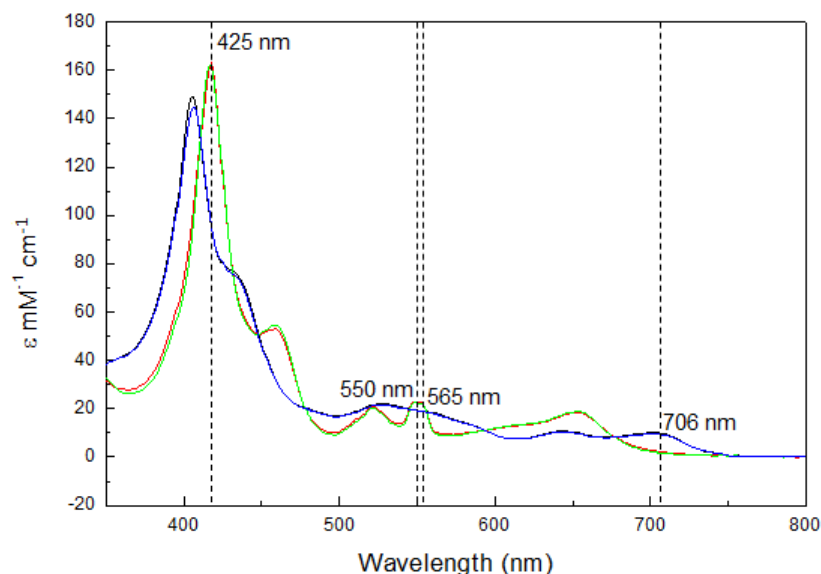


Figure 3.3.3: Electronic absorbance spectra of *P. pantotrophus* *cd*₁. — As prepared, 13.5 μ m, — fully-reduced with 0.19 mM sodium dithionite, — the fully-reduced sample after passing down a PD10 column to remove excess reductant, — the sample 60 minutes after re-oxidation by 4 mM hydroxylamine hydrochloride. Samples were in 48 mM 'mixed' buffer (see Section 3.2.4 for details), pH 7.50. Concentrations were calculated using the molar extinction coefficient of 148 $\text{mM}^{-1} \text{cm}^{-1}$ and 161.5 $\text{mM}^{-1} \text{cm}^{-1}$ for the oxidised (20) and fully reduced (8) monomer respectively.

This may indicate a slight difference in the environment around this heme following re-oxidation by hydroxylamine. The reaction that is believed to be taking place is shown in *Figure 3.3.4*.

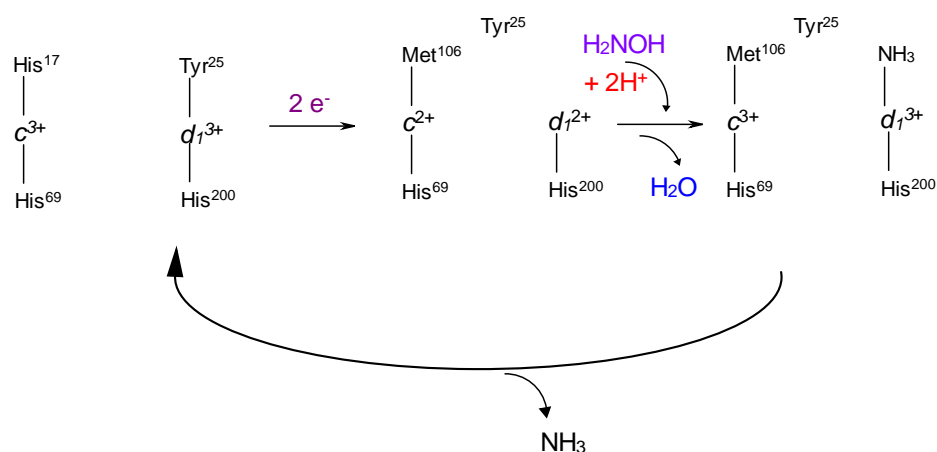


Figure 3.3.4: Reaction scheme showing the two-electron reduction of hydroxylamine by *P. pantotrophus* *cd*₁ to yield the products ammonia and water.

The re-oxidation at the *d*₁-heme can be thought of as a two-step process (*Figure 3.3.5*): The first step, with the Tyr²⁵ already dissociated from the *d*₁ metal centre upon

reduction, is likely to be rapid, with the NH_2OH binding and reacting with two protons to yield the putative $d_1^{3+}\text{-NH}_3$ intermediate. It was shown previously by Allen *et al* (10) that the lifetime of this intermediate is at least four minutes. The second step, in which the NH_3 molecule is released and the Tyr^{25} returns to the distal d_1 site occurs at a slower rate, the structural changes involved being associated with a significant reorganisation energy (2).

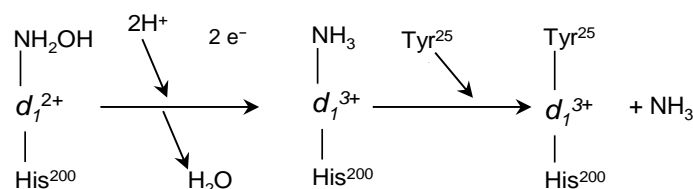


Figure 3.3.5: Re-oxidation of the d_1 -heme can be thought of as occurring in two stages; the first being the formation of the $d_1^{3+}\text{-NH}_3$ intermediate and the second being the rebinding of Tyr^{25} to the metal centre.

By recording a time trace at 706 nm it is possible to track the rate of return of the Tyr^{25} to the metal centre. This particular spectroscopic feature is unambiguously attributable to tyrosine rebinding, not just because of the wavelength but also because it is one of a pair of features resulting from the re-establishment of the low/high spin thermal equilibrium.

The time course traces for the hydroxylamine re-oxidation reaction at 548 nm and 706 nm for each pH are shown in *Figures 3.3.6* and *3.3.7*. The k_{obs} ('observed rate constant') values calculated from the time traces are shown in *Table 3.3.1*, along with the respective values of τ – quantities resulting from a fit of the data to an exponential decay function of the form:

$$y = y_0 + A_1 e^{-(x-x_0/\tau_1)} \quad (1)$$

In Equation 1, A_1 represents the change in the molar extinction coefficient, ϵ , for a particular process in the reaction⁶, with a time constant (equivalent to $1/k$) given by τ in seconds. The R^2 values (indicates how well a regression line approximates the real data

⁶ As the hydroxylamine re-oxidised spectra at all pH values investigated compared well with those obtained for the 'as prepared' samples, it was not deemed necessary to tabulate these A_1 values. Changes in extinction coefficient observed in the pH 5.50 are discussed specifically later in this chapter.

points, with an R^2 value of 1 equating to a perfect fit) calculated for all fittings to the data were between 0.9731 and 0.9996.

| pH | Wavelength measured (nm) | τ_1 (s) | k_{obs} (min^{-1}) |
|------|--------------------------|------------------|--|
| 5.50 | 706 | 119 ± 3 | 0.50 |
| | 548 | 92 % 75 ± 0 | 0.80 |
| | | 5 % 150 ± 0 | 0.40 |
| | | 3 % 1580 ± 0 | 0.038 |
| 6.50 | 706 | 248 ± 2 | 0.24 |
| | 548 | 248 ± 2 | 0.24 |
| 7.00 | 425 | 273 | 0.22 |
| | 700 | 273 | 0.22 |
| 7.50 | 706 | 293 ± 0.2 | 0.20 |
| | 548 | 298 ± 0.2 | 0.20 |

Table 3.3.1: Summary of the time trace results obtained from the addition of hydroxylamine hydrochloride to *P. pantotrophus cd₁* at different solution pH values. Values of τ_1 and k_{obs} at pH 7.00 (shown in red) are published data by Allen *et al*(10).

From the k_{obs} values shown in *Table 3.3.1* it is clear that the ligand reversion process following hydroxylamine re-oxidation occurs with a faster rate at a lower solution pH. This is at least consistent with the consumption of protons during the reaction believed to be taking place (*Figures 3.3.4* and *3.3.5*). Note that while it has been suggested that NH_3 is bound to the ferric d_1 -heme as an intermediate, this assumption was made only on the basis of the observed EPR signal at $g = 2.67$ (10). These authors have also claimed elsewhere (22) that the substrate, nitrite, will bind to the d_1 -heme following cd_1 re-oxidation. It is therefore entirely possible that this signal arises due to a $d_1^{3+}\text{-NH}_2\text{OH}$ intermediate.

The time trace results at 706 nm for solution pH values 5.50, 6.50 and 7.50 at 706 nm are shown in *Figure 3.3.6*. At all three pH values there is an initial rapid increase in absorbance for the first 3–5 minutes, followed by a slower increase, which tapers off until a plateau (a state of little or no change) is reached. This plateau, the point at which all of the Tyr^{25} is rebound at the d_1 -heme, is reached at approximately 15, 17 and 20 minutes for

pH values 5.50, 6.50 and 7.50 respectively. This indicates that as the pH of the sample solution is increased (and the concentration of protons subsequently decreased), the time taken for the Tyr²⁵ ligand to rebind to the d_1 centre also increases. For all pH values, each of the fittings to the 706 nm time course measurements yield one value of k_{obs} .⁷ This indicates that at the solution pH values measured, just one process at the d_1 -heme occurs during the reversion. At pH 5.50, this process takes place within 119 ± 3 seconds, giving a k_{obs} value of 0.504 min^{-1} . When the solution pH is raised by one unit to 6.50, the k_{obs} value (and therefore the rate of reaction) decreases by over 50 % to 0.242 min^{-1} . Raising the solution pH to 7.50 results in a further decrease in k_{obs} to 0.205 min^{-1} , although this value is only 15 % less than that calculated for the pH 6.50 sample. Allen *et al* (10) calculated a k_{obs} value of 0.22 min^{-1} for the return of the high-spin d_1 band, with measurements being made at a sample pH of 7.00.

⁷ Attempts at fitting bi-exponential curves resulted in poorer fittings with lower R^2 values.

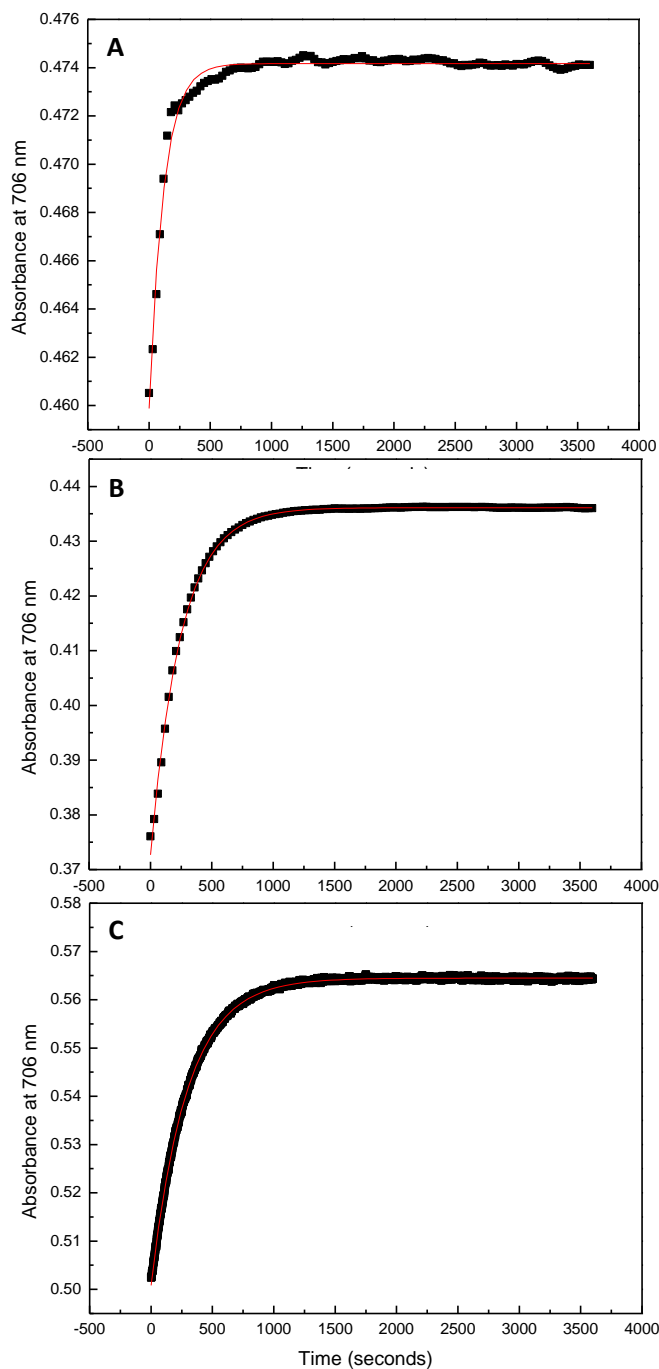


Figure 3.3.6: ■ Time course measurement of the relative absorbance at 706 nm after the addition of 4 mM hydroxylamine hydrochloride to dithionite-reduced *P. pantotrophus* cd_1 at solution pH (A), 5.50; (B), 6.50; (C), 7.50 — Non-linear curve-fittings to data. Samples were in 48 mM ‘mixed’ buffer (see Section 3.2.4 for details), adjusted to the required pH values. $R^2 = 0.9803, 0.9982$ and 0.9996 for (A), (B) and (C) respectively.

The value of k_{obs} calculated by Allen *et al* is intermediate between those obtained in this work at a pH of 6.50 and 7.50. It can therefore be concluded that a decrease in solution pH leads to an increased rate of Tyr²⁵ rebinding following re-oxidation of the fully reduced

protein by hydroxylamine. The fact that the Tyr²⁵ rebinds in a one-step process also indicates that this action occurs simultaneously at the *d*₁-hemes in each monomer.

Absorbance time course traces recorded at 548 nm for pH values 5.50, 6.50 and 7.50 are shown in *Figure 3.3.7*. When Allen *et al* (10) followed the hydroxylamine re-oxidation of reduced *P. pantotrophus cd*₁ at pH 7.00 by absorbance spectroscopy; they found that the time constants calculated for the 425 nm and 700 nm measurements were identical. From this it was concluded that concomitant processes take place at both the *c*- and *d*₁- hemes following re-oxidation of the fully reduced enzyme by hydroxylamine. In this work, at pH 6.50, the *k*_{obs} values at 706 and 548 nm are also identical, which would again suggest cooperative processes at the two centres. As with the 706 nm measurement, the 548 nm time trace gives a single value for the rate constant, indicating that a single process is taking place. At a solution pH of 7.50, the *k*_{obs} values for the 706 nm and 548 nm measurements are once more identical. While the 706 nm time course spectrum at pH 5.50 gives a single rate constant, the most accurate non-linear curve fit to the 548 nm data results in three *k*_{obs} values of 0.8, 0.4 and 0.0380 min⁻¹ and the plot is very different in appearance. Of these three events, only one is associated with a positive change in absorbance; the first and most rapid process with a τ_1 of 75 seconds.

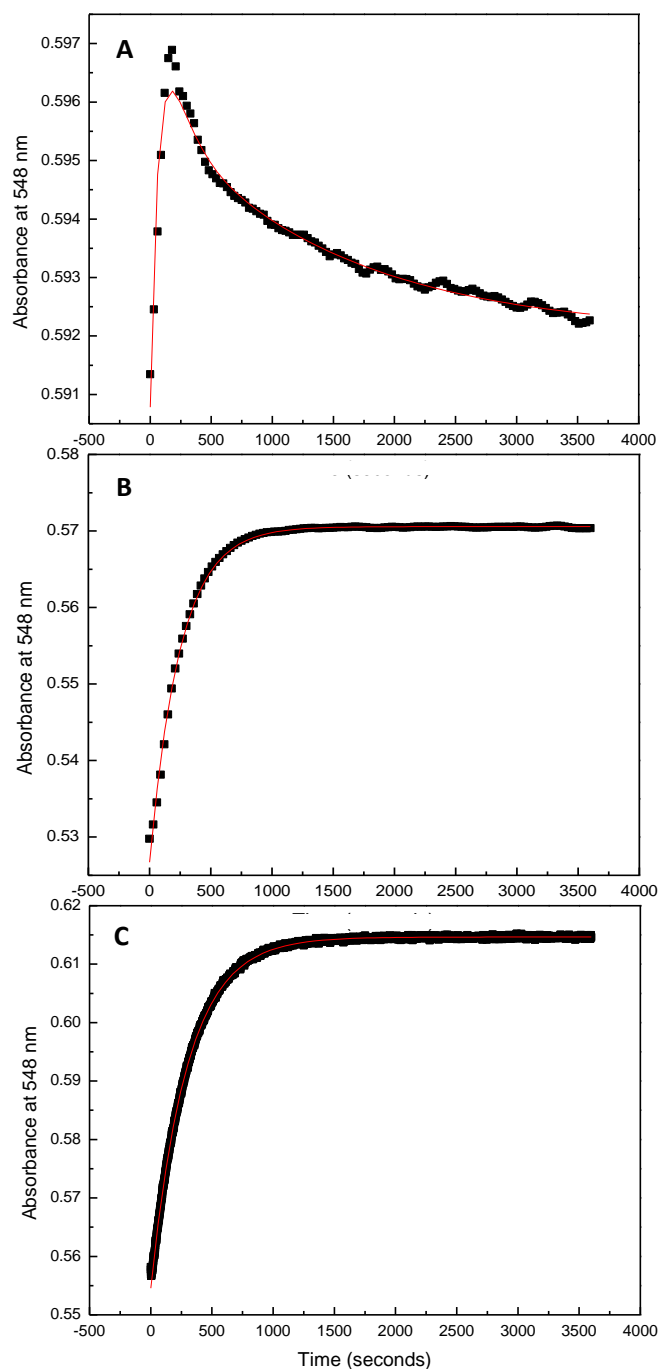


Figure 3.3.7: ■ Time course measurement of the relative absorbance at 548 nm after the addition of 4 mM hydroxylamine hydrochloride to dithionite-reduced *P. pantotrophus cd₁* at solution pH (A), 5.50; (B), 6.50; (C), 7.50 — Non-linear curve-fittings to data. Samples were in 48 mM 'mixed' buffer (see Section 3.2.4 for details), adjusted to the required pH values. $R^2 = 0.9731, 0.9973$ and 0.9996 for (A), (B) and (C) respectively.

None of the k_{obs} values calculated from the 548 nm measurement at pH 5.50 compare particularly well to the single rate constant derived from the 706 nm time trace. This would suggest that there are three processes taking place at the *c*-heme following re-oxidation by hydroxylamine at this pH (with weightings of 92: 5: 3) and that none of these events occur synchronously with the single process taking place at the d_1 centre.

It is widely accepted that features occurring at ~ 425 and 550 nm are almost exclusively due to the *c*-type heme in oxidised *P. pantotrophus* cd_1 (10,12,16). However, previous experiments (23) on chloride-ferriheme d_1 have shown that a strong $g = 6$ feature in the EPR spectrum (indicating that the ferric d_1 -heme is in the high-spin state) is correlated with bands in the absorbance spectrum centred at ~ 425 and 565 nm. The latter feature (which is approximately 4.5 times less intense than the former) is relatively broad and asymmetric in appearance and spans the region 517–620 nm. Chang (24) reported the absorbance spectrum of d_1 ferriheme chloride, showing that it exhibits an absorption maximum at 430 nm and a broad band between ~ 530 and 610 nm. Additionally, a comparison of the reduced minus oxidised visible difference spectra obtained for the native and semi-apo forms of the enzyme (16) showed some absorbance in the region of 420–425 nm and ca. 550 nm that could be attributed to ferrous low-spin d_1 -heme. Consequently, it cannot be assumed that *c*-heme changes are monitored exclusively at 425 nm or 548/550 nm as there could be underlying d_1 bands in both the reduced and oxidised forms of the enzyme.

It should be noted that as the pH 6.50 and 7.50 measurements made at 548 nm in this work are fitted to a single time constant, there is no evidence of a second process occurring as viewed by Allen *et al* (10) when they monitored the absorbance at 425 nm. It may be the case that this second slower process induces little or no change in intensity in the 550 nm region compared to that observed at 425 nm. An alternative explanation would

be that baseline drift, possibly caused by precipitation of the protein led to the apparent slower process being visible in the 425 nm spectrum. Allen *et al* used a hydroxylamine to protein ratio of $\sim 1300:1$, just over four times the ratio used for the time course experiments in this work, which may have increased the likelihood of protein precipitation.

If the absorbance changes viewed at 548 nm are partly due to the d_1 -heme, this still does not explain why three processes (as opposed to just one) should be viewed for the pH 5.50 sample. The best possible non-linear curve fitting of the three-part exponential decay function gives an R^2 value of 0.9731, the lowest of all six time-course spectra recorded. A fitting that produced realistic 'A' values could only be achieved by fixing the values of τ_1 and τ_2 to 75 and 150 s respectively, Consequently, the accuracy of these values (and therefore the rate constants calculated) is questionable. It should also be noted that the changes in molar extinction coefficient over the course of the time traces (represented by the A_1 value in Equation 1) are markedly less for the pH 5.50 sample than those calculated for the samples at pHs 6.50 and 7.50 at both wavelengths. For example, the A_1 value calculated for the pH 5.50 sample from the 706 nm time trace at 0.0143 ± 0.00023 is markedly less than those given for pH values 6.50 and 7.50 (0.0634 ± 0.00031 and 0.0637 ± 0.00003 respectively). This discrepancy is unlikely to be attributed to small differences in enzyme concentration between samples. The reaction at pH 5.50 occurs very rapidly (more than twice the rate of that at pH 6.50) and there is an approximate 5–10 second delay between the addition of hydroxylamine and the registration of the first data point by the spectrometer. It is therefore very probable that a larger portion of the reduced protein at pH 5.50 would have reacted with the substrate during this delay time period compared with those in the pH 6.50 and 7.50 samples. This would account for the reduced A_1 value and apparent decreased change in ϵ of the pH 5.50 sample over the course of reaction.

3.3.3 Monitoring the hydroxylamine re-oxidation of *P. Pantotrophus cd₁* by X-band EPR spectroscopy

Figure 3.3.8 shows the X-Band CW EPR spectra of *P. pantotrophus cd₁* for the ‘as prepared’ and fully reduced enzyme, ~ one minute after re-oxidation with hydroxylamine hydrochloride and at four other time intervals over the course of ~ 80 minutes. The *c*-heme region of the spectrum is shown in more detail in Figure 3.3.9. The features observed in the EPR spectrum of the ‘as prepared’ enzyme are typical of oxidised *P. Pantotrophus cd₁* (as described in Chapter 2, Section 2.5) and compare well to those previously reported in the literature (13). Features at $g \sim 6.88$ and $g \sim 5.08$ are characteristic of rhombically-distorted high-spin ferric heme and are assigned to the high-spin portion of Tyr-bound ferric *d₁*-heme. As expected, full reduction of both hemes (in each monomer) to the diamagnetic low spin ferrous state renders the resulting spectrum featureless.

The *c*-heme in the ‘as prepared’ enzyme gives rise to two overlapping g_z features, the relative sizes of which can vary between preparations. One, typically at $g \sim 3.17$, represents a ‘Large g_{\max} ’ spectrum. This type of feature is observed in low-spin ferric hemes with *bis*-histidinyI axial coordination where the orientation of the ligand planes is closer to perpendicular rather than parallel (15). Specifically, for *P. Pantotrophus cd₁*, crystal structure data for the oxidised enzyme has shown the angle between the axial ligand planes of the *c*-heme to be approximately 60 ° (2).

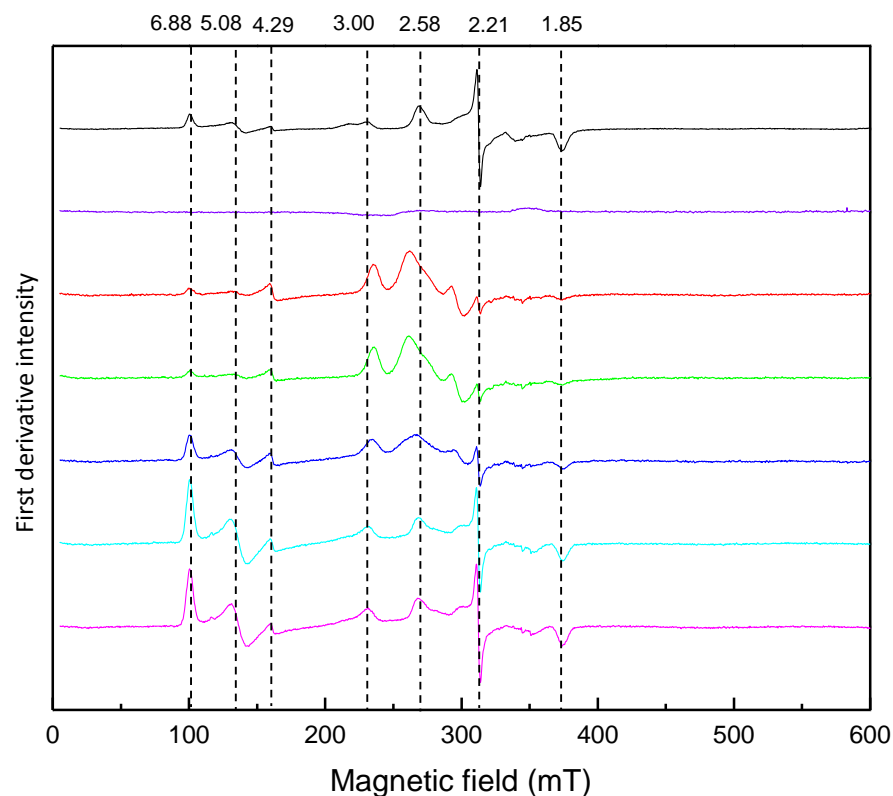


Figure 3.3.8: The X-Band CW EPR spectra of — *P. pantotrophus cd₁* (as prepared, ~ 124 μ M) and — fully-dithionite reduced, — ~ 50-60 seconds after complete reduction with sodium dithionite and re-oxidation with 28 mM hydroxylamine hydrochloride, — approximately 2 minutes after re-oxidation with hydroxylamine, — approximately 13 minutes after re-oxidation with hydroxylamine, — approximately 46 minutes after re-oxidation with hydroxylamine — approximately 79 minutes after re-oxidation with hydroxylamine. Samples were in 48 mM 'mixed' buffer (see Section 3.2.4 for details) at pH 6.50. Spectrometer parameters: power, 2 mW; modulation amplitude 1 mT; temperature, 10 K.

However, the heterogeneity of g_z with a second feature at ~ 3.00 suggests that the axial ligation to the *c*-heme exists in two forms in solution *as opposed to the crystal* that could differ at least in terms of orientation but also perhaps in identity. A weak band in the region of 1650-1900 nm has been observed (13) in the NIR-MCD spectrum of oxidised *P. pantotrophus cd₁*, which may due to His/Met coordination.

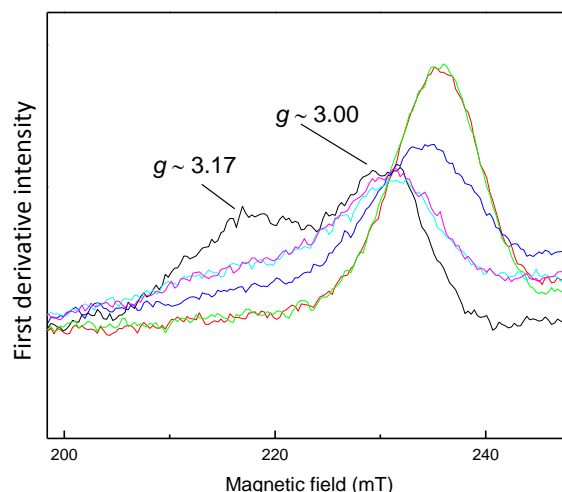


Figure 3.3.9: The X-Band CW EPR spectra of *P. pantotrophus* cd_1 (as prepared, $\sim 124 \mu\text{M}$) and after complete reduction with sodium dithionite followed by re-oxidation with 28 mM hydroxylamine hydrochloride, showing the *bis*-histidiny *c*-heme region in more detail. — *P. pantotrophus* (as prepared, $\sim 124 \mu\text{M}$) and — ~ 50 – 60 seconds after complete reduction with sodium dithionite and re-oxidation with 28 mM hydroxylamine hydrochloride. — Approximately 2 minutes after re-oxidation with hydroxylamine, — approximately 13 minutes after re-oxidation with hydroxylamine, — approximately 46 minutes after re-oxidation with hydroxylamine, — approximately 79 minutes after re-oxidation with hydroxylamine. Samples were in 48 mM ‘mixed’ buffer (see Section 3.2.4) at pH 6.50. Spectrometer parameters: power, 2 mW; modulation amplitude 1 mT; temperature, 10 K.

The low spin ferric d_1 -heme gives rise to a ‘rhombic trio’ of features at $g \sim 2.58$, 2.21 and 1.85, with a $\sum g^2$ of 14.96, less than the typical value of 16 generally observed for low-spin ferric *c*-type hemes (15) and is attributed to the atypical d_1 ground state (13). While the two features at $g \sim 6.88$ and $g \sim 5.08$ are assigned to high-spin ferric d_1 -heme, the feature at $g \sim 4.29$ is attributed to adventitiously-bound ferric iron. In the spectra recorded at approximately one minute and \sim two minutes after the addition of hydroxylamine, the features at $g \sim 6.88$ and $g \sim 5.08$ are barely detected, again confirming that all of the ferric d_1 -heme exists in the low-spin state at this point. As the reaction progresses, this feature is observed to increase in intensity as the proportion of high-spin ferric d_1 -heme in the sample increases.

The $g \sim 6.88$ peak is at maximum intensity in the spectrum recorded approximately 46 minutes after hydroxylamine addition, although in the final spectrum it appears to have reduced slightly. This reduction in the intensity of the high spin ferric d_1 feature between

46 and 79 minutes occurs in conjunction with a concomitant increase in the intensity of the low-spin d_1 rhombic trio. From this it can be assumed that as an equilibrium exists between high and low-spin forms of the tyrosine-bound d_1 -heme, any decrease in the former will lead to a subsequent increase in the proportion of the latter and vice versa.

Approximately one minute after the addition of hydroxylamine a homogeneous feature can be observed at $g \sim 2.94$ (g_z of a rhombic trio) that has been previously attributed to His/Met coordinated *c*-heme (10). At 13 minutes this feature has decreased in intensity and moved downfield, indicating that the ligation is reverting back to the perpendicular *bis*-histidinyll coordinated state of the ‘as prepared enzyme’. At the 46-minute point a homogenous feature at $g \sim 3.00$ is observed and this peak is unchanged by the end of the experiment, approximately 79 minutes after hydroxylamine addition. This feature is assigned to the *bis*-histidinyll coordinated *c*-heme, although now only one of the previous two forms is present. This feature is clearly different in appearance to that observed in the ‘as prepared’ enzyme, as shown in Figure 3.3.9.

The ‘as prepared’ enzyme showed a ‘Large g_{\max} ’ feature at $g \sim 3.17$ plus the $g \sim 3.00$, feature. Simulations of the X-band EPR spectra (run at 10 K, 2 mW microwave power) of ‘as prepared’ *P. pantotrophus cd₁* in 50 mM BIS-TRIS propane (BTP) have shown that the contributions to this feature (termed c_a and c_b) are virtually identical at pH 6.00 and 8.50 (Figure 3.3.10).

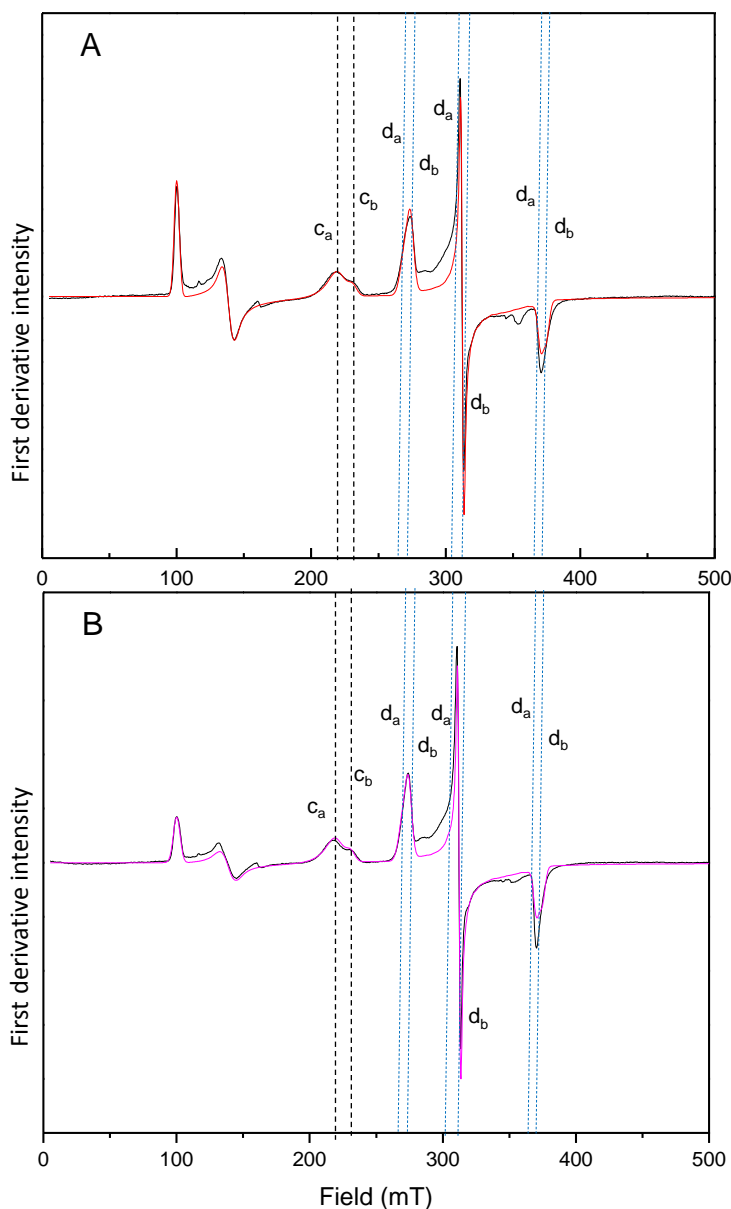


Figure 3.3.10: X-Band CW EPR spectrum — of *P. pantotrophus* (as prepared, $\sim 100\mu\text{M}$, in 50 mM BTP, pH 6.00 [A] and pH 8.50 [B]) and corresponding simulated spectra (— and — respectively). Black and blue dotted lines indicate c_a/c_b and d_a/d_b respectively. Spectrometer parameters: Power, 2 mW; modulation amplitude 1 mT; temperature, 10 K. Simulations were performed using ‘in house’ program, ‘Spin Half’⁸.

At both pHs the ratio of $c_a:c_b$ is $\sim 70:30$, indicating this heterogeneity is independent of H^+ concentration in this pH range. The d_1 -heme rhombic trio also displays some heterogeneity, with contributions ($d_a:d_b$) at both pHs existing in the ratio of $\sim 50:50$. As these ratios for the c and d_1 -heme signals are markedly different, it is unlikely that they

⁸ Program developed by Dr. Justin Bradley at University of East Anglia

are linked. Van Wonderen *et al* (20) made a similar observation in the EPR spectra of ‘as prepared’ *P. pantotrophus* and *P. stutzeri*. It should be noted that the purpose of this experiment was to primarily obtain the relative proportions of the *c*-type heme alone. As the d_1 heme has a longer spin-lattice relaxation time (compared with that of the *c*-heme), running the spectra at 10 K 2 mW would have led to partial saturation of this particular centre.

It was suggested by Allen *et al* (10) that immediately after re-oxidation with hydroxylamine, the ferric d_1 -heme is axially coordinated by His²⁰⁰ and an NH₃ molecule. This d_1^{3+} -NH₃ species was assigned by the authors to a feature with a g value of 2.67. In the spectra recorded for this experiment, the feature at g ~ 2.65 (observed up to two minutes immediately after hydroxylamine addition) will therefore be discussed as arising from His²⁰⁰- d_1 -NH₃.

In the third spectrum measured after hydroxylamine addition, at approximately 13 minutes, this g ~ 2.65 feature has decreased in intensity by approximately 48 % (compared to the spectrum obtained immediately after hydroxylamine addition), indicating the release of the ammonia as the heme reverted back to the tyrosine-bound state. By 46 minutes this feature is no longer visible in the spectrum and the low-spin d_1 rhombic trio (with g values of ~ 2.58, 2.21 and 1.85) representing tyrosine-bound heme is once again present. This is consistent with the absorbance time course results discussed earlier in this chapter which suggested that at pH 6.50, the Tyr²⁵ returns to the d_1 centre within approximately 17 minutes.

The work carried out by Allen *et al* (10) stated that following re-oxidation by hydroxylamine; the *c*-heme had reverted back to the ‘as isolated’ (*bis*-histidiny) ligand conformation over the course of approximately 20 minutes. Comparison of the spectrum measured at ~ 46 minutes in this work with the ‘as isolated’ spectrum shows clear

differences, in both the *c* and *d*₁-heme regions. Even the spectrum recorded at the end of this experiment after approximately 79 minutes shows a number of very noticeable differences compared to the ‘as isolated’ spectrum. This, and previous work by Van Wonderen *et al* (20) has shown that prior to reduction and re-oxidation the axial ligation to the *c*-heme exists in two different states. These two states could differ in terms of ligand plane orientation (i.e. both perpendicular and parallel).

Another noticeable difference between the ‘as isolated’ spectrum and that obtained approximately 79 minutes after hydroxylamine addition is that the overall intensity of the low-spin ferric *d*₁ ‘rhombic trio’ is less in the latter spectrum. It seems unlikely that there is some NH₃-bound *d*₁ persisting as the feature at *g* ~ 2.65 is no longer observed in the 46-minute or the 79-minute spectrum. Although there is a subsequent increase in high-spin ferric *d*₁ signal in the 46- minute and 79-minute spectra compared with the ‘as isolated’ this is not large enough to explain the deficit in the low-spin ferric *d*₁ signal (for equimolar high- and low-spin ferric heme, the *g* = 6.0 EPR signal of the high-spin tends to be some 10–20 times more intense than the low-spin *g*_z signal (25)). One possibility is that a portion of the *d*₁-heme became dissociated from the protein due to exposure to a high concentration hydroxylamine. Another explanation for the deficiency could be the coupling of the unpaired electron spin on the ferric *d*₁ with a nearby paramagnetic centre, which would not be detected in the absorbance spectra. This will be discussed in more detail later.

3.3.4 *Monitoring the c-heme ligand reversion of P. Pantotrophus cd₁ using a novel time-resolved NIR-MCD method*

In order to track corresponding changes in *c*-heme ligand identity, a novel, time resolved NIR-MCD study was carried out. Used in conjunction with the previously obtained

absorbance and EPR data, it was hoped that these NIR-MCD results would help to provide a definitive picture of the *c*-heme ligand-reversion process. The use of NIR-MCD spectroscopy as a method for assigning the identity of the axial ligands coordinating a *c*-type heme has been discussed in Chapter 1. In the case of cytochrome *cd*₁, bands exclusively occurring due to the *c*-type heme, can be monitored using this method. This is due to the relative low intensity of the *d*₁-heme bands in the NIR-MCD spectra, a consequence of the unusual $(d_{xz}d_{yz})^4(d_{xy})^1$ ground state. An electronic transition from a porphyrin HOMO to a hole in the *d*_{xy} orbital is formally symmetry forbidden. It was also hoped that this method could also be used to correlate the ligation changes at the *c*-type heme with those occurring at the *d*₁ centre monitored by UV-visible spectroscopy. This was previously investigated by Allen *et al* (10), although for reasons discussed earlier in this chapter, the use of this method alone does not allow for exclusive monitoring of the changes at the *c*-heme. The NIR-MCD time course spectra for the re-oxidation of fully reduced *P. Pantotrophus cd*₁ by hydroxylamine hydrochloride at pH*s 6.50 and 7.00⁹ are shown in *Figure 3.3.11*. The results of the data fittings at both pH values are summarised in *Table 3.3.2*, including the rate constant (*k*_{obs}) values.

| | pH* 6.50 | pH* 7.00 |
|---|----------|----------|
| Re-oxidation rate (min ⁻¹) | 2.4 | 2.4 |
| His/Met to His/His rate (min ⁻¹) | 0.12 | 0.047 |
| Parallel His/His to crossed His/His rate (min ⁻¹) | N/A | 0.09 |
| Percentage of His/Met at end point | 24 | 44 |
| His/Met to His/His rate (min ⁻¹) as calculated by Allen <i>et al</i> (10) | | 0.22 |

Table 3.3.2: Summary of the rate constants (*k*_{obs}) obtained from the NIR-MCD time trace results at 1550 nm and 1800 nm obtained from the addition of hydroxylamine hydrochloride to *P. pantotrophus cd*₁ at pH* 6.50 and pH* 7.00.

⁹ The ‘*’ indicates the use of deuterated buffer.

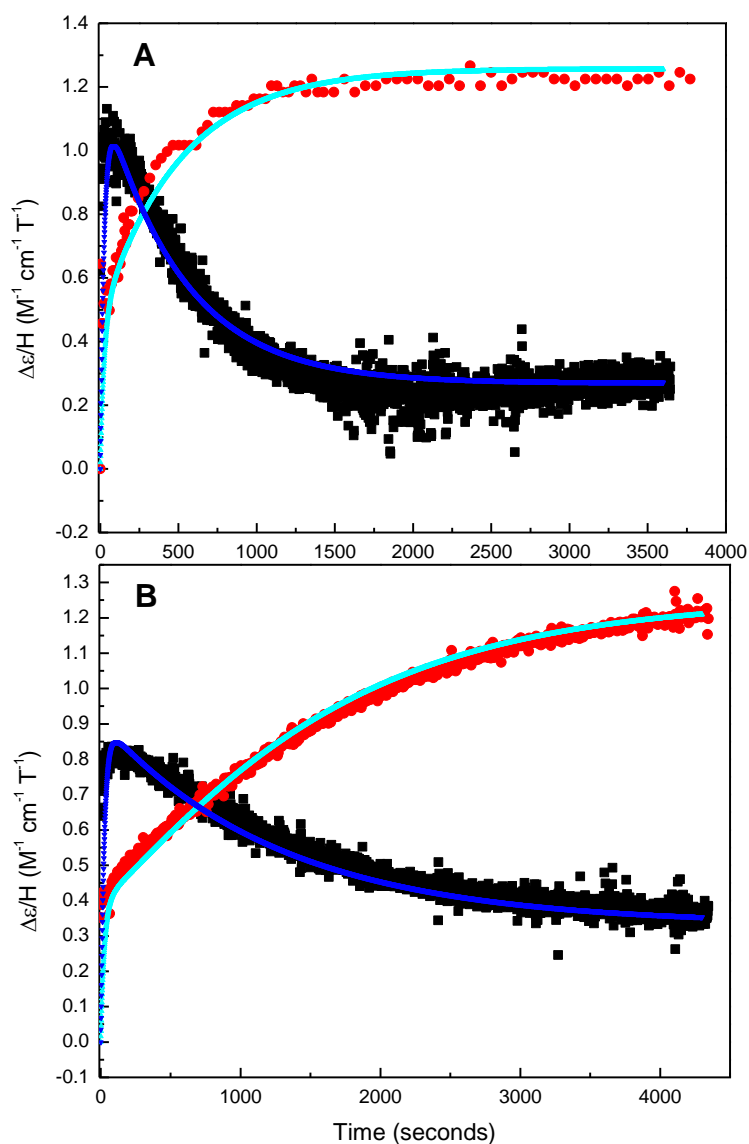


Figure 3.3.11: NIR-MCD time course traces of dithionite-reduced *P. pantotrophus* *cd₁* ($\sim 160 \mu M$) re-oxidised with 43 mM hydroxylamine hydrochloride and monitored at \circ 1550 nm (His/His) and \circ 1800 nm (His/Met). — and — represent fittings to the data using an in-house program¹⁰. Samples were in 48 mM ‘mixed’ buffer (see Section 3.2.4 for details) at pH* 6.50 [A] and 7.00 [B].

A control experiment was also carried out (*Figure 3.3.12*) in which de-oxygenated pH 7.00 buffer was injected into the reduced protein sample in place of hydroxylamine and the NIR MCD time course monitored at 1550 nm. No change in intensity at this wavelength was observed following the addition of buffer, indicating the sample remained

¹⁰ Program developed by Dr. Justin Bradley at the University of East Anglia, 2010.

fully reduced and that the absorbance changes viewed in *Figure 3.3.11* were due to re-oxidation by hydroxylamine, not residual O₂ from the atmosphere.

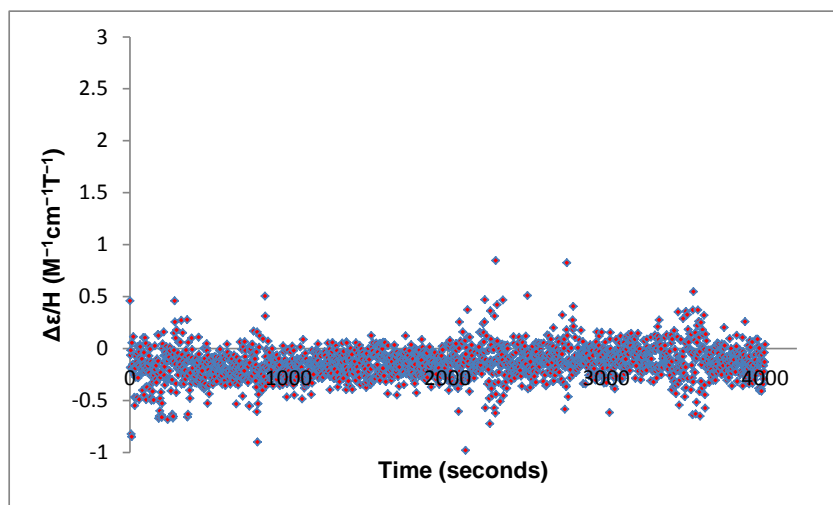


Figure 3.3.12: NIR-MCD time course trace showing the result of adding pH 7.00 buffer to a sample of dithionite-reduced *P. pantotrophus cd₁* (~ 160 μM). The NIR absorbance was monitored 1550 nm.

As with the absorbance time course spectra, the NIR-MCD results demonstrate that the reversion process occurs more rapidly at a lower solution pH. At a solution pH* of 6.50, the His/Met to His/His conversion is estimated to occur at a rate of 0.12 min⁻¹. At pH* 7.00, the rate of this process decreases by ~ 2.5 times, to 0.047 min⁻¹. The immediate observation that can be made from these data is that the ligand reversion proceeds at a much slower rate in D₂O-based buffer than in buffer which is H₂O-based. The rate constant calculated from the absorbance time course trace recorded at 548 nm in pH 6.50 H₂O-based buffer is 0.242 min⁻¹, approximately double the NIR-MCD equivalent in D₂O-based buffer. This observation is discussed in more detail below.

Allen *et al* (10) found that when they followed the (assumed) His/Met → His/His reversion by absorbance spectroscopy at 425 nm (in pH 7.00 H₂O-based buffer), the rate constant calculated from the data for the overall process was 0.22 min⁻¹. In this work, when the ligand reversion was followed by NIR-MCD at pH* 7.00 (in D₂O-based buffer),

the rate constant calculated from the data is 0.047 min^{-1} , a reduction of more than four fold.

The reversion following hydroxylamine addition was next followed by UV-visible absorbance spectroscopy in D_2O -based buffer at 706 nm and 548 nm. It was hoped that the rate constant(s) calculated from the former time trace could be correlated with that obtained from the NIR-MCD to prove (or otherwise) that a concomitant change occurs at both hemes following re-oxidation by hydroxylamine. The reversion process was followed at pH* 6.50 by the same UV-visible time course method employed previously (as detailed in Section 3.2.1), although on this occasion the 48 mM mixed buffer was made using D_2O rather than H_2O . Time course spectra were recorded at 548 nm and 706 nm, correlating with the previous experiments reported in Section 3.3.2 and therefore allowing the processes occurring at both the *c*- and *d*₁-hemes to be followed.

However, as discussed in Section 3.3.2, it cannot be ruled out that tracking the absorbance changes at these two wavelengths specifically corresponds to the individual processes of the His/Met \rightarrow His/His *c*-heme reversion and the Tyr²⁵ reattaching (and the low/high spin *d*₁ equilibrium returning). This is due to the fact that high-spin *d*₁-heme may contribute to the absorbance at 548 nm. The results of the D_2O absorbance measurements made at 548 nm and 706 nm are shown in *Figure 3.3.13*.

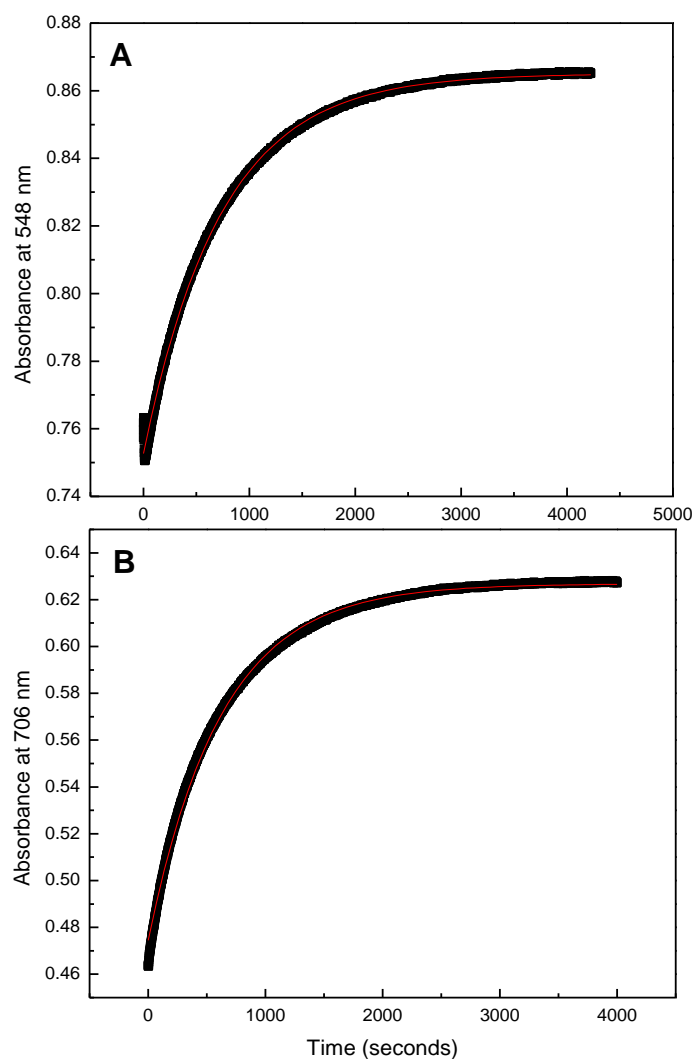


Figure 3.3.13: ■ Time course traces of the relative absorbance at [A] 548 nm and [B] 706 nm after the addition of 4 mM hydroxylamine hydrochloride to dithionite-reduced *P. pantotrophus cd₁* (~ 21.1 μM). — Non-linear curve fitting to data. $R^2 = 0.9990$ and 0.9979 for [A] and [B] respectively. Samples were in 48 mM D₂O ‘mixed’ buffer, pH* 6.50.

From the time trace recorded at 548 nm, the calculated k_{obs} value is 0.082 min^{-1} , while at 706 nm the reaction appears to progress a little more rapidly, with a k_{obs} of 0.097 min^{-1} . These values compare well to the k_{obs} of 0.12 min^{-1} calculated from the NIR-MCD time course spectrum of the pH* 6.50 sample. Both absorbance time course spectra show a decrease in the rate constant (k_{obs}) when D₂O-based buffer is used as opposed to H₂O-based buffer. The previous absorbance time course measurements made at pH 6.50, (reported in Section 3.3.2) resulted in identical k_{obs} values for the processes occurring at

548 nm and 706 nm. At 0.242 min^{-1} , these are more than double those obtained in pH* 6.50 D₂O based buffer from both the absorbance and NIR-MCD time course measurements. This observation indicates that a kinetic isotope effect (KIE) led to the reduction in the reversion rate rather than discrepancies between the absorbance and NIR-MCD time-resolved experimental methods.

The relationship between the KIE and the rate constants (k_A and k_B) of the individual reactions involving different isotopes is shown in Equation 2 below. In the case of the reaction discussed here, k_A will be the rate constant calculated in H₂O-based buffer, while k_B will refer to the corresponding value obtained when D₂O-based buffer is used.

$$\text{KIE} = k_A/k_B \quad (2)$$

Comparing the absorbance time-course measurements; the KIE (at pH* 6.50) for the reversion followed at 548 nm is 2.95, while at 706 nm this value is 2.50, giving a mean value for the two wavelengths of 2.73.

From these data, the indication is therefore that the use of deuterated buffer (as opposed to hydrated) leads to an approximately three-fold decrease in the rate of ligand reversion in *P. pantotrophus cd*₁.

The effect of an isotopic substitution on the rate of reaction is greatly pronounced when the atom in question is involved in a bond that is either broken or made during the rate-limiting step (26). The reduction in zero-point energy of an X-D bond (compared to an X-H bond, where X is any bonded atom such as N or O) will lead a subsequent increase in activation energy and a decrease in the corresponding rate constant for the reaction. The rate of re-oxidation of the two metal centres in a monomer of *P. pantotrophus cd*₁ by a molecule of hydroxylamine would be subjected to a kinetic isotope effect as this reaction consumes protons. It would appear that as both k_{obs} values calculated from the absorbance time course spectra (in D₂O-based buffer) compare well with those obtained from the 1550

nm NIR-MCD spectrum at pH* 6.50, there are indeed concomitant processes occurring at the two hemes.

The time-resolved NIR-MCD method and subsequent analysis (discussed below) has also allowed an estimate for the rate constant of a second process occurring at the *c*-heme to be obtained. This second rate constant is assumed to correspond to the rotation of the *bis*-histidinylligands from the parallel orientation back to perpendicular (as observed in the ‘as isolated’ enzyme) following the initial reversion from the His/Met conformation. Analysis of the NIR-MCD data estimated that this process occurs at a rate of 0.09 min⁻¹ at pH* 7, almost twice as rapidly as the His/Met → His/His (parallel) switch, for which the calculated rate constant is 0.047 min⁻¹. A His/His (parallel) → His/His (perpendicular) rate constant for the pH 7.00 sample only was obtained, indicating that at pH* 6.50 this second process could either not be resolved, or does not occur. This will be discussed in more detail later in this chapter

While the absorbance time course traces were fitted to a simple exponential decay function (discussed in Section 3.3.2) to obtain values for the rate constants, the analysis of the NIR-MCD data was carried out using an in-house program¹¹. This program makes use of a set of linked first order reactions to simulate the observed data, which allows the processes taking place at the *c*-type heme during the reaction to be separated. To apply this to the data obtained for the NIR-MCD time course spectra recorded at 1550 nm and 1800 nm, it was assumed that there are four species formed at the *c*-heme in the *P. pantotrophus* enzyme during the reaction with hydroxylamine and subsequent ligand reversion. These are: [A] His/Met ligated *c*²⁺, [B] His/Met ligated *c*³⁺, [C]His/His ligated *c*³⁺ with the axial histidines orientated parallel with respect to each other and [D] His/His ligated *c*³⁺ with the axial histidines orientated in the perpendicular conformation, as observed in the ‘as

¹¹ Program developed by Dr. Justin Bradley at the University of East Anglia.

isolated' enzyme. The rate of change in the concentrations of these four species can be given by Equations 3–6:

$$d[A]/dt = -k_{ox}[A] \quad (3)$$

$$d[B]/dt = k_{ox}[A] - k_r[B] \quad (4)$$

$$d[C]/dt = k_r[B] - k_{rr}[D] \quad (5)$$

$$d[D]/dt = k_{rr}[D] \quad (6)$$

Where k_{ox} is the rate constant for the conversion of ferrous His/Met-ligated *c*-heme to ferric His/Met-ligated *c*-heme, k_r is the rate constant for the His/Met \rightarrow His/His (parallel) reversion and k_{rr} is the rate constant for the rotation of the histidine ligands back to the perpendicular conformation. Expressions for the intensities at 1550 nm and 1800 nm (Equations 7 and 8 respectively) as a function of time can be obtained using values of $\Delta\epsilon$ for the His/Met, parallel *bis*-histidinyl and perpendicular *bis*-histidinyl species (13,20,27).

$$I_{(1800\text{ nm})}(t) = \Delta\epsilon_{(\text{His/Met})}[B] \cdot l \quad (7)$$

Where $I_{(1800\text{ nm})}(t)$ is the intensity at 1800 nm at specific time point during the time course measurement, $\Delta\epsilon_{(\text{His/Met})}$ is the molar extinction coefficient of the His/Met band at 1800 nm and l is the pathlength. This expression for the intensity at 1550 nm is complicated by the fact that the His/Met band shows some intensity at this wavelength in the form of a 'tail', which is approximately 46 % the maximum intensity at 1800 nm. An expression for the intensity at 1550 nm will therefore need to include any intensity due to the 'tail' of the His/Met band:

$$I_{(1550\text{ nm})}(t) = (0.46 \times \Delta\epsilon_{(\text{His/Met})}[B]) + (\Delta\epsilon_{(\text{His/His}\parallel)}[C]) + (\Delta\epsilon_{(\text{His/His}\perp)}[D])t \quad (8)$$

Where $\Delta\epsilon$ (His/His_{||}) and $\Delta\epsilon$ (His/His_⊥) are the molar extinction coefficient values for the parallel and perpendicular *bis*-histidinyI conformations respectively. Application of Expressions 7 and 8 require the concentration of each of the species (A, B, C or D) at a particular point during the reaction be known. This value can be given by Relation 9:

$$[X]_{t+\delta t} = [X]_t + d[X]/dt \times \delta t \quad (9)$$

Where X is any of the four species A, B, C or D and δt is a small time window, i.e. 0.1 seconds. Substitution of Expressions 3–6 into Relation 9, followed by substitution of (9) into either (7) or (8) allows a time course for that specific wavelength to be simulated. As the values for the rate constants in Expressions 3 to 6 were unknown, they were optimised by trial and error until a fit to the data was obtained. Fitting Expressions 7 and 8 simultaneously to the time course spectra measured at 1550 nm and 1800 nm allowed an overall value of the rate of His/Met \rightarrow His/His conversion for each pH value to be obtained. Interestingly, an estimated 24 % and 44 % of the *c*-heme present in the pH 6.50 and pH 7.00 samples respectively were still His/Met ligated at the end of the time course measurement. This will be discussed further in the final section of this chapter.

The room temperature NIR-MCD spectra of *P. pantotrophus* *cd*₁ (pH* 6.50) pre- and post-hydroxylamine addition (to the fully-reduced sample) is shown in *Figures 3.3.14*.

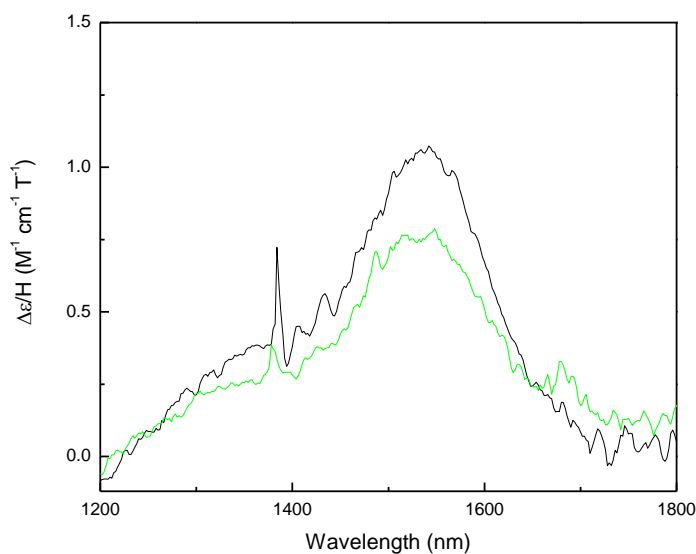


Figure 3.3.14: NIR-MCD spectrum of *P. pantotrophus* cd_1 ($\sim 160 \mu\text{M}$), — as prepared and — re-oxidised with 43 mM hydroxylamine hydrochloride. Samples were in 48 mM ‘mixed’ buffer (see Section 3.2.4 for details) at pH* 6.50.

Despite the fact that the time course trace at this solution pH showed no further changes after ca. 30 minutes, indicating the reversion process was complete, the intensity of the His/His band at 1550 nm is clearly not the same post-hydroxylamine addition as in the ‘as prepared’ sample. This therefore adds further proof that following re-oxidation by hydroxylamine of the fully-reduced enzyme, the ligation of *P. pantotrophus* cd_1 does not return to the ‘as isolated’ conformation (at the *c*-heme), as stated by Allen *et al* (10).

Figure 3.3.15 shows a comparison of the UV-visible absorbance spectra of the NIR MCD pH* 6.50 sample before and after the re-oxidation by hydroxylamine. While these two spectra do compare well, there is a slight red shift in the centre of the *c*-heme Soret band in the post-MCD sample by 0.5 nm compared with that of the ‘as prepared’ enzyme. The shape of the d_1 -heme Soret in the post-MCD sample is also slightly altered compared to the ‘as-prepared’. These observations indicate that the environments around the *c*- and d_1 - centres differ slightly after reaction with hydroxylamine compared with those in the ‘as prepared’ enzyme.

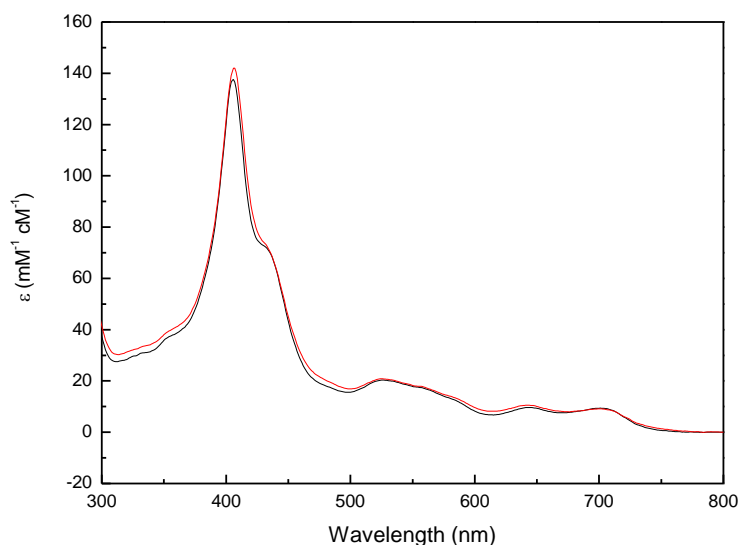


Figure 3.3.15: Absorbance spectra of — the ‘as prepared’ *P. pantotrophus* cd_1 NIR-MCD sample ($\sim 166 \mu\text{M}$) and — after dithionite reduction and re-oxidation with $\sim 43 \text{ mM}$ hydroxylamine hydrochloride (final concentration in sample solution). Samples were in 48 mM ‘mixed’ buffer (see Section 3.2.4 for details) at pH* 6.50.

3.4 Discussion and conclusions

The sequential events that follow the hydroxylamine re-oxidation of stoichiometrically reduced cytochrome cd_1 have been tracked using electronic absorption, EPR and MCD spectroscopic studies in parallel. This combination of methods has allowed the processes of ligand exchange and ligand rotation at each heme to be monitored as a function of time and thus correlated. The re-oxidation itself has been shown previously, using stopped-flow methods, to occur on a timescale of $\sim 30 \text{ ms}$ (12). The approaches used here involve mixing of enzyme and oxidant on the timescale of seconds. Thus, the spectroscopic changes observed result only from conformational changes in the re-oxidised enzyme.

The simultaneous presence of bands at 640 and 706 nm in the electronic absorbance spectrum of as-prepared enzyme is unique to the *Paracoccus* cd_1 and is due to a low-spin/high-spin thermal equilibrium established at the $\text{Fe}^{3+} d_1$ -heme as a consequence of the intermediate strength of the distal tyrosine ligand. There are no significant electronic bands of the *c*-heme in the 600–800 nm region. The re-emergence of the

706 nm band has therefore been used as a reporter for the rebinding of the distal Tyr²⁵ to Fe³⁺ *d*₁-heme. At pH values of 6.50 and 7.50, this process is observed with apparent rates $k_{\text{obs}} = 0.24$ and 0.20 min^{-1} respectively, in good agreement with the value of 0.22 min^{-1} reported at pH 7.00 (It is not clear why 700 nm was the wavelength chosen to monitor this band, although this would not influence the conclusions) (10). Interestingly, as suggested by these values, the process is pH dependent. At a pH of 5.50, the rate increases to $\sim 0.50 \text{ min}^{-1}$. It should be noted that, as these are events following the re-oxidation, this is not due simply to protons being consumed in the hydroxylamine reaction.

Investigating the rate of ligand reversion by UV-visible time course spectroscopy alone does not provide proof that concomitant changes occur at the *c*- and *d*₁-hemes following re-oxidation by hydroxylamine, as previously claimed by Allen *et al* (10). This is because the *d*₁-heme will also contribute to the overall electronic absorbance between 300 and 600 nm (16,23,24,28,29). Recording the time course at 425 nm (10) or 548 nm (this work) will not guarantee that processes occurring at the *c*-heme alone are being observed.

The novel time-resolved NIR-MCD method described here allows the processes exclusively occurring at the *c*-heme to be monitored. Because the MCD experiment requires D₂O-based buffer systems, it was necessary to repeat the UV-visible absorption experiments in such buffers for comparison. The changes observed in moving from H₂O to D₂O again demonstrate the importance of proton concentration in the reversion process. By comparing the rates obtained from the NIR-MCD method at pH* 6.50, with that derived from the 706 nm absorbance time course recorded in D₂O-based buffer it was demonstrated that concomitant reversion processes do indeed occur at both hemes following hydroxylamine re-oxidation. A k_{obs} value of 0.12 min^{-1} was calculated from the NIR-MCD time trace at pH* 6.50, in good agreement with the value of 0.097 min^{-1} obtained from the UV-visible time course spectrum recorded at 706 nm. Thus the

rebinding of Tyr²⁵ to the *d*₁-heme is correlated with the switch from His/Met to His/His ligation at the *c*-heme.

The conjunctive use of EPR and MCD spectroscopies has demonstrated that the report claiming (on the basis of EPR spectroscopy) that re-oxidised enzyme reverts to the as-prepared form within 20 minutes is clearly in error (10). In the EPR spectrum of as-prepared cytochrome *cd*₁, Fe³⁺ *c*-heme gives rise to two *g_z* features at ~ 3.17 and ~ 3.00. It is proposed that, in solution, the latter arises from a population of the *c*-heme with parallel histidine ligands. The near-perpendicular orientation of the two histidine ligands at both *c*-hemes in the crystal structure of oxidised *cd*₁ suggests that again the nature of the protein in solution differs from that observed in the crystal. It is anticipated that crystalline *cd*₁ containing the *c*-heme with only perpendicular histidine ligands would give one *g_z* EPR feature at ~ 3.17. Following reduction and re-oxidation, the first *g_z* feature observed for the *c*-heme is at *g* ~ 2.94. The MCD can be used to assign this EPR feature to His/Met ligated *c*-heme. Over minutes, the *g* ~ 2.94 signal moves to *g* ~ 3.00 as the ligand switch occurs but, in contrast to previous assertions, this is not a reversion to the as-prepared form but to a new form in which the *c*-heme ligands are parallel. Rebinding of Tyr²⁵ to the *d*₁-heme occurs concomitantly with the conversion to this form and not to that observed in the crystal structure of as-prepared enzyme. Indeed the ligation at the *c*-heme in the sample at ~ 80 minutes post-hydroxylamine re-oxidation is clearly different to that observed for the 'as prepared' enzyme. In the EPR spectrum of the pH 6.50 sample, only the signal at *g_z* ~ 3.00 was observed. Although the *bis*-histidinyl ligation of the *c*-heme in the as-prepared enzyme exists in two conformations, after re-oxidation only one is present.

Comparison of the full-wavelength NIR-MCD spectra obtained for the 'as prepared' enzyme, with that obtained following hydroxylamine addition supported the EPR

observations. These spectra again showed that the enzyme did not revert to the ‘as isolated’ conformation at the *c*-heme following re-oxidation. Additionally, in the absorbance spectra, small differences in the maximum intensity and central wavelength position of the Soret band were observed between the ‘as prepared’ and hydroxylamine re-oxidised samples.

The specific processes that take place at the active site *d*₁-heme during re-oxidation by hydroxylamine remain unclear. Sam *et al* observed a pH dependence (30,31) of the release of nitric oxide in the early stages (within 2–3 ms following substrate addition) of nitrite reduction. They postulated that increased protonation of the His³⁴⁵ and His³⁸⁸ residues located in the pocket of the active site would lead to a subsequent increase in the rate of dehydration of the bound nitrite. It can reasonably be assumed that these active site histidine residues also provide the protons for the dehydration of hydroxylamine to form ammonia. The hydroxylamine molecule would bind to the *d*₁-heme when the protein is in the fully reduced state and the two-electron reduction of hydroxylamine to ammonia and water would subsequently occur, facilitated by two protons provided by the His³⁴⁵ and His³⁸⁸ residues. In this work, a signal at $g \sim 2.67$ was observed in the first two EPR spectra, recorded at 50–60 seconds and two minutes immediately following re-oxidation by hydroxylamine. This feature has been previously assigned (10) to ammonia-bound *d*₁ heme, with a lifetime of ~ 4 minutes.

However, the rapid rate of re-oxidation of the ferrous *c* and *d*₁-hemes compared with the rate of ligand reversion would suggest that the former process is not rate-limiting. At first glance, the NIR-MCD time course results would indicate that at least at pH* 6.50 and pH* 7.00, the re-oxidation rate at the *c*-heme is independent of H⁺ concentration, occurring at a rate of 2.4 min⁻¹ in both cases. However, the rate of re-oxidation seen here is limited

by mass transport, due to the stirring method, not enzyme kinetics. To ascertain for certain whether the rate of re-oxidation to the ferric state is independent of pH, a method such as stopped flow absorbance spectroscopy would be required.

Although the pH dependence of nitrite reduction by the enzyme (30-32) has been investigated previously, the effect of H^+ concentration on the rate of ligand reversion following hydroxylamine re-oxidation has remained unexplored until now. As discussed above, the fact that the rate of His/Met \rightarrow His/His reversion at the *c*-heme is different at pH* 6.50 and pH* 7.00 (0.12 min^{-1} for the former and 0.047 min^{-1} for the latter) would indicate that the actual rate of reversion itself is pH-dependent. The reason(s) for these observations are unclear, although protonation of the His³⁴⁵ and His³⁸⁸ residues in the active site pocket may be a factor. The work carried out in Chapter 4 of this thesis has indicated that one (known as the ‘principle’ histidine residue) or both of the active site histidine residues has a pKa of ~ 7.1 . The equivalent pKa in deuterated buffer would be ~ 7.2 (33). Previous crystallography investigations have shown that the His¹⁷ and Tyr²⁵ ligands are connected by a seven-residue *c* domain loop that extends into the *d*₁ domain (1,7). Additionally, the Tyr²⁵ has been observed (in crystal form) to hydrogen-bond to the active site histidine residues when the nitric oxide product is bound to the *d*₁-heme (1).

These active site histidine residues have been seen to coordinate CN^- (34), SO_2^- and NO_2^- (1) in various crystal structures reported. Mutation of either of the invariant His³²⁷ and His³⁶⁹ residues in *Pseudomonas aeruginosa* *cd*₁ to alanine has been shown to cause impairment of nitrite reductase activity to approximately 1 % of that observed for the wild type enzyme (9). Interestingly, oxidase activity does not appear to be affected by either mutation, throwing into question the mechanism for this reaction previously suggested by Fülöp *et al* (2) for the *P. pantotrophus* enzyme, which shows these residues forming hydrogen bonds to a $d_1^{IV}=O$ intermediate. Stopped flow absorbance experiments

showed that the presence of the His³⁶⁹ residue in *P. aeruginosa* is integral if nitric oxide is to bind to the d_1 -heme. This was not the case with the His³²⁷ mutant indicating that the two residues may perform different functions during catalysis. In both mutants, upon reaction with nitrite, progression from the fully-reduced enzyme to the ferrous NO-bound complex occurred at an increased rate compared with the wild type enzyme. The inter-heme distance between the c and d_1 centres was unaffected by the mutation, indicating that the rate of intramolecular electron transfer could not cause the loss of nitrite activity observed in the mutants (35).

Topological structural changes to the c domain (but not the d_1) were visible in both mutants, resulting in movement of the N-terminal arm and displacement of the Tyr¹⁰ away from the d_1 active site. It was suggested by the authors that the removal of the His³²⁷ and His³⁶⁹ residues leads to a loss of a positive electrostatic potential in the active site pocket, resulting in an environment that is no longer favourable for interaction with Tyr¹⁰. Movement of the c domain in the adjoining monomer subsequently occurs in order to facilitate removal of this residue from the energetically unfavourable surroundings. Quantum mechanical calculations (3) have indicated that nucleophilic ligands present in the d_1 active site (such as the hydroxyl observed in crystal structures of the wild type enzyme (27)) would be stabilised by the positive electrostatic environment facilitated by the histidine residues. It has been suggested (9) that the presence of these ligands would most likely impose an unfavourable orientation on the bound nitric oxide, promoting its release from the metal centre. This would explain the increased rate of formation of the ferrous ‘dead end’ complex observed in the mutants.

Despite the differences between their respective structures, the findings discussed above for the *P. aeruginosa* enzyme could well be applied to *P. pantotrophus cd₁*. It may be the case that protonation of one (or both) of these histidine residues is required to induce

a conformational change (via the seven-residue loop) at the *c*-heme leading to His/Met \rightarrow His/His reversion. If there is an ‘intrinsic’ (or constant) rate of reversion that is pH independent but can only be achieved when the ‘principle’ histidine residue’ (or both histidine residues) is protonated, raising the pH would mean that reversion is taking place from a diminishing sub-population, leading to decreased apparent rate of reversion and therefore a smaller effective k_{obs} . This is shown in Equation 10.

$$\text{Apparent rate of reversion} = [\text{His-H}^+] k_{\text{in}}[\text{reverted His/Met } c\text{-heme}] \quad (10)$$

Where $[\text{His-H}^+]$ is the concentration of protonated ‘principle’ histidine residues in the sample and $[\text{reverted His/Met } c\text{-heme}]$ is the concentration of *c*-heme that is able to undergo reversion as a direct consequence of this protonation. This reversion occurs at an intrinsic rate (k_{in}) that is in itself, pH-independent. The fact that there is a greater proportion of His/Met ligated *c*-heme present in the pH 7.00 sample at the end of the measurement would appear to support this. However, this theory requires the assumption that the time taken for the external pH to re-establish the ‘equilibrium’ concentration of His/Met ligated *c*-heme/protonated principle histidine residue is relatively long compared to the His/Met \rightarrow His/His reversion process itself.

The NIR-MCD time trace results show that at pH* 7.00, there are two separate processes occurring at the *c*-heme. The first of these, assumed to be the His/Met \rightarrow His/His (parallel) reversion, is the slower of the two processes, occurring at a rate of 0.047 min^{-1} . The second process, occurring at a rate of 0.09 min^{-1} is assumed to be the rotation of the His/His (parallel) ligands back to the perpendicular conformation observed for the ‘as isolated’ enzyme. These two processes are not separated at pH* 6.50, leading to the

question of whether the rate of conversion of His/His (parallel) \rightarrow His/His (perpendicular) at this solution pH* is too rapid to be observed by the NIR-MCD method.

Site directed mutagenesis of these active site histidine residues in conjunction with a spectroscopic study would potentially inform on their importance (or otherwise) to the rate of ligand reversion. However, it is not immediately clear why it would be catalytically relevant for the enzyme to adopt this pH dependence of the ligand reversion process. The fact that ligand reversion is a slow compared to the rate of product formation means that it is unlikely that this process occurs as part of the catalytic cycle. Hence, *in vivo*, the enzyme may very rarely (or never) actually undergo reversion at the *c*-heme and the pH dependence observed in this work may be limited to *in vitro* conditions.

As discussed in this chapter, the d_1 rhombic trio of the hydroxylamine re-oxidised sample at ~ 80 minutes did not reach full intensity compared with that in the ‘as prepared’ spectrum. As the d_1 regions in the corresponding UV-visible absorbance spectra of these samples showed good comparison, it may be the case that a radical species, in the nature of that proposed by Van Wonderen *et al* (20) couples to this centre, rendering it EPR silent. To ascertain whether this is the case, further work would need to be carried out in terms of MCD ratio-data analysis.

When fitting the NIR-MCD time course spectra to Equations 7 and 8 described earlier, estimates were set of the intensities of the His/His (both parallel and perpendicular) and His/Met ligated *c*-heme present in the sample. The magnitude of the 1800 nm intensity at $t = \infty$ provided an estimate of the percentage of His/Met ligated *c*-heme present in the sample at the end of the time course. The percentage of His/Met ligated *c*-heme present post-measurement was calculated as being 24 % and 44 % for pH* values 6.50 and 7.00 respectively. Allen *et al* (17) claimed to have ‘locked’ the *c*-heme in the His/Met ligated

state after the addition of NO_2^- to hydroxylamine re-oxidised *P. pantotrophus cd*₁.

However, the fittings to the NIR-MCD time course spectra reported here indicate that some His/Met ligated *c*-heme persists at least one hour post hydroxylamine addition and that the extent of this is pH*-dependant.

As discussed in Section 3.3.4, the tail of the His/Met band at 1800 nm contributes to the intensity at 1550 nm by ~ 46 % and this was accounted for in the expression (Equation 8, this chapter) fitted to the 1550 nm spectrum. For this equation to fit the data, the initial concentration of His/His ligated *c*-heme present in the sample immediately after hydroxylamine addition had to be set to zero. This indicates that the *c*-heme in fully reduced *P. pantotrophus cd*₁, is entirely His/Met ligated. This has not been previously proven when the enzyme is in solution form, as reduction to the low-spin ferrous state means conventional NIR-MCD and EPR measurements cannot be made. This is contrary to the observations made by Allen *et al* (17), that indicated ~ 30 % of the *c*-heme is *bis*-histidinylligated ~ one minute after hydroxylamine addition. However, during the one minute time period following hydroxylamine addition, some ligand reversion would have occurred, so this is not necessarily a reliable indicator of the ligation of the enzyme in the fully reduced state.

How the pH of the sample solution could affect the rate of ligand reversion is summarised diagrammatically in *Figure 3.4.1*.

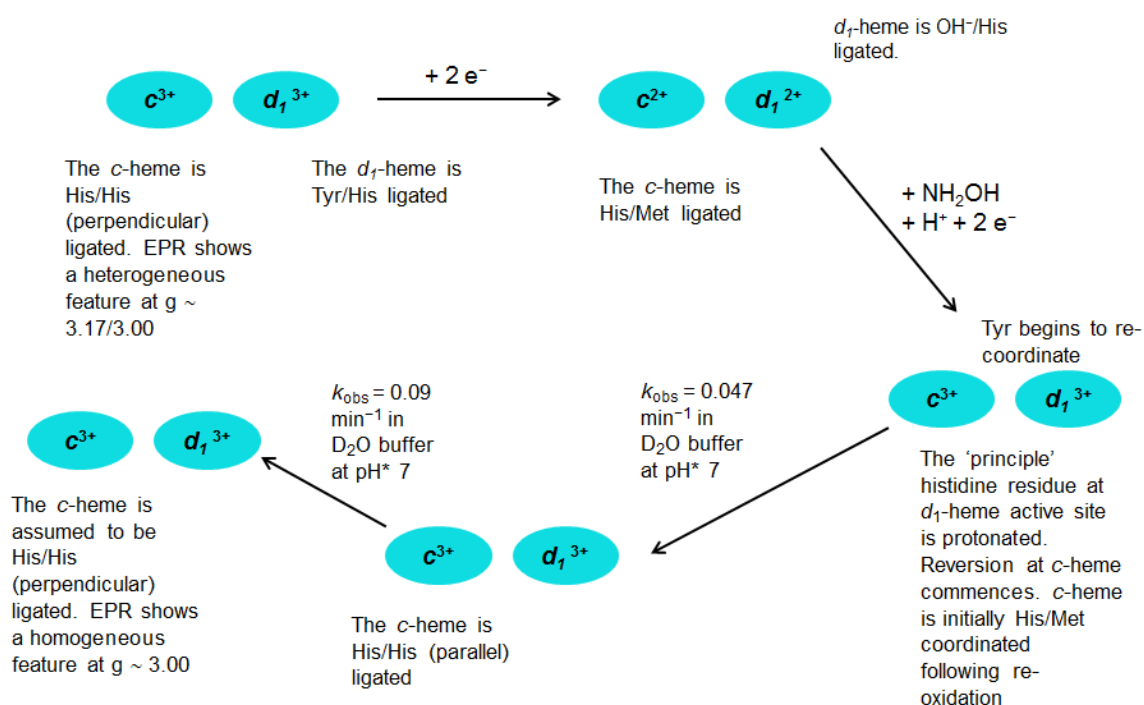


Figure 3.4.1: A summary of the ligand reversion processes occurring at the c-heme following re-oxidation by hydroxylamine and the accompanying observations in the X-band EPR spectra.

In summary, the following conclusions have been made from this section of work:

There are concomitant processes occurring at both *c* and *d*₁-hemes following re-oxidation of the fully-reduced enzyme by hydroxylamine. Although this has been previously stated in the literature (10), the methods used to reach this conclusion were ambiguous for reasons already stated. The actual process of ligand reversion is influenced by H⁺ concentration, an unexpected result that may be linked to the extent of protonation of the active site His³⁴⁵ and His³⁸⁸ residues. A time-resolved NIR-MCD experiment has allowed a second ligand reversion process, assumed to be His/His (parallel) → His/His (perpendicular) to be observed at a solution pH* of 7.00. Despite previous claims (10), the enzyme does not revert back to the 'as isolated' conformation following re-oxidation – this is evident in comparison of the UV-visible, EPR and NIR-MCD spectra recorded before and after hydroxylamine re-oxidation. Finally, the fittings to the NIR-MCD time course

traces indicate that the *c*-heme is fully His/Met ligated at the instant of re-oxidation and therefore in the reduced state. A sub-population proportion the *c*-heme retains this ligation state for at least one hour post-re-oxidation.

3.5 References

1. Williams, P. A., Fulop, V., Garman, E. F., Saunders, N. F. W., Ferguson, S. J., and Hajdu, J. (1997) *Nature* **389**, 406-412
2. Fulop, V., Moir, J. W. B., Ferguson, S. J., and Hajdu, J. (1995) *Cell* **81**, 369-377
3. Ranghino, G., Scorza, E., Sjogren, T., Williams, P. A., Ricci, M., and Hajdu, J. (2000) *Biochemistry* **39**, 10958-10966
4. Sam, K. A., Fairhurst, S. A., Thorneley, R. N. F., Allen, J. W. A., and Ferguson, S. J. (2008) *J Biol Chem* **283**, 12555-12563
5. Rinaldo, S., Brunori, M., and Cutruzzola, F. (2007) *Biochem Biophys Res Commun* **363**, 662-666
6. Rinaldo, S., Arcovito, A., Brunori, M., and Cutruzzola, F. (2007) *J Biol Chem* **282**, 14761-14767
7. Sjogren, T., and Hajdu, J. (2001) *J Biol Chem* **276**, 29450-29455
8. Gordon, E. H. J., Sjogren, T., Lofqvist, M., Richter, C. D., Allen, J. W. A., Higham, C. W., Hajdu, J., Fulop, V., and Ferguson, S. J. (2003) *J Biol Chem* **278**, 11773-11781
9. Cutruzzola, F., Brown, K., Wilson, E. K., Bellelli, A., Arese, M., Tegoni, M., Cambillau, C., and Brunori, M. (2001) *Proc Natl Acad Sci U S A* **98**, 2232-2237
10. Allen, J. W. A., Watmough, N. J., and Ferguson, S. J. (2000) *Nat Struct Biol* **7**, 885-888
11. Singh, J. (1973) *Biochim Biophys Acta* **333**, 28-36
12. Koppenhofer, A., Little, R. H., Lowe, D. J., Ferguson, S. J., and Watmough, N. J. (2000) *Biochemistry* **39**, 4028-4036
13. Cheesman, M. R., Ferguson, S. J., Moir, J. W. B., Richardson, D. J., Zumft, W. G., and Thomson, A. J. (1997) *Biochemistry* **36**, 16267-16276
14. Muhoberac, B. B., and Wharton, D. C. (1983) *J Biol Chem* **258**, 3019-3027
15. Walker, F. A. (1999) *Coord Chem Rev* **186**, 471-534
16. Kobayashi, K., Koppenhofer, A., Ferguson, S. J., and Tagawa, S. (1997) *Biochemistry* **36**, 13611-13616
17. Allen, J. W. A., Cheesman, M. R., Higham, C. W., Ferguson, S. J., and Watmough, N. J. (2000) *Biochem Biophys Res Commun* **279**, 674-677
18. Cheesman, M. R., Greenwood, C., and Thomson, A. J. (1991) *Adv Inorg Chem* **36**, 201-255
19. Cheesman, M. R., and Walker, F. A. (1996) *J Am Chem Soc* **118**, 7373-7380
20. Van Wonderen, J., Knight, C., Oganessian, V. S., George, S. J., Zumft, W. G., and Cheesman, M. R. (2007) *J Biol Chem* **282**, 28207-28215
21. Bradley J.M., Marritt S.J., Kihlken M.A., Haynes K., Hemmings A.M., Berks B.C., Cheesman M.R., Butt J.N. (2012) *J Biol Chem* **287**, 40350-40359
22. Allen, J. W. A., Higham, C. W., Zajicek, R. S., Watmough, N. J., and Ferguson, S. J. (2002) *Biochem J* **366**, 883-888

23. Walsh, T. A., Johnson, M. K., Barber, D., Thomson, A. J., and Greenwood, C. (1981) *J Inorg Biochem* **14**, 15-31
24. Chang, C. K., and Wu, W. (1986) *J Biol Chem* **261**, 8593-8596.
25. Oganessian, V. S., Butler, C. S., Watmough, N. J., Greenwood, C., Thomson, A. J., and Cheesman, M. R. (1998) *J Am Chem Soc* **120**, 4232-4233
26. Westheimer, F. H. *Chem Rev* **61**, 265-273
27. Cheesman, M. R., Kemp, G., and Bennett, M. S. *Unpublished*
28. Chang, C. K. (1985) *J Biol Chem* **260**, 9520-9522.
29. Stolzenberg, A. M., Strauss, S. H., and Holm, R. H. (1981) *J Am Chem Soc* **103**, 4763-4778
30. Sam, K. A., Strampstead, M. J. F., de Vries, S., and Ferguson, S. J. (2008) *J Biol Chem* **283**, 27403-27409
31. Sam, K. A., Tolland, J. D., Fairhurst, S. A., Higham, C. W., Lowe, D. J., Thorneley, R. N. F., Allen, J. W. A., and Ferguson, S. J. (2008) *Biochem Biophys Res Commun* **371**, 719-723
32. Richter, C. D., Allen, J. W. A., Higham, C. W., Koppenhofer, A., Zajicek, R. S., Watmough, N. J., and Ferguson, S. J. (2002) *J Biol Chem* **277**, 3093-3100
33. Krężel, A., and Bal, W. (2004) *J Inorg Biochem* **98**, 161-166
34. Jafferji, A., Allen, J. W. A., Ferguson, S. J., and Fulop, V. (2000) *J Biol Chem* **275**, 25089-25094
35. Page, C. C., Moser, C. C., Chen, X., and Dutton, P. L. (1999) *Nature* **402**, 47-52

4. Spectroscopic investigations of the *P. pantotrophus* cd_1 NO-bound ferrous d_1 intermediates

4.1 The formation of NO-bound d_1^{2+} intermediates

4.1.1. *The *P. pantotrophus* cd_1 reaction mechanism*

The structural changes undergone by *P. pantotrophus* cytochrome cd_1 upon reduction and re-oxidation by nitrite have already been discussed in Chapter 2. A reaction mechanism for the one electron reduction of nitrite to nitric oxide was initially proposed by Fülöp *et al* in 1995 (1). The key points of this mechanism (*Figure 4.1.1.*) were discussed in Chapter 2.

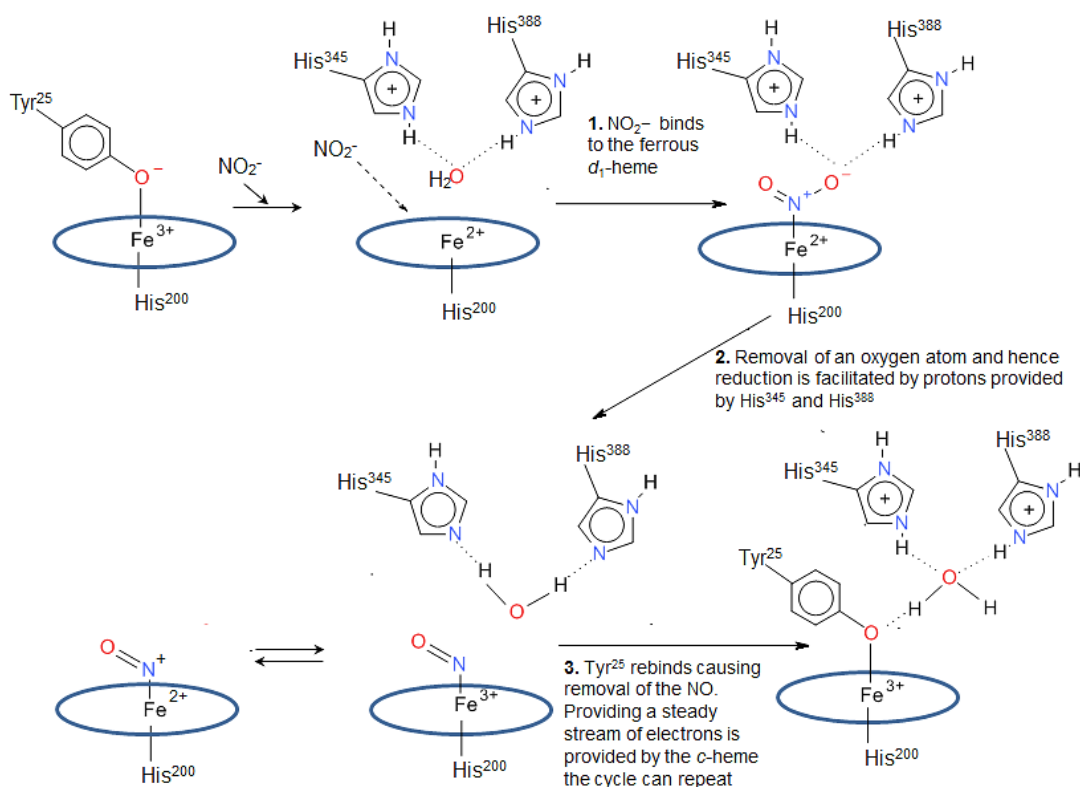


Figure 4.1.1: The reaction mechanism for the reduction of NO_2^- at the d_1 -heme for *P. pantotrophus* cytochrome cd_1 as proposed by Fülöp *et al* (1).

The initial step involves the displacement of the distal Tyr²⁵ following reduction of the d_1 -heme and the subsequent binding of a nitrite ion. Electron transfer occurs within the d_1^{2+} -

NO_2^- complex, resulting in a $d_1^{2+}\text{-NO}^+$ intermediate (2). This intermediate is isoelectronic with “ $d_1^{3+}\text{-NO}$ ”, although complexes of Fe(III) are generally more accurately represented with electron transfer from the NO ligand to the Fe(III) ion having occurred. However, heme d_1 may be an exception to this – the nitrite is reduced to nitric oxide, with two protons being provided by the adjacent His³⁴⁵ and His³⁸⁸ residues (both conserved) to form water (1).

In the Fülöp mechanism, rebinding of Tyr²⁵ to the ferric heme d_1 causes dissociation of the nitric oxide product and prevents further substrate binding prior to re-reduction of the d_1 -heme to the ferrous state. The cycle is then repeated and catalytic turnover continues. Electrons required for substrate reduction are provided by the physiological donor proteins pseudoazurin and cytochrome c_{550} (3), which bind to the c domain of the cytochromes cd_1 . The c -heme acts as a site for electron transfer to the d_1 active site.

Previous electrochemical studies (4-7) have shown that the electron transfer rate between the c and d_1 centres within each monomer is slower than would be expected given the shortest heme edge-to-edge distance of 11.0 Å (8). According to Marcus theory (9) the rate of electron transfer between two chemical species is governed by three main factors; the electronic coupling between the initial and final states, the difference in Gibbs free energy for the reaction and the magnitude of the reorganisation energy. The third parameter refers to the energy required for all the necessary structural adjustments taking place over the course of the reaction. Fülöp *et al* (1) argued that the conformational changes occurring at the d_1 heme add to the reorganisation energy of the complex and thus decrease the rate of electron transfer.

4.1.2. Spectroscopic characterisation of the reaction intermediates

This suggested mechanism was, in effect tested by George *et al* (10) using stopped-flow infrared and UV-visible spectroscopies to investigate the kinetics of the reduction of nitrite by the *P. pantotrophus* enzyme. The purpose of this investigation was to characterise the intermediates that form over the course of the reaction. These are summarised in *Figure 4.1.2*. Samples of enzyme purified according to Moir *et al* (11) were reduced anaerobically, with one equivalent of either sodium dithionite or electrochemically-reduced methyl viologen. By ensuring that reduction was complete with no excess of electrons remaining in the sample, the enzyme was prevented from undergoing steady state turnover. This meant that any NO-bound intermediate structure(s) would be trapped.

The spectrum was recorded immediately after mixing with an equal volume of $\text{Na}^{14}\text{NO}_2$ (in 50 mM phosphate D_2O buffer, pH* 7¹²) in the stopped-flow infrared (SF-IR) apparatus. This process was repeated with a solution of isotopically-substituted substrate, $\text{Na}^{15}\text{NO}_2$, with the aim of observing a shift in the frequency of the Fe-NO stretch. This band blue shifted from 1913 cm^{-1} to 1876 cm^{-1} when $\text{Na}^{14}\text{NO}_2$ was replaced with $\text{Na}^{15}\text{NO}_2$, indicating that the intermediate formed on substrate addition was a heme-(Fe^{2+} -NO⁺) species. (Intermediate 'C' in *Figure 4.1.2*) Measurement of the formation of the 1913 cm^{-1} ^{14}NO -Fe peak as a function of time showed that the intensity of the band increased rapidly over 0.1 seconds with a rate constant of 38 s^{-1} .

¹² The '*' indicates the use of deuterated buffer.

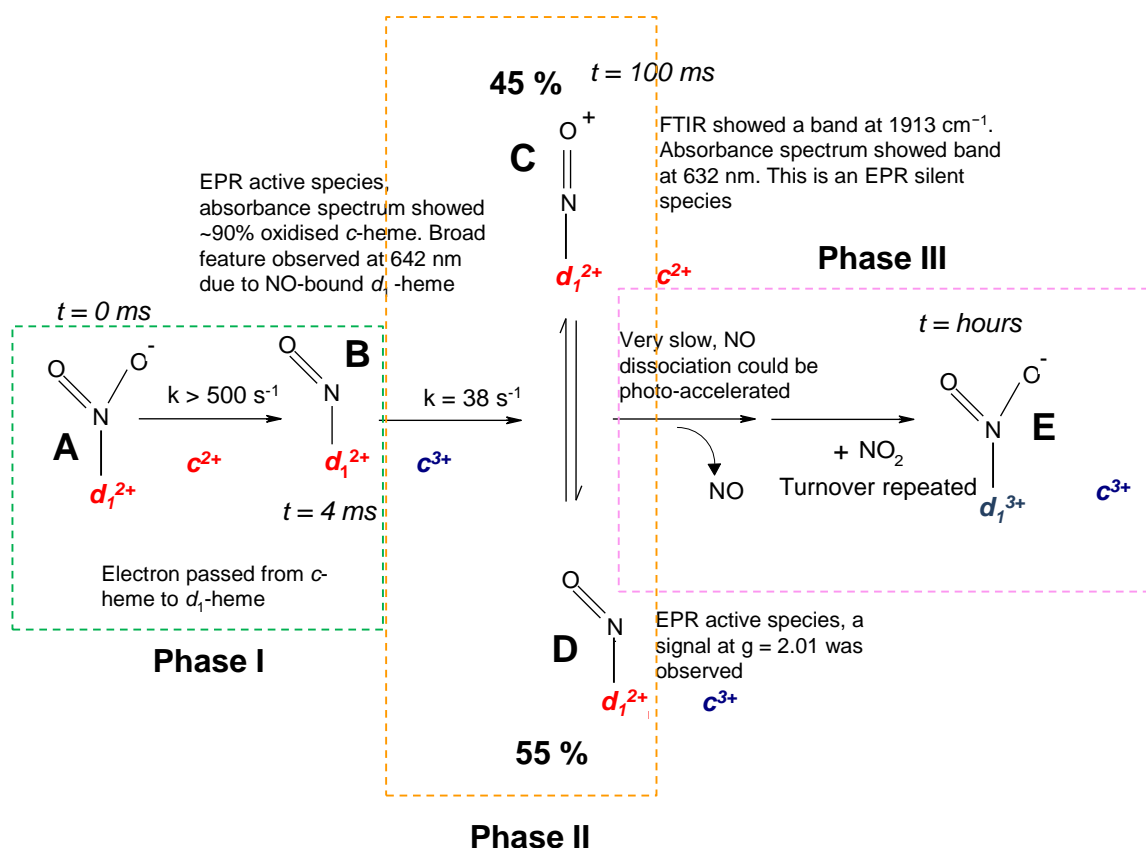


Figure 4.1.2: Schematic representation of the reaction mechanism suggested by George *et al* (10) for the reduction of NO_2^- by reduced *P. pantotrophus* cytochrome cd_1 . Phase I ($t = 4 \text{ ms}$) involved the formation of a $d_1^{2+}\text{-NO}$, c^{3+} intermediate [B], which gave rise to a band at 642 nm in the UV-visible absorption spectrum. By 100 ms an equilibrium was established between a $d_1^{2+}\text{-NO}$, c^{2+} intermediate species (C; showed a FTIR band at 1913 cm^{-1} , an absorption band at 632 nm and was EPR silent) and a $d_1^{2+}\text{-NO}$, c^{3+} species (D; EPR active). The final phase (Phase III) appeared to be photocatalytic and reached completion over hours in the dark. All experiments were carried out at pH 7.00 ($\text{pH}^* 7.00$ in the FTIR measurements) in 50 mM potassium phosphate buffer.

Stopped-flow UV-visible measurements showed three phases of reaction; Phase I occurred $\sim 4 \text{ ms}$ after substrate addition and showed the c -heme to be $\sim 87 \%$ oxidised, while the d_1 -heme peak had broadened and blue-shifted from 652 nm to 642 nm . These spectral observations were assigned to the formation of a $d_1^{2+}\text{-NO}$, c^{3+} intermediate species ('B' in Figure 4.1.2).

Approximately 5 ms after mixing the enzyme with nitrite, Phase II showed re-reduction of the *c*-heme to the ferrous state and the formation of a stable intermediate. By 100 ms, the *c*-heme content of this stable intermediate was estimated to be ~ 45 % ferrous, and a prominent d_1 band at 632 nm was present in the spectrum ('C' in *Figure 4.1.2*). It was suggested that at this point in the reaction an equilibrium existed between d_1^{2+} -NO, c^{3+} ('D' in *Figure 4.1.2*) and d_1^{2+} -NO⁺, c^{2+} intermediate species, with the latter giving rise the 632 nm absorbance band.

Phase III was slow and appeared to be photo-catalytic; taking many hours to reach completion in the dark but only minutes under high-intensity light. The absorption spectrum showed loss of the 632 nm band (and appearance of a band at ~ 643 nm) and complete oxidation of the *c*-heme, although the final product ('E' in *Figure 4.1.2*) did not show the high-spin d_1 band at 702 nm observed in the as-prepared spectrum (12). This led to the conclusion that the final product was a ferric nitrite-bound species, and hence all of the d_1 -heme was in the low-spin state. The position of the Soret band was similar to that observed in His/Met coordinated *c*-heme, although this observation could not be used for unambiguous ligand identification. When stoichiometric ratios of d_1 -heme to nitrite close to unity were used, the reaction did not show this third phase, strongly suggesting that it arises from the enzymatic turnover of the substrate.

The X-band EPR spectrum freeze-quenched at 5 ms after mixing with nitrite showed a sharp band at $g = 2.01$, assigned to the paramagnetic d_1^{2+} -NO complex. Other features at $g = 2.93$ and $g = 2.32$ were assigned to His/Met coordinated *c*-heme on the basis of previous observations (13). A plot of the EPR intensity versus time showed that the signal at $g = 2.01$ decayed concomitantly with the growth of the 632 nm band indicating the formation of the EPR-silent d_1^{2+} -NO⁺, c^{2+} species.

Although the mechanism illustrated in *Figure 4.1.2* would initially (within the first 4 ms) involve the binding of nitrite to ferrous heme, it is clearly more complex than that previously suggested by Fülop *et al* (1). An EPR spectrum of the suggested d_1^{3+} -NO₂, c^{3+} end product was not reported as additional evidence in support of its formation.

George *et al* agreed with the suggestion that the reduction of the nitrite molecule is facilitated by the donation of two protons from the nearby conserved His³⁴⁵ and His³⁸⁸ residues. Steric hindrance caused by these residues (along with the Tyr²⁵) was cited as a possible contributing factor in determining whether the linear d_1^{2+} -NO⁺ conformation is adopted, or whether the *c*-heme reduces the d_1 centre and the bent d_1^{2+} -NO intermediate is formed. If true, the relative proportions of these intermediates would be likely to be pH-dependent, although this was not investigated in this work.

It was noted that the turnover rate ($k_{\text{cat}} = 8 \text{ s}^{-1}$) of the enzyme at pH 7.00 was slow, while the intermediate d_1^{2+} -NO was formed rapidly (at a rate of at least 500 s^{-1}), indicating that formation of this species is not rate determining. The suggestion that the final product is a ferric nitrite-bound species was not supported by spectroscopic evidence, and raises the question of whether this would actually be the case *in vivo*. There was no evidence to suggest the Tyr²⁵ re-binds at any point, although it is assumed that nitric oxide is released via photo-dissociation before another turnover cycle commences. The actual mechanism of NO release for the *P. pantotrophus* enzyme remains unclear, although it was suggested by George *et al* to be facilitated by the re-reduction of the enzyme by an external electron donor. This hypothesis is supported by recent work by Sam *et al* (14) that showed pseudoazurin to promote dissociation of the NO product when the d_1^{2+} -NO, c^{3+} and d_1^{2+} -NO⁺, c^{2+} intermediates are in equilibrium. This is contrary to previous a previous report (7) which stated that ferrous-NO is a ‘dead end’ complex from which product dissociation does not occur.

Finally, the question is raised as to whether the d_1^{2+} -NO, c^{3+} and d_1^{2+} -NO⁺, c^{2+} intermediates are in simple equilibrium, or whether there is a conformational interaction across the dimer that leads to the co-existence of both states. It was suggested (10) that this three-electron reduced dimer containing both d_1^{2+} -NO, c^{3+} and d_1^{2+} -NO⁺, c^{2+} is the active, ‘NO-releasing’ state of the enzyme. To date, there have been no systematic investigations into the factors influencing the relative proportions of the two intermediates.

The X-band EPR features at $g = 2.93$ and $g = 2.32$ were assigned to His/Met coordinated *c*-heme. That same year, Allen *et al* (13) showed that reduction of *P. pantotrophus* d_1 and the immediate re-oxidation (within 80 seconds) by hydroxylamine hydrochloride gave an EPR spectrum with g values at 2.94, 2.33 and 1.40. Again these were assigned to His/Met coordinated *c*-heme. The ligation to the *c*-type heme following reduction by dithionite and the re-oxidation by hydroxylamine has been investigated and discussed in more detail in Chapter 3.

4.2 Binding nitrite to ferric d_1 -heme

4.2.1. *Binding of nitrite to ferric, hydroxylamine re-oxidised d_1 -heme*

In 2002, Allen *et al* carried out further investigations by X-band EPR and UV-visible absorption spectroscopy with the aim of determining whether nitrite would bind to *P. pantotrophus* d_1 -heme in the ferric state. Following on from the experiments by George *et al* (10) and Fülöp *et al* (1), nitrite was added to the protein 10 seconds after cycling between the fully-reduced and hydroxylamine re-oxidised states with the aim of generating an all-ferric nitrite-bound species with His/Met coordination at the *c*-type heme. The reaction mixture was equilibrated for 1–2 hours following the addition of nitrite, although it is not clear whether regular spectra were recorded during this time to monitor the

reaction progress. Initial absorption spectra were recorded approximately two hours after the addition of nitrite and showed prominent maxima at 410 and 643 nm, with the latter feature being assigned to nitrite-bound ferric d_1 -heme (15).

It was concluded that the position of the Soret band at 410 nm is diagnostic of His/Met coordinated ferric c -heme. This assumption was based on previous work (13,16) and suggests that the binding of nitrite ‘locked’ the c -heme in the His/Met conformation. However, it can be argued that absorption spectroscopy is an even less reliable method of assigning heme ligand identity than CW-EPR, particularly when not supported by NIR-MCD. Therefore, the possibility that the c -heme in this species is not exclusively in the His/Met ligated state cannot be ignored. As discussed in Chapter 3, a later freeze-quench NIR-MCD experiment (17) showed that within one minute following hydroxylamine addition, ca. 25 % of the enzyme was *bis*-histidinyl coordinated. This is despite the fact that the EPR spectrum measured at this point (13) showed a rhombic trio ($g_z = 2.94$, $g_y = 2.33$, $g_x = 1.40$) that was previously assigned to a purely His/Met-ligated c -heme.

Features in the absorption spectrum compared well to those observed by George *et al* (10) for the final ‘Phase III’ product, assumed to be d_1^{3+} -NO₂⁻. After a further 2 hours there were no further changes in the appearance of the absorption spectrum, indicating that a stable product had formed.

The X-band EPR spectra, measured approximately one hour after nitrite addition again showed c -heme features at $g = 2.94$, 2.32 and 1.39 as observed by George *et al*. Once again, this was assigned to His/Met coordinated c -heme. Whilst this study does not definitively show the c -heme ligation to be exclusively His/Met, a subsequent NIR-MCD experiment by Van Wonderen *et al* (18) showed this assignment to be correct.

Minor features were also observed in the EPR spectrum at $g = 2.51$, 2.20 and 1.87, which were attributed to a fraction of d_1 -heme that had returned to the ‘as isolated’,

Tyr²⁵-bound state. No other features were assigned to this centre. These results showed that a sizable portion of this cofactor in the sample was EPR silent and that the simple d_1^{3+} -NO₂⁻ product cannot have been formed, as this complex would be paramagnetic and therefore EPR-active. The EPR silent fraction of the d_1 -heme is unlikely to be in the ferrous oxidation state as stopped-flow experiments (13) showed the re-oxidation of the enzyme by hydroxylamine to be rapid and complete in ~ 30 ms. The formation of the EPR-silent d_1^{3+} -NO (d_1^{2+} -NO⁺) species by auto-reduction was also mentioned as a possible explanation, although this is inconsistent with the absence of a band at 632 nm in the absorbance spectrum, as observed by George *et al* (10). Extensive signal broadening due to g-value heterogeneity was the final possible explanation, although the unusual ground state of ferric d_1 -heme is known to result in narrow features and low g-value anisotropy (12), so again this is unlikely. The possibility of the ferric d_1 metal centre coupling to a radical species (and hence creating an EPR-silent S = 1 species) was not discussed.

4.2.2. Reaction of nitrite with ferric d_1 -heme in the 'as prepared' enzyme

In 2007, Van Wonderen *et al* (18) were able to provide an explanation for the apparent EPR-silence of the alleged heme d_1^{3+} -NO₂⁻ species, as well as the answers to a number of other questions. If formation of the d_1^{3+} -NO₂⁻ product reported by Allen *et al* (15) occurred over a timescale of 1–2 hours then this occurred over a much longer period than the relatively rapid reversion time (circa. 20 minutes). Hence, product formation cannot be the determining factor in preventing reversion back to the 'as isolated' state.

In order to determine whether the final product of the reaction of NO₂⁻ with hydroxylamine re-oxidised protein is in fact d_1^{3+} -NO₂⁻, Van Wonderen *et al* carried out NIR, UV-visible and ratio-data MCD (along with absorbance and X-band EPR) measurements. The product of the reaction of nitrite with cd_1 was known as ' cd_1 *-X' as the

authors were not confident that it was a simple nitrite-bound ferric complex. Samples of *P. pantotrophus cd₁* (and *P. stutzeri cd₁* for comparison) were fully-reduced, re-oxidised with hydroxylamine and reacted with nitrite according to the method employed by Allen *et al* (15).

However, the important observation was that during control experiments, nitrite was shown to react with the *d₁*-heme of the ‘as isolated’ (oxidised) enzyme, under aerobic and anaerobic conditions, to yield a product with the same properties as the so-called *d₁³⁺-NO₂⁻* species. At pH 7.00 this reaction took several hours to reach completion but at pH 6.50 the reaction was found to reach completion within 5-10 minutes. At pH 9.00 there was negligible product formation. Thus, nitrite will react with ferric *d₁*-heme but the rate is strongly pH dependent. Nitrite reductase activity assays confirmed that *cd₁*-X* prepared by this method was catalytically active. These results questioned whether reduction of the enzyme is strictly necessary for activation. All further discussion regarding this publication refers to results obtained by reacting nitrite (5 mM) with the ‘as prepared’ (or oxidised) enzyme.

The absorbance spectra obtained for *P. pantotrophus cd₁*-X* (produced by reacting ‘as prepared’ enzyme with nitrite in pH* 6.50 bis-tris propane [BTP], D₂O) showed an intense feature at 631 nm. This was comparable with that observed at 632 nm by George *et al* (10), previously assigned to the nitrosyl *d₁²⁺-NO⁺* (in equilibrium with *d₁²⁺-NO*) species, and also coincided with the loss of the high-spin ferric *d₁* 702 nm band

Treatment of the *P. stutzeri* enzyme with nitrite also caused changes in the absorbance spectrum, with the *d₁*-heme band exhibiting a small blue shift from 643 to 640 nm. The authors acknowledged that as the oxidised *P. stutzeri cd₁* contains *d₁*-heme exclusively in the low-spin state, any shift in this band upon reaction with nitrite would be less substantial than that observed for the *P. pantotrophus* enzyme.

The EPR spectrum for nitrite-reacted *P. pantotrophus* cd_1 (using the same buffer conditions mentioned above) showed features that were comparable to those observed by Allen *et al* (15). Specifically, the spectrum was dominated by a rhombic trio, with g values of 2.93, 2.32 and 1.42. Previously assigned to His/Met ligation at the *c*-heme, this rhombic trio was markedly different from the ‘Large g_{\max} ’ type spectrum observed for the *bis*-histinyl state in the ‘as prepared’ enzyme. For the *P. stutzeri* enzyme there was no observable alteration in the g-values assigned to the *c*-heme ($g = 2.99, 2.29$ and 1.61) upon addition of nitrite. This is unsurprising, as this form of the enzyme is known to retain its original His/Met ligation upon reaction with substrate (19).

For both the *P. pantotrophus* and *P. stutzeri* forms of the enzyme, the cd_1^* -X X-band EPR spectra reported by Van Wonderen *et al* (18) showed an absence of d_1 signals, as observed by Allen *et al* (15). Double-integration of the cd_1^* -X *c*-heme spectra (for both *P. pantotrophus* and *P. stutzeri*) and comparison to a Cu(II)-EDTA¹³ standard (20) confirmed the observed signals to be indeed due to one low-spin ferric centre. This ruled out the possibility that the rhombic signals previously assigned to the His/Met coordinated *c*-heme (15) could be due to the d_1 cofactor.

As discussed in Chapter 3, the ‘Large g_{\max} ’ signal of the ‘as prepared’ *P. pantotrophus* EPR spectrum displays some heterogeneity. This has been observed during the work carried out for this thesis and was also acknowledged by Van Wonderen *et al*, who also made a similar observation for the ‘as prepared’ *P. stutzeri* spectrum. Interestingly, the simulations of samples of cd_1^* -X for both species did not reveal any heterogeneities in the *c*-heme signals, indicating that the assumed His/Met ligation in this species adopted a single orientation.

¹³ Ethylenediaminetetraacetic acid

NIR-MCD spectra of *P. pantotrophus* and *P. stutzeri* cd_1^* -X showed that the *P. pantotrophus* complex displayed a red shift in the CT band from 1550 nm to 1795 nm, indicating a change in ligation from His/His to His/Met at the *c*-heme. Unsurprisingly, the CT band for the *P. stutzeri* enzyme did not exhibit a similar wavelength shift, indicating that the His/Met ligation at the *c*-heme was retained.

Following this, Van Wonderen *et al* investigated the electronic and magnetic properties of the d_1 metal centre in cd_1^* -X with the aim of providing an explanation for the apparent EPR-silence of this heme. MCD spectroscopic measurements made in the visible region exhibited bands solely due to low-spin ferric *c*-heme between 520 nm and 590 nm and at 557 nm. Between 450 nm and 520 nm, bands from both hemes could be detected and features in the 590–700 nm region could be attributed solely to the d_1 centre (12,21-23). All bands were found to be strongly temperature dependant when measurements were made at 1.7, 4.2 and 10 K, indicating that they arose from paramagnetic centres. This ruled out the possibility that the d_1 -heme in cd_1^* -X was auto-reduced to the diamagnetic $S = 0$ spin state, as suggested by Allen *et al.*(15). Ratio-data MCD spectroscopy was then used to investigate whether the low-spin ferric d_1 centre is spin-coupled to another paramagnet in cd_1^* -X. This would provide an explanation for the d_1 -heme EPR silence, as interaction between the unpaired electron on the metal and another paramagnetic species would give rise to an integer spin system with a large axial zero field splitting.

Ratio data spectroscopy (24) uses the temperature and magnetic field dependence of the MCD intensity to identify spectral transitions that occur due to paramagnetic species with a total spin of $S \neq \frac{1}{2}$. For the case of an $S = \frac{1}{2}$ species, C-term MCD intensity is proportional to H/T , where H is the magnetic field strength, and T is the temperature. The MCD spectrum is recorded at various temperatures, whilst keeping the H/T ratio is constant by adjusting the magnetic field accordingly. Any changes in the MCD intensity

will be due to paramagnetic centres with an S of $\neq \frac{1}{2}$. Van Wonderen *et al* observed changes in the MCD intensity at positions in the spectrum expected to arise from the d_1 -heme as the temperature was varied. However, at positions in the spectrum assigned to the c -heme, no ratio data was observed. This showed unambiguously that the c -heme remained a simple spin half system upon reaction with nitrite whilst the d_1 -heme must have been coupled to another paramagnetic resulting from the reaction.

Analysis of the data suggested a spin-coupling constant, J , of approximately $+3 \text{ cm}^{-1}$, which is more than sufficient to result in an EPR-silent d_1 -heme at X-band. A nearby residue, possibly Tyr²⁶³, was suggested as a possible source for this radical species. If a single turnover was to occur using an electron extracted from this residue, an $R^{\bullet} d_1^{3+}\text{-NO}$ species would be generated. Displacement of the nitric oxide by another substrate molecule (as suggested by George *et al* (10)) would yield a $R^{\bullet} d_1^{3+}\text{-NO}_2^-$ species, in which the two paramagnetic centres (R^{\bullet} and Fe(III)) could interact and hence render the heme EPR silent.

However, as the band in the absorbance spectrum at 631 nm suggests a ferric nitrosyl species, the authors suggest that the unusual $(d_{xz}, yz)^4 (d_{xy})^1$ ground state of the d_1 -heme destabilises the Fe-NO bond and impedes the transfer of electron density from the NO to the metal. This would lead to a $d_1^{3+}\text{-NO}^{\bullet}$ species in which the NO molecule itself is the radical species spin-coupled to the unpaired electron on the d_1 centre. The extra electron would have been scavenged from either the buffer, or a nearby residue. It was pointed out that as oxidised *P. pantotrophus* cd_1 is activated by substrate at a rate considerably lower than that of the enzymatic turnover, it is unlikely that this reaction step forms part of the catalytic cycle *in vivo*. However, if the existence of a novel $d_1^{3+}\text{-NO}^{\bullet}$ species is confirmed, it could be involved in catalysis, but formed by a different route. If

the interacting radical is NO, then this raises the question of whether or not a nearby amino-acid carries the radical that interacts with ferric heme d_1 .

4.3. The aims of this section of work

It would therefore appear that there are two ferrous nitric oxide-bound species formed in the reaction of the ferrous d_1 -heme with nitrite; the linear d_1^{2+} -NO⁺ and the bent d_1^{2+} -NO. The factors influencing the relative proportions of these species remain unexplored to date. If it is indeed the protonation of the His³⁴⁵ and His³⁸⁸ residues that determines the nature of the ferrous d_1 intermediate as suggested by George *et al* (10), then the relative proportions of the linear and bent forms would exhibit pH dependence.

How the relative proportions of the two intermediates could be connected to solution pH is illustrated in *Figure 4.3.1*. At a more alkaline pH (pH > pKa), one of the nearby histidine residues (henceforth known as the ‘principle’ histidine residue) is deprotonated, and the linear d_1^{2+} -NO⁺ intermediate is stabilised by donation of electron density from the lone pair of the nitrogen atom. At this point, the extra electron is located on the *c*-heme, which is therefore reduced to the ferrous state. As the pH is lowered, the His³⁴⁵ is protonated, making the bent d_1^{2+} -NO intermediate the preferred, more stable structure (with the possible formation of a hydrogen bond increasing the stability), and therefore causing the transfer of the electron from the *c*-heme to the NO adduct.

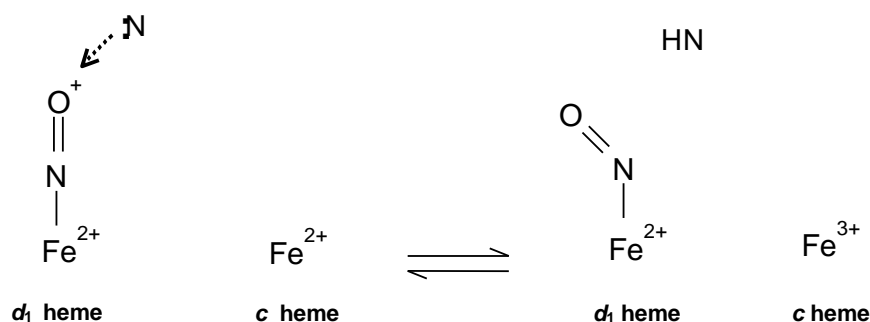


Figure 4.3.1: How the pH of the surrounding environment could indirectly influence identity of the NO-bound d_1 intermediate formed.

Initial measurements by absorbance spectroscopy showed the extent of reduction of the *c*-heme upon addition of nitrite to be pH dependant. However, a more reliable estimate of the pKa of the protonation event controlling this process can be obtained by UV-visible MCD spectroscopy. Ferrous *c*-type heme gives rise to a large derivative Q-band in the UV-visible MCD spectrum at approximately 550 nm (25). The origin of this band has been described in more detail in Chapter 1. The intensity of the Q-band following re-oxidation by stoichiometric nitrite relative to that of the fully-reduced sample provides an estimate of the amount of ferrous *c*-heme present in the sample. This will therefore indicate the relative proportions of the two intermediate species illustrated in *Figure 4.3.1*.

For example at a more acidic pH ($\text{pH} < \text{pKa}$), when the His³⁴⁵ residue is protonated, the d_1^{2+} -NO would be the preferred intermediate and the extra electron would therefore be located at the d_1 centre. As the *c*-heme would be in the ferric oxidation state, this would correspond to a loss in intensity of the 550 nm band.

By measuring the MCD spectra at a range of pH values, it was hoped that the results could be used to ascertain the equivalence point of the proposed equilibrium illustrated in *Figure 4.3.1*. Assuming this equilibrium holds true, the plot of percentage-reduced *c*-heme versus pH will resemble a standard titration curve and can therefore be fitted to the Henderson-Hasselbalch equation to obtain a value for the pKa.

4.4 Experimental

4.4.1 *Investigating the proportions of the NO-bound ferrous d_1 intermediates by absorbance spectroscopy*

‘Mixed’ buffer solutions¹⁴ (as defined in Chapter 3, Section 3.2.4) were prepared at the following pH values: 6.00, 7.50 and 8.50. Samples of *P. pantotrophus* cytochrome cd_1 were prepared and purified according to the method detailed by Moir *et al* (11) with a minor adjustments to the purification stage, as detailed in Chapter 2, Section 2.12.2. Buffer exchange into the relevant pH in each case was carried out using a Microcon centrifugal filter unit (500 μ L volume) with a YM10 membrane. Sample concentrations of *P. pantotrophus* cd_1 for absorbance measurements were between 10 and 23 μ M and were determined using a molar extinction coefficient of 141 $\text{mM}^{-1} \text{cm}^{-1}$ for the Soret-band (406 nm) intensity of the oxidised monomer (18). A sample volume of 1.5 mL was used for each measurement. Samples were fully-reduced in an anaerobic glove box (< 5 ppm O_2) by titrating in sodium dithionite gradually and monitoring the disappearance of the 702 nm high-spin d_1 band in the absorbance spectrum. Once full reduction had been achieved, sodium nitrite (NaNO_2) was added (from a 1.5 mM stock solution in ‘mixed’ buffer at the relevant pH) so that there were equimolar amounts of substrate and monomer present in the sample. After the solution was allowed to equilibrate for 20–30 minutes a full wavelength UV-visible absorbance spectrum was recorded between 250 and 800 nm. All absorbance spectra were recorded using a JASCO-4100 spectrometer as detailed in Chapter 3, Section 3.2.4.

¹⁴ The standard ‘mixed’ buffer solution used in this work was prepared to cover a wide pH range (3.6–9.0).

4.4.2. *An overview of UV-visible MCD experiment*

Although the $d_1^{2+}\text{-NO}^+/d_1^{2+}\text{-NO}$ equilibrium is established within 100 ms, the formation of the ferric nitrite-bound species (from reduced enzyme) was shown by George *et al* (10) to reach completion within hours. This would suggest that once established, the equilibrium between the two intermediates is stable for a relatively long period of time, reducing the need for rapid measurements. However, it is vital that the measurements are made in the absence of O_2 to prevent re-oxidation of the protein by molecular oxygen. For this reason, the novel cell holder described in Chapter 3, Section 3.2.2 was again employed. However, for reasons outlined in the following section, substrate addition was made via the injection lines for the first two samples only.

4.4.3 *Experimental details of UV-visible MCD measurements*

Buffer solutions each containing 12 mM sodium acetate, 12 mM MOPS, 12 mM MES and 12 mM TRIS were prepared at the following pH values: 6.00, 6.51, 6.90, 7.50, 8.00 and 8.50. *P. pantotrophus* cytochrome cd_1 prepared and purified as described in Chapter 2, Section 2.12 was buffer exchanged into the relevant pH using a Microcon centrifugal filter unit (500 μL volume) with a YM10 membrane. Initially, in the case of the pH 6.00 and 6.51 samples, the ‘as prepared’ protein solution concentrations were 30.4 and 21.1 μM respectively (concentrations were determined by absorbance spectroscopy using a molar extinction coefficient of $141\text{ mM}^{-1}\text{ cm}^{-1}$ for the Soret (406 nm) intensity of the oxidised monomer (18)), with a sample volume of 1.5 mL in each case. This required the use of a 1 cm pathlength quartz cell for the MCD measurements, which was fitted with a specially designed stirrer (as shown in Chapter 3, *Figure 3.2.2*) to ensure an even, rapid mixture of reactants.

In the case of the pH 6.00 and 6.51 samples, sodium dithionite was titrated *in situ* to fully-reduce the sample. After each addition of dithionite, the UV-visible MCD spectrum between 450 and 850 nm was recorded and the reduction monitored by observing the intensities of the 547 and 685 nm bands. A fully-reduced spectrum was also measured between 250 and 480 nm, using a bandwidth of 2 nm. Once reduction was complete, NaNO₂ was added stoichiometrically (again *in situ*) so that the molar ratio of nitrite to monomer was exactly equal. Immediately following substrate addition, further spectra were measured in the UV and visible regions, and the sample solution was allowed to equilibrate for a further 30 minutes before final measurements were taken.

The experimental process described above was repeated with the remaining four samples at pH 6.90, 7.50, 8.00 and 8.50, with one significant adjustment: These measurements were made using an ‘as prepared’ protein concentration of 160-235 μ M in each case and using a quartz cell with a 0.1 cm pathlength. The *in situ* injection of dithionite through anaerobic lines was found to not deliver the loaded aliquots reproducibly leading to incomplete reduction of the sample in some instances. Since stirring and collection of real time data was not critical for determining the pK_a, the compromised datasets were repeated using the shorter pathlength (0.1 cm) anaerobic cells, the sample being loaded into the cell and reduced in an anaerobic glove box with an atmosphere of < 5 ppm O₂. Once sufficient dithionite had been added to fully reduce the sample, as judged by the absence of the high-spin *d*₁-heme band at 685 nm the sample was reacted with stoichiometric nitrite, again in the anaerobic glove box. A full wavelength MCD spectrum of the endpoint was taken once no further change in the 550 nm intensity with time was apparent. The stoichiometric molar ratio of nitrite to protein monomer was maintained in each case.

4.4.4. Instrument details

The room temperature MCD apparatus (as described in Chapter 3, Section 3.2.4) comprised a JASCO circular dichrograph with a UV-visible spectrometer (JASCO J-810). The progress of the *ex situ* dithionite reduction of the pH 6.90, 7.50, 8.00 and 8.50 samples was monitored by UV-visible absorbance spectroscopy using a JASCO-V550 spectrometer.

4.5 Results

4.5.1 Nitrite addition monitored by absorbance spectroscopy

The *P. pantotrophus* sample re-oxidised by nitrite at pH 6.00

The absorbance spectrum of the sample of *P. pantotrophus* *cd*₁ re-oxidised by nitrite at pH 6.00 is shown in *Figure 4.5.1*. Summaries of the spectral features observed in the nitrite-reacted, fully-reduced and ‘as-prepared’ samples are presented in *Tables 4.5.1–4.5.3*.

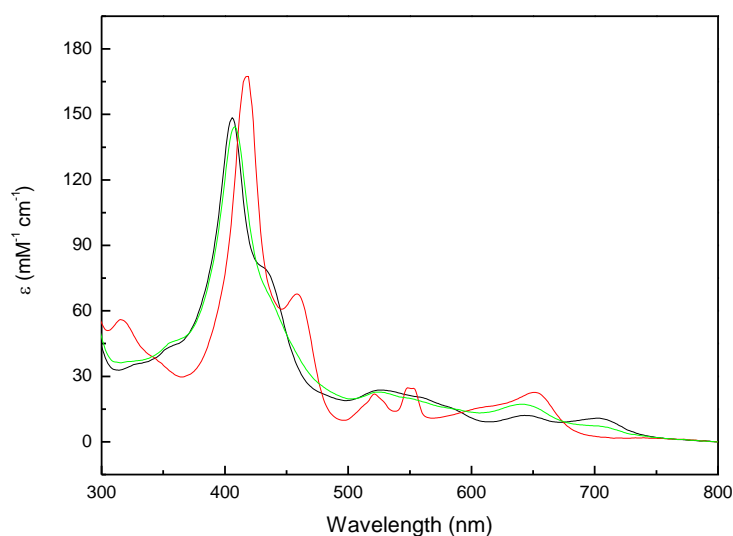


Figure 4.5.1: Room-temperature UV-visible absorbance spectra of *cd*₁ from *P. pantotrophus*. — As prepared, 19.0 μM , — sodium dithionite-reduced, — after the addition of 19.0 μL NaNO_2 (0.019 mM), allowing 20–30 minutes equilibration time. Samples were in 48 mM ‘mixed’ buffer (see Chapter 3, Section 3.2.4 for details), pH 6.00.

According to the scheme proposed in *Figure 4.3.1*, if the solution pH is less than the pKa of the principle histidine residue, a greater proportion of the enzyme will exist as the d_1^{2+} -NO c^{3+} species upon reaction with substrate as the principle histidine side chain will be protonated. In this instance the electron will be predominately located on the d_1 -heme, and the c -heme will be in the ferric state. The imidazole side-chain of free histidine has a pKa value of approximately 6.00. In reality however, the effect of the protein environment can significantly alter this value. The absorbance spectrum of cd_1 re-oxidised with nitrite at pH 6.00, shown in *Figure 4.5.1*, contains features that are characteristic of low-spin ferric c -heme. The position of the Soret band at 408 nm is virtually identical to that in the ‘as prepared’ sample and the α/β region shows no sign of the reduced species. The low-spin d_1 band is centred at 642 nm, which is slightly blue-shifted compared with that in the ‘as-prepared’ enzyme, where it is typically observed as a symmetric band centred at 645 nm. The amount of high-spin d_1 -heme in the nitrite re-oxidised pH 6.00 sample is ~ 58 % that observed in the ‘as-prepared’ sample.

The *P. pantotrophus* sample re-oxidised by nitrite at pH 7.50

The absorbance spectrum of the protein re-oxidised by nitrite (in addition to the ‘as prepared’ and fully-reduced samples) at a solution pH of 7.50 is shown in *Figure 4.5.2*. At pH 7.50, the Soret band of the c -heme is centred at 413 nm in the nitrite re-oxidised sample, a red shift of 7 nm compared to the spectrum observed for the ‘as-prepared’ enzyme. After re-oxidation by the substrate, the α/β region continues to display characteristics of ferrous low-spin c -type heme (in cytochrome cd_1), indicating that the electron is mainly localised at this centre. The spectrum of the nitrite re-oxidised sample at pH 7.50 displays a d_1 low-spin band centred at 642 nm. The position of this band is

slightly blue shifted (1-3 nm) compared with the ‘as prepared’ samples at this pH (see *Tables 4.5.1* and *4.5.3*).

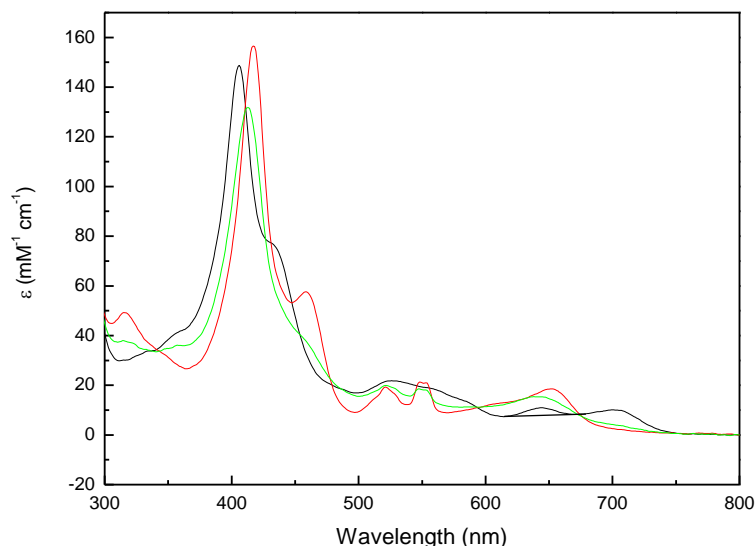


Figure 4.5.2: Room-temperature UV-visible absorbance spectra of cd_1 from *P. pantotrophus*. — As prepared, 10.3 μM , — sodium dithionite-reduced, — after the addition of 10.3 μL NaNO_2 (0.010 mM), allowing 20–30 minutes equilibration time. Samples were in 48 mM mixed buffer (see Chapter 3, Section 3.2.4 for details), pH 7.50.

Thomson *et al* (26) observed that extracted alkaline ferric d_1 -heme from *P. aeruginosa* will bind nitric oxide, undergoing auto-reduction and exhibiting a band at ~ 642 nm in the electronic absorbance spectrum. There is a negligible amount of high-spin d_1 -heme in the nitrite re-oxidised spectrum shown in *Figure 4.5.2*; with this band (centred at 706 nm) displaying an ϵ of $1.6 \text{ mM}^{-1} \text{ cm}^{-1}$. In the ‘as prepared’ sample at this pH, this feature has an ϵ of $\sim 10.0 \text{ mM}^{-1} \text{ cm}^{-1}$.

The *P. pantotrophus* sample re-oxidised by nitrite at pH 8.50

The absorbance spectra of the ‘as-prepared’, ‘fully-reduced’ and ‘nitrite re-oxidised’ samples at pH 8.50 are shown in *Figure 4.5.3*. At this pH the peak of the Soret band of the c -heme is red shifted further to 415 nm in the nitrite re-oxidised spectrum, almost identical to that of the fully-reduced enzyme.

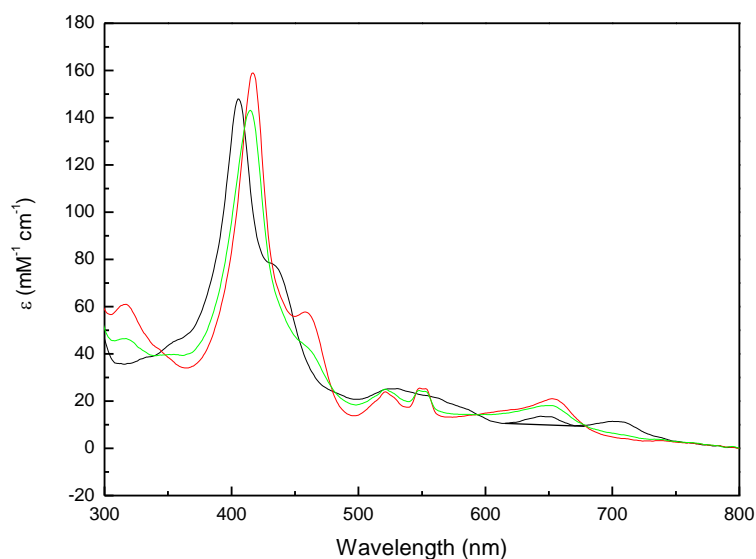


Figure 4.5.3: Room-temperature UV-visible absorbance spectra of cd_1 from *P. pantotrophus*. — As prepared, 10.7 μM , — sodium dithionite-reduced, — after the addition of 10.7 μL NaNO_2 (0.011 mM), allowing 20–30 minutes equilibration time. Samples were in 48 mM mixed buffer (see Chapter 3, Section 3.2.4 for details), pH 8.50.

Again, the α/β region shows the characteristics of low-spin ferrous c -heme (in cytochrome cd_1). At pH 8.50 the d_1 band in the nitrite-re-oxidised spectrum is centred at 650 nm and again a negligible amount of high-spin is present ($\epsilon = 1.4 \text{ mM}^{-1} \text{ cm}^{-1}$). Therefore the extra electron in the ‘mixed valence’ form of cd_1 obtained on one-electron oxidation with nitrite switches from residing mainly at d_1 -heme to mainly at c -heme on raising the solution pH from 6.50 to 8.50.

| Sample (pH) | λ Soret band (nm) | λ low-spin d_1 band (nm) | High-spin d_1 band present? | α/β shows features of ferrous c-heme? |
|-------------|---------------------------|--|--|--|
| 6.00 | 406 | 645 ($\epsilon = 3 \text{ mM}^{-1} \text{ cm}^{-1}$) | Y ($\epsilon = 8.5 \text{ mM}^{-1} \text{ cm}^{-1}$) | N |
| 7.50 | 406 | 643 ($\epsilon = 3.2 \text{ mM}^{-1} \text{ cm}^{-1}$) | Y ($\epsilon = 7.7 \text{ mM}^{-1} \text{ cm}^{-1}$) | N |
| 8.50 | 406 | 647 ($\epsilon = 3.5 \text{ mM}^{-1} \text{ cm}^{-1}$) | Y ($\epsilon = 7.1 \text{ mM}^{-1} \text{ cm}^{-1}$) | N |

Table 4.5.1: A summary of the main features in the absorbance spectra of 'as-prepared' *P. pantotrophus* cd_1 at solution pH values 6.00, 7.50 and 8.50.

| Sample (pH) | λ Soret band (nm) | λ low-spin d_1 band (nm) | High-spin d_1 band present? | α/β shows features of ferrous c-heme? |
|-------------|---------------------------|------------------------------------|-------------------------------|--|
| 6.00 | 418 | 609, 651 | N | Y |
| 7.50 | 417 | 609, 651 | N | Y |
| 8.50 | 417 | 615, 653 | N | Y |

Table 4.5.2: A summary of the main features in the absorbance spectra of dithionite-reduced *P. pantotrophus* cd_1 at solution pH values 6.00, 7.50 and 8.50.

| Sample (pH) | λ Soret band (nm) | λ low-spin d_1 band (nm) | High-spin d_1 band present? | α/β shows features of ferrous c-heme? |
|-------------|---------------------------|--|--|--|
| 6.00 | 408 | 642 ($\epsilon = 6.4 \text{ mM}^{-1} \text{ cm}^{-1}$) | Y ($\epsilon = 4.9 \text{ mM}^{-1} \text{ cm}^{-1}$) | N |
| 7.50 | 413 | 642 ($\epsilon = 7.2 \text{ mM}^{-1} \text{ cm}^{-1}$) | Y ($\epsilon = 1.6 \text{ mM}^{-1} \text{ cm}^{-1}$) | Y |
| 8.50 | 415 | 650 ($\epsilon = 8.4 \text{ mM}^{-1} \text{ cm}^{-1}$) | Y ($\epsilon = 1.4 \text{ mM}^{-1} \text{ cm}^{-1}$) | Y |

Table 4.5.3: A summary of the main features in the absorbance spectra of nitrite re-oxidised *P. pantotrophus* cd_1 at solution pH values 6.00, 7.50 and 8.50.

4.5.2. Nitrite addition monitored by room temperature UV-visible MCD spectroscopy

The room temperature UV-visible MCD spectra recorded between 250 and 750 nm in the pH range 6.00–8.50 are shown in *Figures 4.5.4-4.5.9*. These spectra are compared in *Figure 4.5.10*. A summary of the typical bands observed in the UV-visible region of *P.*

pantotrophus cd₁ (both reduced and oxidised) is presented in *Table 4.5.4* (12,18,27).

Changes in the Soret and Q-bands are discussed under each spectrum, while observations relating to the *d₁* bands are discussed in Section 4.5.4.

The main spectral features are summarised in *Tables 4.5.5-4.5.10* (displayed underneath the respective spectra). A summary of how the percentage of ferrous *c*-heme (as judged by the intensity of the 547.5 nm band in the visible MCD spectrum) varies with pH is presented in *Table 4.5.11*. When plotted, the results presented in *Table 4.5.11* have the appearance of a typical pH curve (*Figure 4.5.11*) for the titration of a weak acid with a weak base (or vice versa) and can be fitted to the Henderson-Hasselbalch equation to obtain a value for the p*K_a*.

At pH 6.00, MCD spectra (between 250 and 800 nm) of the following samples are shown here to provide an overview of the experiment: ‘as prepared’ *P. pantotrophus cd₁*: the enzyme after full chemical reduction with sodium dithionite, immediately after the addition of NaNO₂ (one heme equivalent, known here as the ‘immediate NO₂⁻’ spectrum), and ~ 30 minutes after the addition of sodium dithionite (known here as the ‘final NO₂⁻’ spectrum).

At all solution pH values, in the region between 450 and 800 nm, spectra of the samples after full reduction, immediately after substrate addition and after the 30 minutes equilibration are shown. The former and the latter spectra were used to calculate the relative intensity of the Q-band.

Between pH 6.90 and 8.50, absorbance spectra were recorded prior to commencing the experiment to ascertain the concentration of the enzyme. As the enzyme was dithionite-reduced and substrate added *ex situ* (see Section 4.4.3), spectra of the ‘as prepared’ enzyme were not recorded for these pH values. Features in ‘as prepared’ *cd₁* spectrum would not be expected to vary within the pH range investigated here.

| Wavelength (nm) | Band assignment | Additional information |
|-----------------|---|--|
| 520-590 | Low-spin Fe^{3+} <i>c</i> -heme | Solely due heme of this type. Seen in as prepared |
| 590-700 | d_1 -heme transitions | Solely due heme of this type. Seen in spectrum of 'as prepared' enzyme |
| 450-520 | Low-spin ferric <i>c</i> and d_1 transitions overlap | |
| 405-406 | B (Soret), band, $\pi \rightarrow \pi^*$ transitions on the porphyrin ring of low-spin ferric <i>c</i> -heme dominate spectrum | |
| 415 | B (Soret), band, $\pi \rightarrow \pi^*$ transitions on the porphyrin ring of low-spin ferrous <i>c</i> -heme dominate spectrum | |
| ~546 | Q-band, $\pi \rightarrow \pi^*$ transitions on the porphyrin ring of low-spin ferrous <i>c</i> -heme | Observed as a derivative-shaped band |
| ~ 550 | Q-band, $\pi \rightarrow \pi^*$ transitions on the porphyrin ring of low-spin ferrous <i>c</i> -heme | Observed as an absorption-shaped band |
| ~ 633 | Low spin Fe^{3+} d_1 band | Strong opposite sign A-term contributions begin to dominate above 10 K |
| ~ 685 | High spin Fe^{3+} d_1 band | Strong opposite sign A-term contributions dominate at room temperature |
| ~ 695 nm | CT-band due to His/Met coordinated ferrous <i>c</i> -heme | |

Table 4.5.4: A summary of the typical bands observed in the UV-visible room temperature MCD spectrum of *P. pantotrophus cd₁*.

The *P. pantotrophus cd₁* sample re-oxidised by nitrite at pH 6.00: Soret and Q-band observations

The features between 300 and 580 nm observed in the 'as-prepared' *P. pantotrophus cd₁* spectrum at pH 6.00 (displayed in *Figures 4.5.4*) are typical of low-spin ferric *c*-heme (25) A prominent derivative-shaped Soret band is centred at 405 nm with a peak to trough intensity of $\sim 141.4 \text{ M}^{-1} \text{ cm}^{-1} \text{ T}^{-1}$, in good agreement with previous observations (12).

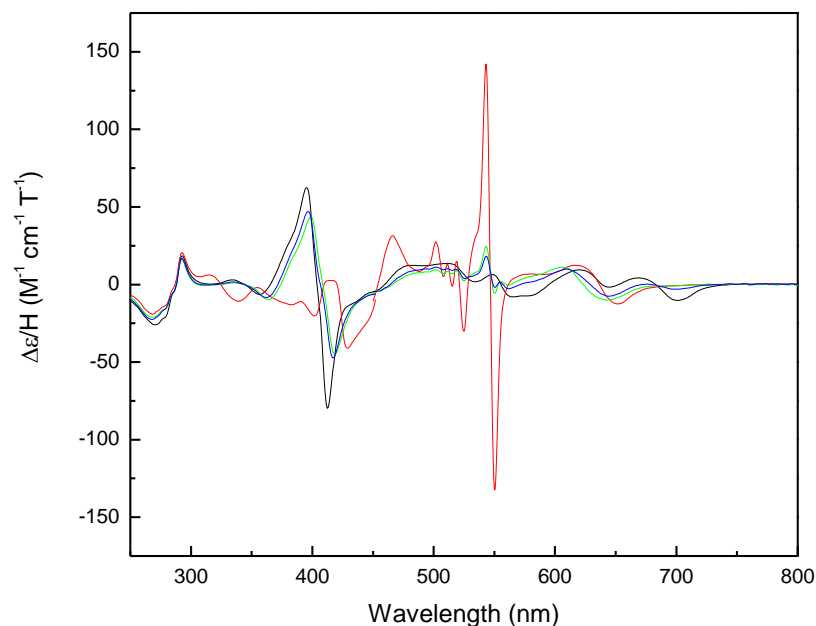


Figure 4.5.4: Room-temperature UV-visible MCD spectra between 250 and 800 nm of cd_1 from *P. pantotrophus*. — As prepared, 30.4 μM , — sodium dithionite-reduced, — after the addition of 30.4 μL NaNO_2 (0.03mM), — 30 minutes after the addition of NaNO_2 . Samples were in 48 mM ‘mixed’ buffer (see Chapter 3, Section 3.2.4 for details), pH 6.00. Spectra were recorded at a magnetic field of 8 T.

Typically, a single low-spin ferric protoheme will display a peak-to-trough intensity for the Soret band of around $160 \text{ M}^{-1} \text{ cm}^{-1} \text{ T}^{-1}$, although the exact value will be dependent upon the specific heme environment for the individual protein (25). As discussed in Chapter 1, the Soret and Q-bands observed in the UV-visible MCD spectra of protohemes are due to $\pi \rightarrow \pi^*$ transitions on the porphyrin ring. The latter feature occurs in the ‘as prepared’ sample spectrum as an absorption-type band at approximately 550 nm. Upon reduction of the *c*-heme to the low-spin ferrous state at pH 6.00, the Soret band undergoes a red shift to 424 nm and decreases in intensity. The Q-band observed at ~ 547 nm for the low-spin ferrous *c*-heme increases in intensity and adopts a derivative shape.

Immediately after the addition of nitrite, the Soret band blue shifts again to 409 nm and adopts a similar shape to that observed in the ‘as isolated’ spectrum. After 30 minutes equilibration, the band blue shifts further to 407 nm, with a peak-to-trough (known as

PTT hereafter) intensity of $\sim 93 \text{ M}^{-1} \text{ cm}^{-1} \text{ T}^{-1}$. The centre of this derivative feature is positioned at a wavelength 2 nm greater than that of the Soret band in the ‘as prepared’ spectrum, with the PTT intensity of this feature being approximately 65 % of that of the unreacted enzyme.

At pH 6.00, according to the equilibrium illustrated in *Figure 4.3.1*, the majority of the *c*-heme would be oxidised to the ferric state after the addition of nitrite. This is evident from the reduction of the PTT intensity of the Q-band immediately after nitrite addition. After 30 minutes equilibration only a minor amount of the *c*-heme in the sample remains in the ferrous state, $\sim 7 \%$ of that in the fully-reduced enzyme (as judged by the relative height of the Q-band), indicating that the unpaired electron is mainly located on the *d*₁-heme. As the Tyr²⁵ would be blocked from re-coordinating to the *d*₁-heme by the bound NO, it can be assumed that ligand reversion at the *c*-heme to the ‘as prepared’ conformation has not occurred. Consequently, the position and intensity of the Soret band of the pH 6.00 final NO₂⁻ re-oxidised sample after 30 minutes equilibration is similar, but not identical to that in the ‘as prepared’ spectrum.

| Sample | Spectral feature | Band wavelength (nm) | Peak to trough intensity or peak height ($\text{M}^{-1} \text{cm}^{-1} \text{T}^{-1}$) |
|---|----------------------|--|--|
| pH 6.00, as prepared | Soret band | 405 | (+ 62.37, - 79.06) 141.43 |
| “ | Q band | 550 | 9.75 |
| “ | d_1 low-spin band | 633 | (+ 9.10, - 1.71) 10.81 |
| “ | d_1 high-spin band | 685 | (+ 4.34, - 10.29) 14.63 |
| pH 6.00, dithionite reduced | Soret band | 424 | (+ 2.76, - 40.66) 43.42 |
| “ | Q band | 547 (isosbestic point with NO_2^- spectra) | (+ 141.98, - 132.78) 274.76 |
| “ | d_1 low-spin band | 636 | (+ 12.40, - 12.71) 25.11 |
| “ | d_1 high-spin band | <i>Absent</i> | <i>Absent</i> |
| pH 6.00, initial NO_2^- addition | Soret band | 409 | (+ 43.98, - 43.96) 87.94 |
| “ | Q band | 547 | (+ 25.02, - 5.30) 30.32 |
| “ | d_1 low-spin band | 624 | (+ 11.10, - 9.96) 21.06 |
| “ | d_1 high-spin band | <i>Absent</i> | <i>Absent</i> |
| pH 6.00, NO_2^- addition, 30 minutes | Soret band | 407 | (+ 46.37, - 46.59) 92.96 |
| “ | Q band | 547 | (+ 18.25, - 1.34) 19.59 |
| “ | d_1 low-spin band | 628 | (+ 10.03, - 7.58) 17.61 |
| “ | d_1 high-spin band | 685 | (+ 0.13, - 2.97) 3.10 |

Table 4.5.5: UV-visible MCD bands observed during the reaction of dithionite-reduced *P. pantotrophus* cd_1 with one molar equivalent (per monomer) of nitrite at pH 6.00.

The *P. pantotrophus* cd_1 samples re-oxidised by nitrite at pH 6.51 and 6.90: Soret and Q-band observations

The as-prepared *P. pantotrophus* cd_1 sample at pH 6.51 gives rise to an MCD spectrum between 250 and 480 nm (*Figure 4.5.5*) that contains comparable features to those observed at pH 6.00. After reduction and addition of nitrite, the Soret band in the pH 6.51 spectrum undergoes a red shift and (unlike the pH 6.00 sample) displays a small derivative shoulder centred at ~ 420 nm. This Soret-shoulder viewed immediately after substrate addition represents the emergence of the $d_1^{2+}\text{-NO}^+ c^{2+}$ species. However, after 30 minutes equilibration, the shoulder disappears and the Soret band becomes comparable in appearance to that observed in the pH 6.00 spectrum. After 30

minutes equilibration, the Soret band is centred at 407 nm, a red shift of 2 nm compared to the ‘as prepared’ sample.

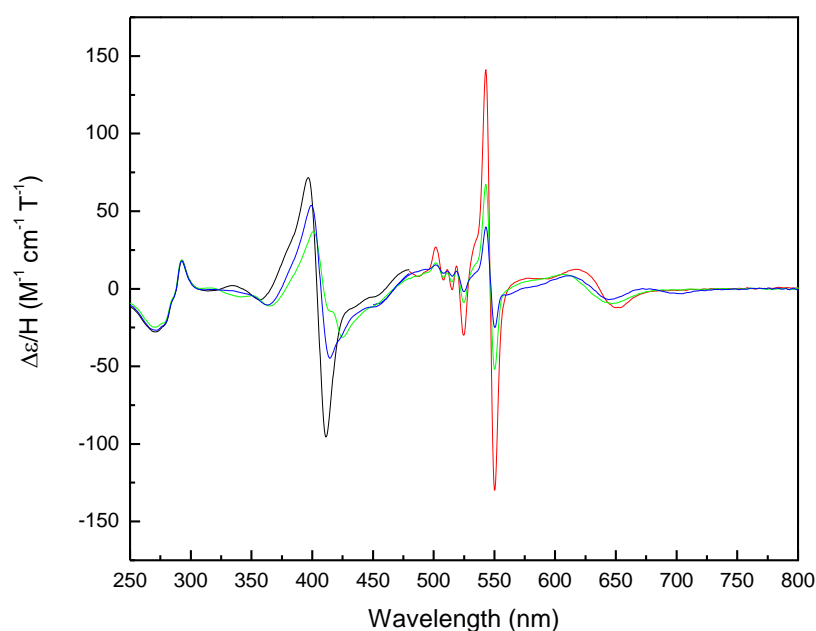


Figure 4.5.5: Room-temperature UV-visible MCD spectra of cd_1 from *P. pantotrophus*.— As prepared, 21.1 μM , — sodium dithionite-reduced, — after the addition of 21.1 μL NaNO_2 (0.02 mM), — 30 minutes after the addition of NaNO_2 . Samples were in 48 mM mixed buffer (see Chapter 3, Section 3.2.4 for details), pH 6.51. Spectra were recorded at a magnetic field of 8 T.

At pH 6.90 (*Figure 4.5.6*) when the relative proportion of $d_1^{2+}\text{-NO}^+ c^{2+}$ in the sample would be expected to increase (compared to pHs 6.00 and 6.51), the shoulder to the right of the Soret band is once again visible immediately after nitrite addition. Again this shoulder has a derivative profile, centred at 422 nm, and is still visible after 30 minutes equilibration, albeit at 418 nm. Importantly, at pH 6.90, the main Soret band immediately after nitrite addition and after 30 minutes equilibration is centred at 414 and 410 nm respectively. At both stages of the reaction, this feature has red-shifted in comparison to the pH 6.00 and 6.51 samples and is indicative of an increased proportion of reduced ferrous *c*-heme.

| Sample | Spectral feature | Band wavelength (nm) | Peak to trough intensity or peak height ($\text{M}^{-1} \text{cm}^{-1} \text{T}^{-1}$) |
|---|----------------------|--|--|
| pH 6.51, as prepared | Soret band | 405 | (+ 71.25, - 96.25) 167.50 |
| “ | Q band | 550 | 9.88 |
| “ | d_1 low-spin band | 633 | (+ 9.88, - 2.38) 12.26 |
| “ | d_1 high-spin band | 685 | (+ 4.13, - 10.50) 14.63 |
| pH 6.51, dithionite reduced | Soret band | 424 | * |
| “ | Q band | 546.3 (isosbestic point with NO_2^- spectra) | (+ 141.22, - 130.14) 271.36 |
| “ | d_1 low-spin band | 636 | (+ 12.23, - 12.43) 24.66 |
| “ | d_1 high-spin band | <i>Absent</i> | <i>Absent</i> |
| pH 6.51, initial NO_2^- addition | Soret band | 409 (A second small derivative function is appearing at 421 nm) | (+ 36.25, - 31.25) 67.50 |
| “ | Q band | 546 | (+ 66.25, - 51.25) 117.50 |
| “ | d_1 low-spin band | 627 | (+ 9.25, - 9.38) 18.63 |
| “ | d_1 high-spin band | <i>Absent</i> | <i>Absent</i> |
| pH 6.51, NO_2^- addition, 30 minutes | Soret band | 407 | (+ 53.75, - 45.00) 98.75 |
| “ | Q band | 546 | (+ 39.92, - 24.57) 64.49 |
| “ | d_1 low-spin band | 629 | (+ 8.38, - 7.00) 15.38 |
| “ | d_1 high-spin band | 685 | (- 0.036, - 3.25) 3.29 |

Table 4.5.6: UV-visible MCD bands observed during the reaction of dithionite-reduced *P. pantotrophus* cd_1 with one molar equivalent (per monomer) of nitrite at pH 6.51.

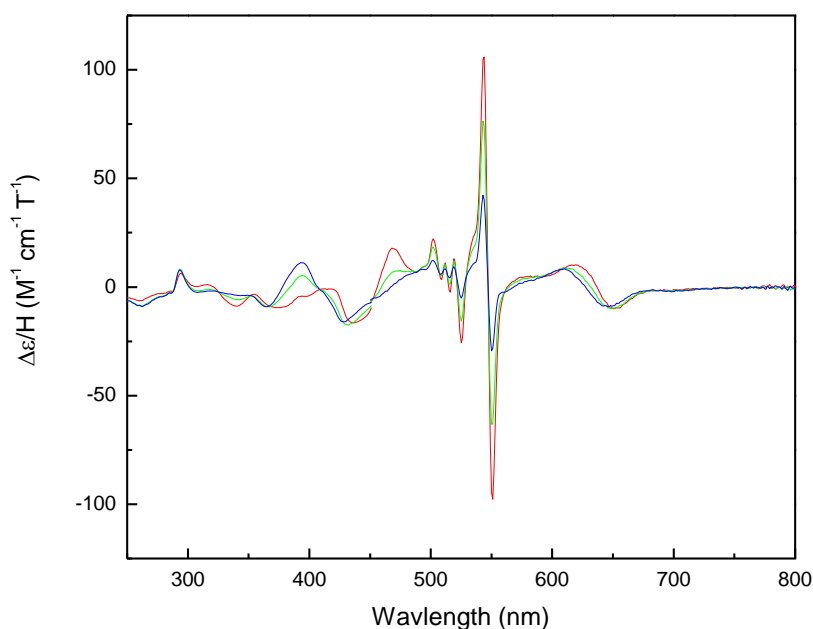


Figure 4.5.6: Room-temperature UV-visible MCD spectra (bandwidth 2 nm) of cd_1 from *P. pantotrophus*. — sodium dithionite reduced, 228.4 μM , — after the addition of 1.93 μL NaNO_2 (0.23 mM), — 30 minutes after the addition of NaNO_2 . Samples were in 48 mm mixed buffer (see Chapter 3, Section 3.2.4 for details), pH 6.90. Spectra were recorded at a magnetic field of 8 tesla.

As expected, in the visible region of the spectrum, the greater proportion of reduced *c*-heme in the pH 6.51 (*Figure 4.5.5*, above) and 6.90 (*Figure 4.5.6*) samples (compared to the pH 6.00 sample) is reflected in the higher intensity of the Q-band both immediately and 30 minutes after nitrite addition. After 30 minutes equilibration time, the Q-bands of the pH 6.51 and 6.90 nitrite-reacted samples displayed PTT intensities of $64.5 \text{ M}^{-1} \text{ cm}^{-1} \text{ T}^{-1}$ and $71.7 \text{ M}^{-1} \text{ cm}^{-1} \text{ T}^{-1}$ respectively.

| Sample | Spectral feature | Band wavelength (nm) | Peak to trough intensity or peak height ($\text{M}^{-1} \text{ cm}^{-1} \text{ T}^{-1}$) |
|---|----------------------|--|--|
| pH 6.90, as prepared | Soret band | 405 | * |
| “ | Q band | 550 | * |
| “ | d_1 low-spin band | 633 | * |
| “ | d_1 high-spin band | 685 | * |
| pH 6.90, dithionite reduced | Soret band | 427 | (− 0.94, − 16.62) 17.56 |
| “ | Q band | 547 (isosbestic point with NO_2^- spectra) | (+ 105.08, − 96.35) 201.43 |
| “ | d_1 low-spin band | 637 | (+ 10.20, − 10.07) 20.27 |
| “ | d_1 high-spin band | <i>Absent</i> | <i>Absent</i> |
| pH 6.90, initial NO_2^- addition | Soret band | 414 (a second derivative is appearing to the right of this feature, centered at 422 nm) | (+ 5.30, − 17.34) 22.64 |
| “ | Q band | 547 (isosbestic point with reduced spectrum) | (+ 75.86, − 63.87) 139.73 |
| “ | d_1 low-spin band | 633 | (+ 8.71, − 9.77) 18.48 |
| “ | d_1 high-spin band | <i>Absent</i> | <i>Absent</i> |
| pH 6.90, NO_2^- addition, 30 minutes | Soret band | 410 (a second derivative is appearing to the right of this feature, centered at 418 nm) | (+ 11.14, − 16.01) 27.15 |
| “ | Q band | 547 (isosbestic point with reduced spectrum) | (+ 41.80, − 29.85) 71.65 |
| “ | d_1 low-spin band | 630 | (+ 8.30, − 8.95) 17.25 |
| “ | d_1 high-spin band | <i>Absent</i> | <i>Absent</i> |

Table 4.5.7: UV-visible MCD bands observed during the reaction of dithionite-reduced *P. pantotrophus* cd_1 with one molar equivalent (per monomer) of nitrite at pH 6.90.

The *P. pantotrophus* cd_1 sample re-oxidised by nitrite at pH 7.50 and 8.00: Soret and Q-band observations

An increase in sample pH to 7.50 leads to a change in the shape and central wavelength of the Soret band (Figure 4.5.7) of the fully-reduced spectrum. At pH 6.90 (Figure 4.5.6), the Soret band of the fully-reduced protein is positioned at 427 nm, and appears to be attributable to two different species. There is also a shoulder appearing to the left of the feature, just below the maxima of the Soret bands of the NO-bound spectra. As the sample pH is raised to 7.50, the bandwidth of the Soret band in the dithionite-reduced spectrum narrows and blue-shifts to 421 nm.

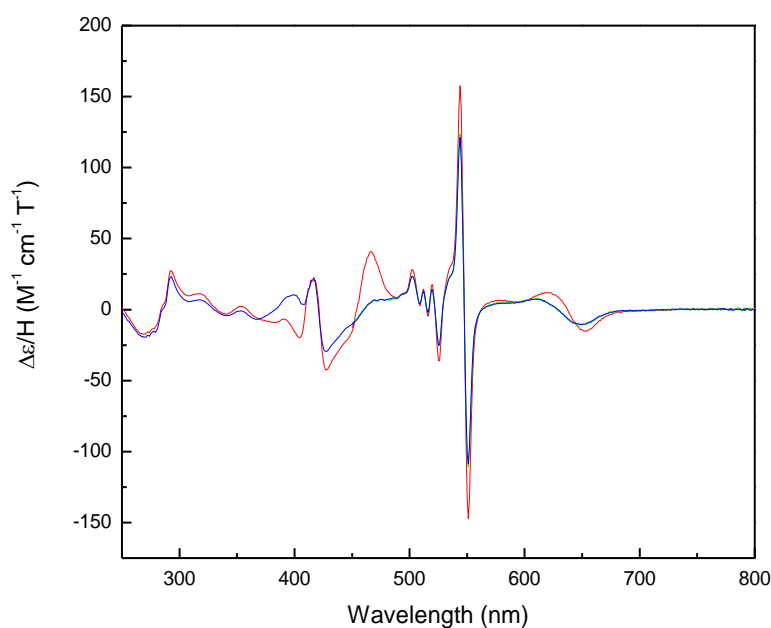


Figure 4.5.7: Room-temperature UV-visible MCD spectra of cd_1 from *P. pantotrophus*. — Sodium dithionite reduced, 223.6 μM , — after the addition of 1.90 μL NaNO_2 (0.23 mM), — 30 minutes after the addition of NaNO_2 . Samples were in 48 mM mixed buffer (see Chapter 3, Section 3.2.4 for details), pH 7.50. Spectra were recorded at a magnetic field of 8 T.

The Soret band of the spectrum recorded after nitrite addition is also centred at 421 nm and is of similar bandwidth. At this pH, the UV region of the NO-bound spectrum is comparable in appearance to that of the fully-reduced, indicating the ferrous c intermediate ($d_1^{2+}\text{-NO}^+ c^{2+}$) is dominant. As judged by the relative intensity of the Q-

band (compared to that of the fully-reduced spectrum), approximately 75 % of the *c*-heme in the bulk sample at this pH is ferrous. In the pH 8.00 sample (*Figure 4.5.8*) this figure has increased to ~ 89 %, and the position and bandwidth of the Soret band in the dithionite-reduced and nitrite re-oxidised spectra (both centred at 421 nm, PTT ~ 80 and $68 \text{ M}^{-1} \text{ cm}^{-1} \text{ T}^{-1}$ respectively) is virtually identical. This supports the proposed hypothesis that at a solution pH above the pKa the electron is located at the *c*-heme in the majority of NO-bound sample, thus reducing it to the ferrous state.

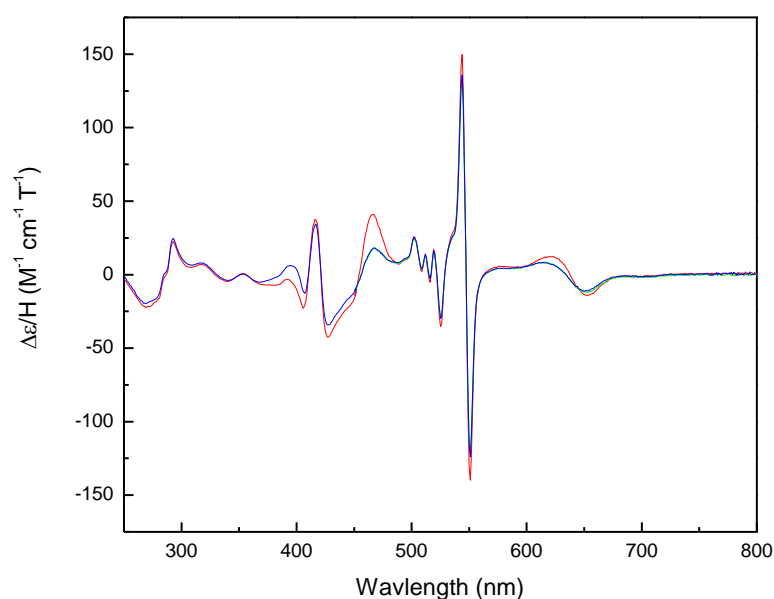


Figure 4.5.8: Room-temperature UV-visible MCD spectra (sl40) of *cd*₁ from *P. pantotrophus*. — Sodium dithionite reduced, 217.7 μM , — after the addition of 1.84 μL NaNO_2 (0.23 mM), — 30 minutes after the addition of NaNO_2 . Samples were in 48 mM mixed buffer (see Chapter 3, Section 3.2.4 for details), pH 8.00. Spectra were recorded at a magnetic field of 8 T.

| Sample | Spectral feature | Band wavelength (nm) | Peak to trough intensity or peak height ($\text{M}^{-1} \text{cm}^{-1} \text{T}^{-1}$) |
|---|----------------------|--|--|
| pH 7.50, as prepared | Soret band | 405 | * |
| “ | Q-band | 550 | * |
| “ | d_1 low-spin band | 633 | * |
| “ | d_1 high-spin band | 685 | * |
| pH 7.50, dithionite reduced | Soret band | 421 | (+ 20.19, - 42.75) 62.94 |
| “ | Q-band | 547 (isosbestic point with NO_2^- spectra) | (+ 157.17, - 147.00) 304.17 |
| “ | d_1 low-spin band | 638 | (+ 11.62, - 14.94) 26.56 |
| “ | d_1 high-spin band | <i>Absent</i> | <i>Absent</i> |
| pH 7.50, initial NO_2^- addition | Soret band | 422 | (+ 21.96, - 29.05) 51.01 |
| “ | Q-band | 547 (isosbestic point with reduced spectrum) | (+ 122.84, - 110.75) 233.59 |
| “ | d_1 low-spin band | 631 | (+ 7.10, - 10.61) 17.71 |
| “ | d_1 high-spin band | <i>Absent</i> | <i>Absent</i> |
| pH 7.50, NO_2^- addition, 30 minutes | Soret band | * | * |
| “ | Q-band | 547 (isosbestic point with reduced spectrum) | (+ 119.95, - 107.86) 227.81 |
| “ | d_1 low-spin band | 631 | (+ 7.10, - 10.61) 17.71 |
| “ | d_1 high-spin band | <i>Absent</i> | <i>Absent</i> |

Table 4.5.8: UV-visible MCD bands observed during the reaction of dithionite-reduced *P. pantotrophus* cd_1 with one molar equivalent (per monomer) of nitrite at pH 7.50.

| Sample | Spectral feature | Band wavelength (nm) | Peak to trough intensity or peak height ($\text{M}^{-1} \text{cm}^{-1} \text{T}^{-1}$) |
|---|----------------------|--|--|
| pH 8.00, as prepared | Soret band | 405 | * |
| “ | Q-band | 550 | * |
| “ | d_1 low-spin band | 633 | * |
| “ | d_1 high-spin band | 685 | * |
| pH 8.00, dithionite reduced | Soret band | 421 | (+ 37.40, - 42.60) 80.00 |
| “ | Q-band | 547 (isosbestic point with NO_2^- spectra) | (+ 149.03, - 140.14) 289.17 |
| “ | d_1 low-spin band | 638 | (+ 12.04, - 14.10) 26.14 |
| “ | d_1 high-spin band | <i>Absent</i> | <i>Absent</i> |
| pH 8.00, initial NO_2^- addition | Soret band | 421 | (+ 33.59, - 34.47) 68.06 |
| “ | Q-band | 547 (isosbestic point with reduced spectrum) | (+ 129.93, - 119.43) 249.36 |
| “ | d_1 low-spin band | 635 | (+ 8.21, - 11.73) 19.94 |
| “ | d_1 high-spin band | <i>Absent</i> | <i>Absent</i> |

| | | | |
|---|--------------------------------------|--|------------------------------------|
| pH 8.00, NO ₂ ⁻ addition, 30 minutes | Soret band | * | * |
| “ | Q-band | 547 (isosbestic point with reduced spectrum) | (+ 133.74, - 123.94) 257.68 |
| “ | <i>d</i> ₁ low-spin band | 635 | (+ 8.21, - 11.19) 19.40 |
| “ | <i>d</i> ₁ high-spin band | <i>Absent</i> | <i>Absent</i> |

Table 4.5.9: UV-visible MCD bands observed during the reaction of dithionite-reduced *P. pantotrophus* *cd*₁ with one molar equivalent (per monomer) of nitrite at pH 8.00.

The *P. pantotrophus* *cd*₁ sample re-oxidised by nitrite at pH 8.50: Soret and Q-band observations

When the pH of the protein solution is increased to 8.50, the oxidation state of the *c*-heme in the overall sample is estimated (from the height of the Q-band) to be almost 98 % ferrous. The Soret band (see *Figure 4.5.9*) in the dithionite-reduced spectrum and that of the sample immediately after nitrite addition is identical in position and bandwidth.

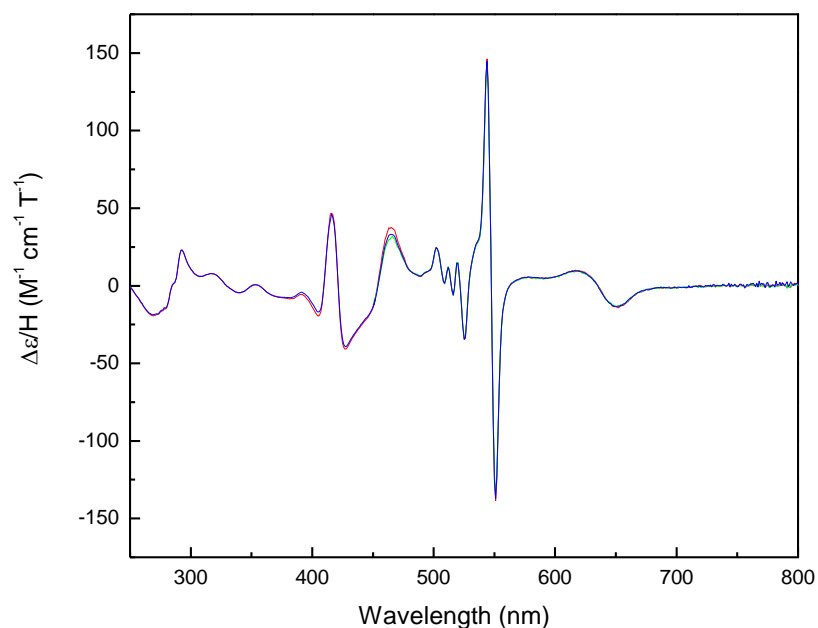
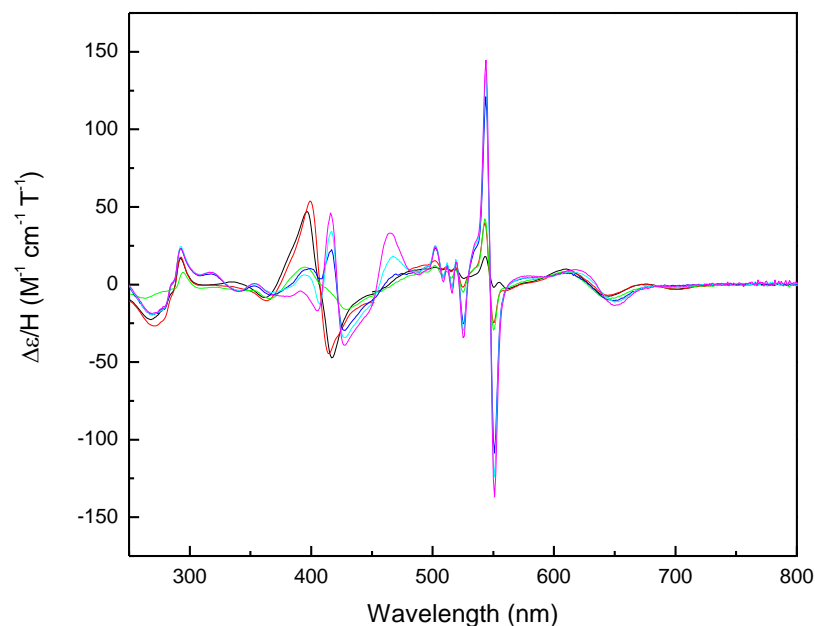


Figure 4.5.9: Room-temperature UV-visible MCD spectra of *cd*₁ from *P. pantotrophus*. — Sodium dithionite reduced, 162.4 μM, — after the addition of 1.40 μL NaNO₂ (0.17 mM), — 30 minutes after the addition of NaNO₂. Samples were in 48 mM mixed buffer (see Chapter 3, Section 3.2.4 for details), pH 8.50. Spectra were recorded at a magnetic field of 8 T.

This supports the hypothesis that the electron in the NO-bound sample will tend to shift its location to the *c*-heme as the pH increases. Judged by the relative height of the Q-band, at pH 8.50 the electron will be located at the *c*-heme in 98 % of the sample and the NO-bound intermediate will exist almost entirely in the d_1^{2+} -NO⁺ form.

| Sample | Spectral feature | Band wavelength (nm) | Peak to trough intensity or peak height ($\text{M}^{-1} \text{cm}^{-1} \text{T}^{-1}$) |
|--|----------------------|---|--|
| pH 8.50, as prepared | Soret band | 405 | * |
| “ | Q-band | 550 | * |
| “ | d_1 low-spin band | 633 | * |
| “ | d_1 high-spin band | 685 | * |
| pH 8.50, dithionite reduced | Soret band | 421 | (+ 46.38, – 40.41) 86.79 |
| “ | Q-band | 547 (isosbestic point with NO ₂ [–] spectra) | (+ 146.70, – 137.40) 284.10 |
| “ | d_1 low-spin band | 637 | (+ 9.63, – 13.43) 23.06 |
| “ | d_1 high-spin band | <i>Absent</i> | <i>Absent</i> |
| pH 8.50, initial NO ₂ [–] addition | Soret band | 421 | (+ 46.38, – 39.20) 85.58 |
| “ | Q-band | 547 (isosbestic point with reduced spectrum) | (+ 141.92, – 133.04) 274.96 |
| “ | d_1 low-spin band | 637 | (+ 9.63, – 13.43) 23.06 |
| “ | d_1 high-spin band | <i>Absent</i> | <i>Absent</i> |
| pH 8.50, NO ₂ [–] addition, 30 minutes | Soret band | * | * |
| “ | Q-band | 547 (isosbestic point with reduced spectrum) | (+ 142.85, – 134.68) 277.53 |
| “ | d_1 low-spin band | 637 | (+ 9.63, – 13.43) 23.06 |
| “ | d_1 high-spin band | <i>Absent</i> | <i>Absent</i> |

Table 4.5.10: UV-visible MCD bands observed during the reaction of dithionite-reduced *P. pantotrophus* cd_1 with one molar equivalent (per monomer) of nitrite at pH 8.50.



Figures 4.5.10: Room-temperature UV-visible MCD spectra of *cd*₁ from *P. pantotrophus* ~ 30 minutes after the addition of NaNO₂. — *Pp cd*₁ (~ 29.7 μM, pH 6.00), 0.03 mM NaNO₂, — *Pp cd*₁ (~ 20.7 μM, pH 6.51), 0.02 mM NaNO₂ — *Pp cd*₁ (~ 224.8 μM, pH 6.90), 0.23 mM NaNO₂, — *Pp cd*₁ (~ 220.3 μM, pH 7.50), 0.22 mM NaNO₂, — *Pp cd*₁ (~ 214.6 μM, pH 8.00), 0.21 mM NaNO₂, — *Pp cd*₁ (~ 160.7 μM, pH 8.50), 0.17 mM NaNO₂. Samples were in 48 mM ‘mixed’ buffer (see Chapter 3, Section 3.2.4 for details). Spectra were recorded at a magnetic field of 8 T. The pH 6.00 and 6.51 spectra were measured in a 1 cm pathlength quartz cell. All other pH measurements were made using a 0.1 cm pathlength quartz cell.

4.5.3. Calculation of the pK_a for the NO-bound equilibrium

The standard Henderson-Hasselbalch (HH) equation for acid-base equilibria (Equation 1) can be rearranged so that the relative proportions of acid and conjugate base are the subjects of the equation (Equation 2):

$$\text{pH} = \text{pK}_a + \log [\text{A}^-] / [\text{HA}] \quad (1)$$

$$\Rightarrow 10^{(\text{pH}-\text{pK}_a)} = [\text{A}^-] / [\text{HA}]$$

$$10^{(\text{pK}_a-\text{pH})} = [\text{HA}] / [\text{A}^-] \quad (2)$$

By defining the $d_1^{2+}\text{-NO}^+ c^{2+}$ intermediate species on the left of *Figure 4.3.1* as the deprotonated ‘conjugate base’ and therefore $[A^-]$, and the protonated $d_1^{2+}\text{-NO} c^{3+}$ species as $[HA]$, the proportion of reduced *c*-heme at a particular pH can be calculated from Equation 3:

$$\% \text{ reduced } c\text{-heme} = ([A^-] / ([A^-] + [HA])) \times 100 \quad (3)$$

This quantity is expressed by the intensity of the 547.5 nm band in the MCD spectrum. If Equation 2 is substituted into Equation 3, Expression 4 is given:

$$\% \text{ reduced } c\text{-heme} = (1 / (1 + 10^{(pK_a - pH)})) \times 100 \quad (4)$$

Table 4.5.11 summarises the estimated percentage of ferrous *c*-heme in each sample 30 minutes after NO_2^- addition. If these values are plotted as percentage reduced *c*-heme versus sample pH, Expression 4 (also versus sample pH) can be fitted to the data (*Figure 4.5.11*). As the value for the pKa is unknown, this was found by trial and error until the best possible fit to the data could be obtained. This value was found to be 7.10, and can be assumed to be the pKa of the principle neighbouring histidine residue discussed in Section 4.3 and illustrated in *Figure 4.3.1*.

At a protein solution pH of 7.10 (and therefore the pKa), 50 % of the principle histidine residues will be deprotonated with the substrate being coordinated to the d_1 -heme in the $d_1^{2+}\text{-NO}^+ c^{2+}$ conformation. Increasing the solution pH to alkaline will lead to a greater proportion of this intermediate. At pH 8.50, the proportion of reduced *c*-heme, as judged by the intensity of the 547.5 nm band in the NO-bound species, is 97.7 %. Conversely,

decreasing the solution pH below the pKa value will lead to a greater relative proportion of the $d_1^{2+}\text{-NO } c^{3+}$ intermediate for the NO-bound species.

| Actual pH | Percentage ferrous <i>c</i> -heme |
|-----------|-----------------------------------|
| 6.00 | 7.1 |
| 6.51 | 23.8 |
| 6.90 | 35.6 |
| 7.50 | 74.9 |
| 8.00 | 89.1 |
| 8.50 | 97.7 |

Table 4.5.11: How the percentage of ferrous *c*-heme present in the sample, as judged by the intensity of the Q-band at 547.5 nm varies with the pH of the sample solution. In all cases the intensity of the Q-band ~ 30 minutes after nitrite addition is expressed as a percentage of the corresponding feature in the fully-reduced spectrum. Sample solutions at all pH values were allowed to equilibrate for 30 minutes following nitrite addition.

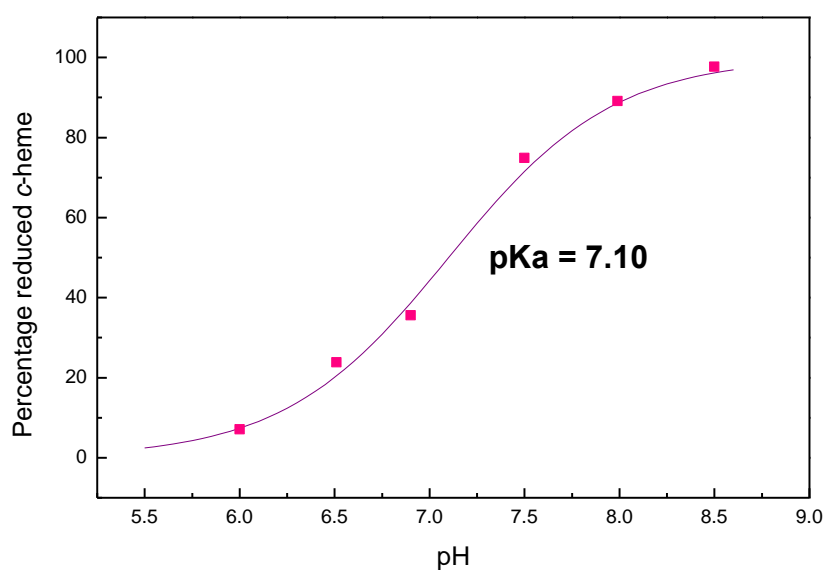


Figure 4.5.11: — Henderson-Hasselbalch (HH) fit of the results obtained for the ■ percentage of reduced *c*-heme in the sample (as judged by the intensity of the band at 547.5 nm in the room temperature MCD spectrum) according to pH. Samples were in 48 mM mixed buffer (see Chapter 3, Section 3.2.4 for details). Spectra were recorded at a magnetic field of 8 T.

According to the Henderson Hasselbalch curve illustrated in Figure 4.5.11, at pH 6.00, only ~ 7.1 % of the *c*-heme will be in the reduced state, indicating that the $d_1^{2+}\text{-NO } c^{3+}$ intermediate is the more prevalent species.

The implications of these observations will be discussed further in Section 6 of this chapter.

4.5.4. *Observations relating to the d_1 -heme features*

It was hoped that the central wavelength positions of the 633 and 685 nm bands in the nitrite re-oxidised spectra at contrasting pH values would provide an indication of whether the two intermediates have a differing effect on the relative energies of the d_1 -heme orbitals. In a typical MCD spectrum of *P. pantotrophus cd₁*, features observed between 590 and 700 nm are exclusively due to low-spin d_1 -heme (28). The ‘as prepared’ pH 6.00 spectrum (*Figure 4.5.1*) shows low- and high-spin d_1 ferric bands at 633 and 685 nm respectively. As expected, when the sample is dithionite-reduced, the 685 nm high-spin band completely disappears. The d_1 band at 633 nm undergoes a red shift to 636 nm and a corresponding increase in PTT intensity, from $\sim 10.8 \text{ M}^{-1} \text{ cm}^{-1} \text{ T}^{-1}$ to $25.1 \text{ M}^{-1} \text{ cm}^{-1} \text{ T}^{-1}$. This observation mirrors those typically observed in the absorption spectrum of *P. pantotrophus cd₁* where, upon reduction, disappearance of the high-spin d_1 band at 702 nm occurs concomitantly with a red shift of the d_1 band from 644 to 653 nm. These changes in the MCD and absorption spectra upon reduction indicate that the Tyr²⁵ has dissociated from the metal centre, and that the d_1 -heme exists entirely in the high-spin ferrous state.

At pH 6.00, the binding of nitrite at the d_1 -heme and its subsequent reduction to give the NO-bound intermediate leads to another wavelength shift in the low-spin ferrous MCD band, from 636 nm in the fully-reduced spectrum to 624 nm upon initial substrate addition and to 628 nm after 30 minutes equilibration. According to the equilibrium illustrated in *Figure 4.3.1*, at pH 6.00, the sample would mainly exist in the $d_1^{2+}\text{-NO } c^{3+}$ state. This initial blue shift can therefore be assigned to the formation of the $d_1^{2+}\text{-NO}$ species. This is comparable with the blue shift from 652 to 642 nm observed by George

et al (10) in the absorption spectrum as the protein made the transition from the fully-reduced state to the d_1^{2+} -NO c^{3+} species.

An increase in solution pH from 6.00 to 6.90 (*Figures 4.5.4–4.5.6*) results in a gradual red shift of the low-spin d_1 -heme band in the NO-bound sample. At pH 6.00, the central position of this derivative feature is 628 nm, gradually moving to 629 and finally 630 nm as the solution pH is increased from 6.51 to 6.90. This indicates an alteration in the relative energies of the d_1 -heme orbitals as the d_1^{2+} -NO⁺ species becomes more prevalent. There appears to be minor amounts of high-spin d_1 -heme present in the pH 6.51 NO₂[−] re-oxidised sample (after 30 minutes equilibration), as reflected in the appearance of a small feature at 685 nm. With a PTT intensity of 3.3 M^{−1} cm^{−1} T^{−1}, this band is of approximately equal height to the equivalent feature in the pH 6.00 spectrum (3.1 M^{−1} cm^{−1} T^{−1}). In the spectrum of the ‘as prepared’ sample at pH 6.00, this feature almost five times more intense, with a PTT intensity of ~ 14.6 M^{−1} cm^{−1} T^{−1}.

At pH 6.90 the high-spin species is not present in the NO-bound sample. Whether the small amounts of this high-spin d_1 species observed in the pH 6.00 and 6.51 spectra is due to partial air-re-oxidation of the sample (and hence re-coordination of the Tyr²⁵) or a metal spin-state equilibrium for the NO-bound species in the manner of that seen for the ‘as isolated’ protein is currently unclear. There is also the possibility that a third, minority species is formed at lower pH values.

As discussed above, the low-spin d_1 band in the NO-bound sample exhibits a red-shift from 629 nm to 630 nm as the solution pH is increased from 6.51 to 6.90. This trend appears to continue as the pH of the reaction solution is raised; the pH 7.50 visible region spectrum measured 30 minutes after nitrite addition (*Figure 4.5.7*) exhibits a low-spin d_1 band that is centred at 631 nm, with a PTT intensity of 17.7 M^{−1} cm^{−1} T^{−1}.

At pH 8.00 (*Figure 4.5.8*) the PTT intensity of this band is almost identical at $19.4 \text{ M}^{-1} \text{ cm}^{-1} \text{ T}^{-1}$, although the central wavelength has increased by 4 nm to 635 nm. This gradual red shift of the low-spin d_1 -heme band can be attributed to an increase in the relative proportion of the $d_1^{2+}\text{-NO}^+$ species in the sample. There is no additional band at 685 nm as observed in the ‘as-prepared’ and NO_2^- re-oxidised spectra at pH 6.00 and 6.51. This indicates that the metal in the $d_1^{2+}\text{-NO}^+$ intermediate exists entirely in one spin state.

The d_1 band has red shifted further in the equivalent pH 8.50 spectrum to 637 nm (*Figure 4.5.9*) and after 30 minutes equilibration is still positioned at the same wavelength and is of identical intensity. As the sample is $\sim 98\%$ in the $d_1^{2+}\text{-NO}^+ c^{2+}$ form at pH 8.50, this band can be assigned to NO^+ -bound d_1 -heme. As with the pH 6.90, 7.50 and 8.00 nitrite re-oxidised samples, there is no d_1 high-spin band present at 685 nm. When NO_2^- is bound to ferric d_1 -heme, a band is observed in the room temperature MCD spectrum in the region of 640–645 nm (29). As the highest wavelength observed here for the low-spin d_1 band 30 minutes post-addition of NO_2^- is 637 nm, this work has shown that the ‘ $cd_1^*\text{-X}$ ’ species reported by Van Wonderen *et al* was not formed. The nature of the intermediate formed at the catalytic centre upon reaction with the physiological substrate is therefore dependent on the oxidation state of the enzyme. As a consequence the spectroscopic signature can be used to assess whether or not the nitrite-reacted form arose from the reduced state.

4.6 Discussion and conclusions

The aim of this piece of work was to investigate the pH dependence of the $d_1^{2+}\text{-NO}^+ c^{2+} \leftrightarrow d_1^{2+}\text{-NO} c^{3+}$ equilibrium formed upon reacting the fully reduced *P. pantotrophus* cd_1 monomer with stoichiometric amounts of NO_2^- . Experimental investigations were made

initially by absorbance spectroscopy and were furthered by UV-visible MCD spectra recorded at room temperature. The latter technique incorporated the use of a specially-developed cell holder that allowed substrate additions to be made anaerobically *in situ*. By making these MCD measurements at a number of different values of solution pH, an estimate of 7.10 for the pKa has been calculated. This pKa value is assumed to be that of the neighbouring His³⁴⁵ residue (the ‘principle’ histidine residue), which lies within close proximity to the d_1 active site and would appear to influence the distribution of the d_1^{2+} -NO⁺ $c^{2+} \leftrightarrow d_1^{2+}$ -NO c^{3+} equilibrium. It should be noted that the His³⁴⁵ has been assumed here (for simplicity) to be the principle residue that affects steric influence over the active site although this is not necessarily the case. The other neighbouring His³⁸⁸ residue may exercise a greater or equal effect over the d_1^{2+} -NO⁺ $c^{2+} \leftrightarrow d_1^{2+}$ -NO c^{3+} equilibrium distribution. It would not be unreasonable to assume that both histidine residues share an identical pKa, as they are located within very close proximity to each other and would hence share the same local environment.

The possibility that steric hindrance caused by the His³⁴⁵/His³⁸⁸ residues may have an effect on the d_1^{2+} -NO⁺ $c^{2+} \leftrightarrow d_1^{2+}$ -NO c^{3+} equilibrium distribution was first suggested by George *et al* (10). They argued that if the adoption of the linear d_1 Fe(II)-NO⁺ species was sterically hindered by these histidine residues, the electron could be passed from the c -heme leading to formation of the bent d_1^{2+} -NO at the d_1 -heme. To our knowledge, no further investigation into this idea was carried out by the authors. The results presented here substantiate this hypothesis and indicate that one (or both) of the neighbouring histidine residues exert a pH-dependant influence over the equilibrium. However, it can be argued that the actual nature of the effect exerted by the ‘principle’ histidine residue is far more likely to be electrostatic. Hydrogen-bonding by these residues to the Tyr²⁵ has already been observed in the crystal structure (30) and they are thought (31,32) to play a

part in the enzyme mechanism by way of proton donation, leading to the dehydration of the substrate.

The nitrite re-oxidised absorbance spectra show a gradual red shift of the *c*-heme Soret band as the pH of the sample solution is increased. At a solution pH of 6.00 this band is centred at 408 nm respectively, indicating that the majority of the *c*-heme is in the ferric state. At this pH the d_1^{2+} -NO c^{3+} species will predominate and as illustrated in *Figure 4.3.1*, this intermediate structure is adopted when the His³⁴⁵ residue is protonated.

The ‘as-prepared’ absorbance spectra displayed a *c*-heme Soret band centred at 406 nm, regardless of solution pH, which is typical of oxidised *P. pantotrophus cd₁* (12). In the pH 7.50 and pH 8.50 samples the *c*-heme Soret band displays a red shift from 413 nm (pH 7.50) to 415 nm (pH 8.50) as the concentration of H⁺ ions in the solution decreases. This indicates that the d_1^{2+} -NO⁺ c^{2+} species is becoming predominant as the solution pH is raised, leading to the electron becoming located at the *c*-heme in the majority of the sample. This red shift of the *c*-heme Soret band is accompanied by a characteristic sharpening of the α/β region, another indicator that this heme has been reduced to the ferrous state.

The absorbance spectra of the nitrite re-oxidised samples also show differences in the d_1 region compared with the ‘as prepared’ samples. Oxidised *P. pantotrophus cd₁* exhibits two spectral bands that can be attributed exclusively to the d_1 -heme (33). These bands are symmetric in appearance and occur at ~ 644 and 702 nm due to low and high-spin ferric d_1 -heme respectively. The ‘as prepared’ absorbance spectra presented here show low-spin d_1 bands centred between 643 and 647 nm. The positioning (and height) of this feature in the ‘as prepared’ samples appears to be random and does not seem to be influenced by sample pH. In the nitrite re-oxidised samples the low-spin d_1 feature exhibits a blue shift (compared with the ‘as prepared’) to 642 nm in the pH 6.00 and pH

7.50 samples. By contrast, the pH 8.50 sample exhibits a greater red shift to 650 nm. Only the pH 6.00 sample appears to contain appreciable quantities of high-spin d_1 -heme, approximately 50 % less than that observed in the corresponding ‘as prepared’ spectrum. This would suggest that a d_1 spin-equilibrium exists in these samples that predominately contain the d_1^{2+} -NO c^{3+} species.

The above observations made in the absorbance spectra are reflected in the UV-visible MCD results. As the solution pH is increased from 6.00 to 8.50, the intensity of the Q-band in the nitrite re-oxidised spectra subsequently increases. At pH 8.50 the intensity of this band is ~ 98 % of that in the fully reduced spectrum, indicating that virtually all of the c -heme in the sample is in the ferrous state. This increase in Q-band intensity is matched with a corresponding red shift in the Soret band as the solution pH is increased in the absorption spectra. Again, these spectral data support the theory that as the H^+ concentration in the environment decreases, the d_1^{2+} -NO⁺ c^{2+} species becomes the preferred intermediate. The gradual red shift of the d_1 low-spin band as the sample pH is increased is observed in both the absorbance and MCD spectra. Overall, in the MCD, this band exhibits a red shift from 628 nm in the pH 6.00 sample to 637 nm at pH 8.50. As with the absorbance spectra, only the pH 6.00 and pH 6.51 MCD samples exhibited traces of high-spin d_1 -heme. When nitrite is reacted with ‘as prepared’ *P. pantotrophus* cd_1 , an EPR silent d_1^{3+} -NO• species is formed (18) that gives rise to a band in the UV-visible MCD spectrum in the region of 640–645 nm (29). Reaction of the hydroxylamine re-oxidised protein with NO_2^- (to form cd_1^* -X) also gives rise to an EPR silent species, which has been mistakenly assigned to NO_2^- -bound ferric d_1 heme (14,15). However, nitrite bound to ferric heme would give rise to a paramagnetic, EPR-active species, and the EPR silence of cd_1^* -X is likely to be due to the d_1^{3+} -NO• species postulated by Van Wonderen *et al* (18). However, the highest wavelength observed in this work for the d_1 band is 637 nm at pH

8.50, indicating the d_1^{3+} -NO^{*} species is not formed when nitrite is added to the fully reduced enzyme. It is unclear whether this species would be formed as part of the catalytic cycle *in vivo*.

The absorbance and MCD results show that the d_1^{2+} -NO c^{3+} species exhibits both d_1 -heme low- and high-spin bands. The low-spin band exhibited by this species is blue shifted in comparison to the corresponding feature observed for the d_1^{2+} -NO⁺ c^{2+} intermediate. This indicates that the two types of nitrosyl ligand coordinated to the d_1 heme have differing effects on the energy levels of the metal. The linear nitrosonium NO⁺ ligand is isoelectronic with CO and would be expected to adopt similar strong π -acceptor characteristics. In the d_1 Fe(II)-NO c^{3+} species, the extra electron would lead to a ‘bent’ conformation reducing the ability of the ligand to act as a π -acceptor and thus imposing a weaker crystal field onto the metal. As this species appears to exhibit both low- and high-spin d_1 -heme bands, it would appear that the d_1^{2+} -NO species lies sufficiently close to the spin cross-over point to permit the existence of both states. While George *et al* (10) and Sam *et al* (14) observed a single d_1 band at 632 nm due to the d_1^{2+} -NO⁺ c^{2+} \leftrightarrow d_1^{2+} -NO c^{3+} equilibrium, the pH-dependant data presented here has allowed this feature to be separated according to the identity of the intermediate.

The investigations made by George *et al* (10) were carried out at a solution pH of 7.00. The fact that they observed a 45:55 distribution for the d_1^{2+} -NO⁺ c^{2+} and d_1^{2+} -NO c^{3+} species respectively led them to question whether there was a simple equilibrium present or whether there was a conformational interaction across the dimer leading to a coexistence of both states. The results presented here support the former theory although the two are not necessarily mutually exclusive. As George *et al* carried out their experiments at a solution pH just below the pK_a value, the distribution of the two species would have been virtually 50:50, with the d_1^{2+} -NO c^{3+} intermediate predominating slightly. It may be the

case that when the pH of the solution is 7.10, the two NO-bound d_1 intermediate species are distributed equally across the dimer, i.e. one monomer contains $d_1^{2+}\text{-NO}^+ c^{2+}$, the other $d_1^{2+}\text{-NO} c^{3+}$. Raising the solution pH above the pKa value would lead to an increase in the $d_1^{2+}\text{-NO}^+ c^{2+}$ species until eventually both monomers contain the NO-bound d_1 -heme in this form.

Sam *et al* (32) recently investigated the very early ($\sim 100 \mu\text{s}$) kinetics of NO_2^- reduction by the *P. pantotrophus* enzyme using a novel technique called microsecond freeze-hyperquenching (MHQ) (34,35). They observed a feature in the absorbance spectrum at 620 nm that was assigned to the Michaelis complex ($d_1^{2+}\text{-NO}_2^- c^{2+}$) formed upon binding of nitrite to the fully reduced enzyme, in the absence of excess reductant. This feature was seen to decay, as separate peaks at 660 nm and 630 nm (assigned to high-spin d_1 -heme and $d_1^{2+}\text{-NO}^+$ respectively) increased in intensity. The former species is thought to arise following the release of the NO product from the enzyme. The authors suggested that a cooperative process took place across the dimer, where monomer 1 releases NO as the Michaelis complex is converted to $d_1^{2+}\text{-NO}^+$. However, in this work a ten-fold excess of nitrite was added, and hence the purpose was not to trap the $d_1^{2+}\text{-NO}^+ c^{2+} \leftrightarrow d_1^{2+}\text{-NO} c^{3+}$ intermediates. Unfortunately, it still remains unclear to date whether *P. pantotrophus* cd_1 ever actually becomes fully-reduced *in vivo*, and despite a report that pseudoazurin enhances the rate of NO removal from the ferrous d_1 -heme (14), the method of product release is still unconfirmed. However, overall, this work has shown that if the enzyme is fully reduced, the nature of the $d_1^{2+}\text{-NO}$ intermediate formed will be dependent on the pH of the environment.

4.7 References

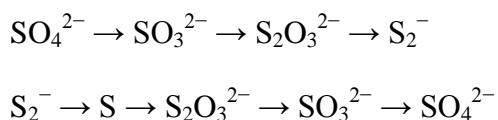
1. Fulop, V., Moir, J. W. B., Ferguson, S. J., and Hajdu, J. (1995) *Cell* **81**, 369-377
2. Johnson, M. K., Thomson, A. J., Walsh, T. A., Barber, D., and Greenwood, C. (1980) *Biochem J* **189**, 285-294
3. Richter, C. D., Allen, J. W. A., Higham, C. W., Koppenhofer, A., Zajicek, R. S., Watmough, N. J., and Ferguson, S. J. (2002) *J Biol Chem* **277**, 3093-3100
4. Yamanaka, T., and Okunuki, K. (1963) *Biochim Biophys Acta* **67**, 379-393
5. Yamanaka, T., and Okunuki, K. (1963) *Biochim Biophys Acta* **67**, 394-406
6. Yamanaka, T., and Okunuki, K. (1963) *Biochim Biophys Acta* **67**, 407-416
7. Silvestrini, M. C., Tordi, M. G., Musci, G., and Brunori, M. (1990) *J Biol Chem* **265**, 11783-11787
8. Page, C. C., Moser, C. C., Chen, X., and Dutton, P. L. (1999) *Nature* **402**, 47-52
9. Marcus, R. A. (1956) *J Chem Phys* **24**, 966-979
10. George, S. J., Allen, J. W. A., Ferguson, S. J., and Thorneley, R. N. F. (2000) *J Biol Chem* **275**, 33231-33237
11. Moir, J. W. B., Baratta, D., Richardson, D. J., and Ferguson, S. J. (1993) *Eur J Biochem* **12**, 377-385
12. Cheesman, M. R., Ferguson, S. J., Moir, J. W. B., Richardson, D. J., Zumft, W. G., and Thomson, A. J. (1997) *Biochemistry* **36**, 16267-16276
13. Allen, J. W. A., Watmough, N. J., and Ferguson, S. J. (2000) *Nat Struct Biol* **7**, 885-888
14. Sam, K. A., Fairhurst, S. A., Thorneley, R. N. F., Allen, J. W. A., and Ferguson, S. J. (2008) *J Biol Chem* **283**, 12555-12563
15. Allen, J. W. A., Higham, C. W., Zajicek, R. S., Watmough, N. J., and Ferguson, S. J. (2002) *Biochem J* **366**, 883-888
16. Koppenhofer, A., Little, R. H., Lowe, D. J., Ferguson, S. J., and Watmough, N. J. (2000) *Biochemistry* **39**, 4028-4036
17. Allen, J. W. A., Cheesman, M. R., Higham, C. W., Ferguson, S. J., and Watmough, N. J. (2000) *Biochem Biophys Res Commun* **279**, 674-677
18. Van Wonderen, J., Knight, C., Oganessian, V. S., George, S. J., Zumft, W. G., and Cheesman, M. R. (2007) *J Biol Chem* **282**, 28207-28215
19. Wilson, E. K., Bellelli, A., Cutruzzola, F., Zumft, W. G., Gutierrez, A., and Scrutton, N. S. (2001) *Biochem J* **356**, 911-911
20. Aasa, R., and Vänngård, T. (1975) *Biochim Biophys Acta* **391**, 259-64
21. Sutherland, J., Greenwood, C., Peterson, J., and Thomson, A. J. (1986) *Biochem J* **233**, 893-898
22. Walsh, T. A., Johnson, M. K., Greenwood, C., Barber, D., Springall, J. P., and Thomson, A. J. (1979) *Biochem J* **177**, 29-39

23. Walsh, T. A., Johnson, M. K., Thomson, A. J., Barber, D., and Greenwood, C. (1981) *J Inorg Biochem* **14**, 1-14
24. Cheesman, M. R., Oganessian, V. S., Watmough, N. J., Butler, C. S., and Thomson, A. J. (2004) *J Am Chem Soc* **126**, 4157-4166
25. Cheesman, M. R., Greenwood, C., and Thomson, A. J. (1991) *Adv Inorg Chem* **36**, 201-255
26. Walsh, T. A., Johnson, M. K., Barber, D., Thomson, A. J., and Greenwood, C. (1981) *J Inorg Biochem* **14**, 15-31
27. Stolzenberg, A. M., Strauss, S. H., and Holm, R. H. (1981) *J Am Chem Soc* **103**, 4763-4778
28. Ferguson, S. J. (1998) *Curr Opin Chem Biol* **2**, 182-193
29. Bradley, J., Holmes, J., and Cheesman, M. R. *Unpublished*
30. Williams, P. A., Fulop, V., Garman, E. F., Saunders, N. F. W., Ferguson, S. J., and Hajdu, J. (1997) *Nature* **389**, 406-412
31. Sam, K. A., Tolland, J. D., Fairhurst, S. A., Higham, C. W., Lowe, D. J., Thorneley, R. N. F., Allen, J. W. A., and Ferguson, S. J. (2008) *Biochem Biophys Res Commun* **371**, 719-723
32. Sam, K. A., Strampraad, M. J. F., de Vries, S., and Ferguson, S. J. (2008) *J Biol Chem* **283**, 27403–27409
33. Kobayashi, K., Koppenhofer, A., Ferguson, S. J., and Tagawa, S. (1997) *Biochemistry* **36**, 13611-13616
34. Cherepanov, A. V., and De Vries, S. (2004) *Biochim Biophys Acta* **1656**, 1-31
35. Wiertz, F. G., Richter, O. M., Ludwig, B., and de Vries, S. (2007) *J Biol Chem* **282**, 31580–31591

5. Ligand-binding trials on recombinant *R. sulfidophilum* SoxAX

5.1 The TOMES mechanism

The concept of biogeochemical cycles, with specific reference to the transformation of nitrogen between its various chemical forms has already been discussed in Chapter 2. Although less well-known, the sulphur cycle is also of high environmental significance. One very important difference between the cycling of sulphur and that of nitrogen is that a large reservoir of biologically useful sulphur already exists in the environment (in seawater and sedimentary rocks) and does not need to be fixed. All gaseous sulphur compounds are readily soluble in water, restricting the majority of the cycle to the liquid phase (1). The most naturally abundant forms of reduced inorganic sulphur are thiosulphate ($\text{S}_2\text{O}_3^{2-}$) and sulphide (S^{2-}). Thiosulphate is formed in both the reductive and oxidative halves of the sulphur cycle, and also occurs naturally in hot springs and geysers. The processes involved in the reductive and oxidative parts of the sulphur cycle are shown below.



Sulphide is produced by the reduction of thiosulphate and the microbial degradation of proteins, and also occurs naturally in a variety of metal ores, such as pyrite. The conversion of these species to sulphate by photosynthetic (e.g. *Chromatium*) and chemolithotrophic (e.g. *Thiobacillus*) bacteria occurs in the oxidative half of the sulphur cycle (1).

The TOMES (thiosulphate oxidising multi-enzyme system) mechanism is the most widely distributed sulphur oxidation pathway employed by both photosynthetic and non-photosynthetic bacteria. The electrons derived from the oxidation of sulphur are used by

the bacteria for the reduction of carbon dioxide or in respiratory chain metabolism (2). The mechanism is detailed in *Figure 5.1.1*.

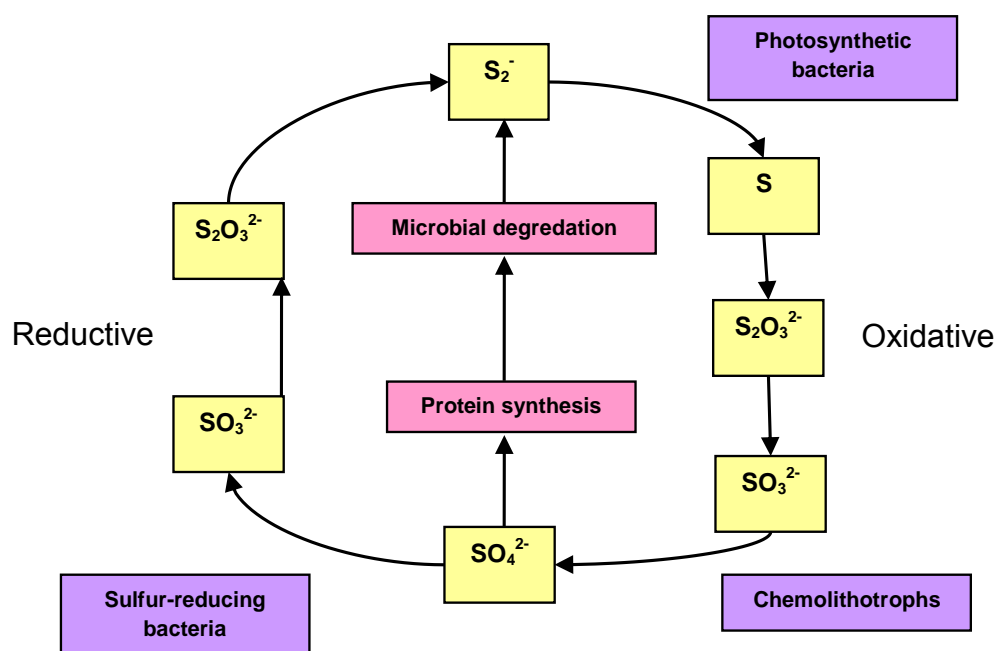


Figure 5.1.1: The Global sulphur cycle, which comprises of oxidative and reductive halves. In contrast to the nitrogen cycle, sulphur does not need to be fixed from the atmosphere.

All four protein complexes (SoxYZ, SoxAX, SoxB and SoxCD) are required for thiosulphate oxidation, and the entire process takes place in the bacterial periplasm, with a turnover number (k_{cat}) of 3 s^{-1} (3). All intermediates in the cycle are bound to a carrier cysteine residue located in the SoxY subunit of the SoxYZ complex. The SoxYZ complex acts as a 'shuttle', transporting the pathway intermediates between the SoxAX, SoxB and SoxCD enzymes. These intermediates are covalently bound to a cysteine residue at the C terminus of the SoxY subunit (4). In contrast, the oxidative part of the nitrogen cycle does not employ a similar shuttle mechanism and this makes the chemical intermediates formed within the process readily detectable. The formation of an oxidative linkage (via a disulphide bond) of thiosulphate to SoxYZ is catalysed by SoxAX, a tri-heme (or di-heme in some species of bacteria (5)) heterodimeric *c*-type cytochrome. Following this step, the

S-thiosulphonate (S-SO_3^-) species is hydrolysed, yielding sulphate and a sulphane (S^-), a process catalysed by the di-manganese containing enzyme SoxB. Subsequent oxidation by the molybdopterin-containing SoxCD complex and further hydrolysis by SoxB again releases sulphate and restores the SoxYZ complex to its unbound state (6). The TOMES mechanism and the roles of the different enzymes involved is illustrated in *Figure 5.1.2*.

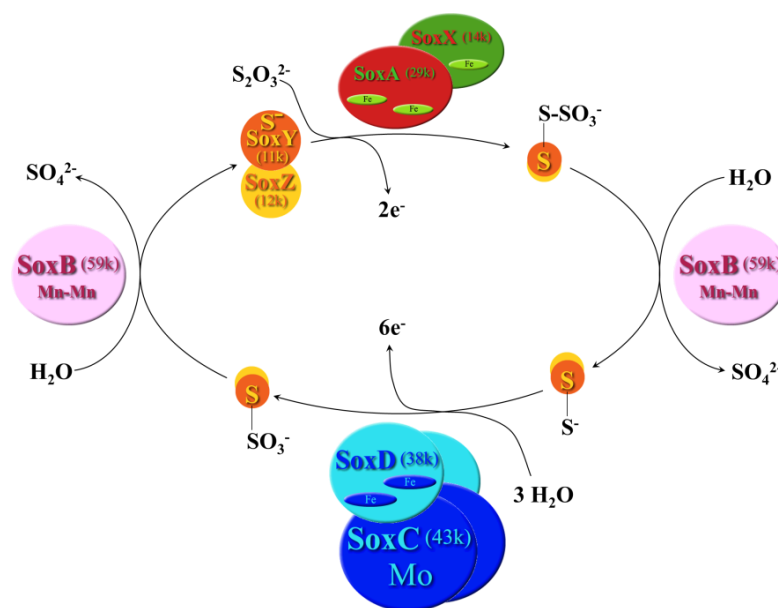


Figure 5.1.2: The Global TOMES mechanism of thiosulphate oxidation to sulphate. The process incorporates the 'shuttle' and is also used in some organisms for sulphur, sulphide, sulphite and tetrathionate oxidation.

5.2 The SoxAX protein

When *R. sulfidophilum* is grown photolithotrophically in the presence of thiosulphate it expresses a *c*-type cytochrome (7). This *c*-type cytochrome (now known as SoxAX) was isolated from the periplasm of the photosynthetic marine bacterium *Rhodovulum sulfidophilum* by Appia-Ayme *et al* in 2001 (8). Analysis by SDS-PAGE and electrospray mass spectroscopy showed that the enzyme is a heterodimer, in which the individual subunits have molecular masses of 18 kDa and 30 kDa. These subunits were designated SoxX and SoxA respectively and sequence analysis showed the former subunit to contain one covalently-bound *c*-type heme, while the latter contained two. This sequence data revealed three CXXCH binding motifs, with the His⁸⁰ and His¹⁸¹ residues ligated in the

proximal position to the two hemes of the SoxA subunit. Subsequent spectroscopic analysis by Cheesman *et al* (9) defined the axial ligation to the two Sox A hemes (known as ‘Hemes 1 and 2’ hereafter) as Cys⁻/His, while the single heme of SoxX (‘Heme 3’) is His⁴⁶/Met⁹² ligated. This made SoxAX the first naturally-occurring *c*-type cytochrome to be isolated with thiolate coordination to a heme centre. The amino acid sequences of the SoxA and SoxX subunits from different strains of sulphur-oxidising bacteria are shown in *Figure 5.2.1*. Crystallographic studies (1.75 Å resolution) on SoxAX isolated from *R. sulfidophilum* (10,11) have shown that the protein is an elongated molecule of dimensions 34 x 36 x 74 Å³. The interplanar distance of closest approach between Hemes 1 and 2 and Hemes 2 and 3 is 23.9 and 10.7 Å respectively. Previous studies by Page *et al* (12) have indicated that for efficient electron transfer to occur between two redox centres, without the inclusion of cofactors, a distance of 14 Å or less must be attained.

SoxA

Rhodovulum sulfidophilum 70
Paracoccus denitrificans
Thiobacillus denitrificans
Roseovarius sp. 217
Starkeya novella

80 110

.....|.....
Rhodovulum sulfidophilum 159
Paracoccus denitrificans
Thiobacillus denitrificans
Roseovarius sp. 217
Starkeya novella

.....|.....
Rhodovulum sulfidophilum
Paracoccus denitrificans
Thiobacillus denitrificans
Roseovarius sp. 217
Starkeya novella

.....|.....
Rhodovulum sulfidophilum 250
Paracoccus denitrificans
Thiobacillus denitrificans
Roseovarius sp. 217
Starkeya novella

.....|.....
Rhodovulum sulfidophilum 261
Paracoccusdenitrificans
Thiobacillus denitrificans
Roseovarius sp. 217
Starkeya novella

SoxX

Rhodovulum sulfidophilum -----
 MRGMGLTTTCTALWASAGPGFAAEVAPGDVAIDGQSHVARPLTDAPGDEVE 29
Paracoccus denitrificans -----
 MSSHLWHAADVVAIAATPAICETAPKDVDAEAGAVEASLTGVPGNDEE
Thiobacillus denitrificans -----
 MRKLHQLITACALGTIALTGNALAAEPAKE--PS
Roseovarius sp. 217 -----MKRSIFTVSLICAAALSASAAEVAPTVDVKFT-
 DGAIDASLITGVAGDEVA
Starkeya novella
 MRFEITLLKRAAOVGALVLLPLAAHAEASAVDPARVDVAVKTSFTKLPEGWESRLOODETORICSVTRNNPSPFOAAAIMKAEVRIKFFPAGPVLGSKWD



46

Rhodovulum sulfidophilum RRLMTDR-----SVENCIACHEVTEMADAQFPITVGPISLDGVAAR---YP-
 EAMIRSLIVNSKNVPEETVPAYYRVEGCFNRPGIAFTSKP 112
Paracoccus denitrificans YRVMTFN-----ALNCVACHQIGALPDVEFPITAIAPPLDGAAAR---WT-
 EAQLRLIVANAKMTFEGTFPAFYKGEQFVRPGDGETGKA
Thiobacillus denitrificans KELAFNN-----KKNCCLACHGMPTVPDAVSTMYGPPLIAMSAR---YPDKAKLRAQIWDATVANPSTTIIPFGK-----

Roseovarius sp. 217 RDLVLDGR-----ALNCVACHQITDMSDVPFHEIGPMLDGAGSR---WS-
 EADLRSLIVVNAKMMFPESLPSFYRTDYTRPGNAFTGEA
Starkeya novella AKVAQNRRGGQFSDPPGTVSGENCYACHQLD--PKEVSYTLGPSLVGYGRERNFSAEDAKIAFAKVYDAQASLACSSIPRFG-----

138

Rhodovulum sulfidophilum IEGEIRFLMTAGQIEDVVAYLMTLTQ
Paracoccus denitrificans GTEPLAFILNAQQIEDVVAFLVTLKE
Thiobacillus denitrificans ---HGVLTEAIEDKVIDFVYGL---
Roseovarius sp. 217 ADSTFGFLLTAQQVEDVVAYLVTLKE
Starkeya novella ---VNGVLTEQQIKDVVALEYLDPESPVNN

Figure 5.2.1: Amino acid sequence of the SoxA and SoxX subunits of the SoxAX protein from different strains of sulphur-oxidising bacteria. The sequence of SoxAX from *R.sulfidophilum* (8) was used in a BLAST search (<http://blast.ncbi.nlm.nih.gov/Blast>) with alignments being generated with the ClustalW program using default parameters (<http://www.ebi.ac.uk/Tools/clustalw2/index.html>).  Denotes amino acid conservation in species that produce Heme-1 containing SoxAX  Denotes amino acid conservation in all species that produce SoxAX cited here.

With this in mind, the current opinion is that electron transfer away from the complex occurs between Hemes 2 and 3. During catalysis, two electrons are transferred from the substrate to Heme 3 (via Heme 2), which then passes consecutive single electrons to two ferricytochromes *c* (13). The X-ray crystal structure of SoxAX is shown in *Figures 5.2.2 and 5.2.3*.

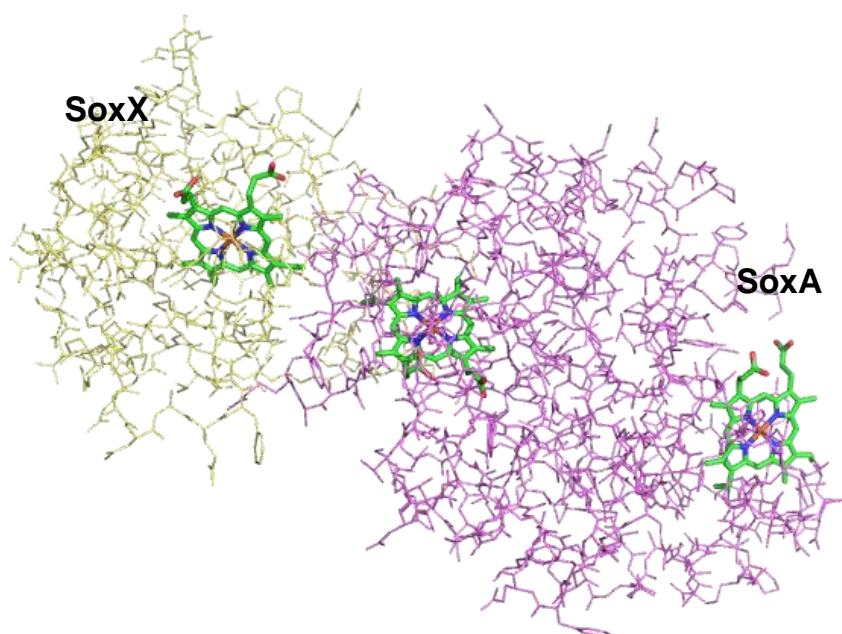


Figure 5.2.2: X-ray crystal structure of SoxAX from *R. sulfidophilum* (PDB 1H31 (10)).

The distal cysteine ligand of Heme 2 lies exposed to the bottom of a solvent-filled channel lined with basic arginine and lysine residues. This, coupled with the fact that this ligand has been seen to undergo a post-translational modification to a cysteine persulphide in the crystal structure has led to the conclusion that this heme is the active site. Inspection of the molecular surface in the Heme 2 region shows an apparent binding site for SoxYZ in the form of a groove (10). The function of Heme 1 is as yet unknown and there is currently no evidence to suggest that it plays any part in the catalytic process. The amino acid sequence alignment would suggest that SoxA (excluding the N-terminal 50 amino acids) evolved from the duplication of a cytochrome *c* gene.

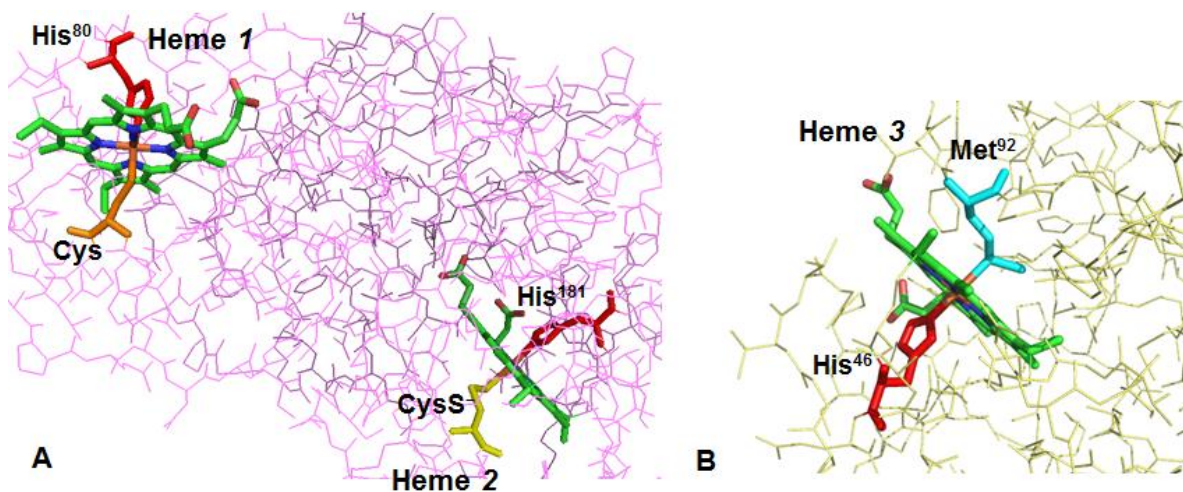


Figure 5.2.3: X-ray crystal structure of SoxAX from *R. sulfidophilum* showing [A] ligation to Hemes 1 and 2 and [B] ligation to Heme 3 (PDB 1H31 (10)).

The SoxAX complex has also been isolated from *Paracoccus pantotrophus* (6,14) and *Starkeya novella* (5), although in the latter the Heme 1 is replaced by a disulphide bond. The possibility must therefore be considered that in *R. sulfidophilum* and *P. pantotrophus*, Heme 1 is an artefact of evolution and serves no relevant function in the catalytic mechanism. However, in these particular species of bacteria, the Heme 1 of SoxAX may fulfil a purpose relevant to the enzyme function that is as yet unresolved.

Bamford *et al* (10) proposed a possible model for the mechanism attachment of thiosulphate to SoxYZ, catalysed by SoxAX. This model is based on the mechanisms employed by the sulphur transferase enzyme rhodanese, a protein that displays activity across all organisms and is thought to play an important role in cyanide metabolism (15). Rhodanese also catalyses the transfer of a sulphane sulphur atom from an anionic donor to an acceptor in a non-physiological mechanism, which proceeds via an intermediate form of the enzyme in which a persulphide linkage is bound to a cysteine residue (16). At the active site, a mobile proximal arginine ligand lies adjacent to the catalytic cysteine residue where it (along with four other basic residues and a number of peptide dipoles) helps to create a strong positive electrostatic field. It has been suggested (10) that this positive

electrostatic field helps to provide a highly-stabilised anionic binding site for the substrate sulphonyl group. SoxAX from *R. sulfidophilum* contains a similar conserved proximal arginine residue, Arg²¹⁸ which has been suggested to provide an anionic binding site for the sulphonyl group of thiosulphate. The mechanism proposed (10) is illustrated in *Figure 5.2.4*.

After binding to Arg²¹⁸, the thiosulphate molecule is transferred to the adjacent cysteine group of Heme 2. This is a two-electron oxidative process that produces a Sox-A-thiocysteine-S-sulphate intermediate (*Figure 5.2.4, Structure b*). When the SoxYZ complex docks on the surface of the active site, the SoxY-S-SO₃ product is formed, and the original complex is restored (*Figure 5.2.4, Structure d*). Alternatively, it is suggested that the binding of SoxYZ could result in a cysteine persulphide intermediate (as observed in the crystal structure), which leads to the subsequent release of a sulphite molecule. However, it is noted that this intermediate could also form in the absence of SoxYZ as a result of the reductive breakdown of the Sox-A-thiocysteine-S-sulphate intermediate.

5.3 Other cysteinate-bound hemes: the cytochromes P450

The cytochromes P450 are an important and well-known superfamily of cysteine-coordinated *b*-type oxygenases. Encountered throughout nature, *cytochrome* P450 enzymes are responsible in mammals for the metabolism of drugs, xenobiotics and fat-soluble vitamins, along with the synthesis of steroid hormones. In plants they perform a similar role, synthesising hormones, and helping to protect the organism by breaking down herbicides (17).

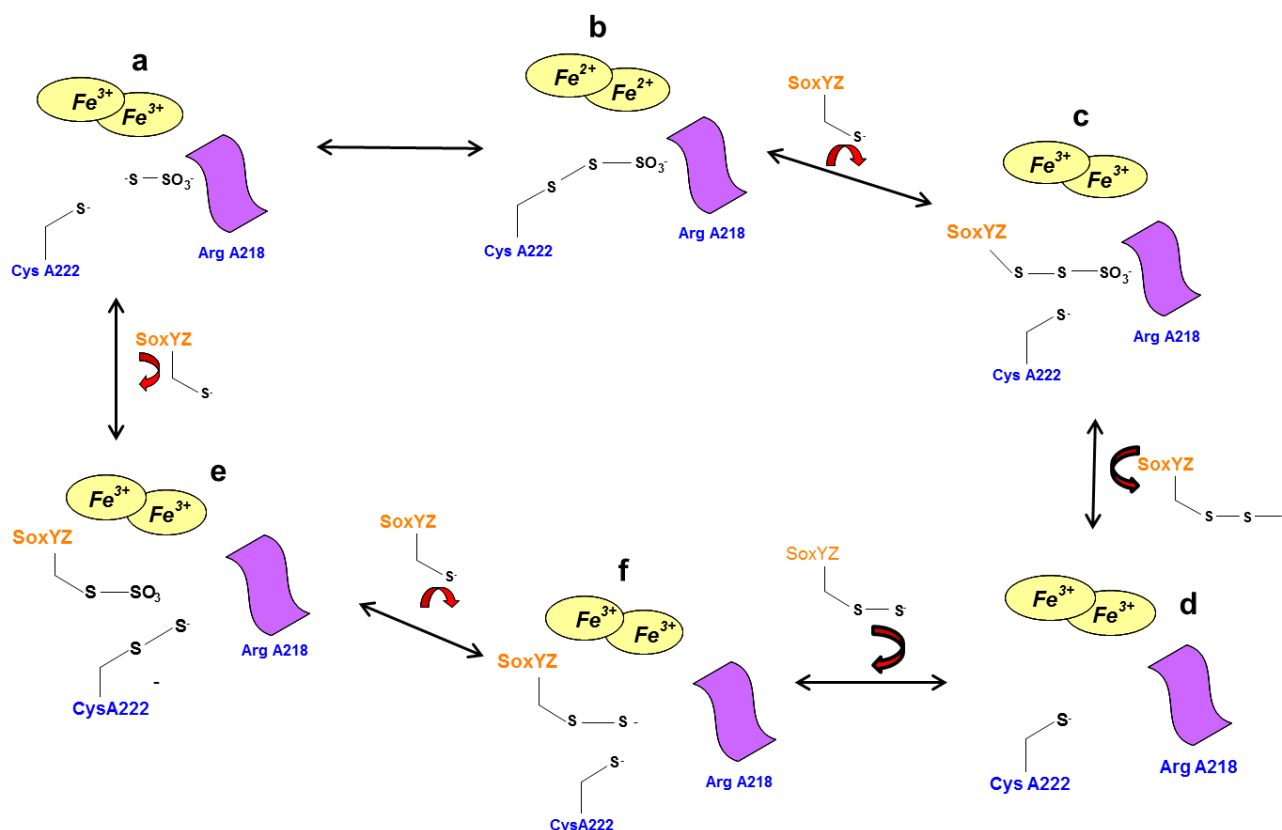


Figure 5.2.4: A possible mechanism for the oxidation of the thiosulphate-SoxYZ complex by SoxAX as proposed by Bamford *et al* (10).

The cytochrome P450 family is comparable to SoxAX in that there is also an axial thiolate ligand coordinated to the metal centre, albeit at the proximal rather than the distal position. In the resting (ferric) state, the other axial ligand is not another amino acid, but is a weakly-bound water molecule. This means that the imidazole-bound cytochromes P450 enzymes represent a decent model for the thiolate-bound Hemes 1 and 2 of SoxAX. The name P450 originates from the characteristic Soret band observed at 450 nm when CO is coordinated to the ferrous heme in place of water. The P450 catalytic cycle (illustrated in *Figure 5.3.1*) begins with the binding of the substrate (perturbing the distal H₂O ligand), generally resulting in a high-spin complex with a higher reduction potential (*Structure b*, *Figure 5.3.1*).

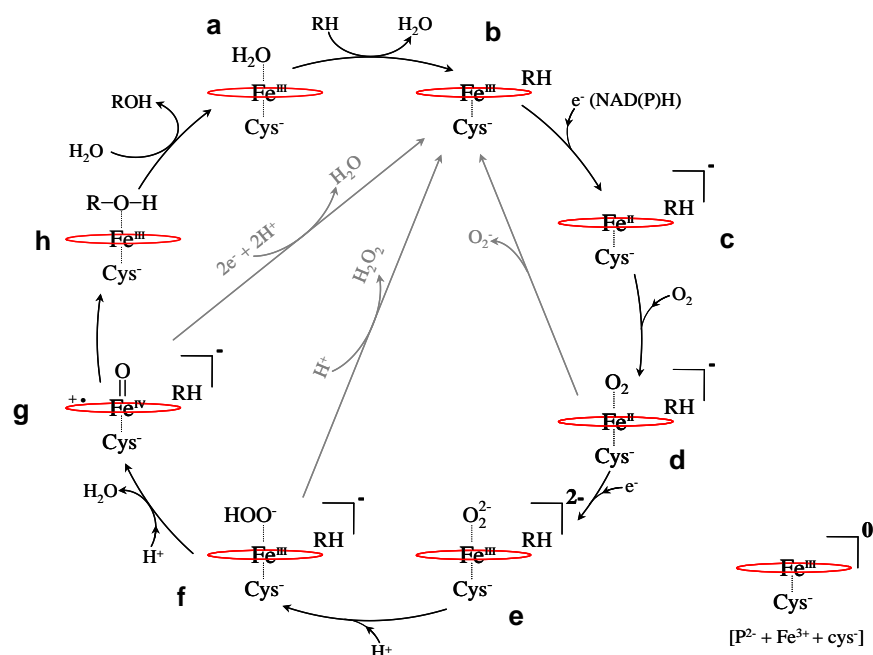


Figure 5.3.1: General oxygenase mechanism of the *cytochromes P450* (Figure courtesy of Dr M. Cheesman).

The binding of di-oxygen then takes place (to yield *Structure d*, *Figure 5.3.1*), followed by reduction and protonation to yield a hydroperoxo-ferric intermediate (*Structure f*, *Figure 5.3.1*). Further protonation results in the release of water and an intermediate consisting of a single oxygen atom bound to the Fe^{4+} metal centre (*Structure g*, *Figure 5.3.1*). The final step involves the monooxygenation of the substrate to form the product complex (*Structure h*, *Figure 5.3.1*).

Replacement of a heme axial ligand with another can affect the appearance of the UV-visible absorbance spectrum, hence the need for a pyridine hemochrome test to accurately calculate the molar extinction coefficient. These changes in ligation often also have a dramatic effect on the g-values of the EPR spectrum. For example, the change that occurs in the EPR signature (from Type 'I' to a 'Type II') on reorientation of the planes of axial histidine ligands from perpendicular to parallel (18).

In the case of thiolate-bound hemes, the appearance of both the electronic absorbance and EPR spectra is largely determined by the RS^- coordination to the iron.

Therefore, regardless of the identity of the distal axial ligand, the P450 enzymes give rise to a distinctive combination of UV-visible absorbance and EPR spectra. The absorbance spectrum of the ferric state is typical of a *b*-type heme, however, upon reduction there is no appearance of the usual sharp α -band. Further, whilst shifting slightly depending on the nature of the distal ligand, the rhombic EPR *g*-values are close to 1.90 (g_x), 2.25 (g_y) and 2.5 (g_z), as opposed to the greater spread in *g*-values associated with typical ‘Type II’ spectra. Additionally, the Cys⁻/H₂O ligation at the *b*-type heme gives rise to a distinctive band in the NIR-MCD spectrum at 1080 nm (19). Comparison of published EPR and MCD data for imidazole-bound P450 (among others) with SoxAX provided compelling evidence that Hemes 1 and 2 are nitrogenous/cysteinate-bound (9).

5.4. Experimental

5.4.1 *SoxAX preparation and purification*

The recombinant cytochrome *c*-type heterodimer SoxAX was purified according to the method of Appia-Ayme *et al* (8) by B. Berks at Oxford University. There were some changes made to this method however; the plasmid was expressed in *Rhodobacter capsulatus* rather than *Rhodobacter sulfidophilum*, and the protein was induced by DMSO. The following gives an overview of the cloning, mating, growth and purification methods undertaken to produce the SoxAX protein used in spectroscopy experiments.

5.4.2 *Cloning of SoxAX for recombinant expression**

Primers MKS001 (forward) and MKS002 (reverse) were used to amplify the SoxX gene from chromosomal DNA extracted from *R. sulfidophilum*. SoxA and the SoxA ribosome binding site were amplified from *R. sulfidophilum* chromosomal DNA using MKS003

* Procedure carried out by Dr B. Berks at Oxford University

(forward) and MKS006 (reverse) primers. The SoxX amplicon was digested with BamHI and ligated into BamHI and SmaI-digested pGEM-7Zf(+) to give plasmid PMKS01. Meanwhile, the SoxA amplicon was digested with SpeI and XbaI and ligated into the same sites in pMKS01, resulting in the plasmid pMKS08.

Plasmid pMKS08 was digested with XbaI and BamHI to remove the SoxXA genes and cloned into the same sites in (XbaI-BamHI) pDorex to give plasmid pMKS10. Following digestion with XbaI and HindIII, pMKS10 was cloned into the same sites in digested (XbaI-HindIII) pRK415 to produce plasmid pMKS12, which was confirmed by sequencing and transformed into *E. coli* S17-1 cells. The *E. coli* S17-1 cells (containing pMKS12) were conjugated with *R. capsulatus* strain 37B4 Δ dorA, resulting in *R. capsulatus*/pMKS12, which was used for preliminary expression and purification.

5.4.3 Growth and purification of the SoxAX protein*

The first starter culture was grown on *Rhodobacter capsulatus* V (RCV) medium containing 1 $\mu\text{g mL}^{-1}$ tetracycline under a tungsten lamp at $\sim 28^\circ\text{C}$. Large scale growth was initiated by adding 80 mL of starter culture to 5 L of RCV, along with 60 mM DMSO and 1 mM sodium molybdate. After a growth period of 5–7 days (at 28°C), the cells were harvested and a periplasmic fraction isolated. Purification of the recombinant SoxAX was carried out according to the method of Appia-Ayme *et al* (8) with two exceptions; spheroplasts were prepared with buffer containing Na_2EDTA (1.5 mg mL^{-1}) and lysosyme (5 mg mL^{-1}) and the final perfusion chromatography step was not performed. Glycerol was added to fractions 13 to 24 (hereafter known as ‘batches’ 13 to 24) of the semi-pure enzyme and the samples sent to UEA for final purification and analysis.

5.4.4 Purification of SoxAX

Purification and spectroscopic characterisation was carried out at the University of East Anglia as part of this work. UV-visible absorbance and X-band EPR (10 K 2 mW) spectra of all batches of semi-pure protein were recorded.

A phenyl sepharose hydrophobic interaction column (HIC) (poured using phenyl sepharose purchased from Sigma; approx. 40 μ moles per mL, 20 % ethanol suspension, approximate total static column volume = 21 mL) was equilibrated with 105 mL of Buffer A (50 mM Tris, pH 7.80, 25 % saturation ammonium sulphate) using an Äkta Prime (Amersham Pharmacia Biotech) at a flow rate of 1 mL min⁻¹. Ammonium sulphate (to 25 % saturation) was slowly added to the sample of *R. sulfidophilum* recombinant SoxAX while stirring. The entire volume of sample (approximately 12 mL depending on the particular batch purified) was introduced directly onto the column without use of the sample loop.

The column was flushed with two volumes of Buffer A to ensure complete loading of the sample. The column was then eluted with an increasing percentage (0–100%) of Buffer B (50 mM Tris, pH 7.80), over a volume of 46 mL (0.5 mL min⁻¹), with the eluent being collected in 2.5 mL fractions. Following this, the column was flushed with a further five column volumes of Buffer B to ensure complete elution of the protein. The purified SoxAX eluted over 6–7 fractions, as evidenced from the red colouration of the solutions. These were analysed by UV-visible absorbance spectroscopy and sodium dodecyl sulphate polyacrylamide gel electrophoresis (SDS-PAGE) using a Coomassie stain.

Fractions of comparable concentration and purity (as judged by UV-visible spectroscopy and gel electrophoresis) were then combined, and the salt removed by ultrafiltration with an Amicon YM10 membrane using 50 mM TRIS pH 7.80 or dialysis (against the same buffer using a Pierce Slide-A-Lyser cassette).

5.4.5 *Ligand additions to R. sulfidophilum SoxAX*

Stock solutions (500 mM) of KCN and NaF in ultrapure Tris/HCl buffer (pH 7.80) were prepared. A 2.6 μL aliquot of the KCN stock solution was added to 220 μL (14 μM) of the ‘as prepared’ SoxAX and the resulting mixture equilibrated for 20 minutes. Following this, the UV-visible absorption spectrum was measured to probe any ligand binding events. This process was repeated twice resulting in a final KCN concentration of 17.1 mM. Binding of fluoride was probed using an identical procedure with NaF in place of KCN, although in this case a larger excess of ligand (up to a maximum of 52.8 mM) was used. X-band EPR spectra were recorded of $\sim 14.9 \mu\text{M}$ ‘as prepared’ SoxAX with $\sim 56 \text{ mM}$ KCN, NaF and NaN_3 .

The addition of KCN (titrated to a maximum final concentration of 22.9 mM) to SoxAX (7.5 μM) pre-reduced with excess sodium dithionite was carried out in an anaerobic glove box ($< 5 \text{ ppm O}_2$) and the UV-visible absorbance spectrum measured. This process was repeated (on 113 μM ‘as prepared SoxAX with 345 mM KCN) and the X-band EPR spectra measured at 10 K, 2 mW.

Absorbance spectra were recorded using a Hitachi U-2900 spectrophotometer. EPR spectrometer instrumental details were as stated in Chapter 3, Section 3.2.4.

5.5. Results

5.5.1 *Spectroscopic characterisation of recombinant R. sulfidophilum SoxAX*

Unless otherwise stated, all spectra reported here refer to the enzyme purified according to the method detailed in Section 5.4 without further modification. A typical absorbance spectrum of SoxAX is shown in *Figure 5.5.1*.

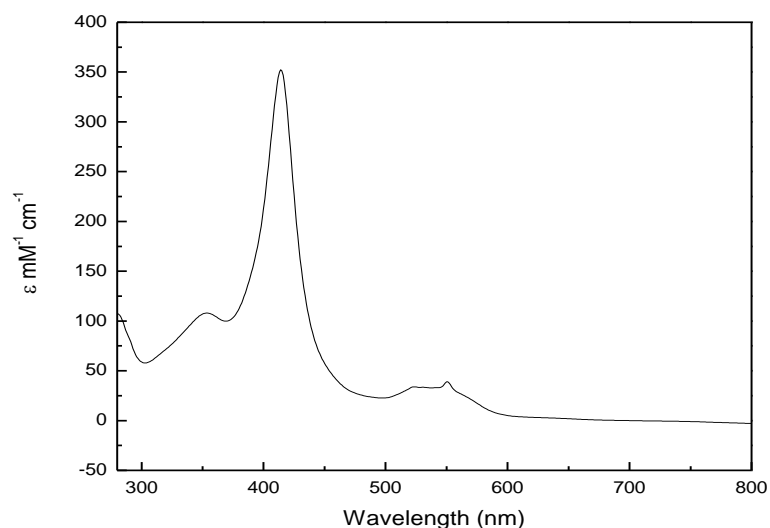


Figure 5.5.1: Room-temperature UV-visible absorbance spectra of SoxAX from *R. sulfidophilum*. — As purified, 47.0 μM . Sample was in 50 mM TRIS buffer, pH 7.80.

Features in the spectrum are comparable with those previously reported (9). Protein concentration was estimated using the Soret band extinction coefficient at 413 nm ($\epsilon_{413 \text{ nm}} = 350 \text{ mM}^{-1} \text{ cm}^{-1}$). An example of the SDS-PAGE gel obtained for *R. sulfidophilum* SoxAX after the final purification stage is shown in *Figure 5.5.2*. Two main bands are observed, corresponding to molecular masses of approximately 31 and 16 kDa, assigned to the SoxA and SoxX subunits respectively. These are in good agreement with the literature values obtained for SoxAX from *R. sulfidophilum* (8).

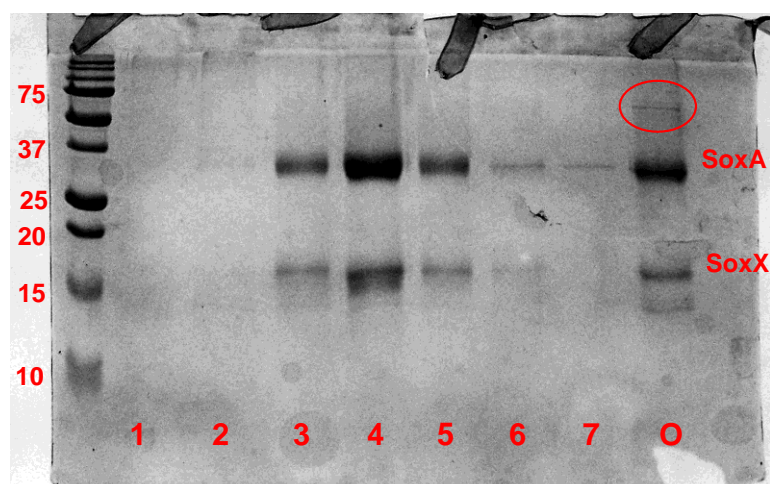


Figure 5.5.2: SDS-PAGE gel (Coomasie stain) of fractions of *R. sulfidophilum* SoxAX after purification with a phenyl sepharose column (details given in Section 2 of this chapter). The sample was in 50mM TRIS buffer,

pH 7.80. Lanes 1–7 contained the fractions obtained from the phenyl sepharose column that was used for purification of the protein (Section 5.4.4).

The X-band EPR spectrum (10 K, 2 mW microwave power) of *R. sulfidophilum* SoxAX is shown in Figure 5.5.3. Features displayed in the spectrum were in good agreement with those described previously by Cheesman *et al* (9). Features at $g = 5.90$, $g = 4.30$ and $g = 2.00$ occur due to small amounts of high-spin ferric heme, adventitious iron and adventitious copper respectively. The remaining spectral features were assigned to least three other low-spin ferric heme centres. The first of these, the His/Met coordinated Heme 3 gave rise to the ‘Large g_{\max} ’ spectrum (18) at $g = 3.50$. The two overlapping rhombic (‘Type II’) spectra (at g -values of $g_{z,y,x} = 2.54, 2.30, 1.86$ and $g_{z,y,x} = 2.42, 2.26, 1.92$ respectively) were assigned to the His/Cys[−] coordinated Hemes 1 and 2.

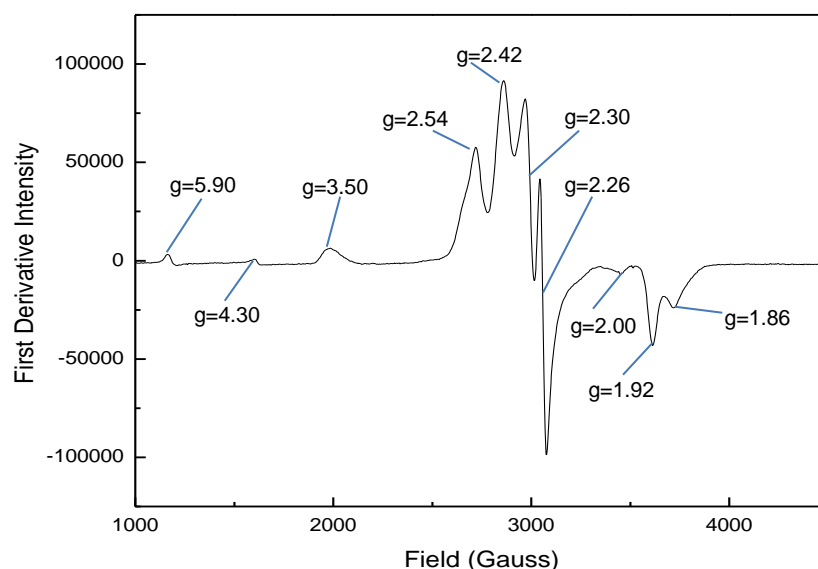


Figure 5.5.3: X-Band CW EPR spectra of —*R.sulfidophilum* SoxAX(as prepared, $\sim 160\mu\text{M}$) in 50mM TRIS buffer, pH 7.80. Spectrometer parameters: power, 2 mW; modulation amplitude, 1 mT; temperature, 10 K. Features are consistent with those previously described in the literature (5).

Cheesman *et al* (9) first published the EPR spectrum of *R. sulfidophilum* SoxAX in 2001, terming these two overlapping rhombic spectra LS₁ and LS₂. Following comparison of the LS₁ and LS₂ g -values with the EPR spectra obtained for the imidazole derivatives of

P450 (19,20), eNOS (21) and CoxA (22), it was concluded that these species were axially-bound by nitrogenous and cysteinate-thiolate ligands. However, although this comparison provided compelling evidence that LS₁ and LS₂ are axially coordinated by a thiolate species, it did not confirm the identity of the nitrogenous ligand in each case. Subsequent X-ray crystal structure determination confirmed the proximal ligand to be histidine in each case (9).

Although the g-values observed for LS₁ and LS₂ corresponded well with those obtained for other nitrogenous/thiolate-bound species, NIR-MCD data was still required to conclusively prove the ligand assignments made from the EPR spectra. The NIR-MCD reported (9) confirmed the EPR assignment, with significant intensity at 1150 nm. However, contrary to the initial assignment, all intensity at longer wavelengths is now attributed to the His/Met-bound Heme 3 (23).

The UV-visible MCD spectra of oxidised *R. sulfidophilum* SoxAX revealed a sharp derivative feature centred at 685 nm (at both room and low temperatures), which was unambiguously assigned to His/Met coordinated ferric *c*-heme based on previous observations (24-26). The observation of a prominent CT band in the low temperature spectrum (at 4.2 K) at 1900 nm (corresponding to the 'Large g_{max}' spectrum observed in the EPR), diagnostic of His/Met coordination (27,28) led to the conclusion that the 685 and 1900 nm MCD bands observed were due to Heme 3, located in the SoxX subunit.

The thiolate-bound Hemes 1 and 2 give rise to NIR-MCD intensity at 1150 nm. It was estimated from the value of $\Delta\epsilon$ that this feature could not account for two *c*-type hemes and as a consequence the feature at approximately 1500 nm was attributed to cysteinate-persulphide coordination at Heme 2 (9). However, it is now thought (23) that the thiolate-bound hemes give rise to intensity exclusively at 1150 nm and therefore either

Hemes 1 or 2 (or both) have an intrinsically weaker CT_{ls} band than those observed for cytochrome P450s.

Recent work (23) carried out with the aim of resolving the heme-based redox chemistry of *R.sulfidophilum* SoxAX has revealed some important implications for the interpretation of the previous spectroscopic findings by Cheesman *et al* (9). EPR and MCD-monitored potentiometric titrations were carried out on recombinant *R. sulfidophilum* SoxAX that had been expressed and purified according to the method outlined in Section 5.4. X-ray crystallographic data revealed that the ligation for the recombinant protein was as observed previously for the native structure (10). However, the potentiometric titrations revealed that Heme 3 has a midpoint potential (vs. SHE) of $+ 210 \pm 20$ mV whilst Hemes 1 and 2 have midpoint potentials of approximately $- 340 \pm 20$ mV and $- 400 \pm 20$ mV respectively (v. SHE).

5.5.2. *Ligand-binding trials on R. sulfidophilum SoxAX*

Although the work by Bradley *et al* (23) prompted re-assignment of the spectral signatures of SoxAX, it does not offer any new insight into whether or not Heme 2 is the active site of the enzyme. In an effort to resolve this, a series of ligand binding trials (LBTs) were carried out using a range of inorganic compounds. This would ascertain whether either Hemes 1 or 2 (or possibly both) have labile axial ligation as would be expected for the active site of an enzyme. Displacement of a thiolate ligand would result in an alteration of either one of the LS₁ or LS₂ EPR spectra, giving rise to g-values that are typical of ‘normal’ c-type heme.

Initial LBTs were followed by UV-visible spectroscopy since displacement of a thiolate ligand(s) would also be expected to influence features in the absorption spectrum.

The experimental procedures used are detailed in Section 5.4.5 of this chapter and the spectra obtained are shown in *Figures 5.5.4* and *5.5.5*.

Figure 5.5.4 shows the UV-visible absorption spectra obtained after a 500 mM stock solution of KCN was titrated into a 14.0 μM solution of ‘as prepared’ *R. sulfidophilum* SoxAX. The initial addition of 5.8 mM CN^- caused a red shift in the λ_{max} of the Soret band from 412 nm to 414 nm (see Inset A of *Figure 5.5.4*), and an increase in the maximum absorbance ($\Delta\epsilon = 4 \text{ mM}^{-1} \text{ cm}^{-1}$). This was coupled with a simultaneous red shift of the α/β region (see inset B of *Figure 5.5.4*). Although it appeared that the intensity of the α/β band had increased very slightly (to a lesser extent than that of the Soret band), this was most likely due to baseline shift. Further additions of CN^- caused a slight increase in the maximum absorbance of the Soret band ($\Delta\epsilon = 1\text{-}2 \text{ mM}^{-1} \text{ cm}^{-1}$), and no further wavelength shift. These observations indicate a CN^- ligand substitution at one or more of the heme centres may have taken place. Adding NaF to a solution of ‘as prepared’ *R. sulfidophilum* SoxAX (*Figure 5.5.5*) did not cause a shift in the Soret wavelength (Inset A, *Figure 5.5.5*), even when the concentration of ligand was increased to as much as 52.8 mM. Any changes in band intensity in both the Soret and α/β regions (Inset B, *Figure 5.5.5*) were due to dilution effects and baseline shift.

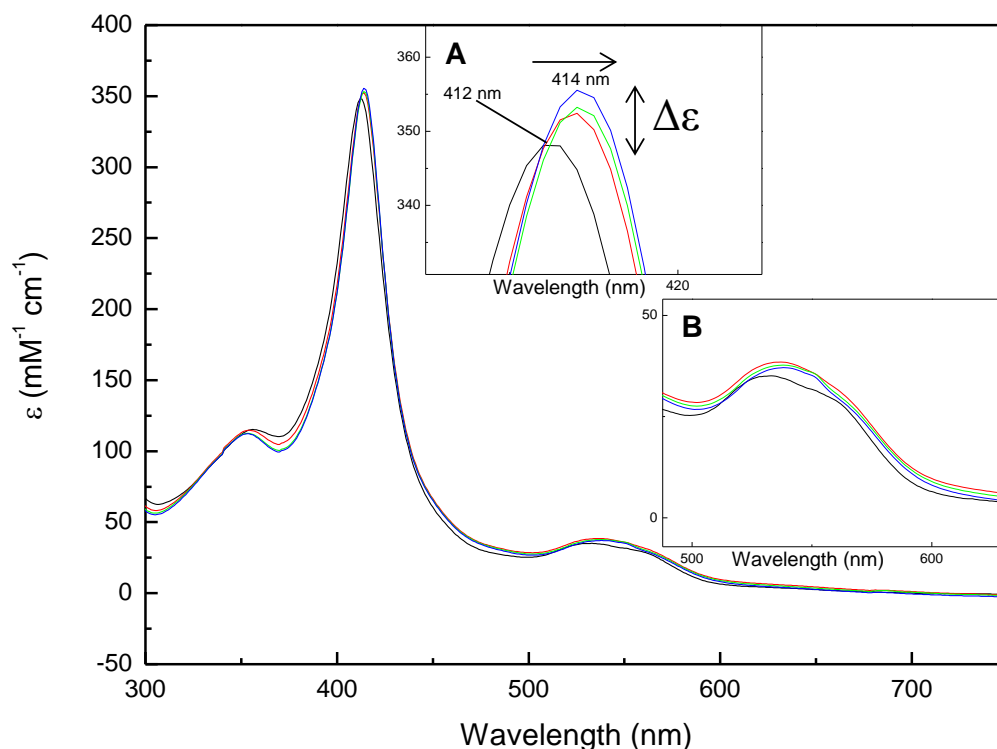


Figure 5.5.4: Room-temperature UV-visible absorbance spectra of SoxAX from *R. sulfidophilum*.— As prepared, 14.0 μM , — after the addition of 5.8 mM KCN, — after the addition of 11.5 mM KCN, — after the addition of 17.1 mM KCN, Samples were in 50 mM TRIS buffer, pH 7.80. Insets A and B show the Soret and α/β regions of the spectra, respectively in detail.

As F^- is a weak field ligand, replacement of a distal cysteinate for this species would cause the ferric iron to adopt the high spin state, causing a blue shift in the Soret and α/β bands in the absorbance spectrum (29). It is therefore very unlikely that an actual ligand substitution took place in which the F^- became coordinated to one of the three low-spin ferric hemes in the protein. Whilst some modification of the absorbance spectrum is evident upon addition of CN^- (Figure 5.5.4), these changes are not sufficient to suggest displacement of a thiolate ligand from one heme equivalent in the enzyme. CN^- (like thiolate) is a strong field ligand and would therefore not cause a change in the spin state of the ferric iron upon binding. Any resulting changes in the electronic absorption spectrum upon binding CN^- will therefore be minor. However, the EPR spectrum of the CN^- -bound form would be expected to display significantly reduced intensity in either the LS_1 or LS_2 envelope.

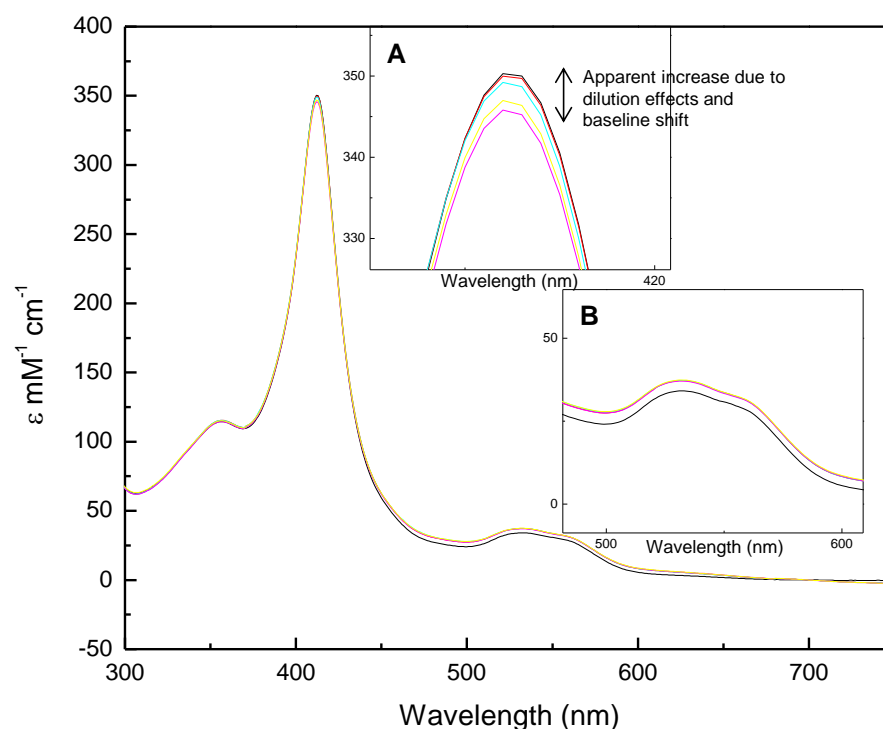


Figure 5.5.5: Room-temperature UV-visible absorbance spectra of SoxAX from *R. sulfidophilum*.— As prepared, 14.4 μM , — after the addition of 5.8 mM NaF, — after the addition of 22.6 mM NaF, — after the addition of 27.9 mM NaF, — after the addition of 52.8 mM NaF. Samples were in 50mM TRIS buffer, pH 7.80. Insets show the Soret and α/β regions of the spectra in detail.

A comparison of the EPR of ‘as prepared’ SoxAX with that obtained post- CN^- is shown in *Figure 5.5.6*. The rhombic LS_1 and LS_2 signals of both spectra were identical, showing that addition of CN^- had not displaced the thiolate ligand from either Hemes 1 or 2. The only apparent changes in the EPR spectrum upon addition of CN^- are the disappearance of the signal at $g \sim 5.90$ (as CN^- binds to the residual high-spin ferric heme) and an upfield shift in the ‘Type I’ signal. The high-spin heme is thought to arise from denatured enzyme and would therefore not be catalytically-relevant.

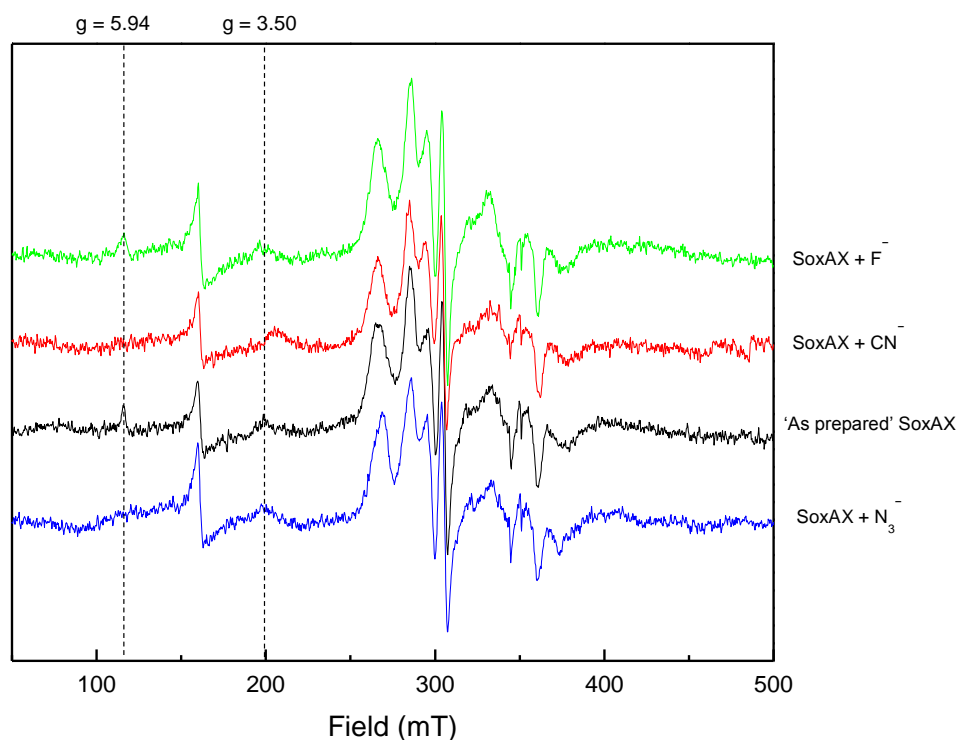


Figure 5.5.6: X-band EPR spectra of SoxAX from *R. sulfidophilum*.— As prepared, 14.9 μM , — after the addition of ~ 56 mM KCN, — after the addition of ~ 56 mM NaF, — after the addition of ~ 56 mM NaN_3 , Samples were in 50 mM TRIS buffer, pH 7.80. Spectrometer parameters: power, 2 mW; modulation amplitude, 1 mT; temperature, 10 K.

The EPR of SoxAX following addition of NaF and NaN_3 (both at ~ 56 mM) were recorded at 10 K. Reaction with NaF would leave the metal spin state unchanged, with the $g \sim 5.90$ feature remaining as F^- is a weak field ligand. N_3^- is situated towards the middle of the spectrochemical series and binding could therefore result in the iron adopting either spin state. The resulting spectra are also shown in *Figure 5.5.6*. Once more, the LS1 and LS2 envelopes are unaltered and neither F^- nor N_3^- cause a shift in the ‘Type 1’ signal at $g = 3.50$.

Upon addition of F^- , the high-spin signal at $g \sim 5.94$ remained in the spectrum, although the linewidth broadened slightly, from ~ 50 Gauss in the ‘as prepared’ sample to ~ 82 Gauss in the NaF-reacted sample. Conversely, the addition of N_3^- causes it to disappear, indicating that as with CN^- a change in spin state has occurred. However, binding of the

N_3^- clearly shows that conversion of the residual high-spin heme to a low-spin state is not sufficient to induce the observed shift in apparent g-value of the ‘Type I’ signal upon addition of CN^- .

As the attempts to displace the cysteine/cysteine persulphide ligands in the ferric state were unsuccessful, the ligand binding trials were repeated on *R. sulfidophilum* SoxAX that had been pre-reduced with excess sodium dithionite. Although the mechanism suggested by Bamford *et al* (10) does not require pre-reduction of Heme 2 to trigger dissociation of the cysteinate-persulphide, this may reduce the affinity of the metal for the thiolate ligand or alternatively lead to an increase in the solvent exposure of the active site.

As-prepared *R. sulfidophilum* SoxAX was reduced with sodium dithionite (3.7 mM) and reacted with a large excess of KCN (~ 490 mM) according to the method outlined in Section 5.4.5 of this chapter. The redox potentials of Hemes 2 and 3 (for SoxAX from *P. pantotrophus*) were previously reported by Reijerse *et al* (30) to be ca. – 496 mV and +184 mV respectively at pH 8.0. Heme 1 was found to be resistant to reduction with sodium dithionite or with 20 mM titanium (III) citrate, indicating that this centre possesses the lowest reduction potential of the three hemes. However, recent work by Bradley *et al* (23) (using a combination of NIR-MCD-, UV-visible- and EPR- monitored potentiometric titrations) has indicated that both thiolate-bound Hemes 1 and 2 in recombinant *R. sulfidophilum* SoxAX (at pH 7.00) are fully reduced at -510 mV. This indicates that sodium dithionite alone, with a reduction potential in the region of – 660 mV (vs. NHE at pH 7.00), should fully reduce both thiolate-bound hemes in the *R. sulfidophilum* enzyme at a solution pH of 7.00. Reijerse *et al* observed that in the case of the *P. pantotrophus* enzyme, increasing the solution pH from 7.00 to 8.00 led to a subsequent decrease in the redox potential of Heme 2 from – 432 mV to – 496 mV (30). If a similar pH-dependence is observed in the recombinant *R. sulfidophilum* enzyme, raising the solution pH to 7.80 (as

in the case of the experiments described here) would cause a similar decrease in the reduction potential of Heme 1, possibly to the extent where it would not be fully reduced to ferrous by sodium dithionite. The X-band EPR spectrum of *R. sulfidophilum* SoxAX reduced with excess sodium dithionite at pH 7.80 is shown in *Figure 5.5.7*.

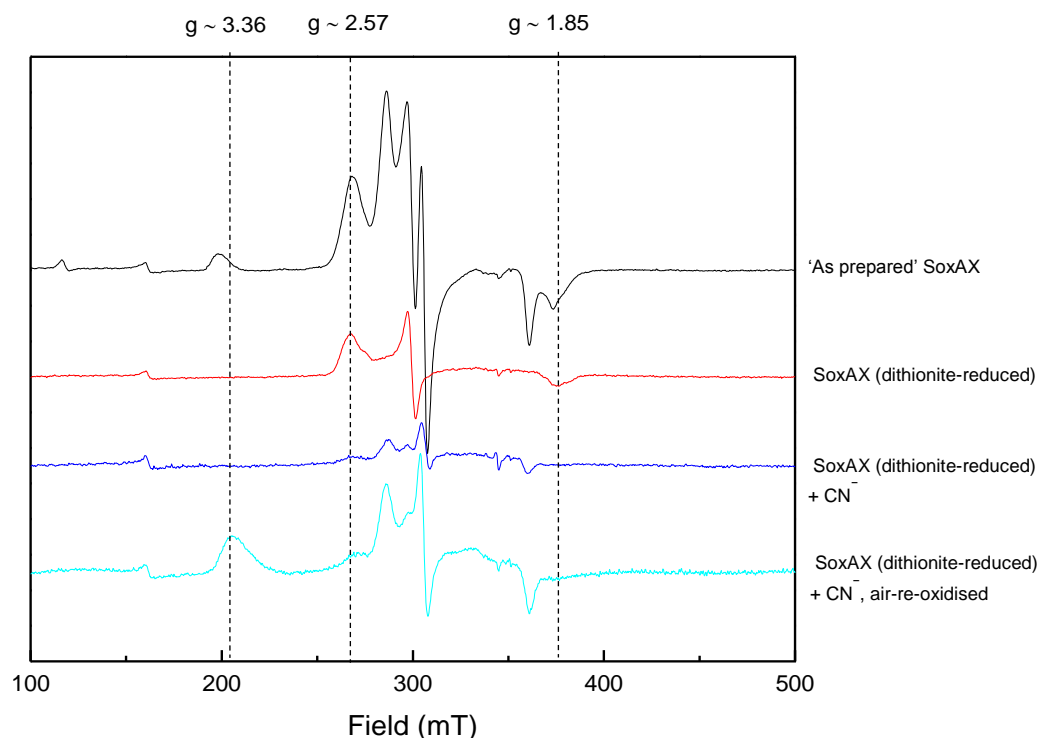


Figure 5.5.7: X-band EPR spectra of SoxAX from *R. sulfidophilum*.— As prepared, 113 μM , — after the addition excess sodium dithionite, — after the addition of $\sim 345 \text{ mM KCN}$, — after re-oxidation of the CN^- reacted sample in air for 90 minutes. Samples were in 50 mM TRIS buffer, pH 7.80. Spectrometer parameters: power, 2 mW; modulation amplitude, 1 mT; temperature, 10 K.

After the addition of dithionite a single rhombic spectrum persists (along with adventitious Fe^{3+} and Cu^{2+} signals at $g = 4.30$ and $g = 2.00$ respectively) with $g_{z,y,x}$ values of 2.57, 2.30 and 1.85, previously assigned to LS_1 .

The intensity of the LS_1 rhombic trio in the dithionite-reduced spectrum is markedly lower than that observed for the 'as prepared' sample, indicating some reduction of this species (or possibly signal saturation). The addition of KCN to the dithionite-reduced sample results in a shift in the LS_1 g values to $g = 2.41$, 2.25 and 1.92, much closer to the values typical of the LS_2 signal. The intensity of this apparent LS_2 envelope is also

markedly reduced compared to the LS_1 signal in the dithionite-reduced sample. Addition of KCN to the partially-reduced sample clearly introduces significant changes to the EPR spectrum. In order to correlate these with those observed for the ‘as prepared’ enzyme, the reduced, CN^- -bound sample was re-oxidised by stirring in air for 60 minutes. The resulting spectrum is also shown in *Figure 5.5.7*. Only a small feature at $g = 2.54$ indicates the presence of ferric LS_1 , indicating the majority of this species has been converted into an ‘ LS_2 -type’ conformation. The ‘Large g_{max} ’ signal, occurring at $g = 3.50$ in the ‘as prepared’ spectrum has shifted upfield to $g = 3.36$ following air re-oxidation, identical to that observed when the ferric enzyme is exposed to CN^- . However, this feature is now markedly increased in intensity and this is clearly associated with a corresponding loss of intensity from the thiolate-bound envelope. Given the similarity between the newly formed ‘Large g_{max} ’ signal and that of the CN^- -exposed ferric enzyme, it is tempting to assign this feature to a His/ CN^- ligated species. This would result from substitution of the Met ligand of Heme 3 and the thiolate ligand of either Heme 1 or 2 (or both) for CN^- .

The effects of binding CN^- to dithionite-reduced SoxAX on the UV-visible absorbance spectrum are shown in *Figure 5.5.8*. Upon addition of CN^- , The Soret band exhibited a red shift from 415 nm (in the fully dithionite-reduced spectrum) to 418 nm and an increase in $\Delta\epsilon$ of $\sim 45 \text{ mM}^{-1} \text{ cm}^{-1}$. Upon re-oxidation in air for 60 minutes, the α/β region resumed the appearance of that in the ‘as prepared’ spectrum. The central wavelength of the Soret band returned to 412 nm upon re-oxidation in air, although this feature remained slightly higher in intensity compared to the ‘as prepared’ spectrum ($\Delta\epsilon \sim 44 \text{ mM}^{-1} \text{ cm}^{-1}$). As with the EPR spectra, these observations indicate that some CN^- remained bound to one of the hemes upon re-oxidation in air.

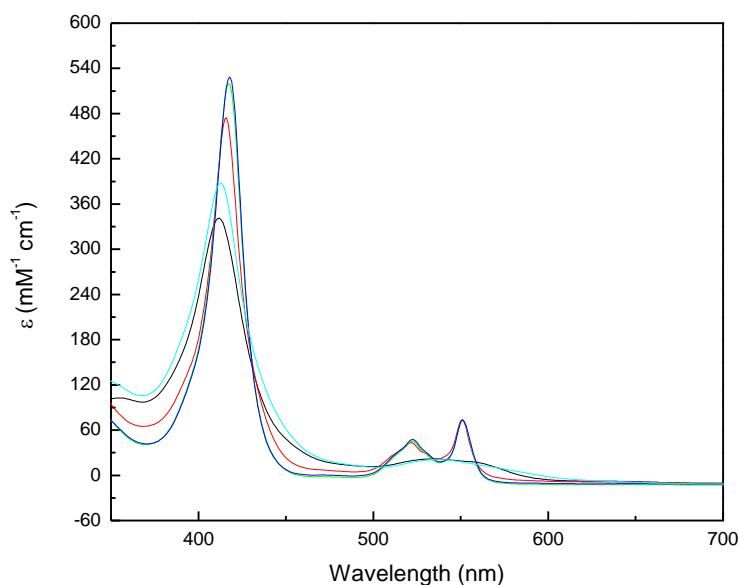


Figure 5.5.8: UV-visible absorbance spectra of SoxAX from *R. sulfidophilum*.— As prepared, 7.5 μM , — after the addition excess sodium dithionite, — after the addition of ~ 5.8 mM KCN , — after the addition of ~ 22.9 mM KCN , — after the addition of ~ 22.9 mM KCN and reoxidation in air for 60 minutes. Samples were in 50 mM TRIS buffer, pH 7.80.

A control experiment was carried out in which *R. sulfidophilum* SoxAX was reduced with excess dithionite and re-oxidised in air without the addition of CN^- . Following re-oxidation in air, the ‘Large g_{max} ’ feature returned to $g = 3.50$, as observed in the ‘as prepared’ spectrum (*Figure 5.5.9*). The feature at $g = 3.36$ viewed previously upon addition of CN^- was not present. However, even after stirring in air overnight, the spectrum did not return to the same intensity as that of the ‘as prepared’ spectrum, indicating some of the sample may have remained in the ferrous state. However, the increase in signals at $g \sim 6.00$ and $g \sim 4.30$ corresponding to high-spin ferric heme and adventitious iron respectively also suggests that some heme may have become detached from the apoprotein.

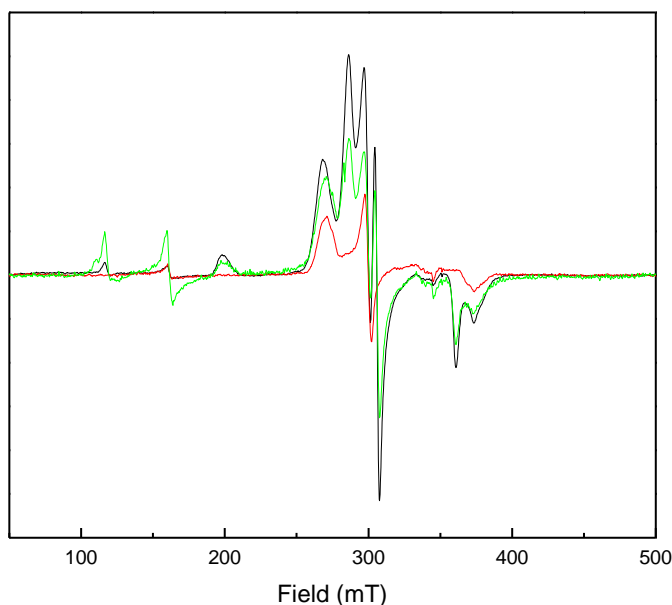


Figure 5.5.9: X-band EPR spectra of SoxAX from *R. sulfidophilum*.— As prepared, 113 μ M, — after the addition excess sodium dithionite, — after the addition of excess sodium dithionite and reoxidation in air overnight. Samples were in 50 mM TRIS buffer, pH 7.80. Spectrometer parameters: power, 2 mW; modulation amplitude, 1 mT; temperature, 10 K.

5.6 Discussion and conclusions

Following a number of observations made from the crystal structure, it was proposed by Bamford *et al* (10) that the Heme 2 of *R.sulfidophilum* SoxAX is the active site of the protein. In an effort to resolve whether this is the case, a series of ligand binding trials (LBTs) were carried out using a range of inorganic compounds. Initially, CN^- , F^- and N_3^- were titrated into samples of the ‘as prepared’ enzyme and the progress of these additions monitored by UV-visible absorbance (CN^- and F^-) and EPR (CN^- , F^- and N_3^-) spectroscopies. Addition of CN^- to a solution of ‘as prepared’ enzyme led to minor changes in the intensity and central wavelength of the Soret and α/β bands of the absorbance spectrum. However, when this experiment was repeated using F^- , a wavelength shift in neither of these features was observed. X-band EPR spectroscopy did not reveal a reduction in the intensity of the LS_1 or LS_2 envelope, indicating binding to the active site

had not occurred. It was concluded that the inorganic ligands had bound to the residual high-spin heme present in the sample that is not thought to be catalytically relevant. Upon addition of CN^- and N_3^- the feature at $g \sim 5.90$ disappeared, indicating this heme had adopted the low-spin state. Conversely, F^- , a weak field ligand caused this feature to persist in the spectrum, indicating the spin state had remained unchanged.

However, when *R. sulfidophilum* SoxAX was reduced with sodium dithionite and reacted with a large excess of KCN, significant changes were observed in the appearance of the LS_1/LS_2 envelope of the EPR spectrum. The addition of sodium dithionite caused a loss in the 'Large g_{max} ' signal attributed to Heme 3 and the $g_{z,y,x}$ values previously assigned (9) to LS_2 . The intensity of the LS_1 rhombic trio was reduced compared to the 'as prepared' spectrum, indicating partial reduction of this centre. Recent spectroelectrochemical studies by Bradley *et al* (23) have shown that all hemes of the protein are reduced at a potential of -500 mV. It is therefore surprising that sodium dithionite, with a reduction potential of -660 mV (vs. NHE at pH 7.00) did not fully reduce all three hemes of the enzyme. The addition of CN^- to the dithionite-reduced sample resulted in a shift in the LS_1 g values to those more typical of the LS_2 signal. This was coupled with a reduction in the intensity of this apparent LS_2 signal compared with that of the LS_1 signal, in the dithionite-reduced sample. Upon re-oxidation of the CN^- -reacted sample in air, the spectrum revealed that the majority of the LS_1 species had been converted into an 'LS₂-type' conformation and the 'Large g_{max} ' signal had shifted upfield to $g = 3.36$, indicating a His/ CN^- ligated species may have been formed.

It is likely that CN^- became bound to either Heme 1 or 2 (or possibly both), replacing an axial thiolate ligand and leading to the appearance of the $g = 3.36$ feature. Additionally, replacement of the methionine ligand at Heme 3 by CN^- may have occurred, again resulting in His/CN coordinated *c*-heme and contribution to the intensity at $g = 3.36$.

More work would need to be carried out, such as investigations by NIR-MCD to ascertain which of the hemes bound the CN^- molecule. However, a complementary NIR-MCD study may still make assignment of the LS_1 and LS_2 rhombic spectra difficult as recent work has shown (23) that both Hemes 1 and 2 contribute to a single CT band at 1170 nm. Site directed mutagenesis may help to assign the LS_1 and LS_2 EPR signals to the relevant hemes. Mutating the Cys⁷⁹ and Cys⁷⁶ residues bound to Heme1 for example, would lead to a loss of some intensity in the rhombic trio that could then be assigned to this centre.

The relevance of the results presented here to the SoxAX catalytic mechanism are currently unclear, although it appears that pre-reduction of the protein is necessary to cause removal of one of the axial thiolate ligands, at least *in vitro*. The mechanism proposed by Bamford *et al* (10) shows that after binding to an adjacent conserved arginine residue, the thiosulphate molecule is transferred to the cysteine group of Heme 2, a two electron oxidative process. This results in the transfer of two electrons to Hemes 2 and 3, and they are subsequently reduced to the ferrous state. It is possible that reduction of these centres *in vitro* led to a conformational change that permitted the removal of the axial ligand of Heme 2. This one result now opens up the possibility of a variety of investigations into the function of Heme 2 at the active site of this protein.

5.7 References

1. Brimblecombe, P., and Yu Lein, A. (1989) *Evolution of the Global Biogeochemical Sulphur Cycle*, Wiley-Blackwell
2. Sauve, V., Bruno, S., Berks, B. C., and Hemmings, A. M. (2007) *J Biol Chem* **282**, 23194-23204
3. Kelly, D. P., Shergill, J. K., Lu, W., and Wood, A. P. (1997) *Antonie van Leeuwenhoek* **71**, 95-107
4. Sauvé, V., Bruno, S., Berks, B. C., and Hemmings, A. M. (2007) *J Biol Chem* **282**, 23194-23204
5. Kappler, U., Aguey-Zinsou, K., Hanson, G. R., Bernhardt, P. V., and McEwan, A. G. (2004) *J Biol Chem* **279**, 6252-6260
6. Dambe, T., Quentmeier, A., Rother, D., Friedrich, C., and Scheidig, A. J. (2005) *J Struct Biol* **152**, 229-234
7. Neutzling, O., Pfeleiderer, C., and Trüper, H. G. (1985) *J Gen Microbiol* **131**, 791-798.
8. Appia-Ayme, C., Little, P. J., Matsumoto, Y., Leech, A. P., and Berks, B. (2001) *J Bacteriol* **183**, 6107-6118.
9. Cheesman, M. R., Little, P. J., and Berks, B. C. (2001) *Biochemistry* **40**, 10562-10569.
10. Bamford, V. A., Bruno, S., Rasmussen, T., Appia-Ayme, C., Cheesman, M. R., Berks, B. C., and Hemmings, A. M. (2002) *EMBO* **21**, 5599-5610
11. Bamford, V. A., Berks, B. C., and Hemmings, A. M. (2002) *Biochem Soc Trans* **30**, 638-642
12. Page, C. C., Moser, C. C., Chen, X., and Dutton, P. L. (1999) *Nature* **402**, 47-52
13. Kappler, U., Bernhardt, P. V., Kilmartin, J., Riley, M. J., Teschner, J., McKenzie, K. J., and Hanson, G. R. (2008) *J Biol Chem* **283**, 22206-22214
14. Reijerse, E. J., Sommerhalter, M., Hellwig, P., Quentmeier, A., Rother, D., Laurich, C., Bothe, E., Lubitz, W., and Friedrich, C. G. (2007) *Biochemistry* **46**, 7804-7810
15. Aminlari, M., Malekhuseini, A., Akrami, F., and H., E. (2007) *Comp Clin Path* **16**, 47-51
16. Bordo, D., Deriu, D., Colnaghi, R., Carpen, A., Pagani, S., and Bolognesi, M. (2000) *J Mol Biol* **298**, 691-704
17. Denisov, I. G., Makris, T. M., Sligar, S. G., and Schlichting, I. (2005) *Chem Rev* **105**, 2253-2277.
18. Walker, F. A. (1999) *Coord Chem Rev* **186**, 471-534
19. McKnight, J., Cheesman, M. R., Thomson, A. J., Miles, J. S., and Munro, A. W. (1993) *Eur J Biochem* **213**, 683-687
20. Dawson, J. H., Andersson, L. A., and Sono, M. (1982) *J Biol Chem* **257**, 3606-3617.
21. Tsai, A. L., Berka, V., Chen, P. F., and Palmer, G. (1996) *J Biol Chem* **271**, 32563-32571
22. Dhawan, I. K., Shelper, D., Thorsteinsson, D., Roberts, G. P., and Johnson, M. K. (1999) *Biochemistry* **38**, 12805-12813
23. Bradley, J. M., Marritt, S. J., Kihlken, M. A., Haynes, K., Hemmings, A. M., Berks, B. C., Cheesman, M. R., and Butt, J. N. *J Biol Chem* **287**, 40350-40359
24. Gadsby, P. M. A., Hartshorn, R. T., Moura, J. J. G., Sinclair-Day, J. D., Sykes, A. G., and Thomson, A. J. (1989) *Biochim Biophys Acta* **994**, 37-46

25. Moore, G. R., Williams, R. J. P., Peterson, J., Thomson, A. J., and Matthews, F. S. (1985) *Biochim Biophys Acta* **829**, 83-96
26. Arciero, D. M., Peng, Q., Peterson, J., and Hooper, A. B. (1994) *FEBS Lett* **342**, 217-220
27. Cheesman, M. R., Greenwood, C., and Thomson, A. J. (1991) *Adv Inorg Chem* **36**, 201-255
28. Gadsby, P. M. A., and Thomson, A. J. (1990) *J Am Chem Soc* **112**, 5003-5011
29. Antonini, E., and Brunori, M. (1971) *Hemoglobin and myoglobin in their reactions with ligands* North Holland Pub. Co
30. Reijerse, E. J., Sommerhalter, M., Hellwig, P., Quentmeier, A., Rother, D., Laurich, C., Bothe, E., Lubitz, W., and Friedrich, C. (2007) *Biochemistry* **46**, 7804-7810

